Obscured activity and the role of environment on galaxy evolution at high redshift

Geach, James Edward

Obscured activity and the role of environment on galaxy evolution at high redshift

James Edward Geach

A Thesis presented for the degree of

Doctor of Philosophy

Extragalactic Astronomy
Department of Physics
University of Durham
England

September 2007

Dedicated to

My family

Obscured activity and the role of environment on galaxy evolution at high redshift

James Edward Geach

Submitted for the degree of Doctor of Philosophy
September 2007

Abstract

A significant amount of activity in the Universe is obscured by dust, produced in the final phases of stellar evolution and in the detonation of Type II supernovae. Re-processed radiation from starlight is emitted from this dust at infrared wavelengths, and this must be taken into consideration when performing surveys of star formation (and nuclear activity) in order to form an unbiased picture of galaxy evolution. It is also clear that the star formation histories of galaxies are significantly modified by their local environment, the outcome of which is the characteristic galaxy populations observed in rich clusters and in the field in the local Universe. In this thesis I examine galaxy evolution in the context of environment from $z \sim 0.5$ to $z \sim 3$, paying attention to obscured activity revealed by observations in the rest-frame infrared.

A mid-infrared (24μm) survey of two intermediate redshift clusters reveals a population of luminous infrared galaxies (LIRGs) which are missed in optical surveys (or significantly underestimated in terms of their star formation rates). Despite there being a large difference between the number of LIRGs detected in the two clusters (likely due to varying global cluster properties controlling the survival of starbursts in the cluster environment), these could be a potentially important population of galaxies. Their large star formation rates mean that they could evolve into local passive S0s by the present day.

Although the S0s must be assembled after $z \sim 0.5$, local clusters are also dominated by massive elliptical galaxies which are mostly already in place by $z \sim 0.5$, and therefore must have assembled their stellar mass at much higher redshifts ($z \gtrsim 3$). At $z = 3.1$ I examine the nature of extreme activity in a rich, primitive environment – an example of a progenitor of a rich cluster of galaxies, and therefore the likely site of formation of local massive ellipticals. A number of giant (100 kpc-scale) Lyman-α emission-line

nebulae (LABs) in the SA 22 protocluster contain bright submillimeter (850μm) galaxies (SMGs). Their extremely luminous rest-frame far-infrared emission suggest very high star formation rates and/or nuclear activity. Given that a large fraction of LABs seem to contain these active galaxies, it is plausible to link LABs' formation with feedback events such as superwind outflows from starburst regions. Indeed, a weak correlation between the SMGs' bolometric luminosity and the LABs' Lyα luminosities appears to suggest that SMGs are powering these extended haloes.

Although feedback from active galaxies appears to be important at early times, it remains a significant factor in galaxy-environment symbiosis at all epochs. The most profound effect a galaxy can have on its surroundings is to impart energy to the surrounding medium. In clusters, this is important for preventing the cooling of baryons and therefore the truncation of star formation. I investigate the environments of four low-power ($L_{1.4\mathrm{GHz}} \lesssim 10^{25}\,\mathrm{W\,Hz^{-1}}$) radio galaxies in the *Subaru–XMM-Newton Deep Field* at $z \sim 0.5$. The environments are all found to be moderately rich groups, and at least one shows evidence that it is in a stage of cluster assembly via sub-group merging. The conclusion is that the radio loud active galactic nuclei are triggered by galaxy-galaxy interactions within sub-groups, prior to cluster virialisation. These radio galaxies are destined to become brightest cluster galaxies, providing a low-power, but high-duty cycle feedback on gas in high-density regions at low redshift – necessary to suppress star formation in massive ellipticals at $z \sim 0$.

The hostility of clusters to star formation (or at least the observation that it is suppressed in the highest density regions of the local Universe) is thought to be in part responsible for the rapid decline in the global volume averaged star formation rate (SFRD) since $z \sim 1$. Tracking the evolution of the SFRD beyond $z \sim 1$ is hard, because optical tracers (e.g. Hα) used in the local Universe become redshifted into the near-infrared, and up until recently the cameras suitable for large surveys have not been available. I have performed the largest ever near-infrared narrowband blank field survey for Hα emission at $z = 2.23$. Understanding the evolution of the SFRD before its decline to the present day is essential if we are to find the 'epoch' of galaxy formation. I present the Hα luminosity function and measure the SFRD at this epoch, finding little evolution in the time between $z = 1.3$ and $z = 2.23$. This is consistent with a flattening of the SFRD, indicating that this is the peak era of star formation in the Universe, before the gradual suppression of activity during the build up of groups and clusters to the present day.

Declaration

The work in this thesis is based on research carried out at the Extragalactic Astronomy Group, the Department of Physics, Durham University, England. No part of this thesis has been submitted elsewhere for any other degree or qualification and it all my own work unless referenced to the contrary here or in the text. Some of this work has, however, been published in the following papers (in chronological order):

"A submillimetre survey of Lyα haloes in the SA22 protocluster at z = 3.1". Geach, J. E., Matsuda, Y., Smail, Ian, Chapman, S. C., Yamada, T., Ivison, R. J., Hayashino, T., Ohta, K., Shioya, Y. & Taniguchi, Y., 2005, Monthly Notices of the Royal Astronomical Society, 363, 1398

Chapter 4 note – §4.2: The VLA data were reduced by R. J. Ivison, who contributed some text in this section regarding this, which was further edited by me prior to publication. The SCUBA jiggle map of SA 22 was reduced by S. C. Chapman & C. Borys (private communication), however I extracted submm fluxes from this map, and these are quoted in the work.

"A Panoramic Mid-Infrared Survey of Two Distant Clusters" Geach, J. E., Smail, Ian, Ellis, R. S., Moran, S. M., Smith, G. P., Treu, T., Kneib, J.-P., Edge, A. C. & Kodama, T., 2006, Astrophysical Journal, 649, 661

Chapter 2 note – §2.2.2: Fully reduced ground based optical imaging was provided by T. Kodama, but I performed source detection and extracted photometry from these images. Similarly the WIRC K-band imaging was provided by G. P. Smith, who also provided some text in this section regarding the observations (which was subsequently edited by me). Again, I performed the source detection and extraction.

Spitzer Identifications and Classifications of Submillimeter Galaxies in Giant, High-Redshift, Lyα-Emission-Line Nebulae Geach, J. E., Smail, Ian, Chapman, S. C., Alexan-

der, D. M., Blain, A. W., Stott, J. P., Ivison, R. J., 2007, Astrophysical Journal, 655, L9

Chapter 4 note – §4.6.1: the *HST*-STIS image presented here was made available by S. C. Chapman, however the ACS image was reduced by me.

"Low-power radio galaxy environments in the Subaru/XMM-Newton Deep Field at z $\sim$ 0.5" Geach, J. E., Simpson, C., Rawlings, S., Read, A. M. & Watson, M., 2007, Monthly Notices of the Royal Astronomical Society, 381, 1369

Chapter 3 note – §3.2.1: The LDSS-2 spectra were observed by S. Morris and R. J. Whitaker, however I reduced the data.

§3.2.2: The *XMM-Newton* data was reduced by A. Read, who provided text regarding the reduction stages. This text was edited by me.

§3.3.4: The spectral fitting was performed by A. Read, who provides text regarding the fitting in this section. This was later edited by me. Note that the subsequent analysis that makes use of L_X and T_X (a result of the fitting) is my own work.

Acknowledgements

There are so many people to thank. Firstly it is a pleasure to say a big thank-you to my supervisor, Ian Smail, for having the faith in me to undertake this Ph.D when I thought I might never get the chance. I look up to Ian as an astronomer, and I aspire to gain similar experience and expertise during my career. I thank him for the many red-pennings which have vastly improved the clarity of my papers; getting me to write telescope proposals (despite the associated stress that often accompanies them); being patient with me when exciting results disappeared with a double checking; and for prodding me awake when I've tried to have a kip at 1 am at 14'000 feet.

Working at Durham I have been lucky enough to have been exposed to some very talented people, who also happen to be great to work with. Mark Swinbank deserves a thank-you for all the time and help he has given me (especially when a quick bit of data reduction needs doing!). There are many others who have been helpful throughout the past three years; and I would especially like to thank Dave Alexander, Richard Bower and Alastair Edge. Alan Lotts also deserves acknowledgement for managing the network so well – all problems I have had (mostly my own doing I should add) have been solved swiftly. I would like to mention Duncan Farrah here – without him I almost certainly would not have embarked on this Ph.D. Duncan took me on as an undergraduate research assistant during the summers of 2002 and 2003 at Imperial College. There is no doubt that the experience I gained from him during that time has held me in excellent stead for getting to where I am now, and for that I am very grateful. I don't think I'd be in this job without him.

I have been lucky enough to meet some great friends amongst my contemporaries at Durham, they have made the past three years a great laugh: Rob Crain, Mark Norris, Craig Booth, Greg Davies, Dave Wake, and of course John Stott. John has been my office mate all this time in the store-room-cum-office that is room 311. A passion for Radio 2 (especially the Jeremy Vine Show, weekdays 12–2pm); Elton John, David Bowie, Billy

Joel, etc.; toilet humour; the BBC website; foul language and incessant gossip has made sharing an office with him a pleasure, and I will miss him.

My family have provided me with unwavering support and love throughout, and I owe a great deal to them. It has been a long road getting here, and I have to be honest, at times I did not think I would make it. Nevertheless, they have never questioned my choice of career, which I understand must sometimes seem like a strange way to earn a living. They know I love what I do. This thesis is dedicated to all my family, and in particular my late grandpa William Nicholas. I'm sad he is not here to see this; I would love to have told him what I have found out about the Universe in the past few years. I hope he would be proud of me.

Finally, in the midst of all this, something came out of the blue. I save my last thank-you for Kristen, who I would never have met had Ian not offered me a studentship three years ago. Falling in love with you was something I could never have imagined when I started out, but it's the best thing that could have happened. You remind me that although I love astronomy, it's certainly not the most important thing in life.

Contents

List of Figures

List of Tables

From the way he spoke he might have been an art critic in a picture gallery. I was astonished. I confessed that I did not know which Aldebaran was – indeed, I had never even noticed that the stars were of different colours. Bozo began to give me some elementary hints on astronomy, pointing out the chief constellations. He seemed concerned at my ignorance. I said to him, surprised:

'You seem to know alot about stars'

'Not a great lot. I know a bit though ... The stars are a free show; it don't cost nothing to use your eyes'

George Orwell, *Down And Out In Paris And London*

Chapter 1

Introduction

1.1. Galactic taxonomy

One of the primary goals of contemporary observational cosmology is simple: to understand the formation of galaxies, and the physical processes that govern their subsequent evolution that culminates in the galaxy populations observed in the local Universe. To Hubble, galactic taxonomy could be pigeon-holed into the familiar 'tuning-fork' arrangement describing the gamut of galactic types (Hubble 1926). This zoo includes complex 'Grand Design' spiral galaxies with arms wound to various degrees of 'tightness' or containing mysterious bars; irregular galaxies with amorphous structures, and the symmetric elliptical galaxies that do not appear to harbour intricate stellar architectures. The tuning fork is aesthetically pleasing in the way it elegantly arranges the rich variety of galaxies observed to exist, however by modern standards it is naïve to connect them with an evolutionary path. We should forgive the Darwinian spirit of Hubble's concept, however, as is common in astronomy, we are left with historical baggage in our jargon: the archaic *late-* and *early-type* nomenclature for spirals and ellipticals respectively is a reminder of the first steps taken in this field where complexity was expected to arise from simple morphologies.

The science of galaxy evolution has progressed a great deal over the past century: our understanding constantly refined with ever improving technology enhancing our view of the early Universe over virtually the entire spectral range. Observations are to be compared to (and form inputs for) sophisticated theoretical models that aim to reproduce the evolution of galaxies from primordial conditions, and are now routinely tested on powerful computers. Needless to say, understanding how a galaxy is assembled from primordial conditions, and tracking the events that shape its destiny, is complicated. Al-

though the physical steps thought to occur at early times to 'seed' galaxies is reasonably well understood[1], there are myriad events and physical processes (not including those we have yet to envisage) that could influence the observable properties of galaxies in the subsequent ~13 Gyr leading to the present day. Unravelling and understanding those processes is the *raison d'etre* of observational cosmology.

Although the galaxies themselves are constructed from dark matter and a small fraction of baryonic material, all we are able to observe *directly* is luminous baryonic matter distributed within the dark matter halo (the differences in the optical light distribution as a function of wavelength dictate the morphological type described above). The sophistication of astronomical instrumentation has improved an incredible amount in the 400 years since Galileo's telescope. With large (currently up to 10 metre wide) collecting mirrors on Earth and somewhat smaller mirrors in space to capture optical and infrared light (not to mention the large range of devices dedicated to other spectral ranges – from radio to γ-rays), coupled to ingenious cameras and detectors, astronomers attempt to exploit the minute quantities of energy received from distant objects to infer information about the physical nature of galaxies. This task at first glance seems bewilderingly difficult, and it is true that it is not easy, but one of the most exhilarating aspects of this science is that it *is* possible to form robust conclusions about the very character of our Universe, to the extent of explaining why the local Universe is the way it is (our place in the Milky Way, the composition of the Local Group, the chemistry of our neighbouring galaxies, and their relative motions to give some examples), despite having a very limited vantage point – the Earth. There remain a vast number of unanswered questions. The new discoveries waiting to be made, and refinements to our standard model of galaxy evolution that need to be addressed make observational astronomy one of the most exciting of the modern sciences.

Since we may only directly observe radiation and not matter, we must rely on light alone to provide clues about the nature of distant galaxies: their mass, composition, luminosity, velocity, etc. At a fundamental level, galaxies can be classified according to their luminosity in a particular waveband. In addition to morphological information, the colour of a galaxy (or parts of a galaxy) can be used to identify those regions that are

[1]At least, in the cold dark matter paradigm, with the sites of formation of galaxies occurring at fluctuations in the relic radiation from the Big Bang, now observable in the power spectrum of the cosmic microwave background

currently forming stars. In fact, morphological data alone cannot really provide this information – it requires a leap of faith to assume that spiral galaxies are active and elliptical galaxies are not based solely on monochromatic observations, no matter how exquisite the resolution is. Colour is defined as the ratio of flux in some band pass to another ($f_{\lambda_1}/f_{\lambda_2}$ where $\lambda_1 > \lambda_2$, or in terms of magnitudes, $m_1 - m_2$). Galaxies undergoing star formation have spectra dominated by young, massive blue (hot) stars, compared to older galaxies where this population has evolved onto the red giant branch, resulting in blue and red colours respectively. Thus 'blue' and 'red' in astronomy are used synonymously with active and passive galaxies.[2] A more sophisticated way to disseminate activity in galaxies is by obtaining a spectrum, sorting radiation according to frequency into an energy distribution. Instead of the relatively crude colours which can only take us so far, spectroscopy allows us to dissect emission originating from specific wavelengths, and is a much more powerful tool to detect emission lines (common in star forming galaxies), absorption systems, and continuum features. Even better than single slit spectra are integral field observations which obtain 2-dimensional 'images', equivalent to placing many small slitlets over a galaxy. The resulting spectral 'map' can be a powerful tool for high redshift galaxy studies.

Although optical wavelengths undoubtedly represents the bulk of classical observational astronomy, the era of *multi*wavelength surveys has truly arrived – at least, in the field of extragalactic astronomy. By combining observational resources: radio, submillimeter, infrared, optical, ultraviolet and X-ray; we can piece together the panchromatic properties of distant galaxies which can provide a wealth more information than relying on an individual wavelength, which may be biasing our interpretation. Indeed, turning to longer wavelengths is crucial in the case of dust enshrouded galaxies as I will discuss shortly. In this thesis I aim to tackle some aspects of galaxy evolution with two main points in mind:

- How does a galaxy's local environment influence its destiny?
- What can dust insensitive observations tell us about galaxy evolution – in other words, how does our model change when we take into account obscured activity?

In the next two sections I will provide a very brief outline of why these two issues are important.

[2]Indeed, the term 'red and dead' is used commonly to describe giant passive ellipticals and lenticulars.

1.2. Galaxy evolution in the context of environment

Galaxies are not distributed haphazardly in space – they reside in a range of environments, from low density regions to massive congregations of objects. On large scales, galaxies are organised into a filamentary structure punctuated by high density cluster regions, and these delineate voids where the space density of galaxies approaches zero. Thus, a galaxy's environment can be parameterised in terms of the local density of neighbouring objects. There is overwhelming evidence that galaxies' destinies are significantly dependent on local environment. Old, passive systems are exclusively found in the cores of rich clusters of galaxies, and their conspicuous absence from the low density 'field'[3] is striking (Dressler 1980; Dressler et al. 1997; Smail et al. 1997; Couch et al. 1998; Fasano et al. 2000; Treu et al. 2003). The morphology-density ($T - \Sigma$) relation presented by Dressler (1980) describes the increasing fraction of elliptical and S0 types with increasing *local* surface density in clusters, compared to the opposite trend for late types. This was a generalisation of the morphology-radius relation ($T - R$), by Melnick & Sargent (1977) who noted that the fraction of early types falls of with increasing radial distance, compared to an increase in the spiral fraction (the $T - R$ relation is is equivalent to the $T - \Sigma$ relation in the case of relaxed clusters where there is a smooth correspondence between radius and local surface density). Dressler noted that it was only the local surface density that affected the morphological mix, suggesting that it is local environmental effects that control transformations between types. This was an important clue that the star formation histories of galaxies are significantly modified in dense regions of the Universe – in short, we observe a suppression of star formation as the local space density of galaxies increases. Tracking this behaviour over cosmic time should therefore reveal when and how gas rich spiral galaxies are transformed into passive early types that are destined to reside in the cores of rich clusters.

Butcher and Oemler made headway in understanding the evolution of environmental dependency by tracing the star formation rates (SFRs) in rich clusters of galaxies out to moderate redshifts ($z \sim 0.5$; Butcher & Oemler 1978), noting that the 'blue' fractions of cluster populations tend to increase out to high-redshift (although this could just be

[3]Throughout this thesis I will use the word 'field' in a general sense to describe the non-cluster environment

mimicking the general increase in star formation seen in all galaxies out to high redshift). This picture was improved with the inclusion of morphological data – i.e. the $T - \Sigma$ relation. Dressler et al. (1997) presented the evolution of $T - \Sigma$ since $z \sim 0.5$. The local $T - \Sigma$ result appears to hold out to $z \sim 0.5$, but only in clusters with high concentrations and that are dynamically relaxed, but not in irregular low-concentration clusters. The fact that the $T - \Sigma$ relation is seen in all types of cluster at $z \sim 0$, suggests that the rate of morphological segregation (as a function of local density) is dependent on the mass of the overall cluster. In addition, there appear to be far fewer lenticular S0 galaxies in $z \sim 0.5$ clusters compared to equivalent environments at low redshift, and a corresponding higher fraction of late types. This co-eval reversal strongly suggests that there is a direct evolutionary path between spiral galaxies in high redshift clusters, and the passive lenticulars that inhabit virialised structures in the local Universe. Elliptical galaxies on the other hand are largely already in place at $z \sim 0.5$ in both regular and irregular clusters, and therefore are likely to have formed at much earlier times, perhaps as early as $z \gtrsim 3$ (e.g. Oemler 1974). However, late assembly of early type galaxies via dry-mergers (i.e. mergers that do not result in additional star formation) could also explain the build-up of the red sequence (e.g. Bell et al. 2006; van Dokkum 2005).

What possible mechanisms (apart from dry merging) could transform gas rich, star forming spiral galaxies into passive S0s? To answer this, we must examine the nature of the cluster environment in greater detail. Clusters of galaxies are not simply characterised by the high spatial density of the galaxies themselves (although this is their most obvious observational property); they also contain large amounts of hot intracluster gas trapped within the potential well. This intracluster medium (ICM) emits bremsstrahlung radiation detected at X-ray frequencies (Sarazin 1988); thus X-ray surveys can be used to detect these massive systems. For a field spiral falling into the cluster potential on a radial orbit, the disc will experience ram pressure from passage through the dense ICM (Gunn & Gott 1972). One outcome of this is to strip gas from the disc and therefore remove the raw material needed for the formation of stars. Other direct influences of the ICM could be evaporation of the interstellar medium (Cowie & Songaila 1977; Haynes et al. 1984; Crowl et al. 2005; Nipoti & Binney 2007), or even pressure triggering of star formation (Dressler & Gunn 1983; Evrard 1991; Fujita 1998). On the other hand, galaxies could be partially shielded from bare exposure to the ICM if they enter the cluster in cold bound groups. There are several other dynamical processes that could occur: mergers and in-

teractions could trigger bursts of star formation (e.g. Icke 1985; Mihos 1995; Bekki 1998), although the rate of merging actually decreases in the dynamically hot cluster environment, again, unless they do so in small cold, bound groups where the relative velocities of galaxy pairs are sufficiently low to enable them to become gravitationally bound); so-called harassment (Moore et al. 1996, 1999; Moore, Lake, & Katz 1998) whereby star formation is triggered by tidal effects during high-speed galaxy-galaxy passes in the cluster potential. The rate of truncation of star formation in cluster galaxies is clearly dependent on a number of factors – competing mechanisms can both promote and terminate star formation. The most likely combined effect is labelled 'starvation': the slow decline in star formation rates in the infall gas-rich population (Treu et al. 2003).

Cluster suppression mechanisms thus appear to be a promising model to explain the apparent hostility of dense environments to active star formation in the local Universe, however there are still remaining issues. What are the relative efficiencies of the competing mechanisms described above, and how do they depend on global cluster properties such as temperature and dynamical state? Moreover, what is the exact nature of the transformation of a spiral into an S0? As it stands, the observed bulge-to-disc ratios of local S0s are too high to be produced from the populations of high redshift cluster spirals – they are not forming enough stars. I will address this issue in Chapter 2 of this thesis, where I examine the possibility of $z \sim 0.5$ clusters harbouring a population of starburst galaxies, but which have been previously been hidden from optical star formation surveys.

There is another important aspect of the cluster population that differs to the field, namely the interplay between active galaxies and the cluster itself: feedback. Although starburst galaxies can produce pressure driven winds that can reach escape velocity and impart energy to the surrounding medium (e.g. Veilleux & Rupke 2005), active galactic nuclei (AGN) can also be major contributors to feedback processes, with collimated jets extending up to 1 Mpc into the intergalactic medium. Although massive, old ellipticals may not be forming stars, they can still contain powerful radio sources (i.e. radio loud AGN), and so it is slightly misleading to discount the 'passive' cluster population as completely devoid of activity. At high redshift, many protocluster regions are associated with overdensities of galaxies around a powerful radio galaxy (e.g. Venemans et al. 2003), and their radio jets can impart large quantities of mechanical energy into the surrounding medium. In the case of rich clusters of galaxies, this medium is a plasma that is further heated by from the pdV work and shock heating from the encroaching jet. It is this heating

that is thought to be responsible for preventing the ICM from cooling at the expected rate. This has an important consequence: namely the ability for radio galaxies to suppress or shut down star formation in galaxies on a cluster-wide scale. Inclusion of AGN in recipes of galaxy formation have proved important in order to suppress the bright end of the luminosity function; feedback can truncate star formation and thus prevent the production of too many very luminous galaxies that semi-analytic models tend to over-predict (e.g. Bower et al. 2006).

As with star formation in dense environments, there is a complicated interplay between the triggering of AGN and global cluster properties. One way to trigger an AGN is similar to that of a starburst, that is, via mergers which can perturb material onto orbits ending on accretion discs around a central black hole. Since large clusters are thought to be assembled from the conglomeration of smaller sub-clusters (groups), one possible method to place AGN in the cores of rich clusters is to trigger them via galaxy-galaxy mergers within these groups during cluster assembly. Prior to relaxation, the ICM of clusters can therefore be heated from the depositing of energy from AGN and the larger scale sub-cluster merging (Randall, Sarazin & Ricker 2002). I discuss this topic further in Chapter 3.

1.3. The importance of obscured activity

Dust – the detritus of star formation (or rather, destruction) – conceals activity and confuses observations by extincting optical light; dimming emission lines and artificially reddening continua. Although the extincting effect of dust has long been known (Trumpler 1930), the exact nature of this interstellar material (its composition, size, geometry, etc.) is still under debate, although ever more accurate models are being developed to explain its spectral properties, aided by recent advances in infrared astronomy which heavily rely on space observational platforms. 'Dust' is a catch-all term that describes a mixture of (mainly) sub-micron and larger scale silicate and graphite grains (Mathis et al. 1997; Draine & Lee 1984) and long chained aromatic molecules containing hundreds or thousands of carbon atoms (polycyclic aromatic hydrocarbons [PAHs], Siebenmorgen & Krügel; 1992; Li & Draine 2002; Draine & Li 2007). The grains are stochastically heated by absorbing energy in the interstellar radiation field, and cool by re-radiating at infrared wavelengths. In the far-infrared (40–500μm) the dominant contribution to the emission

is from thermal radiation of large silicate and graphite grains at fairly cool temperatures (20–60 K), heated in the interstellar radiation field, or by a nuclear source (e.g. Blain, Bernard & Chapman 2003). The mid-infrared emission is thought to arise from heating of smaller ($\lesssim 0.1\mu$m) grains and aromatics around stronger UV radiation fields such as in the vicinity of massive stars (Sellgren 1984), and are therefore much hotter than the dust responsible for the far-infrared continuum, which is at thermal equilibrium with the radiation field. However, larger scale grains in HII regions could also contribute to the mid-infrared continuum (Osterbrock 1989; Mouri et al. 1997). The mid-infrared can exhibit a rich variety of emission and absorption systems, the principle features being PAH emission at 3.3, 3.6, 6.2, 7.7, 8.6 & 11.3μm due to stretching and bending modes of C-H and C-C bonds in aromatic molecules; and a prominent absorption trough at 9.7μm due to a Si-O stretching mode (Draine 2003). These are interspersed with other features (for example neon, argon & iron emission lines; water ice), and superimposed on the mid-infrared continuum. PAH emission tends to be much weaker in AGN powered galaxies, since the molecules responsible are easily destroyed in the intense UV field (compared to a starburst), and the spectral slope of the mid-infrared continuum increases with the hot dust, reducing the contrast of any emission lines present (e.g. Genzel et al. 1998; Rigopoulou et al. 1999). Thus, mid-infrared spectroscopy can be used to probe a range of physical conditions in active galaxies, where optical tracers might be much harder to detect: for example, relative AGN/starburst contribution to the infrared luminosity; optical depth to the power source and star formation rates from the strength of PAH emission features.

The prevalence of dust is exacerbated in the more intensely star forming systems, since it must form primarily in supernovae, novae and the atmospheres of pulsating asymptotic red giant (AGB) stars (Hoppe & Zinner 2000; Andersen 2007). The enhanced rate of formation and destruction of stars in galaxies undergoing a starburst episode should result in a corresponding enhancement in the rate of dust production. Thus observations that rely on the rest-frame UV to infer star formation may significantly underestimate the true level of activity, and miss the bright tail of the luminous population. In the most extreme cases, extinction can have dramatic consequences for observational measurements, for example rendering emission lines undetectable and continua too faint to be included in magnitude limited surveys. An example of a population of extremely luminous but highly obscured galaxies at high redshift are submillimeter galaxies (SMGs),

discovered from their rest-frame far-infrared emission with the Submillimeter Common User Bolometer Array (SCUBA) on the James Clerk Maxwell Telescope (Smail et al. 1997). Although determining the redshifts of SMGs is challenging, it has been suggested that they reside at $z \sim 2.5$ by obtaining optical spectra at the locations of radio counterparts (Chapman et al. 2005). That SMGs are also detected at radio frequencies is not surprising, given the radio-far-infrared correlation (e.g. Condon et al. 2002). These galaxies are extremely hard to detect at other (especially optical) wavelengths (e.g Ivison et al. 2007), making follow-up observations challenging, but assuming reasonable parameters for the form of the far-infrared SED implies that SMGs have extreme bolometric luminosities, $\gtrsim 10^{12} L_{\odot}$, powered by intense star formation at rates of 100–1000$\times$ that of our own Galaxy, or are experiencing significant nuclear activity related to the growth of a supermassive black hole (SMBH) at their core. Their large dynamical masses ($\gtrsim 10^{11} M_{\odot}$) derived from observations of their Hα lines (e.g. Swinbank 2004; 2005; 2006) imply they are some of the most massive galaxies at $z \sim$ 2–3, and are thus good candidates for the progenitor population of local massive ellipticals currently undergoing a period of stellar mass assembly (and/or SMBH growth – the two should be linked, given the observation of the correlation between stellar mass and black hole mass in the bulges of local massive spheroidals; Kormendy & Richstone 1995; Magorrian et al. 1998; Gebhardt et al. 2000).

Including these obscured, but potentially extremely active galaxies is of crucial importance for surveys which aim to track star formation. Over the last two decades or so there has been significant advances in tracking obscured activity with a range of space platforms for observing at mid- and far-infrared wavelengths, the most notable being the *Infrared Astronomy Satellite (IRAS)*, the *Infrared Space Observatory (ISO)* and more recently the *Spitzer Space Telescope (SST)*. *IRAS*'s major contribution to the field was its all-sky survey, which brought with it the discovery of a large population of galaxies that emit the bulk ($\gtrsim$60%) of their bolometric output at infrared wavelengths (see the review by Sanders & Mirabel 1996), and the majority of the most luminous ($\gtrsim 4L_{\star}$) galaxies in the local Universe were found to be highly obscured by dust. What are the implications for the study of galaxy evolution? In a cosmological sense, if we are tracing the evolution of the global star formation rate as function of time, then we may see a boosting of the star formation rate density (SFRD) when the obscured populations are included. It is not quite this simple though: galaxies are much easier to observe in the local Universe, compared to those seen in the past (for the obvious reasons of them being both fainter

and smaller). Our understanding of the evolution of the SFRD out to at least $z \sim 1$ is reasonably good – with a range of star formation tracers agreeing that the SFRD has been decreasing strongly over the past 8 Gyrs. The major problems arise when tying down the level of activity at much higher redshifts, $z \gg 1$. Most of the measurements of the volume averaged star formation rate at early times are from either (a) surveys that rely on rest-frame UV indicators or (b) submm (rest-frame far-infrared) surveys. As we have mentioned, the UV surveys are severely affected by dust extinction, and so large corrections must be made to account for the resultant underestimation of the SFR. Conversely, the bright flux limits of submm observations mean that extrapolations need to be made to account for the faint population. Needless to say, the small survey areas of star formation at high redshift mean that cosmic variance is also a significant problem. The mixture of indicators, and the combination of their inherent uncertainties and limitations results in poor constraints on the evolution of the SFRD since the epoch of reionisation. Measuring this fundamental parameter with better accuracy is a paramount concern of modern observational cosmology, and I discuss this in Chapter 5.

In terms of the galaxies themselves, there is an obvious conclusion arising from the observation of a significant obscured component – namely that they are forming large numbers of stars, or contain an active nucleus that might not be otherwise detected. Obviously this has profound implications for models of galaxy formation, since these are characterised by star formation histories, and to some extent the formation of central SMBHs.

1.4. Outline of this thesis

In this thesis I aim to contribute to the field by investigating the role of environment in influencing the evolution of galaxies, paying particular attention to the star formation activity that is hidden from traditional optical views, revealing the obscured activity with infrared and submillimeter wavelengths. Here I provide a brief overview of the scientific chapters presented in this thesis, outlining the main scientific goal and principle results from each.

1.4.1 Chapter 2 – A mid-infrared survey of two distant clusters

This thesis starts in the relatively low-redshift Universe. In this chapter we present panoramic *Spitzer MIPS* 24-μm observations covering $\sim$9$\times$9 Mpc (25′ $\times$ 25′) fields around two massive clusters, Cl 0024+16 and MS 0451−03, at $z = 0.39$ and $z = 0.55$ respectively, reaching a 5-σ flux limit of $\sim 200\mu$Jy. The observations cover a very wide range of environments within these clusters, from high-density regions around the cores out to the turn-around radius. We find excesses of mid-infrared sources with optical/near-infrared colours expected of cluster members in the two clusters and test this selection using spectroscopically confirmed 24μm members. Mid-infrared spectroscopy suggests that the mid-infrared emission is mainly due to star formation, rather than AGN. There are clearly significant cluster-to-cluster variations in the populations of mid-infrared sources, probably reflecting differences in the intracluster media and recent dynamical evolution of these systems.

1.4.2 Chapter 3 – The environments of low-power radio galaxies at intermediate redshift

We present multi-object spectroscopy of galaxies in the immediate (Mpc-scale) environments of four low-power ($L_{1.4\mathrm{GHz}} \lesssim 10^{25}\,\mathrm{W\,Hz^{-1}}$) radio galaxies at $z \sim 0.5$, selected from the *Subaru/XMM-Newton Deep Field*. We use the spectra to calculate velocity dispersions and central redshifts of the groups the radio galaxies inhabit, and combined with *XMM-Newton* (0.3–10 keV) X-ray observations investigate the L_X–σ_v and T_X–σ_v scaling relationships. All the radio galaxies reside in moderately rich groups – intermediate environments between poor groups and rich clusters, with remarkably similar X-ray properties. We concentrate our analysis on one system that we interpret as a low-power (FR I) source triggered within a sub-group, which in turn is interacting with a nearby group of galaxies, containing the bulk of the X-ray emission for the system – a basic scenario which can be compared to more powerful radio sources at both high ($z > 4$) and low ($z < 0.1$) redshift. This suggests that galaxy-galaxy interactions triggered by group mergers may play an important role in the life-cycle of radio galaxies at all epochs and luminosities.

1.4.3 Chapter 4 – Extreme activity in a rich, primitive environment

We present the results from a submillimetre (submm) and mid-infrared survey of a sample of giant Lyα emitting nebulae in the overdensity at $z = 3.09$ in the SA 22 field. These objects have become known as Lyα Blobs (LABs), however the nature of their power-source remains unclear, with both cooling flows or starburst/AGN ionised winds being possibilities. Using the SCUBA submm camera on the JCMT, we measure the 850 μm flux of a sample of LABs. We present detections of submm emission from four LABs at $> 3.5\sigma$ individually, and obtain a modest statistical detection of the full sample at an average flux of 3.0 ± 0.9 mJy. These submm detections indicate significant activity within the LAB haloes, with bolometric luminosities in the ultraluminous regime ($> 10^{12}\,L_{\odot}$), equivalent to a star formation rate of $\sim 10^3\,M_{\odot}\,\mathrm{yr}^{-1}$. We suggest that the highly-extended Lyα haloes (which define the LAB class) may be a common feature of the submm galaxy population in general, underlining their role as potentially important sources of metal enrichment and heating of the intergalactic medium.

In addition to the submm survey, using *Spitzer Space Telescope* IRAC (3.6–8μm) and MIPS (24μm) imaging, as well as *Hubble Space Telescope* optical observations, we identify the IRAC counterparts of the luminous power sources residing within the two largest and brightest submm-LABs (LAB 1 and LAB 2). From their rest-frame optical/near-infrared colours, we conclude that the SMG in LAB 1 is likely to be starburst dominated and heavily obscured ($A_V \sim 3$). In contrast, LAB 2 has excess rest-frame $\sim$2μm emission (over that expected from starlight) and hosts a hard X-ray source at the proposed location of the SMG, consistent with the presence of an active galactic nucleus (AGN). We conclude that LAB 1 and LAB 2 appear to have very different energy sources despite having similar Lyα spatial extents and luminosities, although it remains unclear whether on-going star-formation or periodic AGN heating is responsible for the extended Lyα emission.

1.4.4 Chapter 5 – A panoramic near-infrared narrowband survey of star forming galaxies at $z = 2.23$

We present results from a pilot narrowband survey of emission-line galaxies at $z = 2.23$, using the Wide Field Camera on the United Kingdom Infrared Telescope. The H_2S1 narrowband filter ($\lambda_c = 2.121\mu$m, $\delta\lambda = 0.021\mu$m) is sensitive to the Hα emission line redshifted into the K-band at $z = 2.23$, thus suitable for selecting 'typical' star forming galaxies and active galactic nuclei at this epoch. The pilot study was un-

dertaken in the well studied *Cosmological Evolution Survey* (COSMOS) field. Our survey is the largest near-infrared narrowband survey at this depth, with a line flux limit of $f_{\mathrm{H}\alpha} \sim 10^{-16}\,\mathrm{erg\,s^{-1}\,cm^{-2}}$ over 0.603 square degrees, probing $\sim$220 $\times$ 10^3 Mpc^3 (comoving) down to a star formation rate limit of $\sim 40\,M_\odot\,\mathrm{yr}^{-1}$. In this chapter we present the initial results of our survey and evaluate the luminosity function of Hα emitters at $z = 2.23$. The integrated luminosity function is used to estimate the volume averaged star formation rate at this epoch, which we find to be $0.27 \pm 0.02\,M_\odot\,\mathrm{yr}^{-1}\,\mathrm{Mpc}^{-3}$. This value appears to support the picture of a plateauing of the star formation rate density at $z \sim$1–2.

1.4.5 Chapter 6 – Conclusions, summary and future work

In this final chapter I summarise the major results from this thesis, and discuss the possible avenues of future research that could result from it.

Chapter 2

A mid-infrared survey of two distant clusters

2.1. Introduction

The galaxy populations within the virialised regions of rich clusters at $z \sim 0$ are characterised by passive elliptical and lenticular (S0) galaxies (Oemler 1974; Dressler 1980). In contrast, 5-Gyrs ago, at $z \sim 0.5$, the galaxy populations in the most massive clusters had larger fractions of star-forming late-type spirals, and a corresponding deficit of luminous S0 galaxies (e.g. Dressler et al. 1997; Smail et al. 1997; Couch et al. 1998; Fasano et al. 2000; Treu et al. 2003). Taken together, these two observations imply that a process (or processes) is transforming many of the star-forming, late-type spirals in these regions into the passive early-type population (specifically S0s) found in local clusters (Poggianti et al. 1999; Moran et al. 2007)

When considering potential pathways to produce this evolutionary change, we need to bear in mind that the typical luminosities of the star-forming spirals appear to be too low for them to transform into typical S0 galaxies found in local clusters, without the addition of significant numbers of new stars (Poggianti et al. 1999; Kodama & Smail 2001). This problem is exacerbated when we include the fading which is likely to take place after the cessation of star formation in these galaxies. This then leads us to concentrate on mechanisms which are capable of increasing the luminosity of the galaxies – mergers and starbursts. There has been a recent upsurge in interest in the potential for so-called "dry" mergers (mergers between dissipationless stellar systems which don't result in additional star formation) to influence the evolution of early-type galaxies (van Dokkum et al. 2003; Bell et al. 2003; van Dokkum 2005). However, the dynamically hot environments

in rich clusters which are the subject of our study are deleterious to the formation and survival of cold, bound-pairs of early-type galaxies – unless these systems arrive in the cluster as existing bound entities. It is not clear, therefore, that dry mergers can provide an effective route to substantially increase the number of luminous, early-type S0 galaxies within clusters.

Unfortunately, the alternative mechanism for enhancing the luminosity of the bulge component – a starburst – also has strong observational evidence stacked against it. Surveys of star-forming galaxies in clusters using optical or UV star formation indicators have failed to detect galaxies with strongly enhanced star-formation which would have to exist to explain the growth of the bulge components of early-type galaxies in clusters at $z \lesssim 0.5$–1 (Balogh et al. 1999; Poggianti et al. 1999; Gerken et al. 2004). However, there is growing body of evidence that at least some of the galaxies in distant clusters may be undergoing bursts of star-formation, albeit ones which are heavily shrouded in dust. Smail et al. (1999) used a deep VLA 1.4-GHz radio map to study a small sample of active galaxies within the core of the cluster Cl 0939+4713 ($z = 0.41$). Combining the radio data with near-infrared and optical morphological information from the *Hubble Space Telescope (HST)* and ground-based spectroscopy, they found that over half the radio-emitting population in the core are dusty late-type galaxies, presumably undergoing vigorous star formation. However, the spectral classification of these spirals placed them in the post-starburst class, and indeed all the post-starburst galaxies in this small region are radio-emitters. Dust has also been used to explain the unusual spectral properties of another class of galaxies found in distant clusters and the field: e(a) galaxies, which show enhanced Balmer absorption compared to normal star-forming galaxies (Poggianti et al. 1999). Poggianti & Wu (2000) and Poggianti, Bressan & Franceschini (2001) discuss models for these galaxies invoking age-dependent dust obscuration of the younger stellar populations – enabling significant activity to be hidden from view in these systems. If the passive lenticular galaxies found in local clusters, but absent from the equivalent rich environments at higher redshift, are the result of infalling late-type galaxies undergoing dusty-starburst in high-z clusters, then a possible signature would be evolution in the total level of obscured star-formation in clusters out to $z \sim 1$.

In principle, mid- and especially far-infrared/submillimeter observations give us a direct probe of the level of obscured activity in distant clusters. In particular, mid-infrared observations with *Infrared Space Observatory (ISO)*, and more recently *Spitzer Space Tele-*

scope (SST), provide sensitive imaging capabilities which can trace dusty star formation in clusters out to $z \sim 1$ and beyond (Bai et al. 2007; Marcillac et al. 2007). Metcalfe, Fadda & Biviano (2005) summarise the results from *ISO* surveys of distant clusters, which have yielded a total of just $\sim$ 40 cluster galaxies detected at 15 μm across seven clusters between $z = 0.18$–0.56 (Duc et al. 2000, 2004; Fadda et al. 2000; Metcalfe et al. 2003; Coia et al. 2005a,b; Biviano et al. 2004). All these studies suggest that there is an increased level of mid-infrared activity in distant clusters, at levels above that suggested by UV/optical tracers of star formation. Submillimeter observations of more distant clusters have also hinted at possible enhanced activity in these environments (Best 2000; Webb et al. 2005). However, the inhomogeneous mix of coverage and depth in the samples coupled with the modest numbers of sources detected in any individual cluster mean that it has proved difficult to use these data to provide quantitative constraints on the origin and evolution of dust-obscured activity in distant clusters.

The *SST*'s sensitive mid-infrared imaging capabilities provide an unique opportunity to undertake complete and representative surveys of the obscured, active populations in distant clusters. To search for a population of mid-infrared sources in rich clusters environments, we have therefore used the Multiband Imaging Photometer for *Spitzer* (MIPS) to detect 24-μm emission from galaxies in two clusters at $z \sim 0.5$ covering a very wide range in environment from $\sim$ 1 Mpc out to the turn-around radius ($\sim$ 5 Mpc) where the clusters merge into the surrounding field. These observations will provide measures of the level of obscured star-formation in these clusters, and so allow us to build up a reliable picture of the evolution of dust-obscured activity in clusters over the past 5 Gyrs.

Finally, to test that mid-infrared detections in the clusters are actually star-forming (rather than nuclear powered) systems, we present mid-infrared spectra of a small sample of LIRGs in Cl 0024+16. The features of these spectra (in the range $\sim$5–20μm) are useful probes of the various contributions of nuclear and star formation to the infrared luminosity. In the case of intense star formation for example, we expect to detect strong emission from polycyclic aromatic hydrocarbons (PAHs), compared to weaker PAH line strengths compared to the continuum emission for AGN.

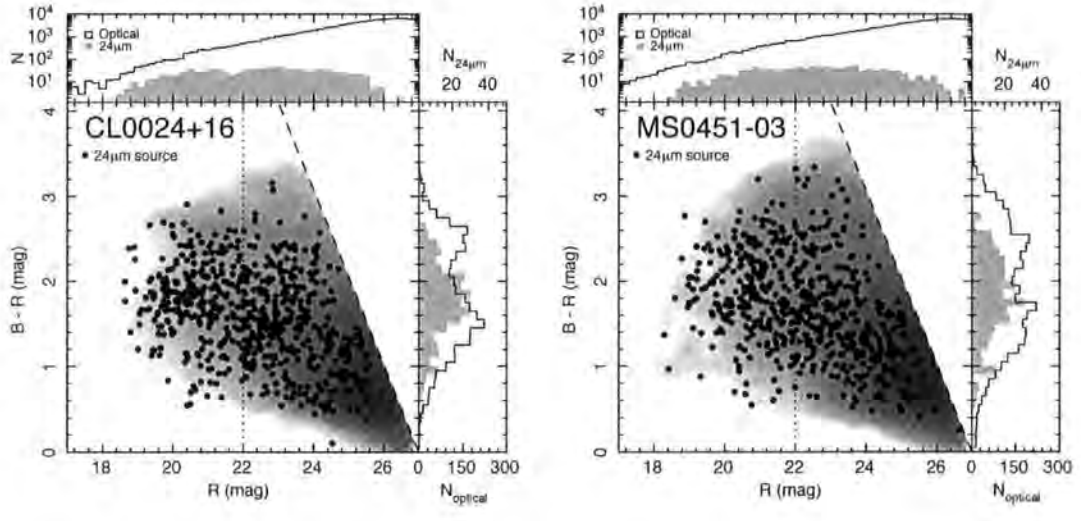

Figure 2.1: The $(B-R)$–R color-magnitude diagram for (left) Cl 0024+16 and (right) MS 0451−03. We identify 24-μm sources brighter than 200μJy and compare these to the distribution for the optically-selected populations in these fields (for clarity, this has been represented by a smoothed density plot). Also shown are histograms showing slices through the distributions, comparing the number counts and colors for the mid-infrared sources to the optically-selected population. To emphasise the location of the sequence of early-type galaxies in the clusters, the $(B-R)$ histogram is limited to $R \leq 22$. The mid-infrared selected population lies between the red and blue galaxy peaks in these fields, most likely because of the influence of dust on intrinsically blue, star-forming galaxies. For the mid-infrared sources in the color-magnitude diagram we have removed those objects morphologically classified as stars. All colors are measured in 2″ diameter apertures, and we use the BEST_MAG estimate of the total galaxy magnitude.

2.2. Mid-infrared survey: observations & reduction

The two clusters chosen for this study are unique in having panoramic *HST* imaging covering $\sim 25'$-diameter fields – extending from the cores out to the turn-around radii of the clusters (Treu et al. 2003; Kneib et al. 2003; Moran et al. 2005). These data have been used for weak-lensing analysis of these clusters, yielding 2-D maps of the dark matter distributions on $\sim$ 5-Mpc scales in the structures (Kneib et al. 2003). Panoramic studies of the galaxy populations in these clusters also benefit from extensive deep, ground-based optical and near-infrared imaging and spectroscopy (Moran et al. 2006 in prep). Although both clusters are relatively rich, they differ in their X-ray luminosities: Cl 0024+16 ($z = 0.39$) has a relatively modest X-ray luminosity, $L_X \sim 3.2 \times 10^{44}$ ergs s^{-1} (Treu et al. 2003), while MS 0451−03 ($z = 0.55$) is some 8$\times$ more luminous. This distinction may lead to differences in the effectiveness of the various processes influencing star formation (Treu et al. 2003), as traced by the distribution of the mid-infrared population. This will be useful in our subsequent detailed study to disentangle the potential mechanisms for triggering and suppressing star formation.

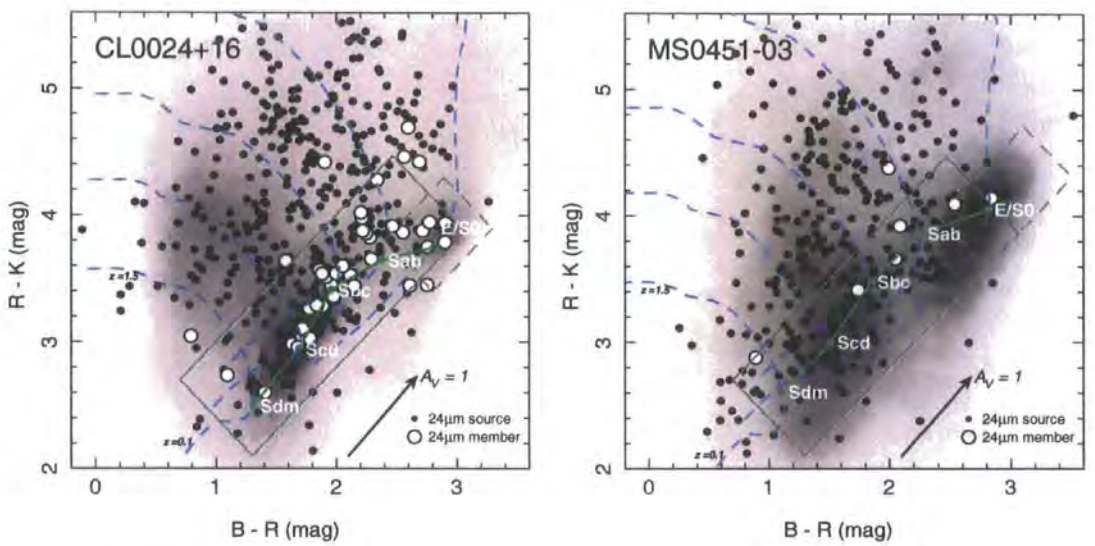

Figure 2.2: We show $(R - K)$ versus $(B - R)$ colors for 24μm-detected sources compared to the optical distribution in the Cl 0024+16 (left) and MS 0451−03 (right) fields. The distributions are limited at $R \leq 24$ and $K \leq 20$ and we represent the optical sample's number density as a slightly smoothed grayscale. The dashed tracks trace the expected colors of galaxies across $z = 0$–2, with star formation histories similar to that of present-day Sdm–E galaxies, and the solid line and points show the location in color–color space of the range of spectral types at the cluster redshift. The arrow indicates the translation in color–color space corresponding to an increase in reddening of $A_V = 1$. To perform a rough photometric cut to select 24μm sources at the cluster redshift, we define a region around the predicted colors of cluster members indicated by the rectangular selection boxes in both panels. To avoid contamination by infrared emission from AGN, we designate a sub-region which should contain the passive galaxies (dashed-line box) – 24μm sources in this region are not included in our analysis of the obscured star-forming populations. We show the efficacy of this selection by plotting the colors of known spectroscopically-confirmed 24μm cluster members, 85% of these fall within the selection box.

Papovich, C., Dole, H., Egami, E., Le Floc'h, E., Perez-Gonzalez, P. G., Alonso-Herrero, A., Bai, L., Beichman, C. A., Blaylock, M., Engelbracht, C. W., Gordon, K. D., Hines, D. C., Misselt, K. A., Morrison, J. E., Mould, J., Muzerolle, J., Neugebauer, G., Richards, P. L., Rieke, M. J., Rigby, J. R., Su, K. Y. L., Young, E. T., 2004, ApJS, 154, 70

Parma, P., Murgia, M., de Ruiter, H. R. & Fanti, R., 2002, New Astronomy Reviews, 46, 313

Pascual, S., Villar, V., Gallego, J., Zamorano, J., Pelló, R., Díaz, C., Aragón-Salamanca, A., 2005, Properties of Hα-selected star-forming galaxies from $z \sim 0.8$ to now, Revista Mexicana de Astronomia y Astrofisica Conference Series, Eds.: Hidalgo-Gámez, A. M., González, J. J., Rodríguez Espinosa, J. M., Torres-Peimbert, S., 24, 268

Poggianti, B. M., Smail, I., Dressler, A., Couch, W. J., Barger, A. J., Butcher, H., Ellis, R. S., Oemler, A. J. , 1999, ApJ, 518, 576

Poggianti, B. M., Wu, H., 2000, ApJ, 529, 157

Poggianti, B. M., Bressan, A., Franceschini, A., 2001, ApJ, 550, 195

Polletta, M. d. C., Wilkes, B. J., Siana, B., Lonsdale, C. J., Kilgard, R., Smith, H. E., Kim, D.-W., Owen, F., Efstathiou, A., Jarrett, T., Stacey, G., Franceschini, A., Rowan-Robinson, M., Babbedge, T. S. R., Berta, S., Fang, F., Farrah, D., González-Solares, E., Morrison, G., Surace, J. A., Shupe, D. L., 2006, ApJ, 642, 673

Ponman, T. J., Helsdon, S. F., Finoguenov, A. 1999, in ASP Conf. Ser. 176: Observational Cosmology: The Development of Galaxy Systems, 64

Ponman, T. J. Cannon, D. B., Navarro, J. F., 1999, Nature, 397, 135

Pope, A., Scott, D., Dickinson, M., Chary, R.-R., Morrison, G., Borys, C., Sajina, A., Alexander, D. M., Daddi, E., Frayer, D., MacDonald, E., Stern, D., 2006, MNRAS, 370, 1185

Popesso, P., Biviano, A., Böhringer, H., Romaniello, M., 2007, A&A, 461, 397

Randall, S. W., Sarazin, C. L. & Ricker, P. M., 2002, ApJ, 577, 579.

Rasmussen, J.; Ponman, T. J.; Mulchaey, J. S.; Miles, T. A.; Raychaudhury, S., 2006, MNRAS, 373, 653

2.2.1 MIPS 24μm observations

MIPS 24μm observations of the fields of Cl 0024+16 ($z = 0.39$) and MS 0451−03 ($z = 0.55$) were obtained with *SST* in fixed-cluster offset mode on 2004 December 24–25. The observations of Cl 0024+16 are centered on 00 26 35.70, +17 09 45 (J2000); while those for MS 0451−03 are centered on: 04 54 10.80, −03 00 57 (J2000). The observations avoided the central $\sim 5' \times 5'$ of each cluster, which are part of Guaranteed Time Observations (*SST* Program #83). For MS 0451−03 we have acquired these data from the archive, and incorporated them into this work to provide coverage of the central region of the cluster. The observations of the core of Cl 0024+16 have only just become available via the *Spitzer* archive at the time of writing, and will be added to this work in a future work when the 24μm data have been reduced and analysed. In the current work we make use of existing mid-infrared observations from *ISOCAM* at 15μm (Coia et al. 2005), which traces similar emission to that sampled by MIPS (namely emission from polyaromatic hydrocarbons). These allow us to place limits on the mid-infrared population in the central regions of Cl 0024+16.

Each field was covered in a 5×5 grid (omitting the central pointing) yielding a 24-point mosaic. We adopted two 10-s cycles for our exposures producing a per-AOR pixel exposure of 312.5s, and the total elapsed time for the AOR was 9.78 ks. The template AOR was repeated three times to provide redundancy and for the identification of cosmic rays and asteroids (the latter can be common in 24μm MIPS data). The total exposure time per pixel is 938 s, which should achieve our goal of a 5-σ detection limit of 200μJy at 24μm.

The basic-calibrated 24μm data provided by the *Spitzer* Science Center were first corrected for gradients, bright latents and the "jailbar" effect using calibration frames generated from the data. These were then mosaiked using the MOPEX package.[1] Due to the 'first frame effect' (frames with a shorter exposure and a depression in response of up to 15%), the initial frame in each pointing was discarded, which improved flatness in the final mosaic. We implemented the the area-overlap interpolation method in the mosaicking procedure (Makovoz & Khan 2005). The mosaics cover total areas of $\sim$0.21 sq. degrees in both clusters.

[1] MOPEX is maintained by the *Spitzer* Science Center: http://ssc.spitzer.caltech.edu

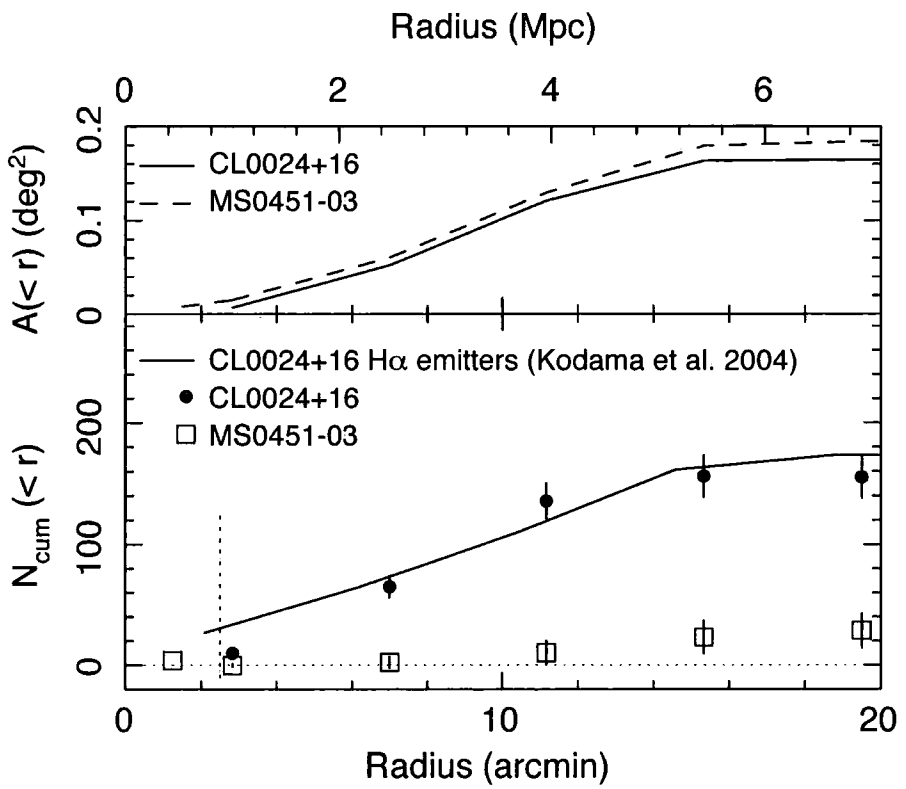

Figure 2.3: The lower panel shows the cumulative number of probable 24μm cluster members (brighter than 200μJy) as a function of radial separation from their respective cluster centers. Probable cluster members are isolated based on their $(R-K)$-$(B-R)$ colors (see Fig. 2.2). We correct the distributions for residual field contamination using a similar color-cut on the SWIRE ELAIS N1 survey (Lonsdale et al. 2003, 2004, Surace et al. 2004), giving an estimated field correction of $\sim 0.16 \pm 0.02$ arcmin^{-2}. The estimated numbers of members could also be increased by $\sim$ 18% to account for the incompleteness in our color-selection, although we have not done so here. We also plot the cumulative number of Hα-emitting (EW(Hα) >40Å) cluster members in Cl 0024+16 from the survey by Kodama et al. (2004), which exhibits a similar rise to that exhibited by the 24μm population in this cluster. In contrast, MS 0451−03 shows little evidence for a strong mid-infrared population. The top panel illustrates the variation in survey area with radius in our two fields, this shows that the slower increase in the cumulative 24μm counts beyond 5 Mpc in Cl 0024+16 is purely due to the decline in coverage in the outskirts of our survey. The errors on our observations are the combination of counting statistics and the measured variance in the field number counts. The physical scale assumes an average redshift of $z = 0.47$.

Source extraction was performed using SExtractor version 3.1 (Bertin & Arnouts 1996) with the criteria that a source consists of at least 3 contiguous pixels (each pixel is 2.5″ square) at $\geq 2\sigma$ above the background. We measure 16-″ diameter aperture fluxes, corresponding to $\sim 3\times$ FWHM of the PSF (FWHM of $\sim 5''$ at 24μm). Using a curve-of-growth analysis on bright isolated point sources, and our completeness simulations, we find that 16″ apertures recover $\sim$ 75% of the total flux and we therefore correct the resulting fluxes by a factor of $1.33\times$ to yield total fluxes. We visually inspect the extracted objects overplotted on the images, and remove sources which appear to be false, e.g. in the slightly noisier regions on the edge of the image.

The flux detection limits and completeness of each mosaic was determined by inserting 10 sets of 10 simulated sources into the mosaics for a range of flux and determining their detection rate and recovered fluxes using identical extraction parameters. The sources used in the simulations were high signal-to-noise composites formed by stacking a large number of real, isolated faint sources. From these simulations we estimate that the 80% completeness limits of our observations are 180μJy in Cl 0024+16 and 200μJy in MS 0451−03.

The archival mid-infrared data for the central region of MS 0451−03 (Program #83), were obtained from the *Spitzer* archive. The observations were taken on 2004 September 23, centered on 04 54 10.8, −03 00 57 (J2000). We use the post–basic-calibrated data, and subject it to the same extraction criteria as described in §2.1. These data are slightly shallower than our mosaic, and we take this into account in our subsequent analysis.

2.2.2 Archival optical & near-infrared imaging

We use existing deep optical and near-infrared imaging to obtain colors for the 24μm sources in these regions. For both clusters we use Subaru SuprimeCam B- and R-band observations taken for the PISCES survey (Kodama et al. 2005). The Cl 0024+16 field was observed on 2002 September 6 under good conditions. The seeing was $\sim$ 0.7–1″ for the R- and $\sim$ 1–1.3″ for the B-band, with exposure times of 5,280 s and 3,600 s respectively, reaching a depth of $R \sim 27$ (we use Vega-based magnitudes throughout). The observations and data reduction technique are described in Kodama et al. (2004). MS 0451−03 was observed on 2001 January 21–22, again in good conditions with 1.0″ seeing in the B-band and 0.8″ in the R-band. Total exposure times were 7200 s in B and 4800 s in R, again yielding photometry for objects as faint as $R \sim 27$.

Panoramic near-infrared K-band imaging of both clusters is also available with WIRC (Wilson et al. 2003) on the Palomar Hale 5.1-m telescope. These data comprise a 3×3 mosaic of WIRC pointings, providing a contiguous observed are of $26' \times 26'$ centered on each cluster. Full details of the observations and data reduction are published elsewhere (Cl 0024+16: Smith et al. 2005; MS 0451−03: Smith et al. 2007, in prep). Point sources in the final reduced mosaics have a full width half maximum of $0.9''$ and $1.0''$ in Cl 0024+16 and MS 0451−03 respectively. The data reach a 5-σ point sources detection threshold of $K = 19.5$ and $K = 20.0$ in Cl 0024+16 and MS 0451−03 respectively. The nominal 24μm coverage of the two clusters is $\sim$0.21 degrees^2. In the case of MS 0451−03, the archival GTO data contribute an extra $\sim$29 arcmin^2. When the optical and near-infrared coverage is taken into account, the total coincident coverage of 24μm, B-, R-, K-bands is 0.165 degrees^2 and 0.184 degrees^2 in Cl 0024+16 and MS 0451−03 respectively.

We detect objects and extract photometry from the optical frames by running SExTRACTOR in two-frame mode such that detections were made in the R-band image and measurements made at identical pixel locations in R and B (the frames were previously aligned to good accuracy). We catalog all sources with 3 contiguous pixels (the pixel scale is $0.204''$) at least 2-σ above the background, and lay down $2''$ diameter apertures to measure colors in the BRK-band frames.

2.3. Analysis & Results

The MIPS observations of our two clusters yield 986 sources in the Cl 0024+16 field and 1071 in MS 0451−03, both with 24μm flux densities above $S_{24\mu m} > 200\mu$Jy (unless otherwise stated, quoted fluxes are always the corrected $16''$ aperture values). In the case of MS 0451−03 the count includes sources in the archival region in the core. We assess the false detection rate by running our algorithm on the inverse of the data, and detect $\sim$ 20 sources in each frame, all with fluxes in the range 200–330μJy, representing $\sim$2% of the detected sample. Our analysis requires matched optical $R < 24$ identifications and so we expect the false rate will be much less than 1%. As we demonstrate below, the achieved source surface density is below 1 object per 40 beams, the classical definition of a confused map (Hogg 2001), and so our maps are not expected to be confused at this depth.

We next use the deep optical and near-infrared imaging of these fields to investi-

gate the photometric properties of mid-infrared sources. The influence of false detections described above is minimised in the main part of our analysis, since we require the mid-infrared sources to have optical and near-infrared counterparts.

2.3.1 Optical properties

Positional matching of multi-wavelength data sets has been a long standing problem in astronomy, and can be particularly troublesome when there is a large disparity in the resolution and sampling in two datasets. We find that a simple nearest-neighbour match is not adequate to pair mid-infrared sources with optical counterparts – the method can fail to match complicated interacting systems for example. Instead, we apply the technique of de Ruiter, Arp & Willis (1977) who use a Bayesian estimator for the probability, $p(\mathrm{id} \mid r)$, that a nearby source is a true match and not a chance unrelated object. In Appendix A, we briefly outline the key elements of the method, but refer the reader to de Ruiter, Arp & Willis (1977) for a thorough derivation. The result of our matching analysis is a list of probable optical counterparts for the 24μm sources in our catalogs. We identify 611 and 650 counterparts to 24μm sources which are brighter than $R = 24$ and 200 μJy in Cl 0024+16 and MS 0451−03 respectively. In MS 0451−03 this includes sources in the archival region.

In Figure 2.1 we plot the $(B - R)$ versus R color-magnitude diagram for each cluster, comparing the distribution of colors for the mid-infrared sources and their apparent magnitudes with the optical population in these regions. The first thing to note is the broad similarity in the distributions on the color-magnitude plane of the 24μm sources in the two fields. Looking at the color distributions in more detail, the median $(B - R)$ color of mid-infrared sources at $R < 22$ is 1.75 and 1.80 for Cl 0024+16 and MS 0451−03 respectively. The 24-μm counterparts exhibit a broad peak in $(B - R)$ color, which lies between the peaks of red and blue galaxies (Fig. 2.1). This association of 24μm sources with galaxies having transition colors is intriguing. It may simply reflect the fact that these galaxies are dustier examples of the general blue star-forming field population, where dust reddening produces somewhat redder colors. Or it may be evidence that some of these galaxies are part of an evolutionary sequence connecting the blue star-forming population, and the passive types inhabiting the red-sequence.

In Figure 2.2 we plot the $(R - K)$ versus $(B - R)$ colors of the mid-infrared sources in Cl 0024+16 and MS 0451−03 compared to the optically-selected populations in the two

fields. We also indicate the expected colors of cluster members with a range of spectral types (King & Ellis 1985). These model colors provide a rough guide to the relative level of current to past star-formation in the galaxies and the reader should note that the influence of dust extinction will move galaxies parallel to this sequence, further complicating any interpretation of the star-formation histories of these galaxies.

Looking at the panel for Cl 0024+16 in Figure 2.2, we see a clear ridge of 24-μm sources with colors comparable to those expected for cluster galaxies. To confirm this association, we indicate on the plots the locations of spectroscopically confirmed 24μm cluster members from the surveys of Czoske et al. (2001) and Moran et al. (2006), and our on-going spectroscopic follow-up of our 24μm sample. There are 45 confirmed 24μm members in Cl 0024+16 and 7 in MS 0451−03 and the vast majority of these lie close to the predicted color-color locus for cluster members, and have colors consistent with star-forming galaxies. However a few fall in the region populated by passive, early-type cluster members, as expected due to the likely presence of active galactic nuclei in some of these galaxies. Nevertheless, it is clear that the information from this $(B-R)$–$(R-K)$ color-color plot can be used to crudely isolate likely 24-μm cluster members to statistically gauge the size of this population in the two clusters.

The 'transitional' colors of the majority of 24μm sources hinted at in the color-histograms in Figure 2.1, is also reflected in the distribution of points around the spectral classes in Figure 2.2 The colors of the bluer, probable 24μm cluster members suggest these are moderately star-forming galaxies (matching the continuum shapes of present-day Sbc/Scd galaxies). However, these could be more actively star-forming systems with additional reddening, $A_V \sim$ 0–1, and there are a small number of galaxies with very red colors which suggest very significant reddening, $A_V \sim 2$ mags. To select the majority of infrared cluster members, we apply a photometric cut in color-color space around the sequence of known cluster members (Figure 2.2) and then account for the residual field contamination using a similar color-selection applied to a blank field 24μm sample. Based on the existing spectroscopic samples of 24μm sources in the two clusters, we estimate that our color-selection criteria identify 39/45 and 5/7 members in Cl 0024+16 and MS 0451−03 respectively, or an average completeness of 85%. We note that the fact that the reddening vector runs approximately parallel to our selection box in Figure 2.2 means that it should contain a significant fraction of the more reddened sources.

In addition, in this work we are investigating the nature of the star-forming cluster

population, so we must be aware of contamination by infrared activity caused by AGN in passive (and also star-forming) galaxies. Therefore we define a sub-region in the color-space around the likely color of cluster E/S0s (Figure 2.2), and do not include the galaxies within this region in our analysis of the obscured star-forming population.

The 24μm galaxy population in the MS 0451−03 field does not exhibit such a pronounced ridge with colors matching those expected for cluster members, as Cl 0024+16. Nevertheless, there is a weak overdensity, which is most obvious in a red clump associated with passive, early-type cluster members. This clump is around 0.2 mags redder in $(B - R)$ and $(R - K)$ than the equivalent feature in Cl 0024+16, as expected from the k-correction for passive galaxies between $z = 0.39$ and $z = 0.55$. Again, the small number of spectroscopically confirmed 24μm members fall close to the locus expected for the colors of cluster members and we therefore use this color-color selection in the subsequent sections to investigate the properties of this population.

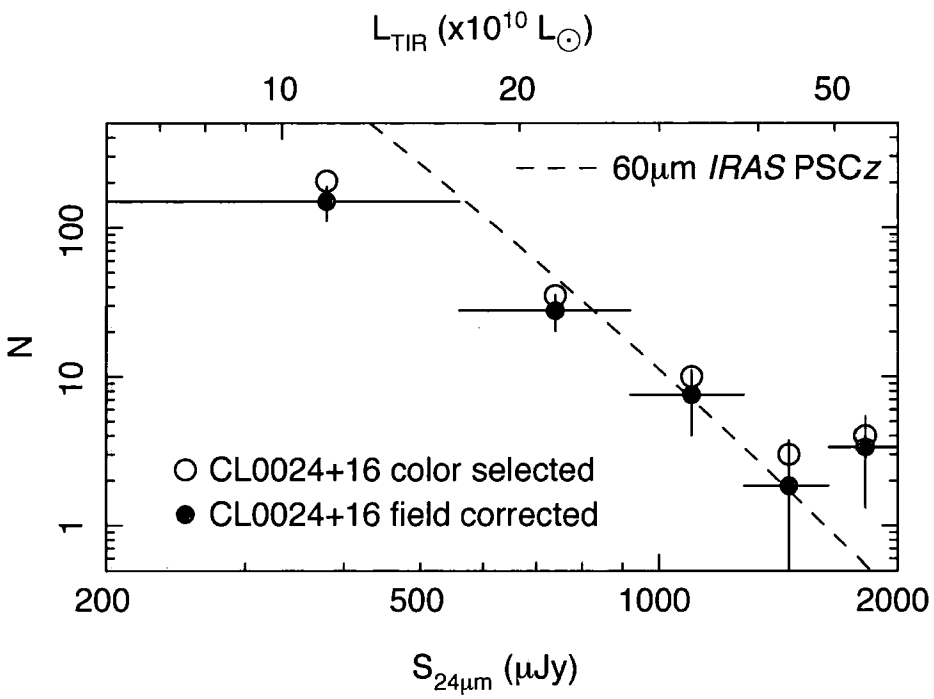

Figure 2.4: The infrared luminosity function for Cl 0024+16, based on the photometrically-selected cluster members and plotted with and without correction for residual field contamination. The total infrared luminosities are derived by extrapolating the monochromatic MIPS 24μm flux, assuming the local 15μm–far-infrared correlation holds at $z \sim 0.5$ (see §2.3.3). The estimated number of 24μm cluster members in MS 0451−03 is insufficient to provide a similar plot for that cluster. For comparison, we plot the luminosity function of the 60μm *IRAS* Point Source Catalog Redshift (PSCz) survey from Takeuchi et al. (2003), with an arbitrary normalisation. The cluster luminosity function is similar in shape with that of local field galaxies, given the large uncertainties.

2.3.2 Counts of mid-infrared sources

To quantify the number of 24μm sources associated with cluster members we first compare the 24μm number counts for each cluster to counts from the literature for large area 24-μm field surveys (e.g. Marleau et al. 2004; Papovich et al. 2004; Chary et al. 2004). The counts in the literature all agree well in the flux density regime covered by our data and we use the model presented in Marleau et al. (2004) to estimate the number of field 24μm galaxies expected with $S_{24\mu m}$ = 200–1000μJy in our fields: $dN/dS = (416 \pm 3)S^{-2.9\pm0.1}$, which is valid for the range 200–900μJy, we extrapolate the bright end to 1000μJy. For this comparison we also correct our counts for completeness in the range 200–300μJy (our simulations show that our observations are ~100% complete at 300μJy).

The predicted numbers of 24 μm sources to our flux limits over the Cl 0024+16 and MS 0451−03 fields are 1280±160 and 939±120 respectively, down to 200μJy. These should be compared to the observed numbers sources of 1032 and 935, respectively. Based on this comparison we can see that the cluster populations do not represent a significant excess over the large field population across the full survey area and down to the flux limits of our survey. This is not particularly surprising as the survey fields are large and our sensitivity limit is sufficient to detect sources in a large volume out to high-redshifts. Instead, if we restrict the comparison to the central regions of the clusters, where the contrast of the cluster over the background might be largest, we see that at projected radii of $\lesssim$ 2 Mpc there is a slight excess of mid-infrared sources compared to the field counts in Cl 0024+16: 134 ± 12 observed sources compared to 115 ± 14 predicted for the field, suggesting a modest cluster population. While in MS 0451−03, including the archival data for the core, and we find that within 2 Mpc there are 104 ± 10 sources compared to 108 ± 13 predicted by the model – showing no detectable overdensity in this cluster even in the central regions.

The lack of a detectable excess in the raw counts of 24μm sources in the cluster fields does not rule out a significant cluster population given the large uncertainties in the contribution from field sources. To provide a more sensitive test we can exploit the optical-near-infrared photometry to remove the bulk of the background field contamination and so reduce the uncertainty in the field correction. In Figure 2.3 we plot the cumulative number of mid-infrared galaxies as a function of clustocentric radius for those galaxies with optical-near-infrared counterparts whose colors lie close to the ridge-lines of cluster members seen in Figure 2.2 (restricted to those with $R < 24$). These are corrected

for residual field contamination by using the optical/near-infrared photometry of mid-infrared sources from the SWIRE ELAIS N1 survey (Lonsdale et al. 2003, 2004; Surace et al. 2004). To achieve this we translate our $(B-R)$–$(R-K)$ selection box in Figure 2.2 to the equivalent region in $(r-z)$–$(g-r)$ space for the SWIRE sample using model spectral energy distributions (Fig. 2.2) to transform between the various colors. Extrapolating the number counts of these color-selected sources to our 200μJy limit (by fitting a power-law, $dN/dS \propto S^{-\alpha}$, to the counts) yields an average surface density of mid-infrared field sources with $R < 24$ of 0.16 ± 0.02 arcmin^{-2} and we correct our counts using this. We also make use of the very large SWIRE survey area to estimate the fluctuations in the field correction in the area of each of our radial annuli in Figure 2.3, by determining the fluctuation in the field counts as a function of survey area. This variance is included in the uncertainty in the field correction used in Figure 2.3.

By selecting 24μm sources with optical-near-infrared colors similar to those expected for cluster members, we have substantially reduced the field contamination in our sample. Figure 2.3 demonstrates a significant 24μm cluster population in Cl 0024+16, with 155±18 sources across our $25' \times 25'$ field (where the uncertainty includes the effects of clustering on the field correction). As can be seen the excess population is distributed across the whole field, with the numbers continuing to increase to $\sim$ 5 Mpc where the coverage of our data begins to decline. In contrast, in MS 0451−03 we find a much weaker excess, 28±17, which is only marginally significant. Nevertheless, we note that our existing spectroscopic survey of this cluster (Fig. 2.2) confirms that there are 24-μm-detected cluster members, but the population appears much less numerous than in Cl 0024+16. In both cases, the estimates of the total cluster populations could be increased by $\sim$ 18% to account for the incompleteness of our color-selection, although to be conservative we choose not to apply this correction.

While it is clear that there are populations of 24μm cluster members, we also need to consider lensing of background sources by these massive clusters, which may affect the predicted numbers of cluster members. Lensing has the effect of a boosting of flux and dilating the projected area. To demonstrate this we model the clusters as simple isothermal spheres. In this case a background source will suffer an apparent deflection in radial direction by $\alpha \simeq 20'' \sigma^2_{1000}$, where σ_{1000} is the cluster velocity dispersion in units of 1000 km s^{-1}. We adopt $\sigma = 1150$ km s^{-1} for Cl 0024+16; $\sigma = 1290$ km s^{-1} for MS 0451−03 (Trentham et al. 1998). At a radius r, the source-plane area of an annular bin of width dr

will be $2\pi(r-\alpha)\mathrm{d}r$, and the flux of a lensed source will be boosted by a factor $r/(r-\alpha)$. We integrate the lensing prediction for our color-selected sample (taking $\sigma = 1200\,\mathrm{km\,s^{-1}}$ – though the actual values may be lower, so this should be a conservative estimate) as a function of radius, finding that it could contribute $\lesssim 20$ sources to our samples, hence in Cl 0024+16 the excess signal we see is greater than can be explained by lensing. The situation with MS 0451−03 is more problematic, although again we note that the spectroscopic identification of a handful of 24μm cluster members confirms that, as with Cl 0024+16, there is a population of mid-infrared sources associated with the cluster.

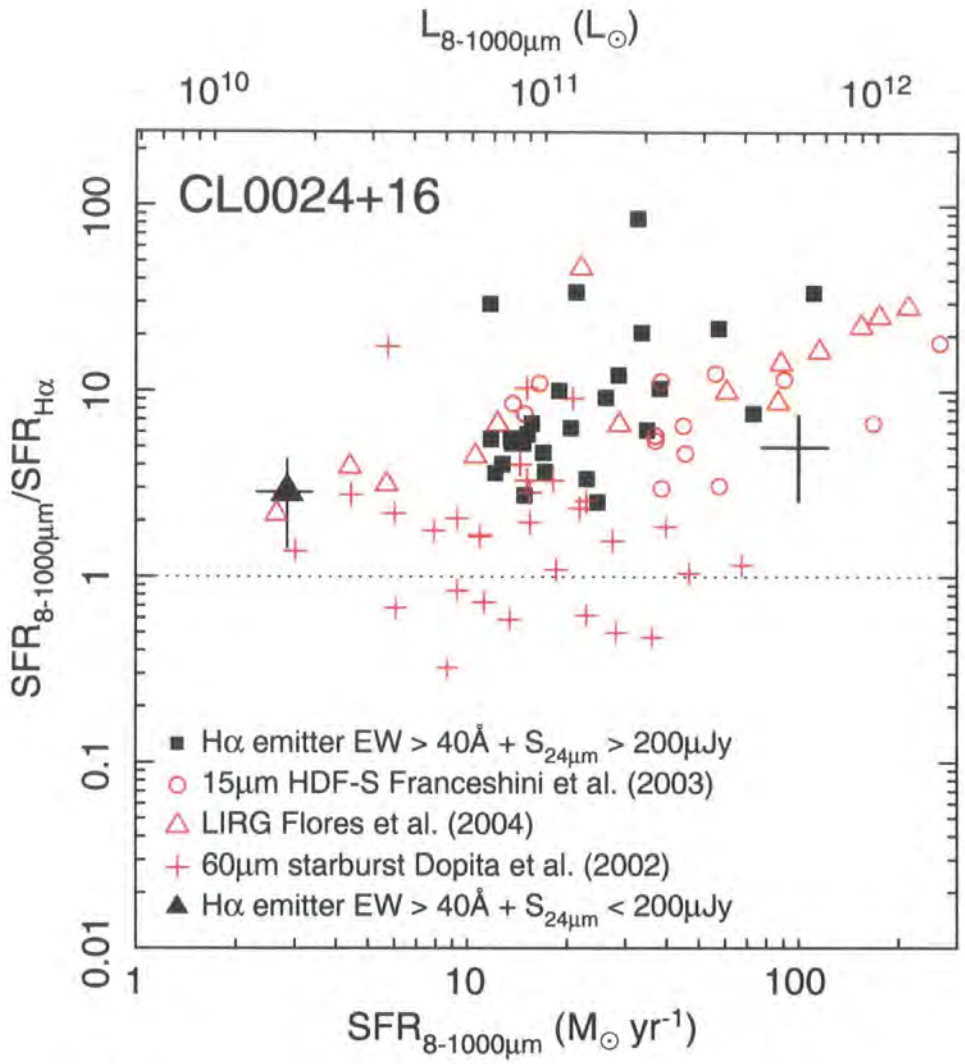

Figure 2.5: A comparison of the star-formation rates derived from Hα (Kodama et al. 2004) and total-infrared luminosities for individual Hα-detected cluster members in Cl 0024+16. The ratio SFR[IR]/SFR[Hα] provides an estimate of the level of obscuration of the starforming regions within these galaxies. We see a typical offset of a factor of 5$\times$ between the infrared and Hα estimates (the latter have not been corrected for extinction), although there is a wide-scatter. We also plot data from the literature of similar studies of infrared-luminous field galaxies from Flores et al. (2004), Franceshini et al. (2003) and Dopita et al. (2002) corrected to our cosmology. It appears that the level of obscuration of star-forming infrared cluster galaxies (in Cl 0024+16) is similar to that of mid-infrared selected field galaxies at this epoch. We do not plot individual error bars for clarity, but show a representative error bar. Finally, to probe obscuration from faint mid-infrared sources, we stack the 24μm data for Hα emitters which are not detected in the MIPS image yielding a 5σ statistical detection. This confirms the general trend seen above our nominal luminosity limit that there appears to be an increase in the level of obscuration (SFR[IR]/SFR[Hα]) with infrared luminosity.

2.3.3 Star formation

To calculate the star-formation rates (SFRs) for our mid-infrared detected galaxies, we begin by estimating the total infrared luminosity over the restframe wavelength range 8–1000 μm. Since we only have MIPS 24μm photometry, we have to determine the correction factor required to convert our 24μm luminosities to total infrared luminosities. To achieve this we assume the correlation between 15μm (corresponding to observed $\sim 24\,\mu$m at $z \sim 0.5$) and total-infrared luminosity seen for local infrared galaxies (Chary & Elbaz 2001) continues to hold at $z \sim 0.5$. We then follow a similar technique to that of Bell et al. (2005) and use the spectral energy distribution (SED) templates from Dale & Helou (2002) to estimate the ratio of the observed-frame 24-μm luminosity to the 8–1000μm luminosity. We calculate the ratio of total-infrared to observed 24-μm luminosities for each SED template, taking the mean value of all the ratios as our correction factor, and the range from the most active to the most quiescent SEDs as a conservative estimate of the systematic uncertainty. The correction factors are 16 ± 2 and 16 ± 3 for Cl 0024+16 and MS 0451−03 respectively. We compare our conversion factors to the relation found by Chary & Elbaz (2001) by calculating the mid-infrared to total infrared ratio with the *ISOCAM LW3* (15μm) filter for the Dale & Helou templates at $z = 0.1$. The Chary & Elbaz conversion for local LIRGs corresponds to $L_{IR} \sim 11^{+6}_{-4} \times L^{0.998}_{15\mu\mathrm{m}}$, while our estimate gives a prefactor of 7 ± 3 over the full range of LIRG templates. Thus these two calibrations are consistent, although the reader should note our estimates are roughly 40% fainter than would be given by Chary & Elbaz (2001).

Our $5\,\sigma$ 24-μm flux limit of 200μJy corresponds to average total infrared luminosities of $6 \times 10^{10}\,\mathrm{L}_\odot$ and $12 \times 10^{10}\,\mathrm{L}_\odot$ in Cl 0024+16 and MS 0451−03 respectively, hence the bulk of the populations we are detecting are Luminous Infrared galaxies (LIRGs) with $\mathrm{L}_{IR} \geq 10^{11}\,\mathrm{L}_\odot$. These luminosities translate into SFRs of $\sim 10\,\mathrm{M}_\odot\,\mathrm{yr}^{-1}$ and $\sim 20\,\mathrm{M}_\odot\,\mathrm{yr}^{-1}$ assuming the far-infrared star-formation calibration given by Kennicutt (1998) with a Salpeter IMF and a mass range of 0.1–100 $\mathrm{M}_\odot$.

In Figure 2.4 we plot the mid-infrared luminosity function for the Cl 0024+16, based on the color-selected sample out to a radius of 5 Mpc. To field correct the luminosity function in Cl 0024+16, we integrate the extrapolated power-law fit to the color-selected 24μm sources in the SWIRE ELAIS N1 field, from §2.3.2. We use the scatter in the normalisation of dN/dS in independent $25' \times 25'$ regions within the SWIRE field, combined with the counting errors in each bin, to give the uncertainty in the field-correction. This

plot demonstrates that the field-corrected luminosity function in Cl 0024+16 is similar in form to that seen for 60μm-selected populations at low-redshift (Takeuchi et al. 2003).

While there are too few sources in MS 0451−03 to allow us to make an equivalent plot to Figure 2.4 for that cluster, we can use the Cl 0024+16 luminosity function to estimate how many sources we would have detected if we place the Cl 0024+16 population at $z = 0.55$. Applying a factor to scale for the effective areas of our surveys in Cl 0024+16 and MS 0451−03, we estimate that we would detect 69 ± 21 galaxies above the luminosity limit, $12 \times 10^{10}\,L_{\odot}$, of the MS 0451−03 survey. This compares to our estimate of 28 ± 17 from our MS 0451−03 catalog, indicating a roughly 2–3× difference in the numbers of mid-infrared sources in the two clusters. This suggests that, although the dearth of mid-infrared sources in MS 0451−03 may be partly due to sensitivity limitations, there may be a real difference in the mid-infrared populations in the two clusters.

Mid-infrared versus Hα tracers of activity

We can also compare the properties of our mid-infrared selected sample in Cl 0024+16 with the Hα survey of this cluster by Kodama et al. (2004). Kodama et al. obtained a deep image of the cluster in a narrow-band filter centered on redshifted Hα. Galaxies with excess emission in this narrow-band filter were identified as cluster members with Hα emission. They estimate their sensitivity limit corresponds to a star formation rate of $\sim 1.5\,M_{\odot}\,yr^{-1}$ – significantly below the estimated SFR limit of our mid-infrared survey, $\sim 10\,M_{\odot}\,yr^{-1}$.

To start with, we compare in Figure 2.3 the cumulative radial profile of the mid-infrared sources with the Hα-emitting galaxies from Kodama et al. (2004). As can be seen the two tracers show very similar trends, with a steep rise from 1 Mpc out to ~5 Mpc, beyond which our coverage declines. The reader should also note that the lack of mid-infrared coverage for the core of the cluster will contribute to the steeper drop of the 24μm counts in the innermost bin in Figure 2.3. Surprisingly, Figure 2.3 also shows there are similar numbers of Hα emitters and 24μm-detected members, even though there is a significant difference in the relative sensitivity of the two surveys. We therefore next compare the estimates of the SFR for individual galaxies from Hα and the mid-infrared, to relate these two star-formation indicators for confirmed cluster members.

In Figure 2.5 we compare the star-formation rates for Hα narrow-band-selected sources

and their 24μm counterparts[2]. From this figure, it can be seen that the star formation rates for the mid-infrared-detected members, derived from the Hα emission line (but not corrected for extinction), appears to underestimate the SFR from the mid-infrared by factors $\gtrsim 5\times$. Including the standard assumption of 1 magnitude of extinction and correcting for a 30% contribution to the measured fluxes from [NII] (see Kodama et al. 2004) would reduce this offset to a factor of $2.5\times$. However, such a simplistic correction would miss the fact that the discrepancy in SFRs appears to increases with infrared luminosity, such that the most active systems are also the most obscured.

To test for biases due to our 24μm sensitivity limit, we stack thumbnail images from the MIPS image of Cl 0024+16 for Hα emitters from Kodama et al. (2004) which are not individually detected, i.e. $S_{24\mu\mathrm{m}} < 200\,\mu$Jy. We find a $\sim$5-σ detection with $S_{24\mu\mathrm{m}} = 57 \pm 11\,\mu$Jy. In terms of star-formation, this corresponds to $\sim 3\,\mathrm{M}_\odot\,\mathrm{yr}^{-1}$. We plot this point on Fig. 2.5, with the corresponding average Hα derived SFR for the stack, $\sim 1\,\mathrm{M}_\odot\,\mathrm{yr}^{-1}$. This point seems to be roughly consistent with the trend seen, that obscuration (i.e. SFR[IR]/SFR[Hα]) increases with the level of infrared activity.

We estimate that the correction required to bring the Hα derived SFRs in line with the infrared SFRs corresponds to a reddening of $A_V \sim 2.5$, slightly larger than the value used to explain the broadband colors of these galaxies on the $(R-K)$–$(B-R)$ color–plane. This reddening estimate will also be affected by the choice of adopted SED when deriving total infrared luminosities, although in this work we have chosen a conversion which represents infrared galaxies of a wide range of activities, and so our estimates are conservative. We also note that there is a factor of 40 range in infrared to Hα derived star formation rates within our sample which is larger than expected from our measurement errors and indicates that there may be a wide range of extinction amongst the individual LIRGs – in part probably due to the patchiness of the dust within these galaxies.

We also compare our relation between mid-infrared- and Hα-derived SFRs to that seen in samples of field galaxies from the literature: a sample of LIRGs in the range $0.2 < z < 0.7$ from Flores et al. (2004), 15μm detected *ISO* sources from the *Hubble Deep Field South* at $(0.2 < z < 1.5)$ (Franceshini et al. 2003), and *IRAS* 60μm warm infrared galaxies from Doptia et al. (2002). The typical level of SFR[IR]/SFR[Hα] is similar to Hα/MIR detected objects in Cl 0024+16, suggesting that these cluster galaxies are similar

[2]The optical star-formation rates are derived from the Hα and adjacent [N II]$\lambda\lambda$6548,6583 emission lines after Kennicutt, Tamblyn & Condon (1994).

in nature (at least in terms of their mix of star-formation and obscuration) to star-forming LIRGs in the field at similar epochs.

2.4. Mid-infrared spectroscopy of LIRGs in Cl 0024+16

The 24μm survey presented here ignores the possibility that the mid-infrared emission could be powered by star formation or AGN (although we have tried to minimise contamination by AGN with a colour selection). To investigate the power sources of these 24μm emitters, we undertook *Spitzer* Infrared Spectrometer (IRS) observations of several LIRGs in Cl 0024+16. The goal of this survey was to verify that the 24μm detections were indeed starbursts, and to attempt to quantify contamination from AGN, which could also contribute to the mid-infrared output. In the following sections we describe the IRS observations, reduction and analysis, and the implications for conclusions drawn from the 24μm survey.

2.4.1 Sample selection and IRS observations

Our targets are selected from the 24μm MIPS survey of Cl 0024+16 described above, and also have optical spectroscopic redshifts confirming them as members of the cluster. In the target selection, we imposed a 24μm flux limit of $S_{24} > 0.6$ mJy after assuming a spectral shape of $\nu^{-1.5}$ to the underlying continuum, allowing us to estimate the expected continuum flux density at 10.9μm (the PAH 7.7μm feature is redshifted to this wavelength at $z \sim 0.4$). The precise redshifts already known for these galaxies will facilitate identification of emission and absorption features, and allow more accurate stacking of the spectra to search for statistical properties of the mid-infrared spectra.

The observations were executed in the Cycle 3 GO project #30621. IRS was used in fixed single staring in modes Short Low 1 (SL1, 7.4–14.5μm) and Long Low 2 (LL2, 14–21.3μm), with peak-up acquisition on a nearby 2MASS selected star (HD 2292 was a suitable peak-up object for all of our targets). After peak-up and slew the exposure time is divided into 5×60 s cycles in SL1 and 20×120 s cycles of LL2, yielding a total on-object integration time of ~5490 s. The infrared backgrounds were dominated by Zodiacal Light in each module, and are in the 'medium' category.

At the time of writing, further IRS observations are being undertaken as part of the same campaign. Thus in this thesis we present five completed spectra, and the completed

sample will be presented in a future work.

2.4.2 Data reduction

We use data products generated by the *SST* IRS pipeline (version 14.4.0). This processing involves dark subtraction, linearity correction, ramp correction and flat fielding. Backgrounds were removed by subtracting two different nod positions, and the 1D spectra optimally extracted using the SPICE software package. This took into account uncertainty and mask images, and the resulting spectra from each nod position were co-added, rejecting outliers. Note that all of our targets are treated as point sources (the width of the IRS slit is 10.5″, larger than the optical and mid-infrared extent of the sources). Although the spectra are flux calibrated within SPICE, our existing 24μm photometry provides a secondary check for the expected continuum emission at a rest-frame wavelength of 17μm.

2.4.3 Results

We present the spectra in Figure 2.7, for all five galaxies in our sample with the SL1 and LL2 modes concatenated, along with the continuum flux at 24μm from our MIPS observations extending the continuum measurement. Four of these galaxies show evidence for strong PAH emission at 6.2, 7.7, 8.6, 11.3 and 12.7μm, which in itself is evidence for star formation. The 7.7μm emission line is used as a diagnostic for measuring the relative contribution of nuclear and star forming activity (Genzel et al. 1998). The strength of the line relative to the underlying continuum is diminished in the presence of the intense radiation field of an AGN, and the continuum itself tends to have a steeper slope than is found in starburst galaxies. The line-to-continuum ratio (l/c) can thus be used to classify emission dominated by star formation or AGN ($l/c > 1$ for starbursts and $l/c < 1$ for AGN, see Genzel et al. 1998 and Rigopoulou et al. 1999), and we also we calculate the equivalent width (EW) and ratio of line luminosity to total (8–1000μm) infrared luminosity (e.g. Menéndez-Delmestre 2007; Yan et al. 2007). Since we have precise redshifts for these objects, we coadd the rest-frame spectra into a composite 'star forming' spectrum revealing the emission line features with better signal to noise than in the individual spectra. There is little or no silicate absorption at 9.7μm, which indicates that the infrared emission does not originate from a centrally obscured component (we note though that at this redshift the Si absorption feature falls at the red end of the SL1 module and the blue end of the LL2 module – regions with lower signal to noise).

To calculate the equivalent width of the 7.7μm emission line we first estimate the continuum emission by linearly interpolating between regions away from strong line emission at 5.5–6.8μm and 13.6μm (e.g. Menéndez-Delmestre 2007, see Figure 2.6). After subtracting the continuum emission, the line feature is fit with a Gaussian profile which is used to calculate the line flux, and therefore the equivalent width. We present the line luminosities and equivalent widths for the cluster LIRGs with measurable 7.7μm emission in Table 2.1. The uncertainties in the equivalent width and line luminosities are dominated by the estimation of the continuum emission. We quantify this uncertainty by recalculating the equivalent width and line flux using continuum estimations using a range of randomly selected 'anchor points' in the range ~5–6μm and 6.5–7μm. By repeating this calculation many times, we build up a statistical measure of the expected scatter in line measurements introduced by the choice of continuum slope. We estimate this is quite large, with errors being on average ~40% of the measured value.

In Figure 2.7 we plot the equivalent widths as a function of the ratio of 7.7μm line luminosity to the total infrared (8–1000μm) luminosity (this is calculated using the 24μm flux and the method described in §2.3.3). This can be used to separate AGN and starburst dominated galaxies since strong dusty star formation will result in large equivalent widths and large $L_{7.7\mu\mathrm{m}}/L_{\mathrm{IR}}$ (the PAH emission can contribute a large fraction of the total infrared luminosity in these cases, up to ~20%, see Smith et al. 2007). We compare these galaxies to other objects spanning AGN–starburst dominated classification from the literature. The cluster LIRGs with PAH emission are consistent with starburst dominated objects, similar to local LIRGs such as M 82. This is strong evidence that the vast majority of the mid-infrared emission detected in the 24μm survey is from pure star formation rather than nuclear activity. However, we note that one of our sample does not exhibit strong PAH emission, and has a relatively flat continuum. The absence of PAH emission could indicate emission from AGN, which has destroyed or modified the emission properties of the grains and macro-molecules thought to be responsible for PAH emission (only the 11.3μm emission line feature is obvious in contrast to the continuum). To lend support to the AGN power source is the detection of [Ar V] and [Ne V] emission lines – these high excitation lines tend to be found in the presence of an AGN (Farrah et al. 2007; Sturm et al. 2002, 2006). Indeed, the ratio of line strengths [Ne V]/[Ne II] flux ratio can be used as another diagnostic of starburst/AGN contribution (Sturm et al. 2002), with [Ne V]/[Ne II] in the range ~0.8–2 for AGN dominated systems, compared to strict upper

limits for starburst dominated systems of <0.01 (Sturm et al. 2002; Verma et al. 2003). We do not detect [Ne II] at 12.8μm which suggests that this object is almost certainly dominated by an AGN. We note that the continuum is weak, and does not show any evidence for strong silicate absorption, implying that the AGN is not extremely obscured. [Ar V] is a relatively rare line (Farrah et al. 2007), but is also associated with AGN (Fig. 2.7). Although star formation appears to be the major contributor to the mid-infrared emission in cluster LIRGs, these results suggest a ~20% 'contamination' from AGN. This will have an impact on estimates of the total cluster star formation rate which we address in the next section.

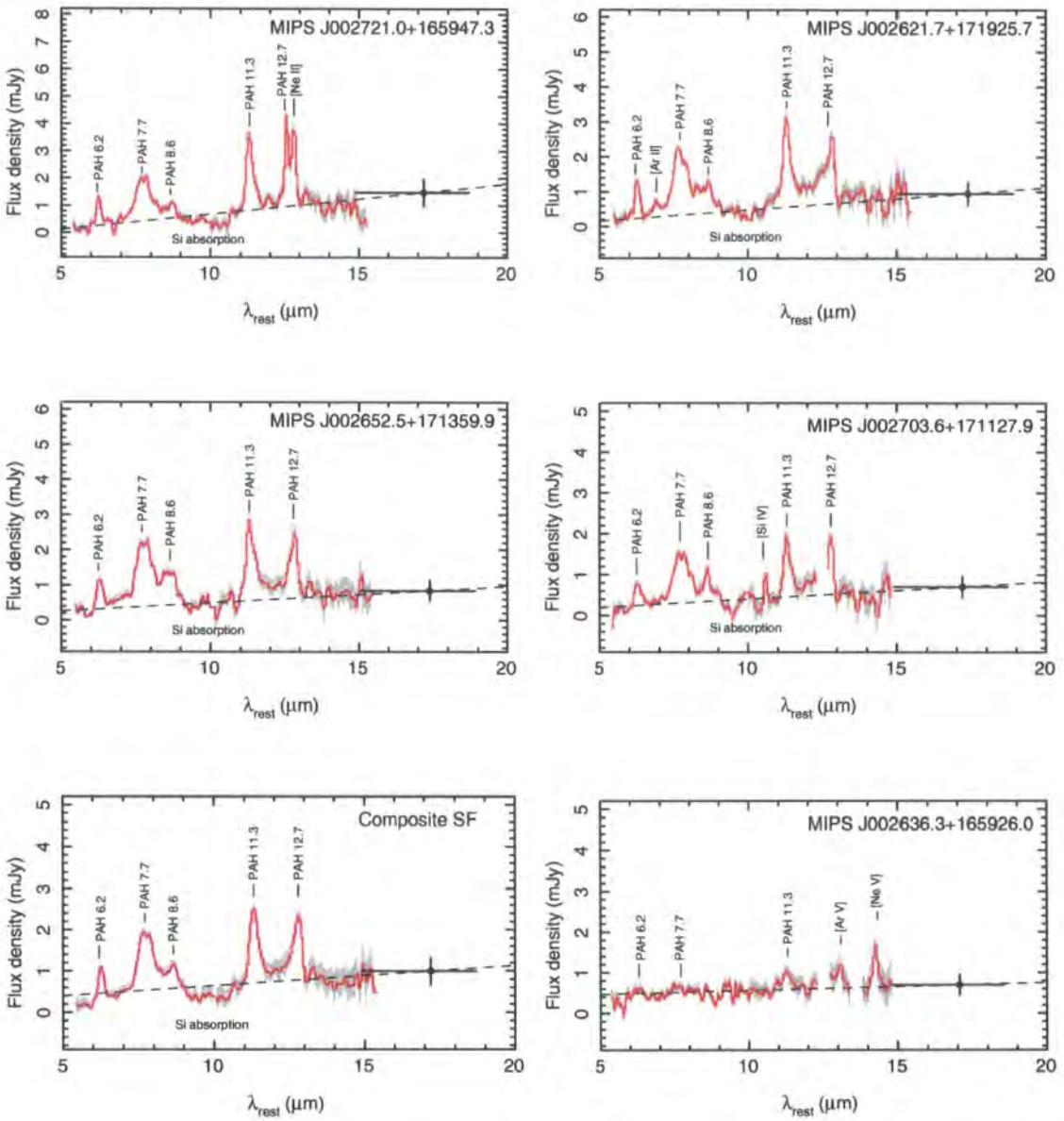

Figure 2.6: Mid-infrared spectra of LIRGs in Cl 0024+16. Four galaxies exhibit strong PAH emission lines, and these contribute significantly to the total infrared luminosity (see Table 2.1) – they are classified as starburst galaxies. To improve contrast of the PAH emission lines, we stack these four spectra into a composite spectrum which shows strong PAH emission at 6.2, 7.7, 8.6, 11.3 and 12.7μm. There is little silicate absorption at 9.7μm, suggesting little obscuration of the line emitting regions. One galaxy (MIPS J002636.3+165926.0) does not have strong PAH emission, with the strongest feature being [Ne V] at 14.3μm. This high excitation line is strong evidence for an AGN, and the lack of a [Ne II] line suggests that this object is powered by nuclear activity (Sturm et al. 2002). The dashed lines indicate linear interpolations of the estimated continuum, which is derived from two 'anchor' points at regions ~5–7μm free from line emission, and at our observed 24μm point (shown at rest frame ~17μm). Gaps in the spectra indicate regions masked out due to poor sky subtraction artifacts.

Name	z	S_{24}	EW PAH7.7μm	$L_{7.7\mu m}$	$\log(L_{7.7\mu m}/L_{IR})$
		mJy	μm	10^{36} W	
MIPS J002721.0+165947.3	0.3964	1.48	2.77	2.79	-1.80
MIPS J002621.7+171925.7	0.3801	0.95	2.71	2.80	-1.59
MIPS J002652.5+171359.9	0.3799	0.84	1.86	2.77	-1.54
MIPS J002703.6+171127.9	0.3956	0.71	2.41	2.76	-1.47
Composite SF	–	0.99	1.59	2.77	-1.62
MIPS J002636.3+165926.0	0.4063	0.70	<0.03	<0.04	<-3.25

Table 2.1: Strength of the 7.7μm PAH emission line compared to the total infrared luminosity of LIRGs in Cl 0024+16. The uncertainties in the equivalent width are dominated by the estimate of the continuum flux, and are estimated to be about 40% (we describe the derivation of this uncertainty in §2.5.3.) The continuum is fit by interpolating between clean continuum at ~5–7μm free from emission and our 24μm flux measurement – it is the uncertainty in deriving the continuum flux which dominates the error on the equivalent width. The total infrared luminosities are calculated using the method described in §2.3.3, and this dominates the uncertainty in this measurement (see text for details). The measurements for MIPS J002636.3+165926.0 include 3σ upper limits.

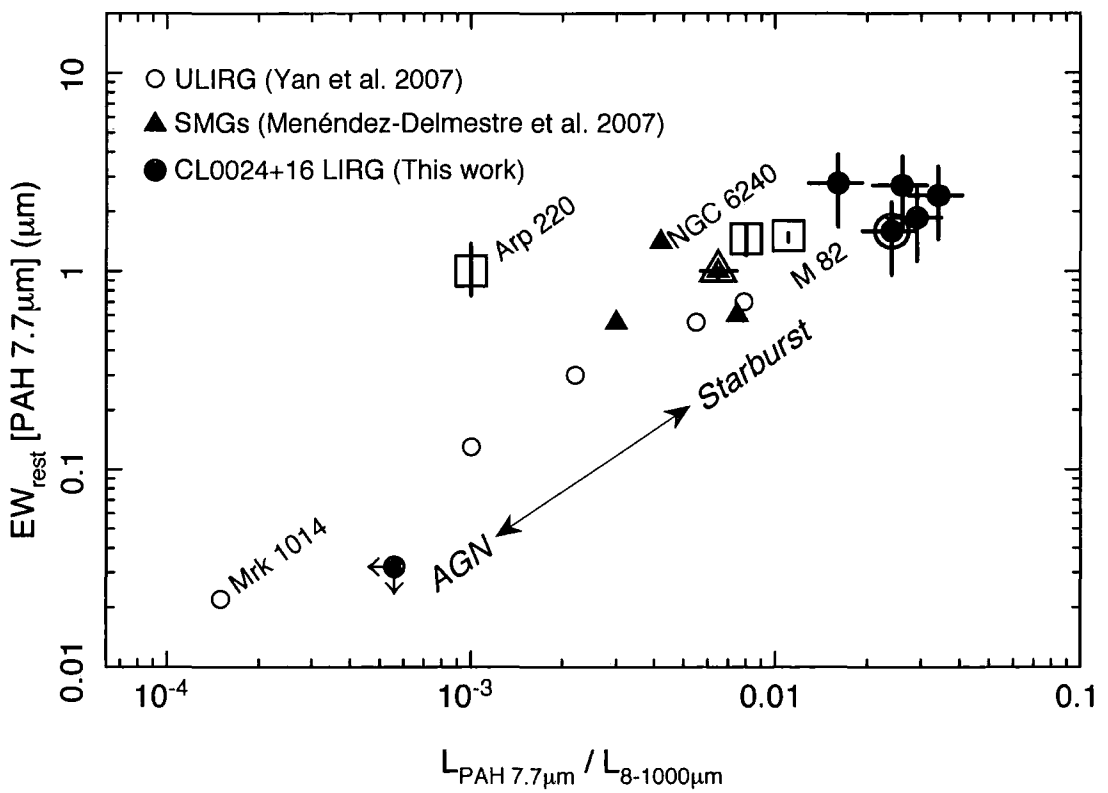

Figure 2.7: Diagnostic plot comparing the strength of the PAH 7.7μm emission line to the total infrared luminosity. The vertical axis shows the equivalent width, and this is plotted as a function of the ratio of the line luminosity to the total (8–1000μm) infrared luminosity. This diagram can be used to distinguish LIRGs dominated by AGN and starbursts, since in starburst galaxies the PAH features are strong and contribute a significant fraction of the total infrared output, compared to nuclear powered systems where the PAH features are typically weak. All the galaxies in our sample with measurable 7.7μm lines are in the starburst sector of the plot, similar to LIRGs at lower redshift (the circled point indicates the 'average' value derived from the composite spectrum, see Figure 2.7). For the LIRG where PAH is not detected, we plot 3σ upper limits, which place the galaxy in the AGN sector of the plot. We compare our data to a range of infrared luminous galaxies from the literature (selected at both high and low redshift) to indicate the general trend from AGN to starburst dominated systems.

2.5. Total cluster star-formation rates

We now estimate a total star-formation rate for the clusters using the typical SFR of the likely star-forming mid-infrared members. Since we lack observations in the central $\sim$ 1 Mpc in Cl 0024+16 due to the unobserved GTO region, we also need to correct for this missing population using the 15μm *ISO* observations from Coia et al. (2005).

2.5.1 Cl 0024+16

As shown by the radial number counts presented in Figure 2.3, the 24μm members are widely distributed across the clusters out to a projected radius of $\sim$2 Mpc (corresponding to $\sim$ R_{200}, Carlberg et al. 1997. Note that throughout, we use projected distances) and beyond. To compare the mid-infrared-estimates of the total star formation rates within representative regions of different clusters we therefore adopt a 2 Mpc radius for our calculations, which roughly matches the size of the surveyed regions in some of the earlier small-field surveys.

We integrate over the luminosity function in Figure 2.4 for sources with projected radii $<$ 2 Mpc, correcting for the expected contamination from field galaxies using the SWIRE data for the ELAIS N1 field (see §2.3.2). To account for the missing sources in the unobserved GTO core region we need to add the SFR in the 15μm members in this region found by Coia et al. (2005), after converting their 15μm fluxes to star-formation rates using an identical method to that presented in §2.3.3.

Our derived total-infrared luminosities are lower than those derived by Coia et al. (2005) by a factor of $\sim$2. This difference can be attributed to the different methods of conversion used. Coia et al.'s method involves extrapolating their observed 15μm photometry to 15μm in the rest-frame, using an SED fitted to their optical and mid-infrared photometry. This is then converted to a total infrared luminosity using the empirical conversion of Chary & Elbaz (2001) described above. In contrast our observations correspond to $\sim$15μm in the rest-frame. Hence some of this offset is due to the differences in conversion from 15μm luminosity to total infrared emission discussed in §2.3.3 and the remainder is due to the choice of SED by Coia et al. (2005), which overpredicted the observed 24μm fluxes. As we have stated earlier, our calculations should yield conservative limits on the SFR. We note that, with our total-infrared calibration, the 5σ detection limit of the Coia et al. (2005) *ISO* observations corresponds to $\sim 3 \times 10^{10}$ $L_{\odot}$.

With our conversion, we find three galaxies in the Coia et al. (2005) sample that exceed our luminosity limit of $6 \times 10^{10}\,L_{\odot}$, and so we can add their SFR to our total within 2 Mpc of the core. We thus find a total star-formation rate for the 40 sources within 2 Mpc to be $1000 \pm 210\,M_{\odot}\,yr^{-1}$. The error is derived by boot-strap resampling the flux distribution of sources within 2 Mpc, and integrating the new luminosity function. The median SFR per galaxy in our sample within 2 Mpc is $\sim 16\,M_{\odot}\,yr^{-1}$. We note that correcting for the estimated incompleteness in our color-selection of cluster members would increase our estimate of the total SFR by a factor 1.07, which corresponds to a change less than its quoted uncertainty. Our IRS observations suggest that a direct integration of the 24μm flux into a total star formation rate is not sufficient – we must correct for ~20% AGN contamination to the total SFR. Thus, the true level of star formation in the cluster is likely to be $\sim 800\,M_{\odot}\,yr^{-1}$, but a more accurate appraisal of the level of AGN contamination will require a larger spectroscopic sample (Geach et al. in prep).

For comparison, we also note that the Hα observations of Kodama et al. (2004) detect 100 galaxies within a similar region to that discussed here. They find a cumulative SFR of $\sim 470\,M_{\odot}\,yr^{-1}$, above their approximate sensitivity limit of SFR of $1.5\,M_{\odot}\,yr^{-1}$, or about $4.7\,M_{\odot}\,yr^{-1}$ per galaxy. Restricting the Hα sample to the $> 10\,M_{\odot}\,yr^{-1}$ limit of our mid-infrared survey, we find that the Hα survey would yield an integrated SFR of $\sim 220\,M_{\odot}\,yr^{-1}$. This confirms the effect seen in Figure 2.4, that although Hα and mid-infrared surveys are detecting a similar population, the Hα tracer severely underestimates the underlying activity in the most active sources in the cluster: these star-bursting systems are producing dust at a more copious rate and therefore optically obscured. In addition, we can state that the mid-infrared survey detects the bulk of the total star-formation activity within this region, requiring only a ~20% correction for the star-formation activity in sources with $1\text{–}10\,M_{\odot}\,yr^{-1}$.

2.5.2 MS 0451−03

We have seen that, compared to Cl 0024+16, this cluster appears to be deficient in mid-infrared sources (at least down to our luminosity limit). Nevertheless, even a small excess of mid-infrared sources in the cluster could contribute a non-negligible star-formation rate to the overall activity of the cluster. We therefore estimate the total star-formation rate within ~2 Mpc using the small number of excess sources identified using our $(R - K)$–$(B - R)$ color–color selection. The median SFR within 2 Mpc is $\sim 35\,M_{\odot}\,yr^{-1}$ per

galaxy (reflecting the brighter luminosity limit in this cluster). Applying the same approach as used for Cl 0024+16, we find a total star-formation rate within a 2 Mpc radius of the cluster center of $200 \pm 100\,M_{\odot}\,yr^{-1}$. Again, this might be an over-estimation of the star formation rate due to AGN contamination. It is not clear whether there is strong cluster-to-cluster variation in the relative AGN/starburst fraction, but assuming a similar contamination rate to Cl 0024+16, then we expect a total star formation rate in this cluster to be $\sim 160\,M_{\odot}\,yr^{-1}$.

In §2.3.3 we estimated the number of mid-infrared sources we would detect if MS 0451−03 had the same mid-infrared luminosity function to Cl 0024+16, taking into account the slightly different areal coverages between the clusters. Similarly, we can estimate the total star-formation rate in MS 0451−03 if we reached a luminosity limit identical to Cl 0024+16. Assuming the faint end of the luminosity function in MS 0451−03 follows a similar shape to Cl 0024+16, we estimate that the total star-formation rate down to $6 \times 10^{10}\,L_{\odot}$ in this cluster is $< 460\,M_{\odot}\,yr^{-1}$. Although the small number of excess sources in MS 0451−03 can lead to a relatively high star-formation rate (compared to what might be found using an optical tracer for example), there is a clear difference in the population of mid-infrared sources in the two clusters – but what is the physical cause of this?

Although the clusters are of similar mass, and at a similar redshift, they differ strongly in their intra-cluster environments and dynamical status (Treu et al. 2003). Cl 0024+16 is dynamically active (Czoske et al. 2001; Kodama et al. 2004) and this may provide the impetus for the triggering of star-formation via mergers and interactions of gas-rich spirals within the cluster – even in the apparently high-density core. The intracluster medium (ICM) of MS 0451−03 is much hotter and denser (by nearly an order of magnitude) than Cl 0024+16, and this will have an impact on the radii that processes such as starvation and ram-pressure stripping operate (Treu et al. 2003). In MS 0451−03 the hot ICM will be much more effective at starving galaxies of their gas reservoirs at a larger clustocentric radii than in Cl 0024+16. The relative dearth of mid-infrared sources in MS 0451−03 might then suggest that the active regions within the mid-infrared population are comparatively sensitive to these gas removal mechanisms. Unlike Cl 0024+16, unfortunately there are no published optical SFR studies of MS 0451−03 to confirm a wholesale decline in the SFR in this cluster. Nevertheless, the small excess of mid-infrared sources in MS 0451−03 show that it hosts quite significant star-formation, so it is unclear at this stage exactly what physical processes control the distribution of star-forming galaxies in

different types of clusters. We will address the issue in our next paper where we study the properties of the 24μm cluster members in more detail using the available spectroscopy, dynamics and *HST* imaging (Geach et al. in prep.; see also Moran et al. 2007).

2.6. Obscured star-formation in clusters out to $z \sim 1$

At the present-day, virialised regions of the Universe are dominated by passive galaxies: ellipticals and lenticulars, with the main contribution to the global star-formation rate density at $z = 0$ coming from late-type spirals in low-density environments. However, at higher redshifts the high-density environments within clusters show increasing numbers of actively star forming galaxies, possibly reflecting a similar increase in the frequency of activity to that seen in the surrounding field. Moreover, it is clear that there is significant hidden star formation in clusters in this redshift range: observations by *ISO* and now our new *Spitzer* observations reveal populations of infrared galaxies in clusters at low and intermediate redshift, with SFRs much higher than would be measured using optical tracers such as Hα or [OII]λ3727, due to the extinction effect of dust.

Given this new information, what is the evolution of the total star-formation rates in massive clusters – i.e. how does the increase in activity in high-density environments at high redshift behave in the mid-infrared? To compare the total mid-infrared derived star-formation rate in clusters from $z = 0$–1 we use the total SFR within $\sim$2 Mpc and normalize by the best-estimate mass of the cluster (for example, see Kodama et al. 2004). For Cl 0024+16 and MS 0451−03 these are $6.1 \times 10^{14} M_{\odot}$ (Kneib et al. 2003) and $15 \times 10^{14} M_{\odot}$ (La Roque et al. 2003) respectively, where the masses are within 2 Mpc of the clusters' centers.

To build up a history of star-formation in clusters out to $z \sim 1$, we compare our results to previous *ISO* and *IRAS* studies of the clusters: Perseus (A 426), A 1689, A 370, A 2218 and J1888.8 CL (Cl 0054−27), summing the known cluster member's star formation rates down to a far infrared limit $6 \times 10^{10} L_{\odot}$ – the limit of the Cl 0024+16 observations. To ensure correct comparison of the rates, if necessary we re-derive the SFRs using our employed calibration from Kennicutt (1998), with a standard Salpeter IMF with a mass range 0.1–100$M_{\odot}$. For the *ISO* observations, we also re-derive the far-infrared 8–1000 μm luminosity using the method we present above, using the band-pass of the *ISO LW3* filter to convert mid to total-infrared. The *ISO* observations of these clusters are summarized in

the review by Metcalfe et al. (2005). Note that the previous *ISO* and *IRAS* observations have concentrated on the core regions of clusters (typically within 1 Mpc), so we restrict our star-formation integration to within a radius of 2 Mpc in Cl 0024+16 and MS 0451−03, and compare to estimates of the total star-formation within the equivalent radius in the other clusters. In the case of MS 0451−03, we estimate an upper limit to the star-formation rate extrapolated to a luminosity limit of $6 \times 10^{10}\,L_{\odot}$ by using the method described in §2.3.4, assuming the faint end of the luminosity function follows a similar shape to that in Cl 0024+16. We estimate that the upper limit to the total star-formation rate down to $6 \times 10^{10}\,L_{\odot}$ in MS 0451−03 is $\lesssim 460\,M_{\odot}\,yr^{-1}$.

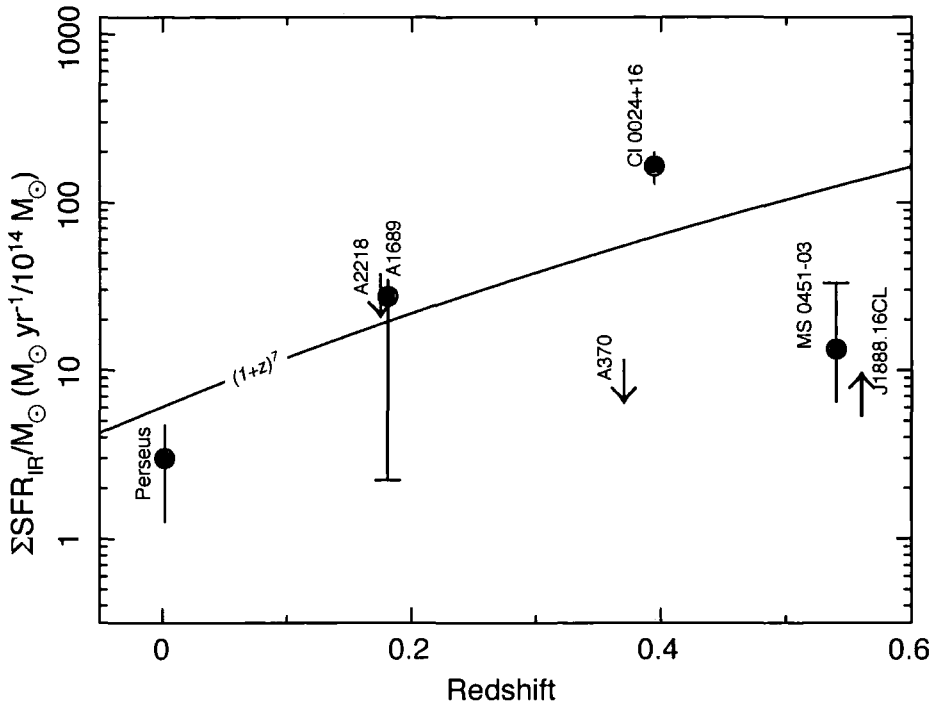

Figure 2.8: The variation in the mass-normalised star-formation rates in clusters out to $z \sim 0.5$. The star formation rates are from the mid-infrared populations within ~2 Mpc and these are normalised to the best estimate of the cluster mass, which is derived via lensing estimates, or from the X-ray luminosities. We also plot an evolutionary model for the counts of star-forming ULIRGs from Cowie et al. (2004), normalised to the mean star-formation rate in Cl 0024+16 and MS 0451−03 (again we note that these could be increased by ~ 18% to account for incompleteness in our color-selection of cluster members). The MS 0451−03 point has an upper limit which corresponds to the extrapolated estimate for the total star-formation down to the luminosity limit in Cl 0024+16 (6×10^{10} L$_\odot$), while the data point shows the cluster's summed SFR down to the limit of our data (12×10^{10} L$_\odot$). There is evidence for an increasing rate of activity in more distant clusters, as traced through their mid-infrared populations. However, there is also clear evidence for a wide variation in activity in even massive clusters at a similar epoch. This suggests that the mid-infrared populations are sensitive tracers of environmental changes within the clusters. The errors on the total star-formation rates for Cl 0024+16 and MS 0451−03 are derived from bootstrap resampling of the mid-infrared distribution, whereas for Perseus and A 1689 the errors are from counting statistics. Note that there are systematic uncertainties in all of the estimates depending on the specific choice of SED in the conversion from mid-infrared luminosity to star formation rate (the plotted uncertainties also do not take into account of the errors in the cluster mass estimates). Upper limits are equivalent star-formation rates for one detected at our luminosity limit of 6×10^{10} L$_\odot$, (and extrapolated to account for the coverage difference in the survey) in those clusters where no sources were detected above this limit.

At low redshifts, we use the nearby rich cluster Perseus, observed with *IRAS* (Meusinger et al. 2000). We sum over the known cluster members with $L_{FIR} > 6 \times 10^{10}\,L_{\odot}$, and convert their luminosities to SFRs, giving a lower limit to the total star-formation rate in the cluster of $> 22\,M_{\odot}\,yr^{-1}$, over an area equivalent to 10 degrees^2, which in terms of physical coverage is similar to the 2 Mpc radius used in Cl 0024+16 and MS 0451−03. We use the mass estimate of Ettori, De Grandi & Molendi (2002) of $3.1 \times 10^{14}\,M_{\odot}$ and extrapolate to 2 Mpc to determine the normalised star-formation rate per mass to be $\sim 3\,M_{\odot}\,yr^{-1}/10^{14}\,M_{\odot}$.

Fadda et al (2000) and Duc et al. (2002) observed A 1689 ($z = 0.18$) at 15 μm with *ISO* detecting 16 cluster members within 0.5 Mpc of the core. With the mid-infrared to total-infrared conversion used in this work, we find two galaxies (detected with the *LW3* 15μm filter) above our luminosity limit. In order to estimate the star-formation expected out to a radius of 2 Mpc we assume a radial profile for the mid-infrared population similar to that found for Cl 0024+16 and extrapolate the star-formation rate from within a radius of 0.5 to 2 Mpc. The resulting star-formation rate is $\sim 280\,M_{\odot}\,yr^{-1}$ within 2 Mpc of the core. We use the mass from King et al. (2002), correcting to 2 Mpc, yielding a mass-normalized value of $\sim 30\,M_{\odot}\,yr^{-1}/10^{14} M_{\odot}$. A 2218 is another rich cluster at a similar redshift to A 1689, with $z = 0.175$, however the mid-infrared activity in this structure is much lower than in A 1689. The 15μm observations of Biviano et al. (2004) found nine members within a similar radius ($\lesssim 0.4$ Mpc), but only one of these corresponds to a star-forming galaxy, and the median infrared luminosity is only $6 \times 10^8\,L_{\odot}$, or just $0.1\,M_{\odot}\,yr^{-1}$. A 370 is at a similar redshift to Cl 0024+16, at $z = 0.37$, but also appears deficient in LIRGs. Only one cluster member was detected at 15μm. We plot these points as upper limits using our luminosity limit, again extrapolating to account for radial coverage out to 2 Mpc using the shape of the radial profile of mid-infrared sources in Cl 0024+16. We use the cluster masses from Pratt et al. (2005) and Girardi & Mezzetti (2001) for A 2218 and A 370 respectively, extrapolating to find the mass within 2 Mpc. The mass-normalised upper-limits for A 2218 is $30\,M_{\odot}\,yr^{-1}/10^{14}\,M_{\odot}$ and for A 370 is $9\,M_{\odot}\,yr^{-1}/10^{14}\,M_{\odot}$.

J 1888.16 (Cl 0054-27) is at $z = 0.56$, and was observed by Duc et al. (2004) using *ISOCAM* at 15μm. Six mid-infrared sources were detected which are confirmed cluster members, whilst a further two have redshifts suggesting they are members of infalling groups at a slightly higher redshift. Using the calibration of Chary & Elbaz (2001), Duc et al. find that all of their detected members are LIRGs, with inferred $L_{FIR} > 1.3 \times 10^{11}\,L_{\odot}$, and with

individual SFRs in the range 20–120 $M_\odot\,yr^{-1}$. We re-calibrate the SFR using the method set out in §2.3.3, and find a conservative lower limit to the total cluster star-formation rate to be $> 70\,M_\odot\,yr^{-1}$. The mass of the cluster is determined by Girardi & Mezzetti (2001), and we extrapolate to 2 Mpc, giving a total star formation rate $> 7\,M_\odot\,yr^{-1}/10^{14}\,M_\odot$.

We present the results in Figure 2.6, in which we plot the sum of the SFRs within ~2 Mpc of the clusters' cores, normalized using the estimated total mass of the cluster (either based on lensing or X-ray models). There is strong evolution in the star-formation rates in the clusters out to high redshifts, but it is important to note that several clusters seem to have very low-levels of activity, below our luminosity limits. For example Cl 0024+16 appears significantly more active than A 370, which is at an almost identical redshift. This might be point to differing environmental influences between clusters being the dominant influence on the star-formation histories of in-falling galaxies. Nevertheless, assuming that we have only selected those clusters with significant activity in Figure 2.6, there still appears to be strong evolution in the sample out to $z \sim 0.5$. This observation could simply reflect the increase in number of star-forming galaxies seen in clusters and the field out to this redshift – these obscured systems representing the high luminosity tail of the general 'blue' population. The idea that the cluster (obscured) star-formation histories mimic that of the field is supported by the rough consistency with the $(1+z)^7$ trend found by Cowie et al. (2004) for the number of star-forming ULIRG radio sources out to $z \sim 1.5$. Kodama et al. (2004) present a similar analysis for the evolution of the Hα-derived star-formation in clusters out to $z \sim 1$. They find relatively strong evolution in the total-SFRs in clusters over this range, $\sim (1+z)^4$, but as in this study, there is considerable scatter in the total star-formations rates between clusters, even after mass-normalisation. This hints that, although there might be a nominal rise in the level of star-formation in clusters out to $z \sim 1$, this is mitigated by the fact that individual cluster environments have a strong influence on the star-formation histories of their constituent galaxies. This scatter is due to the complexity of processes operating solely in the dense environments. A detailed study of the sources in Cl 0024+16 and MS 0451−03 may elucidate this issue.

2.7. Conclusions & summary

We have used the MIPS instrument on *Spitzer* to survey the 24μm populations of

two optically rich clusters at $z \sim 0.5$: Cl 0024+16 and MS 0451−03. The samples are $\sim$ 80% complete at 200μJy, corresponding to total (8–1000μm) infrared luminosities of $6 \times 10^{10}\,L_{\odot}$ and $12 \times 10^{10}\,L_{\odot}$ at $z = 0.39$ and $z = 0.55$ respectively, equivalent to minimum SFRs of $\sim 10\,M_{\odot}\,yr^{-1}$ and $\sim 20\,M_{\odot}\,yr^{-1}$. We detect a total of 986 and 1018 mid-infrared sources above this flux limit across $\sim 25' \times 25'$ fields in Cl 0024+16 and MS 0451−03. Our observations probe from around the cores out to the turn-around radius at ~ 5 Mpc where the clusters merge into the field. In MS 0451−03, we also analyse archival MIPS observations of the central $\sim 5' \times 5'$ of the cluster, which our observations had to avoid. Similarly in Cl 0024+16 we make use of an *ISO* 15μm survey from Coia et al. (2005) in the central region to build up a picture of the distribution of mid-infrared sources over the complete range of cluster environments.

We exploit optical-near-infrared colors for the mid-infrared sources to reduce the background field contamination. We find a statistical excess of mid-infrared sources (within $\sim$ 5 Mpc of the cluster core) at $S_{24\mu m} > 200\mu$Jy associated with Cl 0024+16: 155±18. In contrast MS 0451−03 has a less significant population of mid-infrared sources, 28 ± 17, although we note that there are a small number of confirmed 24μm members in MS 0451−03 in our on-going spectroscopic survey of this cluster.

Using our deep optical and near-infrared imaging of both clusters we show that the 24μm sources in Cl 0024+16 are mostly associated with star-forming galaxies, with typically blue $(B - R)$ colors, but which can be dust reddened by up to $A_V \sim 2.5$ mags. We also compare the infrared star-formation rate to that derived from an optical narrow-band Hα survey of this cluster from Kodama et al. (2004). Typically the Hα-derived rates underestimate the extinction-free infrared rate by $\gtrsim 5\times$, suggesting significant obscuration of the activity in this cluster. We find that the level of obscuration for these individual cluster galaxies is comparable to that found for LIRGs in the field at similar epochs. This suggests that starbursts in clusters are similar (at least in terms of extinction) as those triggered in low-density environments. However the variation in the 24μm populations of Cl 0024+16 and MS 0451−03 suggests that the range of triggering and suppression mechanisms in clusters is complex.

We also present the initial results from our follow-up *Spitzer* IRS survey of LIRGs in Cl 0024+16 (further observations are scheduled at the time of writing). Our results suggest that the majority of the 24μm emission observed in Cl 0024+16 is a result of star formation, indicated by strong PAH emission. However, one of our targets shows clear

evidence for an AGN. Although a larger sample will be required to more accurately quantify the impact of this contamination on our star formation rate estimate for the cluster, this is a cautionary note that 24μm detections alone are not enough to infer the total level of obscured star formation in clusters (although the presence of AGN is itself interesting). We estimate that the fraction of AGN in the 24μm flux-limited sample is $\sim$20%.

We estimate that the total star-formation rate (derived from the infrared) in the central region of Cl 0024+16 ($\lesssim R_{200}$) is $1000 \pm 210\,M_\odot\,yr^{-1}$ (not corrected for 20% AGN contamination). MS 0451−03 is much poorer in mid-infrared sources, and we derive a total star-formation rate estimate by summing over the small excess of objects, giving a total star-formation rate of $200 \pm 100\,M_\odot\,yr^{-1}$ within the same physical radius. We note however that our mid-infrared survey can miss some star-formation if a substantial number of lower-luminosity galaxies also exist in these clusters (as shown by the Hα survey of Kodama et al. 2004). Also, these estimate might be slight over-estimates, given that our small scale IRS observations suggest a 20% contamination by AGN, the mid-infrared output of which should not be included in the SFR estimate. This does not change our conclusions however, and even after this correction both clusters still exhibit strong dusty star formation.

The total star formation rates derived for the clusters allows us to investigate the evolution of the specific unobscured star formation rate in clusters over $z \sim$ 0–0.5. We find that the higher redshift clusters tend to have larger total star-formation rates compared to the more quiescent low-redshift ones, with an evolution similar to that of field LIRGs. However there is considerable scatter in this relation, and the evolution may only apply to the most active clusters. Although it is still unclear exactly what processes govern the star-formation histories of rich clusters, this study has shown that rich environments can sustain significant amounts of hidden star-formation, and that this seems to increase at least out to $z \sim 0.5$. This hidden activity may have a profound influence on the life-cycle of galaxies in high-density regions and the formation of the passive galaxy populations, ellipticals and S0s, which inhabit these environments at the present-day. We will investigate these issues in more detail in our next paper where we bring together spectroscopic and morphological information on the 24μm population in these fields.

2.8. Appendix: Matching of mid-infrared and optical catalogs

Here we provide a brief description of the technique which we have adopted for identifying the optical counterparts to the mid-infrared sources in our catalog. We have chosen to apply the technique of de Ruiter, Willis & Arp (1977) who use a Bayesian estimator for the probability, $p(\mathrm{id} \mid r)$, to identify whether an optical source in close proximity to a mid-infrared source is likely to be a true match, rather than a chance unrelated object.

First we parameterize the radial distances of sources in terms of a dimensionless variable:

$$r = \left(\frac{\Delta\alpha^2}{\sigma_\alpha} + \frac{\Delta\delta^2}{\sigma_\delta} \right)^{1/2} \tag{2.1}$$

where $\Delta\alpha(\delta)$ are the positional offsets of the sources in R.A. and Dec. (in the sense mid-infrared − optical), and $\sigma_{\alpha(\delta)}$ are the uncertainties in the positions (we assume that the optical uncertainties are negligible). A likelihood ratio LR can be constructed representing the probability of finding a genuine match (id) compared to the probability of finding a confusing (c) source within a radius r:

$$LR(r) = \frac{p(r \mid \mathrm{id})}{p(r \mid \mathrm{c})} = \frac{1}{2\lambda} \exp\left[\frac{r^2}{2}(2\lambda - 1) \right] \tag{2.2}$$

where $\lambda = \pi\sigma_\alpha\sigma_\delta\Sigma$, with Σ representing the surface density of optical sources down to some limit. The physical interpretation of equation 2.2 is that we are searching for a trade-off between finding a confusing background source, the distribution of which is governed by Poisson statistics; and the probability that the genuine match is located within $\mathrm{d}r$ of the reference source – this is described by the Rayleigh distribution.

In our case $\lambda \sim 20\Sigma$, and since we know that a cluster exists and the surface density of sources will not be uniform across the frame, we calculate the surface density of R-band sources brighter than the nearest-neighbour – $\Sigma(m > m_{\mathrm{NN}})$ – in annular bins of width $1'$ centered on the cluster at the radial distance of each mid-infrared source. The final part of the calculation requires us to calculate $p(\mathrm{id} \mid r)$ – *having found* a source at some radius r, what is the probability it is the genuine match? Bayes' theorem provides a way to estimate this value, but first we require an *a priori* estimate – namely what fraction θ of mid-infrared sources have optical counterparts? To estimate θ we count the number of sources with $LR > 1$, over the frame, denoting these 'matches' and compare to the number with $LR < 1$. θ is insensitive to the choice of likelihood threshold, and is approximately 0.77 for Cl 0024+16 and MS 0451−03. We can then find:

$$p(\mathrm{id} \mid r) = \quad = \frac{X\,LR(r)}{X\,LR(r) + 1} \tag{2.3}$$

where $X = \theta/1 - \theta$. We define a positive match of sources at some cut-off value L of the likelihood ratio, which we optimize to provide the best completeness C and reliability R of the sample:

$$C = 1 - \sum_{LR_i<L} p_i(\mathrm{id} \mid \mathrm{r})/N_{\mathrm{id}} \tag{2.4}$$

$$R = 1 - \sum_{LR_i>L} p_i(\mathrm{c} \mid \mathrm{r})/N_{\mathrm{id}} \tag{2.5}$$

with $N_{\mathrm{id}} = \sum p(\mathrm{id} \mid \mathrm{r})$. We choose a value of $p(\mathrm{id} \mid \mathrm{r}) = 0.82$ for positive matches, corresponding to $R = C \sim 97$ % in both clusters. To improve the matching algorithm, we perform an identical calculation for the next-nearest neighbour to the mid-infrared sources. Thus for each MIPS source we have a matching probability for both its nearest and next-nearest optical neighbours. This allows us to flag possible mergers (where both probabilities exceed our match threshold). If $p_{\mathrm{NNN}} > p_{\mathrm{NN}}$ then we chose the next-nearest neighbour as the genuine match.

Chapter 3

The environments of low-power radio galaxies at intermediate redshift

3.1. Introduction

In recent years, feedback mechanisms from radio galaxies (that is, galaxies which host radio-loud active galactic nuclei) have become the method of choice for curtailing the bright end of the galaxy luminosity function in models of galaxy formation, since models without feedback tend to over-produce the number of very luminous galaxies compared to what is observed (e.g. Bower et al. 2006). Many high-redshift radio galaxies lie in (proto-)cluster environments (e.g. Venemans et al. 2003) and the energies provided by their radio jets (the bulk kinetic power of the radio jets is several orders of magnitude larger than the radio luminosity; e.g., Rawlings & Saunders 1991) is sufficient to shut down star forming activity throughout a cluster (Rawlings & Jarvis 2004). Furthermore, it has been suggested that powerful radio sources may be triggered by galaxy–galaxy interactions during the merging of subcluster units (Ellingson, Yee & Green 1991; Simpson & Rawlings 2002).

Lower luminosity sources are also believed to be vital in shaping the galaxy luminosity function by providing a low power, but high duty cycle, mode of feedback (e.g., Croton et al. 2005; Bower et al. 2006; Best et al. 2006). This mode of feedback appears to be most common in the most massive galaxies, which are, of course, preferentially located in the centres of galaxy clusters. Therefore there appears to be significant interplay between the formation and evolution of both the radio sources and their cluster envi-

ronments. Studying the environments of low-power radio sources is likely a promising route towards understanding radio galaxy feedback. However, while the radio galaxy itself can influence the thermodynamic history of its environment (i.e. by depositing energy), the picture is complicated by global environmental processes such as the merging of sub-cluster units, which can temporarily boost the X-ray luminosity and temperature of the intracluster medium (e.g. Randall, Sarazin & Ricker 2002), making such systems more readily detectable in X-ray surveys (a matter of caution in using such X-ray detected systems as Cosmological probes). It is essential to perform detailed studies of the radio, optical, and X-ray properties of putative dense regions in the cosmic web to ascertain how mergers and radio source activity affect the life-cycle of clusters.

The luminosity and temperature of a cluster are known to follow a scaling relationship (the L_X–T_X relation), $L_X \propto T_X^{\alpha}$, where α has been measured in the range ~2.7–3 (Edge & Stewart 1991; David, Jones & Forman 1995; Allen & Fabian 1998; Markevitch 1998; Arnaud & Evrard 1999) This is at odds with that expected for clusters formed by gravitational structure formation, with $L_X \propto T_X^2$ (Kaiser 1986). It is thought that the disparity is due to the interruption of cooling by feedback from active galaxies, which can impart energy via outflow shocks (for example from radio-jets or super-winds), or by performing work by sub-sonically inflating bubbles in the intracluster medium (ICM; Sijacki & Springel 2006). Best et al. (2005) suggest that, given the short life-times of radio-loud AGN (10–100 Myr), episodic triggering must occur in order for feedback to quench cooling. However, much lower luminosity sources ($L_{1.4\,\mathrm{GHz}} < 10^{25}\,\mathrm{W\,Hz^{-1}}$) can impart energy into the IGM with a higher duty cycle than the more powerful, and rarer, sources (Best et al. 2006).

McLure et al. (2004) have recently constructed a sample of radio galaxies at $z \sim 0.5$ which spans three orders of magnitude in radio luminosity, but even the faintest of these sources are close to the Fanaroff–Riley break (Fanaroff & Riley 1974) and it is desirable to push to even fainter radio luminosities to fully investigate the radio galaxy–cluster symbiosis. In this paper we present multi-object spectroscopy of galaxies around four low-power ($L_{1.4\,\mathrm{GHz}} < 10^{25}\,\mathrm{W\,Hz^{-1}}$) radio galaxies at $z \sim 0.5$ in the *Subaru/XMM-Newton Deep Field (SXDF)* (Sekiguchi et al. 2006). The resultant spectroscopic redshifts allow us to investigate the environments of these radio sources which could provide a large proportion of the local volume averaged heating rate if the AGN luminosity function is flat below $L_{1.4\,\mathrm{GHz}} \sim 10^{25}\,\mathrm{W\,Hz^{-1}}$ (Best et al. 2006). We combine these data with X-ray obser-

vations of the radio galaxies' environments in order to investigate the global environmental properties – namely the $L_X - \sigma_v$ and $T_X - \sigma_v$ relations. This parameter space can be used as a diagnostic of the thermodynamic history of groups or clusters, since if an AGN is significantly feeding energy back into the intracluster medium (ICM), then the group or cluster might be expected to deviate from the standard empirical $L_X(T_X) - \sigma_v$ relation for massive systems. Throughout we adopt a flat geometry with $\Omega_{\rm m} = 0.3$, $\Omega_\Lambda = 0.7$ and $H_0 = 100h$ km s^{-1} Mpc^{-1} where $h = 0.75$. All magnitudes in this chapter are on the AB scale.

Table 3.1: Summary of radio galaxy targets. I.D.'s, positions and fluxes are taken from an early version of the 1.4 GHz Very Large Array radio mosaic presented in Simpson et al. 2006 (S06). In this paper for convenience we shorten IAU identifications of the radio galaxies to JEG 1–4. We quote radio luminosities here for completeness, however we discuss the redshift determination in §3.3.2.

I.D.	IAU I.D.	S06 I.D.	R.A. (J2000.0)	Dec. (J2000.0)	$S^{\rm SXDF}_{1.4\,\rm GHz}$ (mJy)	$L_{1.4\,\rm GHz}$ ($10^{24}\,\rm W\,Hz^{-1}$)
JEG 1	VLA J021945−04535	–	02 19 45.3	−04 53 33	11.86±0.13	4.36±0.05
JEG 2	VLA J021823−05250	VLA 0011	02 18 23.5	−05 25 00	7.95±0.10	14.35±0.18
JEG 3	VLA J021737−05134	VLA 0033	02 17 37.2	−05 13 28	2.37±0.06	4.26±0.11
JEG 4	VLA J021842−05328	VLA 0065	02 18 42.1	−05 32 51	0.96±0.08	0.48±0.04

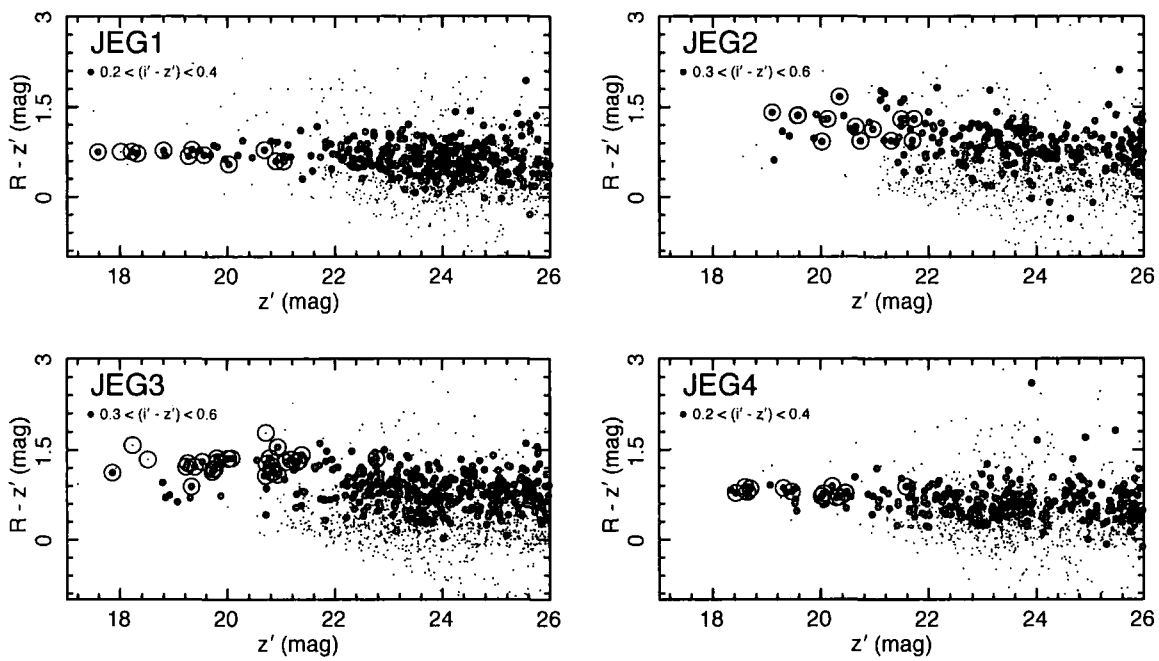

Figure 3.1: $R - z'$ vs. z' Field-corrected colour-magnitude diagrams for each mask. Photometry was extracted from the *SXDF* catalog by choosing all galaxies within an aperture of radius 2.5′ centered on the brightest target galaxy. Colours are measured in 2″ apertures, and we also indicate a secondary colour, $i' - z'$ (arbitrarily chosen), to emphasise the location of the red-sequence as larger points. The colours of targeted galaxies in this work are indicated by larger open circles.

3.2. Observations & Reduction

3.2.1 Sample selection and spectroscopy

Targets were selected from an early version of the 1.4-GHz Very Large Array radio mosaic presented in Simpson et al. (2006), and listed in Table 3.1. The limited red sensitivity of the Low Dispersion Survey Spectrograph (LDSS-2[1], Allington-Smith et al. 1994) placed an upper limit of $z \sim 0.7$ as appropriate for our study, so we selected radio sources whose optical counterparts are resolved and have $19 < R < 20.5$, since the tightness of the Hubble diagram for radio galaxies allows redshifts to be estimated from a single magnitude, and we aim to target moderate redshift environments (Cruz et al. 2007). Colour–magnitude diagrams were produced for $2.5'$ regions around each radio galaxy and the four optically brightest radio galaxies whose environments displayed a red sequence were selected for spectroscopic follow-up. This selection was simply performed 'by eye' – if the colour-magnitude diagram displayed an overdensity of points at $18 < m_{\rm RG} < 20.5$ with tight scatter in colour space. Note that local X-ray properties were not taken into account when choosing the target radio galaxies – this is simply an optical selection of radio galaxies.

Masks were designed using the LDSS-2 mask preparation software, with objects along the red sequence (typically using a colour cut of width 0.3 magnitudes) included in the input file (Figure 3.1). This software allows relative priorities to be assigned to targets, which were set to be equal to the magnitudes of the galaxies, to increase the likelihood of successfully determining redshift.

Observations were conducted using the medium-red (300 lines/mm, $\lambda_0 = 5550$Å) grism of LDSS-2 in multi-object mode on the 6.5-m Magellan telescope in Las Campanas, Chile over the nights 17–20 October 2003 (effective resolution 13.3Å). The MOS frames were trimmed for overscan, flat-fielded, rectified, cleaned and wavelength calibrated using a sequence of Python routines (D. Kelson, private communication); sky-subtraction and spectrum extraction was performed in IDL. Due to a lack of standard-star observations, for flux-calibration and to correct for the wavelength dependent response of the detector, we extracted $BVRi'z'$ photometry for the targets from the *Subaru/XMM-Newton*

[1]These observations were conducted prior to the installation of LDSS-3 with improved red sensitivity

Deep Field (SXDF) catalog. Using the five sources in each mask with the strongest signal-to-noise ratio (SNR), we fit mask-specific response curves to the 1-D spectra, which are then applied to each extracted target spectrum. Although flux-calibration and response correction is not necessary for redshift determination via cross-correlation, we perform these steps in order to present a sample of the spectra in Figure 3.2.

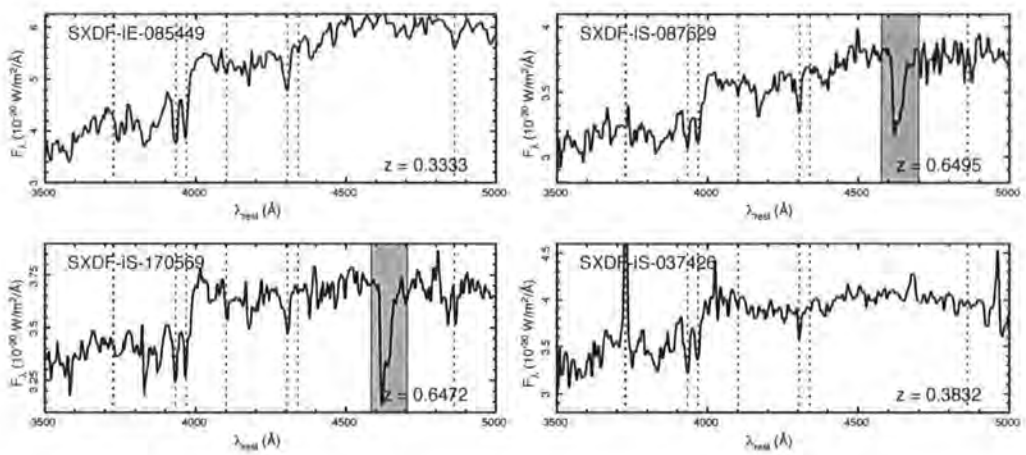

Figure 3.2: Successfully cross-correlated spectra for the radio galaxies field of (top-down) JEG 1–4. The spectra are plotted in the rest-frame. As a guide, we identify as dotted vertical lines the spectral features [OII], K, H, Hδ, G, Hγ, and Hβ. We do not plot wavelengths blueward of 3500Å or redward of 5000Å (restframe) since in these regimes the response and signal-to-noise of the spectra do not allow accurate analysis. Note that the shaded region highlights a sky absorption feature.

3.2.2 X-ray data

The *SXDF* incorporates a deep, large-area X-ray mosaic with XMM-Newton, consisting of 7 overlapping pointings covering $\sim$1.3 deg^2 region of the high-Galactic latitude sky with an exposure time of 100 ks in the central field (in separate exposures) and 50 ks in the flanking fields (see Table 3.2). Four of the pointings were carried out in August 2000, and the remaining three were made in August 2002 and January 2003.

All the *XMM-Newton* EPIC data, i.e. the data from the two MOS cameras and the single PN camera, were taken in full-frame mode with the thin filter in place. These data have been reprocessed using the standard procedures in the most recent *XMM-Newton* SAS (Science Analysis System) – v.6.5. All the datasets where at least one of the radio galaxies was seen to fall within the field-of-view (FOV) of the detectors were then analysed further. JEG 3 was observed in pointings SDS-1a (PN), SDS-1b (PN) and SDS-6 (M1, M2, PN) (part of the field lies off the edge of the MOS FOVs in SDS1a and SDS1b). Both JEG 2 and JEG 4 were observed in pointing SDS-7 (MOS 1, MOS 2, PN). Finally JEG 1 was observed in pointing SDS-2 (MOS 1, MOS 2, PN). Periods of high-background were filtered out of each dataset by creating a high-energy 10–15 keV lightcurve of single events over the entire field of view, and selecting times when this lightcurve peaked above 0.75 ct s^{-1} (for PN) or 0.25 ct s^{-1} (for MOS). It is known that soft proton flares can affect the background at low energies at different levels and times than high energies (e.g. Nevalainen et al. 2005). This was not seen to be the case in the datasets analysed here however, as full energy-band (1–10 keV) lightcurves (extracted from off-source regions) showed essentially identical times of flaring activity as the high energy lightcurves. The high-background times in each dataset are seen to be very distinct and essentially unchanging with energy-band. The exposure times of the resulting cleaned relevant datasets are given in Table 3.2.

Table 3.2: Overview of the *XMM-Newton* observations. Tabulated are the Field IDs, the centres of the pointings and the exposure times of the relevant high-background-cleaned datasets for each camera: MOS 1, MOS 2 and PN. Note that the coordinates are in J 2000.

Field	R.A.	Dec.	Exp. time [MOS 1 MOS 2 PN]
	hh mm ss	° ′ ″	(ksec)
SDS-1a	02 18 00	−05 00 00	– – 40
SDS-1b	02 18 00	−05 00 00	– – 42
SDS-2	02 19 36	−05 00 00	47 48 40
SDS-6	02 17 12	−05 20 47	49 49 47
SDS-7	02 18 48	−05 20 47	40 41 35

Source spectra were extracted from the relevant datasets from apertures centred on the source positions. Extraction radii, estimated from where the radial surface brightness profiles were seen to fall to the general surrounding background level, were set to 50″, 21″, 36″ and 47″ for JEG 1–4 respectively. Note that the surface brightness profiles were co-added for all 3 EPIC cameras for improved S/N. Standard SAS source-detection algorithms, uncovered a large number of X-ray sources, both point-like and extended. Data due to contaminating sources lying within the extraction regions needed to be removed from the spectra. This proved necessary only for JEG 3, where two sources were detected just within the extraction region. Data from the two sources were removed to a radius of 28″ (and the extraction area is thus reduced by $\sim$ 10%). Background spectra were extracted from each cleaned dataset from an annulus of inner radius 60″ and outer radius 180″ around each position. As point sources were seen to contaminate these larger-area background spectra, the data from these detected sources were removed from the background spectra to a radius of 60″. We have verified that all the X-ray sources are clearly extended using both simple (sliding box) and more sophisticated wavelet analysis techniques. The possibility that JEG 2 is an unresolved source complex cannot of course be completely ruled out given its low signal to noise. Given the relative weakness of all of the X-ray sources, we consider that the extraction radii used are close to optimum to provide the best signal to noise in the extracted spectra. Ancillary Response Files (ARFs) containing the telescope effective area, filter transmission and quantum efficiency curves were created for the cluster spectra (taking into account the fact that the extraction regions are extended), and were checked to confirm that the correct extraction area calculations (complicated with the exclusion of contaminating point sources, etc.) had been performed. Finally Redistribution Matrix Files (RMFs) files were generated. These files describe, for a given incident X-ray photon energy, the observed photon energy distribution over the instrument channels. These can be used in conjunction with the ARFs to perform X-ray spectral analysis – we use the most commonly used analysis package: XSPEC. The source spectral channels were binned together to give a minimum of 20 net counts per bin. A detailed discussion of the X-ray spectral fitting and the results is given in §3.3.4

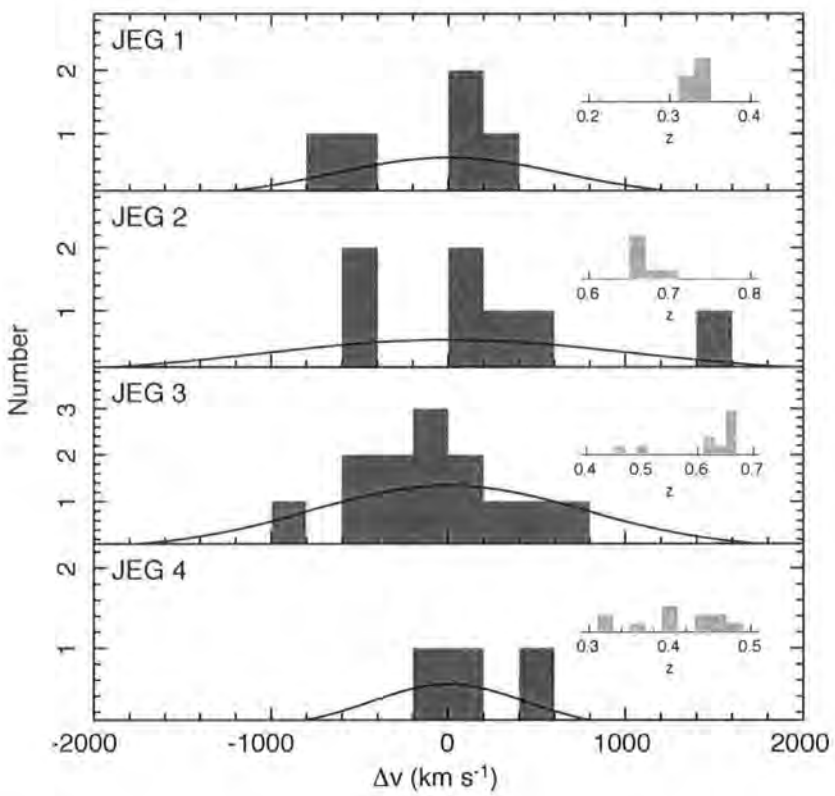

Figure 3.3: Relative velocity distribution of galaxies where successful redshift-determination was performed. Relative velocities are in the cluster frame, over a range $\pm 2000\,\mathrm{km\,s^{-1}}$. Insets show the distribution in redshift space, over a wider velocity range. We overlay Gaussian profiles based on the fitted velocity dispersion in each case.

3.3. Analysis

3.3.1 Colour-magnitude diagrams

In Figure 3.1 we plot the $R - z'$ vs. z' colour-magnitude relations (CMRs) for each field, which have been constructed from the photometry of all galaxies within 2.5′ of each radio-galaxy target. We correct the colour-magnitude diagrams for field contamination using a method similar to Kodama et al. (2004) and Kodama & Bower (2001), which we will briefly describe here. First, colour-magnitude space is divided into a coarse grid ($\Delta z' = 2$, $\Delta(R - z') = 0.8$), and the number of galaxies within each grid-square counted: $N_{ij}^{\rm gal}$. An identical count is performed for a control field, $N_{ij}^{\rm control}$, where control galaxies are selected within an aperture of identical radius to the one used for each target mask, but centered on a random point on the sky (but within the catalog). We then assign the $ij^{\rm th}$ colour-magnitude bin the probability that the galaxies within it are field members: $P_{ij} = N_{ij}^{\rm control}/(N_{ij}^{\rm gal} + N_{ij}^{\rm control})$. For each galaxy in colour-magnitude space, we pick a random number, p, in the interval {0,1} and compare it to P_{ij}; a galaxy is removed from the diagram if $p < P_{ij}$. In order to reduce effects of cosmic-variance (e.g. randomly picking another cluster or void as the control sample), we build up an average probability map by repeating the control sample count and probability calculation 10 times around different random positions in the catalog.

There are clear red-sequences around all four radio galaxies, and to emphasise this, we also plot a secondary colour $i - z'$, and the locations of galaxies in colour space targeted for spectroscopy. The secondary colour-cut is chosen merely to highlight the red-sequence.

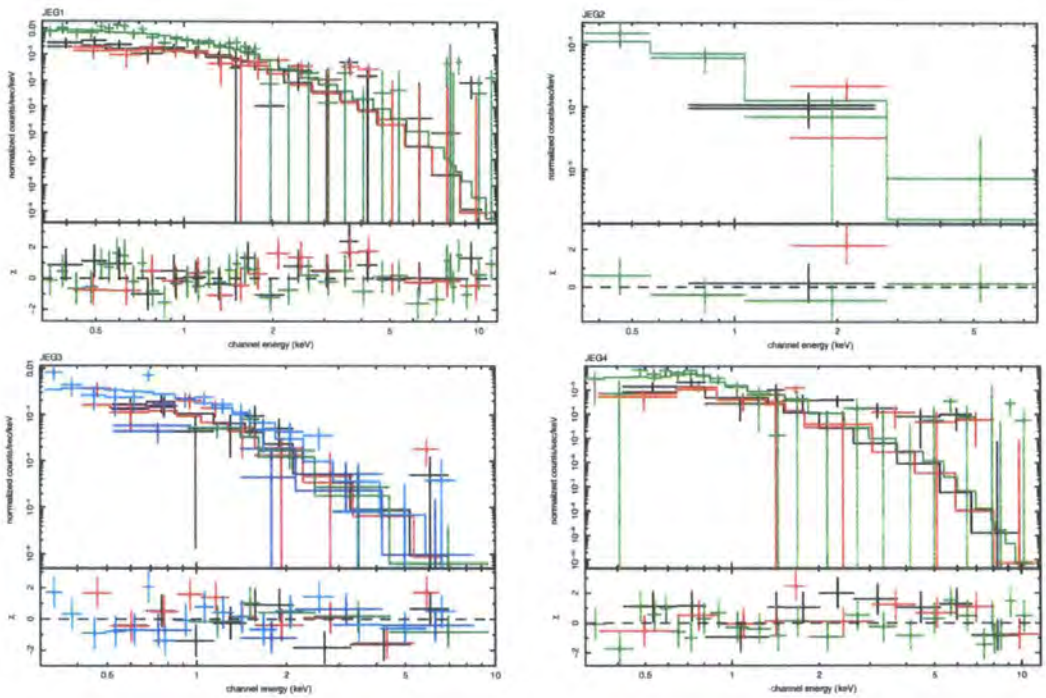

Figure 3.4: The *XMM-Newton* EPIC spectra of (row-wise from top left) JEG 1–4, together with the best-fitting thermal plasma model fitted using XSPEC. χ^2 residuals are shown in the lower panels of each plot. The colour-codings correspond to the MOS 1, MOS 2 and PN cameras and field pointings (see Table 3.2 and §3.2.2). For JEG 1 (SDS-2), JEG 2 (SDS-7) & JEG 4 (SDS-7) black is MOS 1, red is MOS 2 and green is PN. For JEG 3 black is PN (SDS-1a), red is PN (SDS-1b), green is MOS 1 (SDS-6), blue is MOS 2 (SDS-6) and cyan is PS (SDS-6). The resulting cluster parameters of L_X and T_X are presented in Table 3.4.

3.3.2 Redshift determination and velocity dispersions

For redshift determination we use the VELOCITY code of Kelson et al. (D. Kelson, priv. comm.), which cross-correlates target and template spectra. The errors are determined from the topology of the cross-correlation peak (i.e. the width of a Gaussian profile fit to the peak in the cross-correlation spectrum) and the noise associated with the spectrum; typically in the range 30–210 km s^{-1}. We present spectra of the target radio galaxies which have been successfully cross-correlated and shifted to the rest-frame in Figure 3.2. In Table 3.3 we list the coordinates, z' magnitudes and redshifts of successfully cross-correlated targets, with the radio galaxies highlighted.

To calculate the velocity dispersions of each cluster, we follow the iterative method used by Lubin, Oke & Postman (2002) and others (e.g. Willis et al. 2005). Initially we estimate that the cluster central redshift is that of the target radio galaxies, and select all other galaxies with $|\Delta z| < 0.06$ in redshift space. We then calculate the biweight mean and scale of the velocity distribution (Beers, Flynn & Gebhardt 1990) which correspond to the central velocity location, v_c, and dispersion, σ_v of the cluster. We can use this to calculate the relative radial velocities in the cluster frame: $\Delta v = c(z - z_c)/(1 + z_c)$. The original distribution is revised, and any galaxy that lies $>3\sigma_v$ away from v_c, *or* has $|\Delta v| >$ 3500 km s^{-1} is rejected from the sample and the statistics are re-calculated. The final result is achieved when no more rejection is necessary, and the velocity dispersion and cluster redshift can be extracted. The results are presented in Table 3.4, with 1-σ errors on the cluster redshift and dispersion corresponding to 1000 bootstrap resamples of the redshift distribution.

In Figure 3.3 we plot the redshift distribution of those galaxies for which we performed successful cross-correlations. We also plot the velocities of those galaxies within $|\Delta v| < 2000$ km s^{-1} of the cluster central redshift, overlaid with standard Gaussian profiles. JEG 3 is the largest sample of cluster galaxies (in part due to the large number of galaxies targeted in this field). JEG 1 and JEG 4 (at similar redshifts) have relatively few members after the process of rejection described above. JEG 2 has a high velocity dispersion, indicating a non-relaxed system, despite the fairly prominent red-sequence in this region. In part, the high velocity dispersion might be attributed to an outlying galaxy in the velocity distribution, but as we discuss in §3.3.3, JEG 2 might be part of a larger, more complicated structure than a simple group.

Table 3.3: Spectroscopic targets with total z' band magnitudes and cross-correlated redshifts. Redshift uncertainties are derived from the topology of the cross-correlation peak. The radio galaxy is highlighted in bold type in each case.

I.D.	RA (J2000.0)	Dec. (J2000.0)	z' (mag)	Redshift	Member*
		JEG 1			
SXDF-iE-085449	02:19:45.252	−04:53:33.08	18.27	$0.3333^{+0.0001}_{-0.0001}$	•
SXDF-iE-079345	02:19:39.461	−04:53:18.56	18.83	$0.3029^{+0.0002}_{-0.0004}$	○
SXDF-iE-073826	02:19:36.864	−04:53:29.98	18.01	$0.3038^{+0.0001}_{-0.0001}$	○
SXDF-iE-094234	02:19:48.300	−04:53:23.65	19.56	$0.3297^{+0.0001}_{-0.0001}$	•
SXDF-iE-089522	02:19:46.118	−04:51:22.25	19.36	$0.3302^{+0.0002}_{-0.0001}$	•
SXDF-iE-085293	02:19:43.190	−04:52:43.50	19.33	$0.3336^{+0.0001}_{-0.0001}$	•
SXDF-iE-067505	02:19:33.689	−04:51:45.47	18.35	$0.3059^{+0.0001}_{-0.0001}$	○
SXDF-iE-080550	02:19:41.508	−04:52:30.60	17.61	$0.3329^{+0.0001}_{-0.0001}$	•
		JEG 2			
SXDF-iS-087629	02:18:23.532	−05:25:00.65	19.17	$0.6495^{+0.0001}_{-0.0002}$	•
SXDF-iS-105254	02:18:19.109	−05:23:06.32	20.02	$0.6515^{+0.0002}_{-0.0003}$	•
SXDF-iS-100288	02:18:19.066	−05:23:45.74	20.19	$0.6812^{+0.0004}_{-0.0005}$	○
SXDF-iS-111951	02:18:20.074	−05:22:14.13	21.49	$0.6748^{+0.0003}_{-0.0005}$	○
SXDF-iS-108679	02:18:20.374	−05:22:36.40	20.64	$0.6566^{+0.0002}_{-0.0004}$	•
SXDF-iS-087515	02:18:23.777	−05:25:49.89	21.73	$0.6459^{+0.0002}_{-0.0002}$	•
SXDF-iS-090262	02:18:26.772	−05:25:14.35	19.66	$0.6502^{+0.0001}_{-0.0002}$	•
SXDF-iS-070840	02:18:27.202	−05:27:36.30	19.70	$0.6488^{+0.0002}_{-0.0003}$	•
SXDF-iS-102854	02:18:29.954	−05:23:30.49	20.73	$0.6456^{+0.0005}_{-0.0005}$	•
		JEG 3			
SXDF-iS-170569	02:17:37.193	−05:13:29.61	19.30	$0.6472^{+0.0004}_{-0.0004}$	•†
SXDF-iS-157505	02:17:24.230	−05:15:19.53	19.76	$0.6506^{+0.0001}_{-0.0002}$	•
SXDF-iS-173222	02:17:26.530	−05:13:45.93	21.01	$0.6516^{+0.0001}_{-0.0001}$	•
SXDF-iS-182658	02:17:27.502	−05:11:45.34	21.44	$0.6484^{+0.0001}_{-0.0001}$	•
SXDF-iS-168040	02:17:29.052	−05:12:59.61	19.89	$0.6494^{+0.0001}_{-0.0001}$	•
SXDF-iS-154410	02:17:33.286	−05:15:51.00	19.46	$0.6027^{+0.0001}_{-0.0001}$	○
SXDF-iS-184999	02:17:31.322	−05:12:17.11	20.85	$0.6010^{+0.0001}_{-0.0001}$	○
SXDF-iS-172233	02:17:35.309	−05:13:30.71	19.76	$0.6495^{+0.0003}_{-0.0003}$	•
SXDF-iS-172341	02:17:43.358	−05:13:30.69	20.78	$0.6470^{+0.0001}_{-0.0001}$	•
SXDF-iS-172053	02:17:34.202	−05:13:39.44	19.36	$0.4464^{+0.0002}_{-0.0002}$	○

Continued on Next Page...

SXDF-iS-181772	02:17:25.450	−05:11:54.43	19.81	$0.6274^{+0.0002}_{-0.0002}$	○
SXDF-iS-169690	02:17:26.858	−05:13:16.88	21.17	$0.6481^{+0.0001}_{-0.0002}$	●
SXDF-iS-166516	02:17:31.070	−05:12:37.74	21.17	$0.6522^{+0.0001}_{-0.0001}$	●
SXDF-iS-167467	02:17:32.566	−05:12:59.88	19.85	$0.6433^{+0.0001}_{-0.0001}$	●
SXDF-iS-178431	02:17:35.803	−05:14:20.76	20.82	$0.6475^{+0.0002}_{-0.0002}$	●
SXDF-iS-163351	02:17:37.512	−05:14:31.25	20.15	$0.6455^{+0.0002}_{-0.0002}$	●
SXDF-iS-172154	02:17:46.733	−05:13:35.17	21.33	$0.6456^{+0.0007}_{-0.0005}$	●
SXDF-iS-131866	02:17:31.500	−05:19:26.34	23.43	$0.4943^{+0.0002}_{-0.0002}$	○
		JEG 4			
SXDF-iS-037426	02:18:42.067	−05:32:51.03	18.76	$0.3832^{+0.0001}_{-0.0001}$	●
SXDF-iS-029867	02:18:32.484	−05:34:21.33	20.46	$0.4238^{+0.0002}_{-0.0002}$	○
SXDF-iS-049475	02:18:34.486	−05:31:28.97	20.51	$0.4275^{+0.0002}_{-0.0001}$	○
SXDF-iS-048741	02:18:35.635	−05:31:33.23	20.29	$0.3126^{+0.0003}_{-0.0008}$	○
SXDF-iS-035961	02:18:37.447	−05:32:49.61	18.60	$0.4576^{+0.0001}_{-0.0001}$	○
SXDF-iS-041384	02:18:38.986	−05:32:38.25	19.46	$0.4725^{+0.0002}_{-0.0002}$	○
SXDF-iS-029332	02:18:40.183	−05:34:01.32	19.31	$0.4588^{+0.0001}_{-0.0001}$	○
SXDF-iS-024990	02:18:42.938	−05:34:49.71	18.64	$0.3820^{+0.0001}_{-0.0002}$	●
SXDF-iS-035811	02:18:45.775	−05:32:54.73	18.49	$0.3853^{+0.0004}_{-0.0003}$	●
SXDF-iS-032022	02:18:48.029	−05:34:10.07	20.37	$0.3533^{+0.0001}_{-0.0001}$	○
SXDF-iS-046639	02:18:51.972	−05:31:49.76	20.06	$0.3107^{+0.0002}_{-0.0002}$	○

⋆ • (member) ○ (non member)

† Note – serendipitous lensed source on slit, $z = 1.847$, see Figure 3.7 and §3.4.2

Table 3.5: Spectroscopic, environmental and X-ray properties of target clusters. The cluster redshift z_c and line-of-sight velocity dispersion σ_v are calculated using the biweight mean and scale of the distribution (§3.3.2), with 1σ errors corresponding to 1000 bootstrap resamples of the redshift distribution. The environmental richness statistics (see §3.3.3) – are the $N_{0.5}$ counting statistic and $B_{\rm gc}$, the amplitude of the galaxy-cluster cross-correlation function. We also tabulate the results of fitting thermal (*mekal*) plasma models to the X-ray spectra of the clusters (see §3.3.4 for details). The uncertainties represent 90% for a single interesting parameter, determined during the spectral fitting with the XSPEC software.

	Redshift properties			Environmental properties		X-ray properties (0.3–10 keV)				
I.D.	z_c	σ_v	$f^{\rm a}_{\rm mem}$	$N_{0.5}$	$B_{\rm gc}$	kT	Z	L_X	$\chi^2/N_{\rm dof}$	Net counts
		(km s^{-1})			(Mpc$^{1.77}$)	(keV)	($Z_\odot$)	(10^{36} W)		
JEG 1	0.333±0.009	643±223	5/8	24 ± 5	599 ± 198	$1.59^{+0.65}_{-0.40}$	$\lesssim$0.2	$0.62^{+0.07}_{-0.07}$	57.6/64	477.29 ± 37.68
JEG 2	0.649±0.001	1042±394	7/9	4 ± 2	696 ± 557	$1.24^{+4.98}_{-0.84}$	uncon.	$0.58^{+0.52}_{-0.22}$	1.9/3	43.16 ± 12.12
JEG 3	0.648±0.001	774±170	13/18	23 ± 5	1782 ± 585	$1.97^{+1.00}_{-0.59}$	$\lesssim$0.7	$1.79^{+0.29}_{-0.83}$	51.2/51	328.21 ± 33.51
JEG 4	0.38±0.01	436±89	3/11	23 ± 5	388 ± 204	$1.06^{+0.52}_{-0.27}$	$\lesssim$0.8	$0.63^{+0.06}_{-0.11}$	45.2/43	232.77 ± 30.03

[a] fraction of members associated with the radio galaxy environment for successful redshifts

3.3.3 Environmental richness estimates

Although a rigorous spectroscopic environmental analysis of the clusters is not feasible with the sample sizes in this study, we can make an estimate of the richness of the clusters by some simple counting statistics using the photometric information from the *SXDF* catalog. The $N_{0.5}$ measure is perhaps the best tool for a first-order quantitative analysis of a cluster environment – it only relies on an approximate cluster redshift (in order to calculate the angular radius of the counting aperture), and a satisfactorily deep photometric catalog (Hill & Lilly 1991). It has been shown to correlate well with the more complex B_{gg} statistic (Longair & Seldner 1979), which is a more rigorous measure of the density of galaxies in space when spectroscopic data is lacking, but when the shape of the luminosity function is known (see uses in e.g. Farrah et al. 2004, Wold et al. 2000, 2001). In physical terms B_{gg} is the amplitude of the galaxy-galaxy spatial correlation function: $\xi(r) = B_{gg}r^{-\gamma}$, where γ is typically 1.8–2.4 (Lilje & Efstathiou 1988, Moore et al. 1994, Croft, Dalton & Efstathiou 1999), though the low end of the range is typically chosen, with $\gamma = 1.77$ (e.g. Yee & Ellingson 2003). Both these measures can be translated to the more familiar Abell richness scale.

$N_{0.5}$ is calculated by choosing a target and counting the number of galaxies within 0.5 Mpc in the magnitude range $\langle m, m+3\rangle$, where m is the magnitude of the target galaxy, which in this case we choose to be the radio galaxies. A field correction is applied by subtracting the expected number of galaxies in this magnitude range from a control field (this control field was different for each target, chosen to be centred on a random point, >1 Mpc from the radio galaxy). Note that the $N_{0.5}$ statistic will be inaccurate in cases where there is strong differential evolution between the radio galaxy luminosity and companion cluster galaxies, but this can be compensated for by choosing the second or third brightest galaxy in the aperture and applying the same method. More importantly, it is clear from the spectroscopic results that the $N_{0.5}$ statistic is contaminated by line-of-sight structures not associated with the physical environment of the radio galaxies. This is particularly evident for JEG 4 – the slightly higher redshift structure suggested by the number of $z \sim 0.4$ galaxies have magnitudes and colours that not only re-inforce the original red-sequence selection, but will be included in the $N_{0.5}$ calculation. Thus it is important to note that this method can only provide a very rudimentary environmental analysis – a more sophisticated method is required.

For this reason, we also calculate B_{gc} – where 'gc' stands for 'galaxy-cluster centre'.

This is a potentially useful statistic: derived solely from photometry, it has been shown to be in excellent agreement with its spectroscopic counterpart, and can be used as a predictor for global cluster properties such as the velocity dispersion, virial mass and X-ray temperature (Yee & Ellingson 2003). Thus, we have another parameter to compare with our spectroscopically derived cluster velocity dispersions and X-ray observations, as well as a quantitative description of the richness of the radio galaxies' environments.

A full derivation of the $B_{\rm gc}$ statistic was made by Longair & Seldner (1979), and has been used in a practical sense by several other authors (see Wold et al. 2000, 2001, Farrah et al. 2004, Yee & López-Cruz 1999), so we will not give a detailed procedure here, but the form of the statistic is given by:

$$B_{\rm gc} = \frac{\rho_g A_{\rm gc}}{\Phi(m_{\rm lim}, z) I_\gamma} d_\theta^{\gamma-3} \tag{3.1}$$

where ρ_g is the surface density of field galaxies brighter than a limit $m_{\rm lim}$, d_θ is the angular diameter distance to z, I_γ is an integration constant ($I_{\gamma=1.77} \sim 3.78$) and $\Phi(m_{\rm lim}, z)$ is the integral luminosity function to a luminosity corresponding to $m_{\rm lim}$ at z. $A_{\rm gc}$ is the amplitude of the angular correlation function, calculated by comparing the net excess of galaxies within 0.5 Mpc of the target with the number of background sources expected for an identical aperture in the field: $A_{\rm gc} = (N_{\rm net}/N_{\rm bg})((3-\gamma)/2)\theta^{\gamma-1}$. The conversion to $B_{\rm gc}$ effectively deprojects $A_{\rm gc}$ from the celestial sphere into 3-D space.

Perhaps the most important factor to consider is the choice of luminosity function, although $B_{\rm gc}$ is reasonably tolerant of incorrect parameters (as long as they are within $\sim 20\%$ of their true values). We estimate the shape of the luminosity function at $z = 0.35$ and $z = 0.65$ by using the semi-analytic catalog output of the Millennium Simulation[2] (Bower et al. 2006, Springel et al. 2000). At each epoch, we fit a Schechter function to the absolute (simulated) R-band magnitude counts, fixing the faint end slope $\alpha = -0.9$. The resulting ($M_\star$, $\phi_\star$) are (-20.87 mag, 0.0042 Mpc^{-3}) and (-20.65 mag, 0.0021 Mpc^{-3}) at $z = 0.35$ and $z = 0.65$ respectively. The relevant luminosity function used in equation 1 is evaluated from $M_\star + 3$ to $M_\star - 3$, where the faint end is in a relatively flat part of the distribution, and the bright end is expected to include most of the cluster galaxies (note that changing these limits by ± 1 magnitude does not change the value of $B_{\rm gc}$ by more than 1σ). The results are presented in Table 3.4.

It is important to note that JEG2 appears to have an environment almost consistent

[2] http://galaxy-catalogue.dur.ac.uk

with the field (although, as noted the $N_{0.5}$ statistic is likely to suffer contamination). This is inconsistent with the apparent red-sequence around the radio galaxy, which would suggest a moderate overdensity. However, we have seen that the very high velocity dispersion for this group, and structure in the velocity distribution might affect the richness estimates if the group is spatially spread out. JEG 1 and JEG 4 are moderately rich environments (they have very similar levels of overdensity, although note that JEG 4 is contaminated by a slightly higher redshift line-of-sight structure, and so its true richness is likely to be slightly lower),consistent with rich groups. JEG 3 is also an overdensity, but the statistics suggest that the cluster is no more rich than JEG 1 or JEG 4. Thus, the radio galaxy selection is detecting moderately rich groups of galaxies.

3.3.4 X-ray spectral fitting

The X-ray spectral fitting package XSPEC was used to fit X-ray spectral models to the cluster spectra. In terms of X-rays from galaxy clusters, it is commonly believed that the emission is predominantly due to the hot cluster gas trapped in the potential well, absorbed by the hydrogen column density within our own Galaxy (i.e. little in the way of internal cluster absorption is expected). The spectra therefore were fitted with a standard model comprised of a *mekal* hot plasma emission spectrum, together with a *wabs* photoelectric absorption model (Morrison & McCammon 1983). Due to the small number of counts, the hydrogen column of the absorption was fixed at the Galactic hydrogen column density in the line of sight to the Subaru pointings: $N_{\rm H} = 2.55 \times 10^{20}$ atoms cm^{-2} (Dickey & Lockman 1990). Also the redshifts were fixed at the values given in Table 3.4. The temperature and metallicity were left free to optimize. Acceptable spectral fits were found for all the clusters (though only a small number of counts is seen from JEG 2), and these results are given in Table 3.4. We present the best fit gas temperature and metallicity (with respect to the Solar value), the errors being 90% for a single interesting parameter, and the (0.3−10 keV) absorption-corrected X-ray luminosity. Also tabulated are the best fit χ^2 values and the number of degrees of freedom. For none of the clusters were there sufficient counts to warrant the use of a more complex model. We attempted to rebin the spectra into five counts per bin, with a fit based on Cash statistics (i.e. not subtracting the background in order to maintain counting statistics, Cash 1979), however this does not provide stronger constraints on T or Z compared to the adopted method. The data and best-fit models are shown in Figure 3.4.

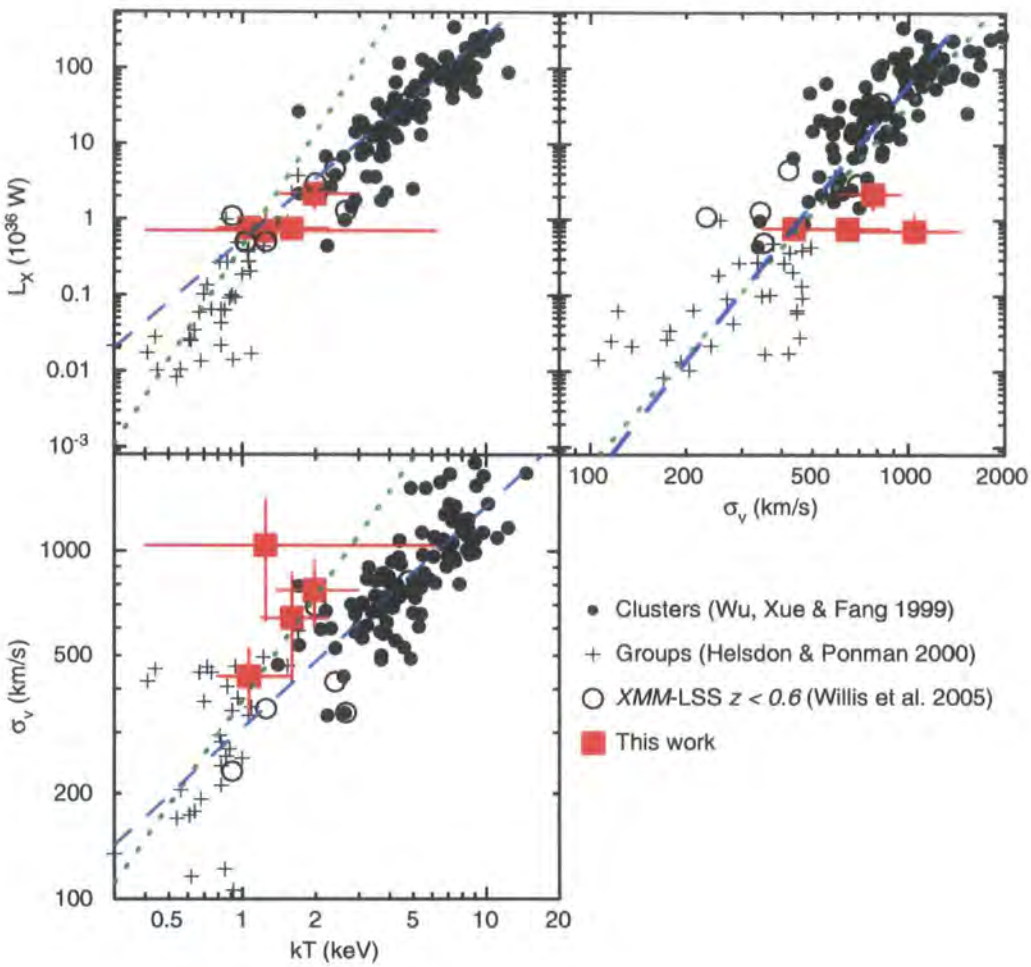

Figure 3.5: The correlation of global cluster properties: (top left) L_X–T_X (bottom left) T_X–σ_v (top right) L_X–σ_v. We compare our results with both rich clusters (Wu, Xue & Fang 1999) and poor groups (both the 'loose' and 'compact' sample from Helsdon & Ponman 2000), as well as more recent results from the *XMM*-Large Scale Structure (*XMM*-LSS) survey (Willis et al. 2005). In all parameter spaces shown, the sample in this work occupy the intermediate space between the rich/poor sample and are similar to the *XMM*-LSS sample. The dotted lines are the relationships derived for the groups sample from Helsdon & Ponman (2000), and the dashed lines show the equivalent relations derived using the rich cluster data from (Wu, Xue & Fang 1999). For clarity, we do not plot errors on the literature points (but these are taken into account in the linear fits). The X-ray data from this work are corrected for aperture losses. To estimate this, we extrapolate a King surface brightness profile of the form: $S(r) = S_0[1 + (r/r_{\rm core})^2]^{-3\beta+0.5}$. Assuming $\beta = 0.5$ and $r_{\rm core} = 200$ kpc, we find that the apertures used recover ~80% of the total flux, extrapolating to $2r_{\rm core}$. All points are corrected to our adopted cosmology, with $H_0 = 75\,{\rm km\,s^{-1}\,Mpc^{-1}}$.

3.4. Discussion

With the exception of JEG 2, the radio galaxies in each of our fields have environmental properties consistent with moderately rich groups at $z \sim 0.5$, in terms of their density statistic and X-ray properties. Despite the presence of a clear red sequence in the field of JEG 2 (Fig. 3.1), a simple $N_{0.5}$ environmental measure suggests that the environment is consistent with the field. However, it is likely that this is in fact a cluster of similar richness to JEG 1, JEG 3 and JEG 4 given that there are several nearby galaxies with colours and spectroscopic redshifts close to the radio galaxy. The low-number statistics for this system makes it difficult to make any robust comments about the radio-galaxy environment, except that this is probably a dynamically young group. There is some evidence for a sheet at $z \sim 0.65$ (Simpson et al. in prep) and JEG 2 may simply lie in an overdensity within this stucture. A large projected distribution of red galaxies around this group would in part explain the failure of the $B_{\rm gc}$ statistic to detect an overdensity: it could be possible that the control aperture itself is contaminated by the larger stucture.

Our observations of JEG 1 and JEG 4 also do not contain enough confirmed spectroscopic members at the radio galaxies' redshifts to comment on their environments from a spectroscopic standpoint. The wide-angle radio tail of JEG 1 suggests rapid movement through a dense medium (S06), consistent with a group-group merger (e.g. Jetha et al. 2006). There is insufficient spectroscopic data to confirm this though. Furthermore, in the case of JEG 4, our results could be affected by a background group, although it is not clear that this is contributing significantly to the X-ray luminosity. This slightly more distant group could also be re-enforcing the strength of the red sequence (Fig. 3.1), and is a cautionary point regarding selection in this way.

3.4.1 Scaling relations

The X-ray luminosities derived by fitting thermal models to the X-ray spectra are remarkably constant over our radio galaxy sample, with the environment of JEG 3 the hottest and intrinsically the most luminous (we note that the small number of counts seen from JEG 2 results in a poorly constrained model). In Figure 3.5 we compare these clusters' prop-

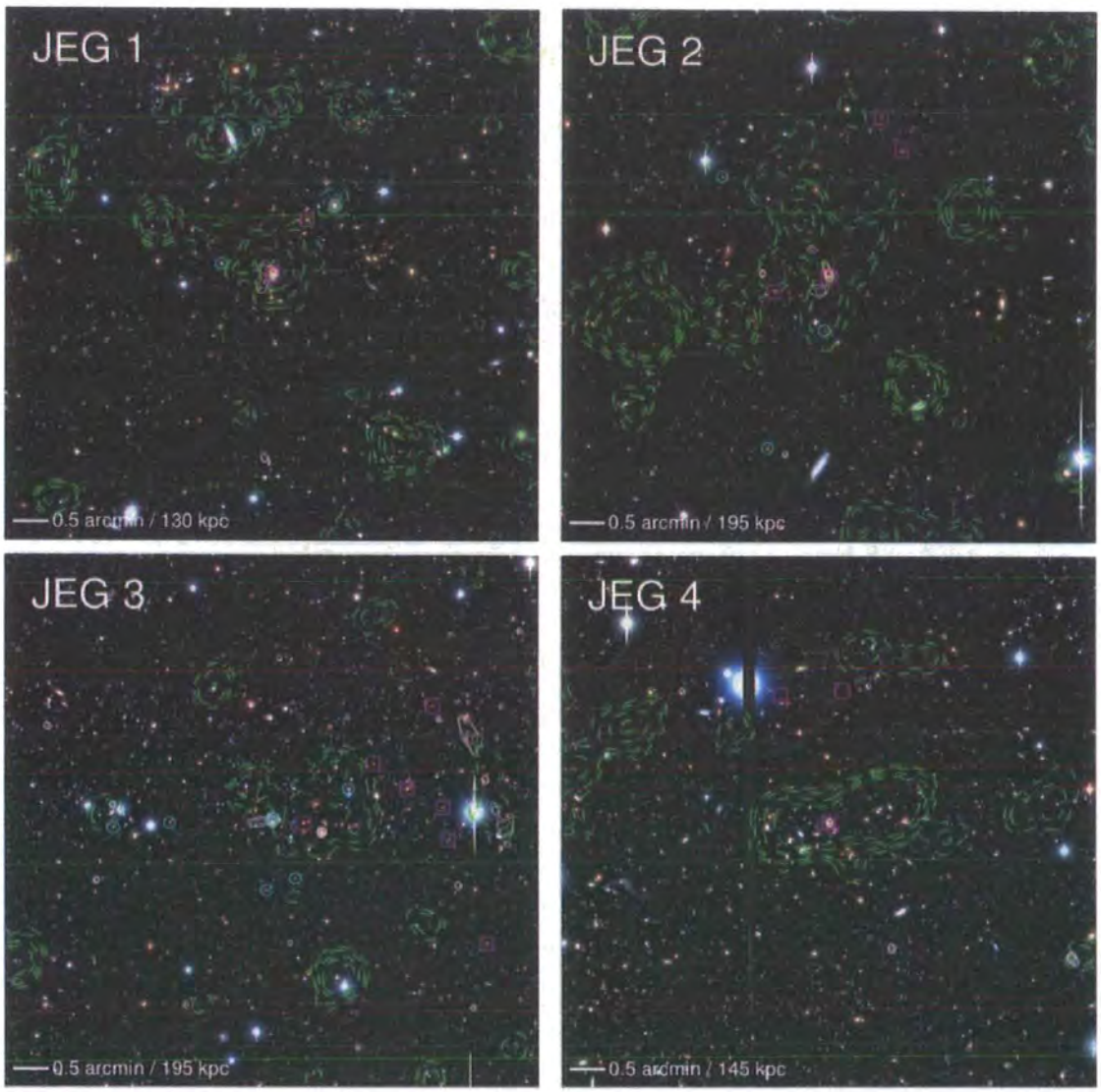

Figure 3.6: Here we present true colour image constructed from *Subaru* BVi-band $8' \times 8'$ images centered on the target radio galaxies JEG 1–4 (orientated North up and East left). In addition to the colour information, we overplot as contours the radio galaxy morphology from the VLA images (white solid), and X-ray (0.3–10 keV) contours (green dashed). The radio contour levels have been chosen to emphasise the lobe morphology (note that these are VLA B-array maps with a beam size of $5'' \times 4''$ with P.A. $= 170°$, see S06), and the X-ray contours are slightly smoothed with a Gaussian kernel of width $\sim 1'$ and at $\sim$2,3,5 & 7σ above the background in the vicinity of the environment. Finally, using the redshift data, we highlight galaxies which have $|\Delta v| < 2000\,\mathrm{km\,s^{-1}}$ relative to the cluster redshift. We plot positive values of Δv as open circles and negative values as open squares.

erties with the L_X–T_X relation of Helsdon & Ponman's (2000) study of galaxy groups and low-luminosity clusters, more luminous and massive systems from Wu, Xue & Fang (1999), as well as more intermediate redshift ($z < 0.6$) X-ray selected groups/clusters from the *XMM*-Large Scale Survey (*XMM*-LSS; Willis et al. 2006).

Firstly, the four clusters all have high-L_X and high-T compared to the group sample, indicating that they bridge the gap between groups and rich clusters – a relatively unexplored region of parameter space. This is likely due to selection effects, thus there is potential in investigating these types of environment using a selection technique similar to the one outlined in this work. However, we note that the radio selected environments are quite similar to X-ray selected groups/clusters at similar redshifts, detected in the *XMM*-LSS (Willis et al. 2006). We show also the disparity between the slopes of the L_X–T_X relation for groups (Helsdon & Ponman 2000) and rich clusters (Wu, Xue & Fang 1999), which differ by a factor $\sim$2. This is probably a real effect – the steepening of the slope for groups reflects the fact that these systems have a propensity to exhibit deviations from the relation seen for the more massive systems due to processes other than cooling (Willis et al. 2005; Ponman, Cannon & Navarro 1999). Note that all the empirical relations found for groups and clusters are steeper than that expected for pure gravitational structure formation (Kaiser 1986); this implies that feedback as a source of energy input is important over all scales of clusters, but is more dominant in the low mass systems.

One can also compare the cluster X-ray luminosity and velocity dispersion with the L_X–σ relations for these environments (Fig. 3.5). Although our small number statistics provide only loose constraints on our environmental parameters, all our environments appear to have slightly large velocity dispersions compared to the temperature of the intracluster gas, although this is not statistically significant. Once again, the velocity dispersions and temperatures reveal that these radio galaxies inhabit intermediate environments between groups and clusters. A similar picture is revealed by the L_X–σ_v relationship, with all clusters having slightly large σ_v for their L_X. This is in good agreement with the observed velocity dispersions for other radio/optically selected samples (e.g. Rasumussen et al. 2006; Popesso et al. 2007).

For the remainder of the discussion we concentrate on JEG 3, which has a spectroscopically-confirmed sample large enough to comment on the Mpc-scale environment of the radio galaxy.

3.4.2 Discussion of JEG 3

Optically, the radio galaxy is intriguing: it appears to be morphologically disturbed, with a blue and red part, suggestive of a recent or ongoing interaction triggering star-formation. In fact, closer inspection of the spectra (and images) provide unambiguous evidence that the blue component is actually a strongly lensed background AGN or starburst galaxy at $z = 1.847$ – not associated with the group (Figure 3.7). This high redshift object does not affect our results in any way, other than the fact that without the spectroscopic confirmation, this might be classified as a merger from the optical images alone. In terms of the radio emission, we are confident that the majority of the emission originates in the lensing source – i.e. the original selection of this target is still secure (the morphology and position of the radio emission support this, see Fig. 3.6). In terms of the impact from X-ray emission from the lensed galaxy, we also estimate that our measurements of the X-ray luminosity of the group will not be affected. The main bulk of the X-ray emission appears to be offset from the radio galaxy itself (Fig. 3.6) and the data were cleaned for point source emission prior to spectral fitting (§3.2.2). In the case that the point source is not cleaned, we estimate the impact on our measurement of L_X: if the lensed galaxy is a starburst, then we expect the X-ray luminosity to be of order $\sim 2 \times 10^{34}$ W (based on an X-ray stack of $z \sim 2$ BM/BX galaxies, Reddy & Steidel 2004), although this will be boosted by the lens. If it is an AGN, then we might expect the X-ray luminosity to be higher by a factor $\sim$2 (Lehmer et al. 2005). In both cases, this has a negligible impact on our results.

The most obvious feature of JEG 3's environment is the apparent spatial offset between the radio galaxy itself and the bulk of galaxies at the group redshift of 0.649 (Fig. 3.6), coincident with the dominant source of X-ray emission. The galaxy's radio lobe morphology is suggestive of infall through a dense intracluster medium towards this higher density region. In Fig. 3.6 we represent the relative velocities of galaxies about the central redshift, indicating objects with $\pm\Delta v$. Note that there are two other radio galaxies in this group; one $\sim$0.5′ to the west of the target radio galaxy, and the other (FR II source) several more arcminutes further to the west. Spectroscopic observations of these objects (Simpson et al. in prep) show that neither of them is associated with the structure surrounding JEG 3. These radio galaxies are not associated with the $z \sim 0.65$ structure identified around the radio galaxy in this work (see Simpson et al. in prep).

The radio galaxy appears to be associated with a small group interacting with the

main body of the structure, thus it is not unreasonable to associate the triggering of the radio galaxy with this interaction. This is a scenario which has been seen in other radio galaxy environments, at both high and low redshifts, and over a wide range of radio powers (Simpson & Rawlings 2002). For example, the high redshift radio galaxy TN J1338−1942 ($z = 4.1$, Venemans et al. 2003) belongs to a 'proto-cluster', but is offset from the centre of the overdensity. Similarly at low-redshift, the FR II source Cygnus A ($z = 0.056$) is involved in an cluster-cluster merger (e.g. Ledlow et al. 2005), with the radio-source offset from the main overdensity (Owen et al. 1997). X-ray mapping of this cluster revealed hot (presumably) shocked gas between the two main peaks of the X-ray emission in the two sub-cluster units (Markevitch et al. 1999), consistent with the model of head-on cluster merging. These well studied radio galaxies are examples of the most luminous objects at their redshifts, whereas the luminosities of the radio galaxies in this work are modest in comparison. Triggering within interacting sub-cluster units seems to be responsible for a proportion of radio-galaxies, and this appears to have been happening at all epochs, and over a wide range of luminosities.

The triggering of the radio galaxy could have occurred via galaxy-galaxy interactions in its immediate group, while the X-ray emission seems to be centred on the richer group in which gas is plausibly being heated by gravitational processes. However, there is a further complication to the L_X–T_X relationship, in that the outcome of the interaction between two sub-groups is a 'boosting' of the X-ray luminosity and temperature of the resulting cluster (Randall, Sarazin & Ricker 2002). In general this will temporarily (i.e. for a few 100 Myr) enhance both L_X and T_X, before the cluster settles down to its equilibrium value. It is not clear what stage of interaction this environment is in. Given the relatively large offset between the X-ray emission and the radio galaxy, we postulate that this is in an early stage. In these environments it appears that we are witnessing radio galaxy activity and group-group merging/interaction at the same time. Although this may hint at radio galaxy triggering in the cluster assembly phase, this does not imply that all clusters containing a radio galaxy are in an unrelaxed state – most relaxed clusters also contain a central radio source. This is interesting in that it appears that radio galaxy activity can be important in the thermodynamic history of the cluster environment over a wide range of scales (i.e. groups to massive clusters) and various stages of development.

Following the assumption made in equation 4 of Miley (1980), and adopting an expansion speed of $0.03 - 0.15c$ (e.g. Scheuer 1995), we estimate the jet power of JEG 3 to

be of the order 0.5–1$\times 10^{36}$ W, which is comparable to the X-ray luminosity of the cluster (the expected contribution to the X-ray luminosity from the radio galaxy itself is not significant). Although the similarity in power is likely coincidental, it is interesting, because the radio output of this low-power source appears to be sufficient to balance the radiative cooling of the gas. However, it is unlikely that the radio galaxy could keep up this balance over a long period: this mechanical injection will end long before the main merger between the two groups stops imparting energy to the system, given the expected timescales of radio activity ($\lesssim 10^8$ yr, Parma et al. 2002) which will likely be the dominant event in the pre-equilibrium thermodynamic history of the cluster. Nevertheless, since the radio-galaxy appears to have been triggered early in the life-time of the cluster (the centres of the radio and X-ray emission are separated by $\sim$200 kpc, Fig. 3.6), it could be important for providing significant energy input to the ICM, and therefore raising its entropy.

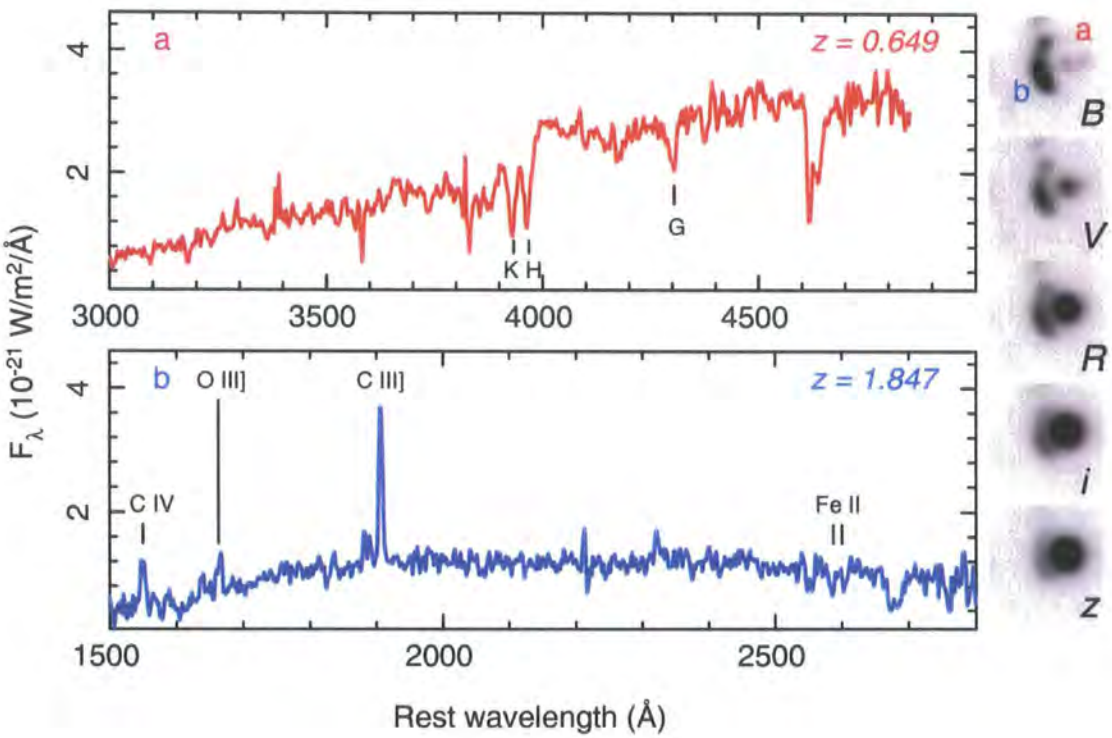

Figure 3.7: Spectra of components 'a' and 'b' of the radio galaxy in the field of JEG3 – SXDF-iS-170569. The inset greyscale images are $6'' \times 6''$ Subaru SuprimeCam thumbnails in $BVRiz$ bands, clearly showing the distinction between a red component 'a' and blue component 'b'. The spectra unambiguously identify 'b' with a galaxy at $z = 1.847$, strongly lensed by the foreground component 'a'. The emission lines at the very blue end of the spectrum 'b' are CIV, OIII] and CIII] in emission, securing the redshift. Fe III is seen in absorption at 2587Å and 2600Å.

3.5. Summary

We have presented multi-object (Low Dispersion Survey Spectrograph 2) spectroscopy, combined with complimentary radio (VLA) and X-ray (*XMM-Newton*) observations of the Mpc-scale environments of a sample of low-power ($L_{1.4\,\mathrm{GHz}} \lesssim 10^{25}\,\mathrm{W\,Hz^{-1}}$) $z \sim 0.5$ galaxies in the *Subaru-XMM Newton Deep Field* (Simpson et al. 2004).

The radio galaxies targeted all appear to inhabit moderately rich groups, with remarkably similar X-ray properties, with JEG 3 (VLA 0033 in Simpson et al. 2006) being the hottest and residing in the richest environment. A statistical interpretation of the environment of JEG 2 (VLA 0011 in Simpson et al. 2006) would suggest that it does not belong to a cluster, but this could be in part due to the spatial distribution of the galaxies – the other evidence that this is a relatively rich group is compelling: there is a relatively strong red sequence and extended X-ray emission seen at this location (suggesting a gravitationally bound structure), and the spectroscopic data (although dominated by small number statistics) suggests that this is indeed a group, or part of a much larger structure, albeit one that is not relaxed. Also, three of the radio galaxies exhibit extended lobe morphology that suggest movement through a dense intracluster medium, again hinting that these systems are undergoing dynamical evolution.

Our analysis concentrates on the environment of JEG 3, which presents us with a 'snap-shot' of radio-galaxy and cluster evolution at $z \sim 0.65$. Overall, this is the richest environment we have studied, and the spectroscopic data reveal sub-structure: the radio galaxy belongs to a small group of galaxies which appears to be interacting (merging) with a larger group of galaxies. The X-ray emission for this system is associated with the richer, but radio-quiet group. We postulate that the radio emission has been triggered by a galaxy-galaxy merger within its local group. Although this may be providing some feedback to the ICM (indeed, the radio output is capable of balancing the overall radiative cooling), the eventual group-group interaction will boost the overall X-ray luminosity and temperature. This process will take longer than the life-time of the radio-source, and so might be the dominating event in the thermodynamic fate of the environment. This scenario is not dissimilar to the situation with other radio galaxies at both high redshift, and in the local Universe. Moreover, radio-triggering within sub-cluster units appears to be important for a proportion of the radio galaxy population over all epochs and luminosities.

Chapter 4

Extreme activity in a rich, primitive environment

4.1. A submillimeter survey of Lyman-α haloes in the SA 22 protocluster at z = 3.09

Since the earliest X-ray spectroscopic observations of clusters of galaxies, it has been apparent that the intracluster medium (ICM) in these systems contains a significant mass of metals. This material must have been processed through stars (most likely residing in galaxies) and then either expelled or removed from the stellar system. The apparent lack of evolution in the ICM metallicity in the high density cores of clusters out to $z \sim 1$ (Tozzi et al. 2003; Mushotzky & Scharf 1997) points to an early phase of ICM enrichment for the highest density regions, while claims of a minimum entropy in the ICM (Ponman et al. 1999) support mechanisms which can transfer both energy and metals to the environment. Outflows or winds driven by star formation or AGN activity have been proposed as an efficient mechanism for dispersing metals from within galaxies and heating the surrounding gas. Local starburst galaxies such as M82 or Arp 220 are known to exhibit spatially-extended structures, visible as haloes of emission line gas and hot X-ray emitting gas. These are believed to be related to wind-driven outflows emerging from the active regions of these galaxies (Heckman et al. 1990). If high redshift galaxies are expelling considerable quantities of enriched material into their environments then similar emission-line structures may be visible around them.

Sensitive narrow-band surveys have uncovered a class of giant Lyα emission-line nebulae at high redshift (Steidel et al. 2000 (S00); Matsuda et al. 2004 (M04)). These surveys both focus on an overdense structure at $z = 3.09$ discovered by S00 in the SA 22 field.

This structure has been interpreted as a cluster in the process of formation (S00), and is therefore an excellent natural laboratory to study galaxy evolution. The extended and morphologically diverse features of the Lyα haloes in SA 22 have led them to be termed Lyα Blobs (LABs, S00). With luminosities of up to 10^{44} ergs s^{-1} and physical extents of up to 100 kpc (S00), these objects have many of the properties expected for high-redshift analogs of the outflowing haloes seen in local galaxies – although their luminosities and sizes would need to be scaled up by at least an order of magnitude to match the high-redshift LABs.

Similarly extended and luminous Lyα halos have been found around bright radio galaxies at comparable redshifts using similar narrow-band imaging techniques (e.g. De Breuk et al. 1999; Kurk et al. 2000; Reuland et al. 2003). These halos are interpreted as tracers of cooling and feedback in merging galaxies at high redshifts (Reuland et al. 2003), with their morphological diversity suggesting the active growth through mergers of these powerful radio galaxies. There is also strong evidence that many of these radio galaxies reside in high-density regions, as traced by overdensities of extremely red objects, Lyman-α emitters, X-ray sources or submillimetre galaxies (e.g. Kurk et al. 2000; Smail et al. 2003; Stevens et al. 2003). Hence there is some circumstantial evidence of a connection between large Lyman-α halos and the earliest formation phase of the most massive galaxies in high-density regions at high redshifts.

M04 present a new catalogue of 35 LAB candidates over a 0.5-degree field at $z = 3.09$ in the SA 22 field from a narrow-band imaging programme using Suprime-Cam on the 8.2-m Subaru Telescope. This survey shows that LABs come in a range of sizes ($\sim$ 20–200 arcsec^2, $\sim$1150–11500 kpc^2) and have Lyα luminosities of the order 10^{42-44} ergs s^{-1}. Their morphologies are complex, including filamentary structures, apparent bubbles and shells. Some LABs also appear to have associated continuum sources which may be capable of providing sufficient ultra-violet photons to power the emission line halo, but some do not. Clearly several possible mechanisms could produce a LAB, not just a wind, and several explanations of the physical processes governing the Lyα emission have been proposed: (a) photo-ionisation by massive stars or an obscured AGN; (b) cooling radiation from a collapsing gaseous halo (Fardal et al. 2001) or (c) starburst superwind shock heating (Taniguchi & Shioya 2000, Ohyama et al. 2003). Additionally, it has been suggested that inverse-Compton scattering of cosmic microwave background photons by a population of relativistic electrons could also contribute (Scharf et al. 2004).

While each of these scenarios are potentially viable, one third of LABs are not associated with ultra-violet (UV) continuum sources luminous enough to produce Lyα emission from photo-ionization (assuming a Salpeter initial mass function, M04), suggesting that the photo-ionization source in (a) would additionally need to be heavily obscured for these LABs, indicative of dust in the system. This is intriguing, since dust heavily suppresses Lyα emission, requiring that the Lyα emission originates well away from the obscuration, or that there is some other mechanism allowing Lyα photons to escape through the dust and into the observer's line of sight. The nature of the processes responsible for producing the extended Lyα emission in LABs thus remains uncertain.

The first LAB to be studied in detail was LAB1 in the SA 22 field (S00; Chapman et al. 2001 (C01); Chapman et al. 2004 (C04)). LAB1 is the most luminous LAB cataloged in the SA 22 structure with a Lyα luminosity of $L_{\mathrm{Ly}\alpha} = 1.1\times10^{44}$ ergs s^{-1} and also has the largest extent of all LABs identified to date, at $\sim$100 kpc. LAB1's morphology is complex, and its includes companion galaxies and other structures visible at high resolution in *Hubble Space Telescope (HST)* imagery from C04. There is now a wealth of multi-wavelength data available for this object. In particular, C01 show that there is a strong submillimetre source coincident with the nebula ($S_{850} = 16.8 \pm 2.9$ mJy), confirming the presence of an extremely luminous power source within LAB1 with a bolometric luminosity in excess of $10^{13}L_{\odot}$. C04 note that deep *Chandra* X-ray observations in the region of LAB1 failed to detect an X-ray counterpart – suggesting the bolometric emission is not powered by an unobscured or partially obscured luminous AGN. However, they suggest that a heavily obscured AGN with a torus orientated at 45° to the sky might be responsible for the Lyα halo and would also explain extended linear features revealed by *HST* imaging, suggestive of jet induced star-formation.

Bower et al. (2004) used the SAURON integral field unit (IFU) to map the 2-dimensional dynamics of the Lyα emission in LAB1, including the haloes of two associated Lyman Break Galaxies (LBGs, C11 and C15). These authors conclude that the nebula has a complex velocity structure which cannot be explained by a simple shell-like outflow; and that the submm source occupies a cavity in the Lyα halo, suggesting that either the region in the immediate vicinity of the SMG is obscured by dust ejecta, or it has completely ionised the material in this region.

The local surface density of 283 Lyα emitters (LAEs, smoothed with a Gaussian with a kernel of $\sigma = 1.5$-arcmin) at LAB1 is 0.63 arcmin^{-2} (3.6×10^{-5} Mpc^{-}2 at $z = 3.09$)

compared to the average density of LAEs over the whole Suprime-Cam field-of-view of $0.39\,\mathrm{arcmin}^{-2}$ (Hayashino et al. 2004, M04). At a shallower limit, the density of the SA 22 Suprime-Cam field is $1.75\times$ that of the other blank (SXDS) field in Hayashino et al. (2004). Thus, the local density at LAB1 is $2.8\times$ that of the blank field. Since LAB1 is located at a peak in the underlying surface density, perhaps it is not surprising that this object is the brightest and largest of all known LABs – as it could represent a massive galaxy in the process of formation. It is equally possible that the large extent and complicated velocity structure of LAB1 is actually generated from several overlapping haloes related to C11, C15 and the submm source, which happen to inhabit the same dense region in the $z = 3.09$ structure.

The other LAB identified by S00 in the SA 22 structure is LAB2, this has a comparable Lyα luminosity to LAB1 and it has recently been shown to contain a hard X-ray source (Basu-Zych & Scharf 2004). These authors suggest that if the X-ray source is point-like, then the unabsorbed X-ray luminosity of $L_X \sim 10^{44}\,\mathrm{ergs\,s}^{-1}$ indicates that LAB2 harbours a super-massive black hole with a high local absorbing column. C01 also report submm emission from the vicinity of LAB2, but with a significantly lower submm flux than LAB1: $S_{850} = 3.3 \pm 1.2\,\mathrm{mJy}$ (C01; C04). The detection of submm emission from both of the LABs studied to date may suggest a strong link between these two populations. This would clearly favour those models for the formation of LABs which rely upon a highly active source to generate the extended emission-line halo. Perhaps more interestingly, if some LABs do not contain bolometrically-luminous sources, then we must consider a variety of processes (cooling, photo-ionisation, etc.) to account for these giant haloes. We have therefore undertaken a survey to detect or place limits on the submm emission from LABs at $z = 3.09$ in the SA 22 field.

Table 4.1: The catalog of LABs in the SA 22 region observed in the submm. We give the coordinates, 850 μm fluxes, isophotal Lyα emission areas and Lyα luminosities for LABs in the full sample. LABs detected at $> 3.5\sigma$ significance at 850 μm are shown in bold face type. For comparison, we also note the results for the well studied LAB1 and LAB2. We also classify the objects based on a simple morphological/Lyα luminosity description: F/C (faint+compact), F/E (faint+extended), B/C (bright+compact) and B/E (bright+extended), see §4.3.1. The compact/extended boundary is 50 arcsec^2 (2900 kpc^2), and the faint/bright boundary is 10^{43} ergs s^{-1}. Note: 10^{44} ergs s^{-1} = $2.6 \times 10^{10}\ L_\odot$.

Name	RA (J2000) (h m s)	Dec. (J2000) (d ′ ″)	S_{850} (mJy)	Area[a] (□″)	$\log_{10} L^b_{\mathrm{Ly}\alpha}$ (ergs s^{-1})	$\log_{10} L^c_{\mathrm{bol}}$ (ergs s^{-1})	Class	Notes[d]
LAB1	**22 17 24.68**	**+00 12 42.0**	**16.8±2.9**	**222**	**44.04**	**47.06**	**B/E**	**2 LBGs**
LAB2	22 17 39.00	+00 13 27.5	3.3±1.2	152	43.93	<46.39	B/E	X-ray
LAB3	22 17 59.15	+00 15 29.1	−0.2±1.5	78	43.76	<46.48	B/E	LAE[†]
LAB4	22 17 25.12	+00 22 11.2	0.9±1.5	57	43.58	<46.49	B/E	
LAB5	**22 17 11.67**	**+00 16 44.9**	**5.2±1.4**	**55**	**43.23**	**46.55**	**B/E**	**LAE**
LAB6	22 16 51.42	+00 25 03.6	−0.5±1.8	42	43.20	<46.56	B/C	LAE
LAB7	22 17 40.99	+00 11 26.9	0.2±1.6	40	43.18	<46.51	B/C	
LAB8	22 17 26.18	+00 12 53.5	0.3±5.3	39	43.23		B/C	M
LAB9	22 17 51.09	+00 17 26.2	1.3±5.3	38	43.11		B/C	LAE, M
LAB10	**22 18 02.27**	**+00 25 56.9**	**6.1±1.4**	**34**	**43.34**	**46.61**	**B/C**	**LAE**
LAB11	22 17 20.33	+00 17 32.1	−0.4±5.3	30	42.96		F/C	M
LAB12	22 17 31.90	+00 16 58.0	3.2±1.6	29	42.93	<46.52	F/C	

Continued on Next Page...

LAB14	**22 17 35.91**	**+00 15 58.9**	**4.9±1.3**	**27**	**43.08**	**46.52**	**B/C**	**LAE, C05**
LAB16	22 17 24.84	+00 11 16.7	2.2±5.3	25	43.00		B/C	LAE, M
LAB18	**22 17 28.90**	**+00 07 51.0**	**11.0±1.5**	**22**	**42.81**	**46.87**	**F/C**	X-ray?
LAB19	22 17 19.58	+00 18 46.5	−8.6±5.3	21	43.11		B/C	LAE, M
LAB20	22 17 35.30	+00 12 49.0	0.4±1.5	21	42.81	<46.49	F/C	
LAB25	22 17 22.59	+00 15 50.8	1.4±5.3	19	42.77		F/C	M
LAB26	22 17 50.43	+00 17 33.4	−2.7±5.3	18	42.79		F/C	M
LAB27	22 17 06.96	+00 21 31.1	0.5±1.6	18	42.83	<46.50	F/C	
LAB30	22 17 32.44	+00 11 34.1	3.3±1.3	17	42.98	<46.41	F/C	
LAB31	22 17 38.94	+00 11 02.0	−3.7±5.3	17	43.04		B/C	LAE, M
LAB32	22 17 23.88	+00 21 56.5	1.8±1.4	17	42.76	<46.46	F/C	LAE
LAB33	22 18 12.56	+00 14 33.3	1.6±1.5	16	42.95	<46.49	F/C	
LAB35	22 17 24.84	+00 17 17.0	1.2±5.3	16	42.95		F/C	LAE, M

[a] M04 – isophotal area determined on corrected narrow-band emission-line map

[b] M04 – luminosity at $z = 3.09$

[c] bolometric luminosity determined from S_{850}, assuming a modified black-body with $T_d = 40\,\mathrm{K}$, $\alpha = 4.5$, $\beta = 1.7$ after Blain et al. (2003).

[d] taken from the literature: S00, M04, Hayashino et al. (2004), Chapman et al. (2005). M = SCUBA scan map extracted flux, see §4.2

[†] Associated optical Lyα emitter from Hayashino et al. (2004).

4.2. Observations & Data Reduction

Our selection was based on Subaru Suprime-Cam narrow-band imaging of a 34 × 27 arcmin region around SA 22, which detected 33 new LABs (M04), in addition to the two LABs previously catalogued by S00. M04 obtained deep narrow- and broad-band imaging of this region using a narrow-band filter, NB497, and *BVR* filters with Suprime-Cam. The central wavelength of NB497 is 4977Å, with a FWHM of 77Å, sensitive to Lyα emission over a redshift range of $z = 3.06$–3.13. By combining the B and V bands they were able to estimate the continuum emission in the narrow-band filter. This allows construction of a continuum-subtracted, emission-line image by subtracting the BV image from the NB497 image. In this paper we adopt the nomenclature of M04, who catalog the 35 LABs in order of descending isophotal area. In this system LAB1 and LAB2 correspond to the "blob 1" and "blob 2" of earlier works (e.g. S00; C01).

We selected 13 of these LABs as targets for our submm observations. These were chosen to cover the full range of properties spanned by the LAB population (area, brightness, morphology, environment, see Table 4.1 and Fig. 4.1). To these 13 we have identified a further SMG, SMM J221735.84+001558.9, a submm source catalogued by Barger, Cowie & Sanders (1999) which corresponds to a Lyα-emitting μJy radio source at $z = 3.09$ from Chapman et al. (2005). This SMG is coincident with the extended Lyα halo, LAB14, from M04. We note that Chapman et al. (2005) have detected a further SMG at $z = 3.098$ within the overdensity, SMM J221735.15+001537.2, with $S_{850} = 6.3 \pm 1.3$ mJy although this SMG has detectable Lyα emission this is not sufficiently spatially extended to class as an LAB based on the selection of M04.

We used the National Radio Astronomy Observatory's[1] (NRAO) Very Large Array (VLA) to target SA 22 during October 1998 and July–September 2003, obtaining 48 hr of data at 1.4 GHz. The observations were taken for approximately 12 hr in B configuration and the remainder in A configuration. The pseudo-continuum correlator mode ('4') was employed, with 28 × 3.25-MHz channels, enabling us to map almost the entire primary beam (27.3′ × 27.3′), recording data every 5 sec in both left-circular and right-circular polarisations. 0137+331 was used to set the flux scale, with 2212+018 (2.8 Jy) used for

[1]NRAO is operated by Associated Universities Inc., under a cooperative agreement with the National Science Foundation.

local phase/amplitude/bandpass calibration.

Finally, in addition to our new submm photometry observations, we also take advantage of an existing shallow submm map to place limits on a further 9 LABs. In total, including the previous published studies of LAB1 & 2, we have submm observations of 25 LABs.

Observations were conducted using the Submillimetre Common User Bolometer Array (SCUBA) on the James Clerk Maxwell Telescope (JCMT) over the nights of 2004 September 18–22. SCUBA was used in photometry mode to search for 850 μm and 450 μm emission from the 13 LABs listed in Table 4.1. We employed two-bolometer chopping, whereby the on- and off-source positions are divided between three bolometers to maximise the signal-to-noise ratio (SNR) in the final coadded flux measurement (discussed further in §4.2). Our goal was a mean r.m.s. noise in our measurements of $\sim$1.5 mJy – requiring $\sim$2–3 ks integration in Grade 1–2 weather conditions ($\tau_{\rm CSO} \leq 0.08$, $\tau_{850} \leq 0.32$).

To achieve sky and background cancellation we chopped in azimuth by 60″. Calibration observations employed Uranus and zenith opacity was measured from regular skydips and the JCMT water vapour monitor, yielding $\tau_{850} \leq 0.25$ for all observations, with $\tau_{850} \sim 0.1$ for some portions of the run. The on-sky exposure times were 2.2 ks for all sources, which in the conditions we experienced yielded mean 1-σ noise limits of 1.5 mJy and 13 mJy at 850 and 450 μm respectively.

We also obtained S_{850} fluxes or limits for ten additional LABs (LAB8, 9, 11, 16, 19, 25, 26, 31, 35, see Table 4.1) which were not observed in photometry-mode, but do fall within a shallow, submm scan-map of SA 22 (Chapman & Borys, priv. comm.). The map data were taken in a combination of SCUBA jiggle map and SCUBA raster map modes at 850 μm during a number of observing runs with good observing conditions ($\tau_{850} < 0.09$). Some of the SCUBA jiggle maps are described in detail in Barger, Cowie, & Sanders (1999) and Chapman et al. (2001, 2003, 2004). The combination of these SCUBA jiggle and raster maps are described in Chapman et al. (2003), using the approach of Borys et al (2003). This map covers an 11 $\times$ 11 arcmin region approximately centred on LAB1 and has a conservative r.m.s. depth of $\sim$5.3 mJy at 850 μm – it therefore is only sensitive enough to detect the brightest submm sources, such as that residing in LAB1. We extract the fluxes from the calibrated map by measuring 15″-diameter aperture fluxes and converting these using an assumed Gaussian beam profile to give fluxes in Jy beam^{-1}. In Figure 4.1 we plot the sky distribution of all 35 LABs from M04, identifying those which are map or

photometry observations.

Standard routines from the SCUBA User Reduction Facility (SURF, Jenness & Lightfoot 1998) were used to reduce each LAB photometry observation. For both long and short arrays (850 μm and 450 μm), demodulated data were flat-fielded and corrected for atmospheric extinction. A sky-estimate was subtracted using REMSKY by subtracting the average (median) signal from all the off-source bolometers in the arrays (avoiding any dead or noisy bolometers). Subtracting the sky gave a marginally better SNR than not removing it. Finally, a 6-σ clip was applied to remove spikes before the signals were coadded. For calibration, we derived the flux-conversion-factor (FCF) from observations of Uranus using the FLUXES program.

The chopping technique we adopted splits the on-source integration over two bolometers in an attempt to maximise the exposure time spent on the source. After the FCF was applied, an inverse-variance weighting scheme was applied to combine the two signals. Compared to the SNR from the main signal bolometer, on average the SNR improved after combining by $\sim$14 per cent for S_{850} and $\sim$8 per cent for S_{450}. We list the fluxes measured for the LABs in Table 4.1. Note that the flux errors in Table 4.1 do not include uncertainties due to absolute flux calibration, which we estimate to be $\sim$10%.

For the VLA data, editing and calibration was performed using standard AIPS procedures. We then employed IMAGR to map the central region, together with 40 satellite fields, running several iterations of the self-calibration procedure described by Ivison et al. (2002). Finally, we corrected for the primary beam response using PBCOR. The final image has a series of north-south stripes, as described by C04, but this affects none of the LABs discussed here. The typical noise level is around 9 μJy beam^{-1}, where the beam has a FWHM of 1.4″.

At the $\gtrsim 4\sigma$ level, the only detections amongst our sample are of LAB1 (as described by C04) and LAB4, which has several weak radio sources near the position listed in Table 4.1, as well as a stronger source to the south-east. The remainder of the LAB sample discussed here have upper limits at 1.4 GHz of around $5\sigma < 45\,\mu$Jy (for unresolved sources).

The *SST* observations used here are part of GTO project #64, which we retrieved from the *Spitzer* Science Center (SSC) archive. LAB 1 and LAB 2 are covered by all four IRAC channels (3.6–8μm), and we use the Post Basic Calibrated IRAC frames generated by the pipelines at the SSC. Both LABs were also observed by MIPS at 24μm as part of the

same project, and for these data we perform post-processing on Basic Calibrated Data frames to remove common MIPS artifacts and flatten small and large-scale gradients using 'master-flats' generated from the data. For mosaicking we use the *SSC* MOPEX package, which makes use of the supplementary calibration files which are supplied with the main science set. We use SExtractor (v2.4.4, Bertin & Arnouts 1996) to detect and extract sources in the mid-infrared images. Fluxes are measured in apertures with diameters chosen to be the same as in the SWIRE ELAIS-N1 catalog[2]: 3.8″ for IRAC and 12″ for MIPS.

In addition to the mid-infrared data, we analyse optical *HST* observations of the LABs, to reveal the rest-frame ultra-violet (UV) morphologies of the galaxies in the LAB haloes. The STIS coverage of LAB 1 has been previously discussed by Chapman et al. (2004), while the Advanced Camera for Surveys (ACS) F814W (*I*-band) imaging of LAB 2 is presented here for the first time. The ACS data was reduced using MULTIDRIZZLE, and will be described in more detail in a forthcoming work.

[2]see Surace, J. A. et al. 2004, VizieR Online Data Catalog, 2255

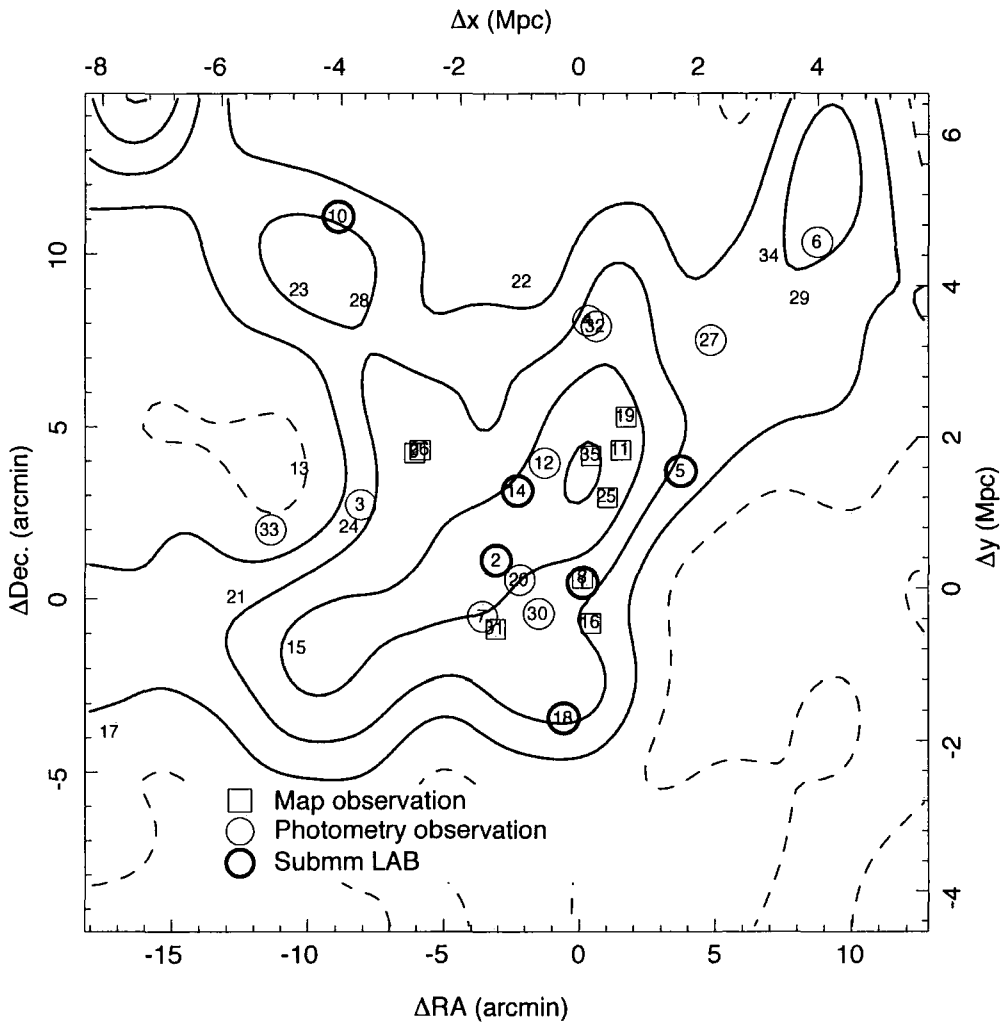

Figure 4.1: The sky-distribution of the 35 known LABs SA 22 from M04. Photometry observations are circled, map observations are identified with squares and submm detected LABs are circled in bold (§4.3.1). The contours represent the surface density of the underlying LAE distribution: solid(dashed) contours show regions of greater(less) than average surface density in steps of 50% of the average surface density. We discuss the environments of LABs further in §4.3.4. The origin of the coordinates are centred on LAB1, and the physical scale corresponds to angular separation.

4.3. Analysis & Results

4.3.1 Submm emission

In Table 4.1 we summarise the results of our submm observations, along with other information collected from the literature. In addition to the photometry mode observations, we tabulate the fluxes extracted from the SCUBA scan-map, and the previously published 850 μm fluxes of LAB1,2 from Chapman et al. (2000). We detect three LABs from the photometry-mode targets with S_{850} fluxes detected at significances of $> 3.5\sigma$: LAB5, 10 & 18. A further target, LAB30, has a flux corresponding to 2.6σ, but we do not classify this as a formal detection. No individual LABs are detected at 450 μm and therefore we have not tabulated individual 450 μm results.

To these three new detections, we can also add a fourth submm-detected LAB, LAB14. This source was detected in jiggle-map observations by Barger et al. (1999) with an 850-μm flux of 4.9$\pm$1.3 mJy (Chapman et al. 2005). The submm galaxy (SMG) was included in the redshift survey of submm galaxies by Chapman et al. (2003, 2005). They identified the counterpart as a Lyα-emitting galaxy at $z = 3.089$, and cross-correlation of their position with the LAB catalog of M04 shows that this SMG has an extended Lyα halo. We can thus add four submm-detected LABs to the two previously known.

Looking at the distribution of 850 μm fluxes for the entire sample, Figure 4.2, we note that there is an excess of positive flux measurements for our sample. We confirm this by deriving a noise-weighted average 850 μm flux for the LABs observed in photometry mode of 2.8 ± 0.9 mJy, where the uncertainty is derived by bootstrap resampling. A more rigorous test is provided by removing the well-detected LABs, averaging the fluxes of the remainder gives a mean flux of 1.2 ± 0.4 mJy. Similarly, when LAB1, 2, 14 and the fluxes of those sources covered by the scan-map are included in this analysis the average flux is 3.0 ± 0.9 mJy (we note that our bootstrap errors are conservative compared to the noise-weighted r.m.s. values). Thus we have $\geq 3\sigma$ detections of the LAB samples with typical fluxes around the level of the blank-field SCUBA confusion limit.

Performing a similar analysis on the 450 μm fluxes for the photometry sample yields a noise-weighted average of 6.2 ± 2.1 mJy, giving a 3-σ detection of the whole sample at 450 μm. The noise-weighted mean 450/850μm flux ratio is $S_{450}/S_{850} = 3.1 \pm 2.8$. This is consistent with a dust temperature of $T_{\rm d} \sim 40$ K at $z = 3.09$ (assuming a dust emissivity

index of 1.5).

We can convert the average 850-μm flux of the LABs into a typical luminosity using the characteristic dust temperature of $T_{\rm d} \sim 40\,{\rm K}$ derived above and knowing that the LABs are at $z = 3.09$. We estimate the typical LAB (with a Lyα luminosity of $6 \times 10^{42}\,{\rm ergs\,s^{-1}}$, or $1.6 \times 10^9\,L_\odot$) has a bolometric luminosity of $5.4 \times 10^{12}\,L_\odot$. If this emission arises wholly from star-formation with a standard IMF (Kennicutt 1998), then this luminosity corresponds to a star formation rate (SFR) of $\sim$900 $M_\odot\,{\rm yr^{-1}}$.

We note that the lack of radio detections for the majority of LABs is consistent with these estimates. Empirically scaling the SEDs of either Arp 220 or M82 to our average 850μm flux for a source at $z = 3.1$ implies 1.4GHz fluxes of 15–35μJy – below our detection limit.

4.3.2 Individually detected LABs

Here we discuss the properties of the individual LABs from our sample. We show the Lyα emission-line images (from M04) of a selection of the LABs in our photometry sample in Figure 4.3. Note that the SCUBA beam size is 15″.

LAB5

LAB5 is a large halo, the second largest submm-detected LAB after LAB1, but much fainter and more diffuse than LAB1. There is some evidence for a slight elongation of the Lyα emission (Figure 4.3), but the halo overall is roughly circular and the brightest region corresponds to a faint continuum source in the centre of the halo. LAB5 is located near the peak in the surface density of LAEs (Figure 4.1).

LAB10

LAB10 has a relatively compact morphology, and is within about 5 arcsec of an extended, bright continuum source. It is unclear whether these objects are related, but if they are independent, then the submm detection of LAB10 combined with the lack of an extended diffuse halo offers several possibilities for its power source: (a) LAB10 is in the initial stages of luminous activity (i.e. the start of a starburst or AGN), and is expelling a wind which has so-far only progressed a small distance into the IGM; (b) the fact that LAB10 is compact is an orientation effect: we are looking face on to a jet or collimated wind emerging from the SMG. A cooling flow cannot be ruled out, but the fact that this LAB has a

significant 850 μm flux (corresponding to a SFR of $\sim$ 1600 $M_{\odot}$ yr^{-1}) is strong circumstantial evidence that the Lyα halo is related to the obscured activity in this source.

Whereas the majority of LABs reside close to the main peak in the underlying distribution of LAEs (see Fig. 4.1), LAB10 lies in a secondary peak which resembles a filamentary structure to the north-west, connected to the main bulk of the proto-cluster.

LAB14

The submm source in LAB14 was identified from cross-correlating the LAB catalog in M04 with the redshift survey of SMGs (Chapman et al. 2005). Its morphology is compact, and comprises a bright component with a diffuse $\sim$ 50 kpc-long extension to the south-east. The source has a bolometric luminosity of $8.7 \times 10^{12} L_{\odot}$, making this a ultraluminous class active galaxy. As with LAB5, LAB14 is located close to the peak of the surface density of LAEs.

LAB18

This is the strongest submm source in the photometry sample ($S_{850} = 11.0 \pm 1.5$ mJy) and has an apparently hour-glass Lyα morphology. It is the second brightest LAB, after LAB1, in terms of its submm emission. It does not possess a continuum counterpart, which suggests that either its ionising source is completely dust-enshrouded, or that the power for the Lyα emission is from a superwind. Unlike LAB1, this object does not have companion LBGs, which may contribute to the large measured extent of LAB1. LAB18's Lyα luminosity is lower than LAB1. We note from Fig. 4.1 that LAB 18 appears to reside in a much lower density environment (reflected in the projected surface density of LAEs) compared to the other LABs.

Using archival *XMM-Newton* data (PI: O. Almaini) of the SA 22 field we tentatively detect a hard X-ray source at the location of LAB18 with a (0.4–10 keV) flux of $\sim 6 \times 10^{-15}$ ergs cm^{-2} s^{-1} at the $\sim 2\sigma$ level. The measured flux is consistent with the X-ray flux of LAB2 (Basu-Zych & Scharf 2003) and corresponds to $L_X \sim 5 \times 10^{44}$ ergs s^{-1} if we assume a photon index of 1.5 and local absorbing column $n_{\rm H} = 4.8 \times 10^{20}$ cm^{-2} as did those authors. We do not detect X-ray emission from any other LABs in this sample. If this detection is confirmed then it would suggest that LAB18 harbours a luminous, obscured AGN which may contribute to the submm emission and which could also couple with the ambient gas in the galaxy's halo.

Non-detected SMGs

Although our study hints at submm emission from LAB12 and 30 at the $\sim$ 2–2.5-σ level, the majority of the LABs we targeted with our photometry observations were not detected. These non-detections could be down to the uncertainty in where the submm source lies within the LAB – this is a particular concern for the largest and most irregular LABs – although the large size of the SCUBA beam and the flux aperture we adopted means we are relatively insensitive to offsets of less than $\sim$ 5 arcsec; or insufficient sensitivity in our submm observations. The fact that we obtain a 3-σ detection of the stacked submm emission from the stacked sources at a flux level of $\sim$ 3 mJy suggests that insufficient depth is likely to be a contributing cause to the non-detection of all but the brightest LABs.

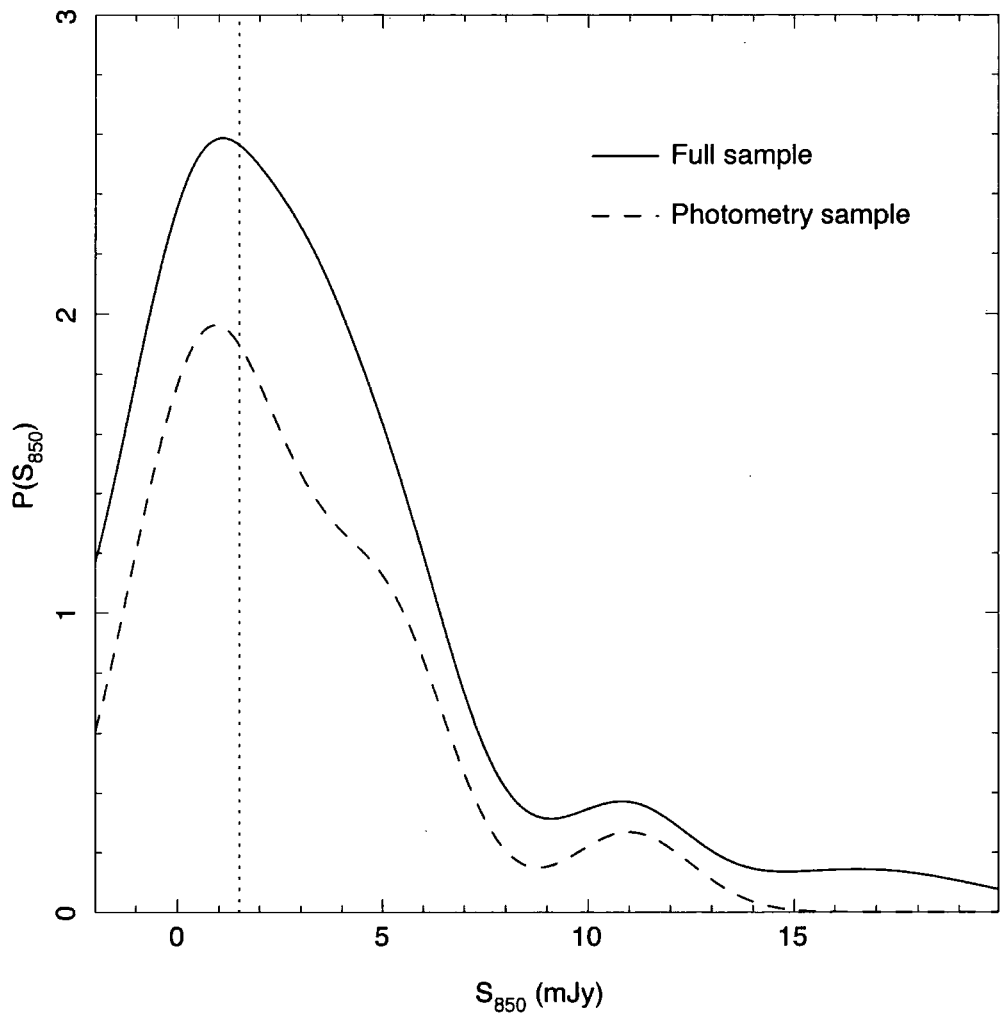

Figure 4.2: The S_{850} flux distribution of LABs in the sample. Here we have represented the distribution in terms of a superposition of Gaussian probability distributions for the full sample (solid line) and just the photometry sample (dashed line). The photometry sample only includes those objects targeted with SCUBA in 'photometry' mode, whereas the full sample includes LAB1, 2 and the map extractions. The vertical dotted line indicates the 1-σ 850μm noise limit for the photometry sample. Note that we assume that the noise associated with the submm fluxes may not be Gaussian or symmetric, and this might adversely affect this conclusion. One method of testing this might be to utilise off-source bolometers or blank map regions to estimate the expected scatter in measured flux for a 'non detection'.

Table 4.3: The mean properties of LABs detected and undetected at $S_{850} > 3.5\sigma$. We give the values for the LABs from our photometry observations, and in "[]" include data from LAB1,2,14 and the extracted fluxes from the map. The S_{850} values are noise-weighted averages and all errors are bootstrapped.

	$\log_{10}\langle L_{\mathrm{Ly}\alpha}\rangle$ (ergs s^{-1})	$\langle$Area$\rangle$ (arcsec^2)	$\langle S_{850}\rangle$ (mJy)
Detected	43.13±0.14	37±8	7.3±1.5
	[43.30±0.16]	[72±31]	[7.1±1.4]
Un-detected	43.10±0.09	34±7	1.2±0.4
	[43.09±0.08]	[36±7]	[1.4±0.4]

Table 4.4: 850 μm fluxes (in mJy) of LABs based on a simple morphological-luminosity classification: the bright/faint boundary is 10^{43} ergs s^{-1} and the extended/compact boundary is 50 arcsec^2 (2900 kpc^2). We give values for the LABs from our photometry observations, and in "[]" values which include LAB1, 2, 14 and our extracted map fluxes. The mean fluxes listed here are noise-weighted and the errors are estimated from bootstrap resampling.

	Bright	Faint
Extended	2.2±1.4	...
	[3.3±1.4]	[...]
Compact	2.4±1.8	3.2±1.3
	[2.8±1.5]	[3.0±1.2]

4.3.3 Lyα properties of LABs

We now search for correlations in the submm detection rate and properties of LABs as a function of their Lyα properties to identify trends which might indicate the nature and origin of their extended haloes. Therefore, in Table 4.2 we compare the properties of detected ($> 3.5\sigma$) and undetected LABs. We do this both for those LABs in our photometry sample and also for the full sample including LAB1, 2, 14 and the limits from the submm map.

The first point to note from Table 4.2 is that there appears to be no difference in the isophotal area of the Lyα emission (measured from the continuum-corrected narrow-band images) or Lyα luminosities between LABs with detected submm emission and those without. Including LAB1 does affect the area significantly, but since this object is the largest known, it could be considered a "special" object and not typical of LABs in general.

We can also perform the reverse test, to determine the submm emission from different samples of LABs differentiated by the extent and brightness of their Lyα haloes. We therefore provide a simple classification based on their isophotal areas and Lyα luminosities. First, we assign four categories: bright-compact (B/C), bright-extended (B/E), faint-compact (F/C) and faint-extended (F/E). The bright/faint boundary is 10^{43} ergs s^{-1} and the extended/compact boundary is 50 arcsec^2 (2800 kpc^2). The noise weighted average 850 μm flux for each category is presented in Table 4.3. Again, we perform this analysis for just the photometry observations, and the full sample including LAB1,2,14 and map observations. There are no F/E LABs in this scheme, in part due to the fact that F/E LABs fall below the sensitivity limit of M04's narrow-band survey. There appears to be no difference between any of these area/luminosity classes.

To look at this question in more detail we also study the morphologies of the Lyα haloes for the detected and non-detected submm sources (Figure 4.3). Generally the LAB's morphologies fall into two classes – those with an elongated or apparently disturbed halo (e.g. LAB5, 12, 18), and those which are compact and less disturbed (e.g. LAB3, 10, 30). The submm-detected LABs have a range of morphology: LAB5 and LAB18 are elongated and diffuse, whereas LAB10 and LAB14 are more compact and circular. To show that the morphologies are not a significant factor for the submm emission we note that each of the four submm-detected LABs has a morphological counterpart in the non-detected sample (e.g. LAB5 versus LAB6 or LAB10 versus LAB4)

In summary, we can find no property of the Lyα emission from the LABs which correlates strongly with their submm detection rate or flux. However, given our statistical detection of submm emission in the whole sample, implying starburst/AGN activity in a large proportion of LABs, it seems likely that this bolometrically-luminous activity must have some relationship with the LAB haloes. For example, if a wind is responsible for the emission, then we may be observing various stages of LAB evolution, governed by the nature and environment of the submm source.

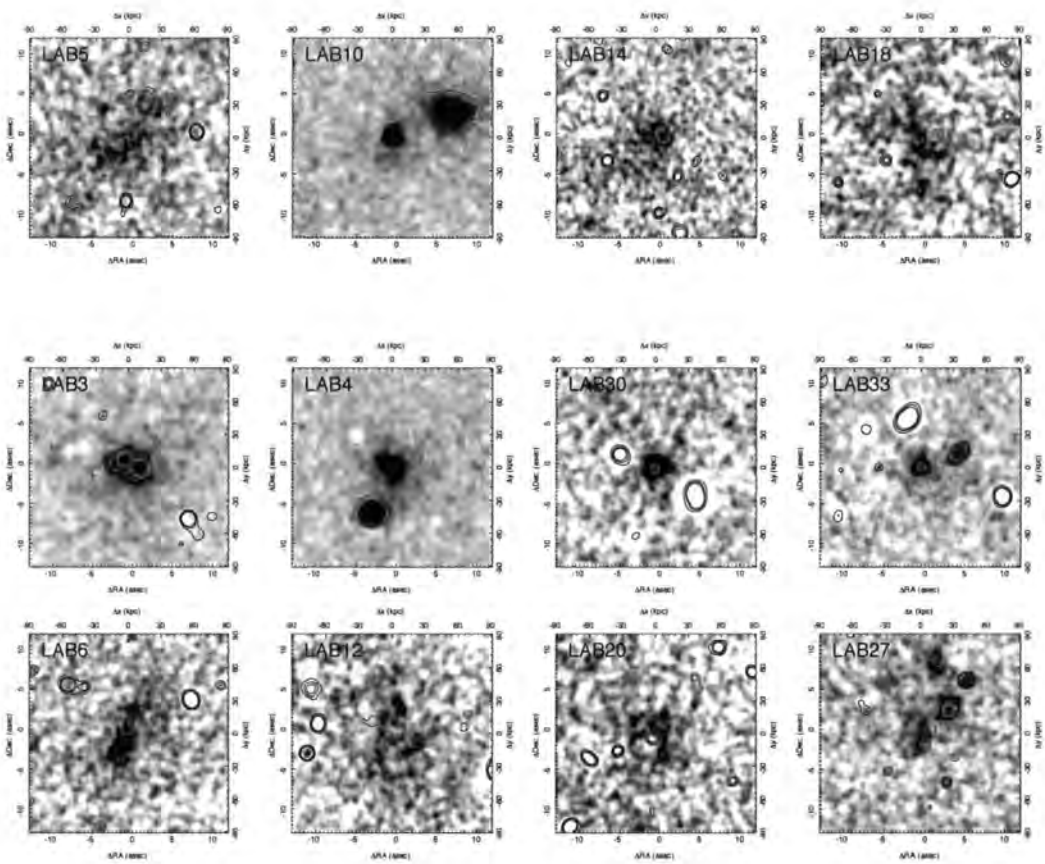

Figure 4.3: Narrow-band Lyα imaging of a subset of the LABs in our submm photometry sample with submm emission (top row) and without detected submm emission (bottom two rows). In this figure we divide the non-detected LABs into two morphological categories: in the top row we show LABs which are compact, with undisturbed haloes; and in the bottom row we show LABs with more complex morphologies – these objects exhibit more elongated and complex structure than the compact objects. Greyscale denotes the Lyα line emission corrected for continuum emission, first presented in M04 (see §4.2 for a description), while the contours show the location of continuum emission at levels of $\sim$ 3, 5 and 7σ (σ taken from the RMS scatter in blank regions of sky in the unsmoothed continuum image, scale 0.2″/pixel). The intensity scales are identical, each panel is 25″ $\times$ 25″ ($\sim$ 190 kpc $\times$190 kpc) and have North at the top and East to the left. The panels are centred on the coordinates listed in Table 4.1.

4.3.4 Environmental properties of LABs

To determine any trend in the environments of the submm-detected LABs, we compare them to the local surface density of 283 Lyα emitters (LAEs) at $z = 3.09$ in SA 22 from M04 in Fig. 4.1. The contours compare the local density of LAEs to the average density over the field-of-view. The LAE distribution was convolved with a Gaussian with a co-moving size of $\sigma = 2.8$ Mpc. The bold contours indicate regions of greater than average local surface density, clearly showing the filamentary large-scale structure in the proto-cluster.

Although LAB1 resides close to a node in the large-scale structure (Matsuda et al. 2005 in prep.), we find no tendency for the other submm-detected LABs to reside in higher density local environments than the average LAE, suggesting that this behaviour isn't reflected in the wider sample. Indeed, if anything it might be argued that our new submm-detected LABs lie in lower-density regions on average, although this is not statistically significant. We note that although the underlying density field may not be correlated with the positions of LABs, the local density may have an effect on the properties of LABs, which may account for the range of sizes and luminosities we observe.

4.4. Discussion of the submillimeter survey

We now discuss the wider insights which our observations provide into the properties and origin of LABs and their environments. We concentrate on the interaction of winds generated from luminous activity within the embedded SMGs with the ICM as the most likely source of Lyα emission.

4.4.1 LAB formation mechanisms

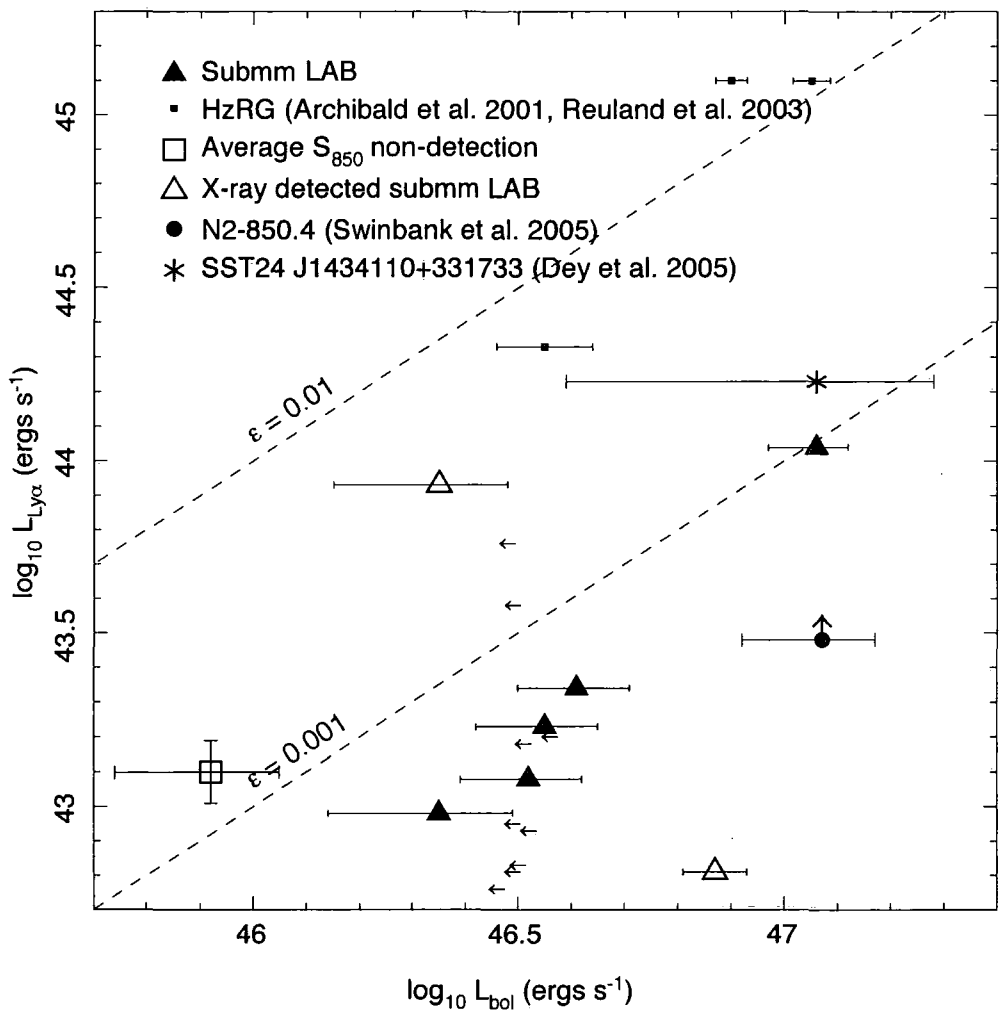

Figure 4.4: Lyα luminosity versus bolometric luminosity (assuming a modified black-body with $T_{\rm d} = 40\,{\rm K}$, $\alpha = 4.5$, $\beta = 1.7$) for submm-detected LABs and potentially related objects. Note that we plot LAB30 as a submm-detected LAB, and 3σ upper limits are plotted for the remainder of the photometry sample. Also shown is the flux obtained from stacking the submm-undetected LABs from the photometry sample. The starburst galaxy N2-850.4 (Smail et al. 2003; Swinbank et al. 2005) is also shown, along with the *Spitzer* detected source SST24 J1434110+331733: both these objects have been identified with extended Lyα haloes. The dashed lines show a simple model where the Lyα luminosity is determined as a fraction ϵ of the bolometric luminosity. We show this model for the scenarios $\epsilon = 0.01$ and $\epsilon = 0.001$. We also plot three submm-detected, high-redshift radio galaxies with extended Lyα emission for comparison.

In Figure 4.4 we plot the Lyα luminosity against the bolometric luminosity calculated for the submm-detected LABs – LAB1, 5, 10 and 14. We have also plotted the flux of the submm-undetected LABs from our stacking analysis and two objects which are proposed to be similar to LABs: the SCUBA galaxy N2-850.4 (Keel et al. 1999, Smail et al. 2003) and the *Spitzer* identified source SST24 J1434110+331733 (Dey et al. 2005). We discuss these analogous systems further in §4.3.4.[3] The bolometric luminosities of the LABs are calculated by integrating over a modified black-body curve with a dust temperature of 40 K and $(\alpha, \beta) = (4.5, 1.7)$.

This analysis allows us to examine any causal connection between the bolometric output of the LAB, and the luminosity of the Lyα halo. As Fig. 4.4 shows there is a weak trend between $L_{\rm bol}$ and the luminosity of the extended Lyα halos for the sample – in the sense that the most bolometrically-luminous sources have more luminous associated Lyα halos.

We adopt a simple model in which the Lyα emission traces a fraction ϵ of the bolometric luminosity, where ϵ combines the fraction of energy output by star formation or AGN which generates a wind and the fraction of that wind energy which produces Lyα emission: $L_{\rm Ly\alpha} = \epsilon L_{\rm bol}$ In Figure 4.4 we plot this behaviour for values of ϵ corresponding to 1 and 0.1 per cent of the bolometric output. A fractional output around ~ 0.1 per cent best describes the LABs, indicating that only a small proportion of the bolometric output from the obscured activity in these galaxies is required to support these luminous haloes. The weak trend we see is consistent with a direct causal link between the extended Lyα emission and that from the obscured sources detected in the submm. The most likely mechanism which could provide this link is winds (Ohyama et al. 2003) and we suggest that winds are the major cause of the extended Lyα emission seen in the LAB population. This proposal would indicate that LABs may be found around a large range of the submm population and we explore this idea further in §4.3.4.

Clearly the trend shown in Fig. 4.4 is not a tight correlation. There are several possible explanations for this – including different efficiencies for coupling energy to the halo from different sources (e.g. AGN or starbursts), potentially cyclic activity, environmental

[3]We note that the Extremely Red Object 2142-4420 B1 (Francis et al. 2001) also has been identified with an extended halo ($L_{\rm Ly\alpha} \sim 10^{44}$ ergs s^{-1}). Those authors suggest that the embedded galaxy's FIR emission could be of the order 5×10^{47} ergs s^{-1}, although a precise far-infrared luminosity is not available. If this predicted FIR luminosity is correct then it would place the source at a similar location to SST24 in this Fig. 4.4.

influences and observational uncertainties. We provide a more quantitative discussion the mechanics of emergent winds and jets, and possible environmental influences on luminosity of Lyα halos in the next section. We note that the two LABs with possible X-ray counterparts – LAB2 and 18 – are not well described by the general trend. These are the two LABs whose tentative X-ray detections suggest they may contain obscured AGN (upper limits for the remainder of the population are consistent with the measured fluxes and luminosities of these two marginal detections). This might explain why they depart from the trend in Fig. 4.4 (i.e. AGN may interact differently with the ICM than starbursts). However, the fact that they lie respectively above and below the trend suggests that other factors may be at work, in particular their local environments. Fig. 4.1 shows that LAB18 lies in one of the lowest density regions in our survey, while LAB2 is close to the peak in the LAE distribution. LAB18 has an submm flux $\sim 3\times$ that of LAB2, but LAB2's Lyα luminosity is over an order of magnitude greater than LAB18. This suggests that although a powerful embedded submm source might be required for the generation of an LAB, it may be the local environment (i.e. the density of ambient intracluster gas) which governs the efficiency of coupling of the bolometric output to the luminosity of the halo. This is a natural explanation for the apparent diversity of these objects' properties. Unfortunately, our survey is too sparse to conclusively test for environmental influences on the properties of submm-bright LABs.

To demonstrate the potential variation in $L_{Ly\alpha}$–L_{bol} which may arise from AGN-driven activity we also plot on Fig. 4.4 three HzRGs from Reuland et al. (2003) with detected 850 μm emission from Archibald et al. (2001), converted to our cosmology. These galaxies show a much higher ratio of Lyα emission at a fixed bolometric output, compared to the LABs indicating the role of powerful radio jets and possible contributions from inverse-Compton ionization (Scharf et al. 2004) in addition to the starburst or AGN activity, shown by the LABs.

4.4.2 Origin of the wind

In this paper we have used the term "wind" to refer to the interaction between any outflowing material whatever its origin and the intergalactic medium (or the young, intracluster medium in the case of SA 22). Are there any observational signatures to distinguish the feedback of starbursts and AGN on the ICM? AGN are very localised – they can impart energy into the galaxy via direct irradiation or jets: highly collimated outflows

from matter accretion onto a black hole. Starbursts are more complex, in the sense that the energy release can be distributed over a wider volume (in giant molecular clouds), and comprises of the output of young massive stars, and a contribution from an enhanced SNe rate. For an AGN, on larger scales the most likely mechanism for generating an outflow is expected to be jets breaking out of the galaxy and into the IGM. These outflows entrain material from the galaxy (in the case of SMGs this would include dust) and the IGM, and create a shock front when they become supersonic in the ambient medium. It is this shock which can heat the ambient gas to ionising temperatures, and therefore dissipate the jet's energy. In this situation the observations will be orientation specific, such that a face-on jet induced LAB will be compact and bright, whereas a side-on jet might resemble an elongated structure. The morphological diversity of the LABs could be explained by this variety of mechanisms, with both these observational classes being found in our sample (e.g. LAB10 and LAB18 respectively), although it is unclear whether an AGN, starburst, or combination of the two is responsible. We note that without detailed spectroscopic evidence to unravel the kinematics of these systems, caution must be exercised in our wind analysis: similar structures could be easily explained by the distribution of tidal material resulting from a merger.

Starburst-driven winds can emerge from a galaxy and interact with the IGM in a similar way to an AGN jet. Although not as concentrated, these winds can still be collimated, and resemble jets with a very wide opening angle (at least for local far-infrared luminous galaxies, e.g. Heckman et al. 1990). For these collimated winds, a similar orientation dependence governs observations, but the loose collimation allows the formation of the extended diffuse haloes present in several of these LABs (e.g. LAB5, LAB6). The escape of galactic winds from dusty, high-redshift starburst galaxies might be different to their lower-redshift counterparts (e.g. M82), and we must take that into account when considering these scenarios. Given that it is possible for AGN and starbursts to generate similar morphological structures in LABs and so with our present observational tools we cannot clearly distinguish between AGN- and starburst-powered winds in the LABs. However, if the obscured activity seen in the LAB population is exactly analogous to that in typical submm galaxies at this epoch, then from detailed studies of the AGN in the latter population we can conclude that it is likely that star formation is responsible for the winds in the LABs (Swinbank et al. 2004; Alexander et al. 2005).

4.4.3 Energy injection, mass loss and age

Supernovae driven superwinds are one method of converting the bolometric (star formation) energy of the galaxy into the Lyα emission surrounding it. In this case, some fraction of the bolometric luminosity should couple to winds, in turn a fraction of which should power the Lyα emission. Heckman et al. (1990) discuss the mechanics of emergent superwinds from the discs of a sample of low-z far-infrared galaxies. Those authors present a simple model for the energy injection rate (into some ambient medium) from the inflation of a bubble due to the combined effect of stellar winds from massive stars and the detonation of supernovae: $dE/dt \sim 3 \times 10^{41} r^2 v^3 n_0$ ergs s^{-1}. Where r is the radius in kpc of the bubble, v is the wind velocity in units of 100 km s^{-1} and n_0 is the density of the undisturbed medium just outside the bubble in cm^{-3}. Applying this to our sample; if we take the radius of the bubble in LABs to be the extent of the emission (in this case between $\sim$10–100 kpc with a median of 22 kpc), a wind velocity of $\sim$ 1000 km s^{-1} (characteristic of the escape velocity from a massive galaxy) and a density of 1 cm^{-3} (Shull & McKee 1979) then the energy injection rate is of the order 10^{45} ergs s^{-1}. The bolometric luminosities of SMGs in LABs are up to two orders of magnitude larger than this, and the typical Lyα luminosities of LABs in this sample are approximately two orders of magnitude lower than this, suggesting that the conversion of bolometric energy to Lyα emission (via winds) is an inefficient process, but ample to provide the energy to power the extended emission.

The conversion efficiency from bolometric to Lyα luminosity derived from the trend in Fig. 4.4 is $\sim$ 0.1 per cent, which would support this interpretation. We note that the effect of the density of the ambient medium on the injection rate is vital in this analysis – a lower ambient density favours a lower coupling of bolometric luminosity (that generated by the starburst or AGN) and a wind into the IGM. This would provide a natural explanation of the fact that there is significant scatter in the trend between $L_{\rm bol}$ and $L_{\rm Ly\alpha}$. For example LAB18, which resides in a much lower density environment to the rest of the LABs has a high bolometric luminosity (second only to LAB1), but a much lower Lyα luminosity.

This simple wind model allows us to estimate the age of the starburst (or AGN activity) by comparing the extent of the haloes with the velocity of the superwind. For the figures estimates above, these LABs could have starbursts of the age $\sim$ 20 Myr – although could be up to $\sim$ 100 Myr for the largest LABs. Caution must be exercised for this interpretation due to the fact that a halo might remain as an emission line nebula for some

time after luminous activity has ceased, or when cyclic models of activity are considered, a succession of which may have illuminated a halo at some former time, but which is now fading. Nonetheless, starbursts of this age are consistent with estimates for other SMGs (e.g. > 10 Myr for N2-850.4, Smail et al. 2003).

4.4.4 LABs around the submm population in general?

About 20 per cent of the LABs in our (photometry) sample contain strong submm sources. Combined with the apparent trend between Lyα and FIR emission, and the morphological analysis, this supports the interpretation that a galactic superwind is responsible for the Lyα emission. We speculate that giant Lyα emission-line haloes may be a feature of the general submm population.

Spectroscopic observations of SCUBA galaxies based on radio-identification (Chapman et al. 2005) have yielded impressive results, with the redshifts of $\sim$100 galaxies currently known. An interesting feature of the spectra is the presence of strong Lyα emission lines which aids in the measurement of redshifts. For example, in Chapman et al's spectroscopic survey of SMGs, of the 73 successful identifications, 34 per cent of them were made primarily with the Lyα line. This runs counter to the expectation that the active regions in submm galaxies should be heavily obscured by dust resulting from an intense starburst, and hence these regions are unlikely to be strong Lyα sources since dust efficiently destroys Lyα photons. The presence of the Lyα line then suggests two possibilities: (a) the dust coverage is patchy, and Lyα photons generated within the galaxy escape through holes in the distribution (Chapman et al. 2004); or (b) the Lyα emission originates well away from the dust in a halo coupled to the galaxy. This latter scenario is consistent with the LAB picture and would suggest that extended Lyα haloes should be found around many SMGs.

There already exists some evidence for extended Lyα halos around luminous, far-infrared galaxies at high redshifts: the first submm-selected galaxy, SMM J02399-0136 (Ivison et al. 1998), also has a large Lyα halo, covering virtually all of the 15″ slit used by those authors. Similarly, Smail et al. (2003) detect four SMGs within $\sim$ 1 Mpc of the radio galaxy 53W002 ($z = 2.39$), and identify one of them, SMM J17142+5016 as a narrow-line AGN with an extended Lyα halo. Finally, the SCUBA galaxy N2-850.4 (SMMJ163650.43+405734.5 Scott et al. 2002; Ivison et al. 2002; Smail et al. 2003) is a hyperluminous class IR galaxy undergoing a starburst at $z = 2.385$. There appears to be a dif-

fuse Hα (and perhaps Lyα) halo surrounding the galaxy, which although apparently compact, may extend to large distances with a surface brightness below the limit of the observations. For comparison, we plot N2-850.4 in Figure 4.4, using a lower limit for the Lyα luminosity of $> 3 \times 10^{43}$ ergs s^{-1} (Swinbank et al. 2005), and $L_{\rm bol} \simeq L_{\rm FIR} = 3.1 \times 10^{13} L_{\odot}$ (Chapman et al. 2005).

Very recently, Dey et al. (2005) identified a *Spitzer Space Telescope* source, SST24 J1434110 +331733, which is surrounded by a 200 kpc-diameter Lyα nebula at $z \sim 2.7$. The nebula has $L_{\rm Ly\alpha} \sim 1.7 \times 10^{44}$ ergs s^{-1} and hosts a bright mid-infrared source ($S_{24\mu{\rm m}}$ = 0.86 mJy), with an implied FIR luminosity of $L_{\rm FIR} \sim 1$–$5 \times 10^{13}\ L_{\odot}$, although the estimate is uncertain as it involves an order-of-magnitude extrapolation. The size and luminosity of the Lyα halo, combined with the potentially hyperluminous source lying within it make this a close analog of LAB1. We plot it for comparison in Fig. 4.4, and note that it follows the trend shown by the majority of submm-detected LABs. This close association between a luminous, obscured source and a highly-extended Lyα halo further supports our proposal that LABs may be a common feature of the high-redshift far-infrared population.

For completeness, however, we should note that our survey of SA 22 contains at least one submm source which does not appear to be associated with an extended halo. SMMJ221735.15+001537.2 is detected with $S_{850} = 6.3 \pm 1.3$ mJy (Chapman et al. 2005) at $z = 3.098$. Lyα is detected for this system, but it is not sufficiently extended to qualify as a LAB. The lack of spatial extent would be consistent with the picture where this is a young submm source and the wind has only just started to propagate into the IGM, thus resulting in a small or faint halo. Alternatively, as discussed above, local environmental conditions could play a role in the lack of emission we observe.

4.4.5 Star formation in the SA 22 region

Our detection of submm emission from the average LAB in our survey within the SA 22 field also allows us to compare the star formation rate density (SFRD) within this structure to that of the field at this epoch. To estimate the volume containing the $z = 3.09$ structure in SA 22 we assume that the star-formation is contained within a co-moving sphere of apparent size 15$'$, corresponding to a volume of $\sim 1.1 \times 10^4$ Mpc^3.

Directly integrating the submm emission from the six detected LABs (1, 2, 5, 10, 14, 18) and the other SMG known to lie at $z = 3.09$ in this field (Chapman et al. 2005) we derive a total SFR in submm galaxies of $\sim 1.4 \times 10^4\ M_{\odot}\ {\rm yr}^{-1}$. This yields a star formation rate

density (SFRD) in SA 22: $\rho_{\rm SFR} > 1.3\,M_{\odot}\,{\rm yr}^{-1}\,{\rm Mpc}^{-3}$. Alternatively, given our average submm flux for LABs of ~3.1 mJy, the entire M04 catalog of LABs would yield a SFRD of $\rho_{\rm SFR} > 3.2\,M_{\odot}\,{\rm yr}^{-1}\,{\rm Mpc}^{-3}$ (star formation rates are calculated assuming $L_{\rm bol} \sim L_{\rm IR}$ after Kennicutt 1998).

A lower limit to the average SFRD at $z \sim 3$ is provided by UV-selected surveys of LBGs at this epoch, giving a SFRD of $\geq 0.1\,M_{\odot}\,{\rm yr}^{-1}\,{\rm Mpc}^{-3}$ (Steidel et al. 1999) after accounting for dust extinction and extrapolating the LBG luminosity function to faint limits. Alternatively, we can use submm surveys to attempt to determine the SFRD from a bolometrically-selected sample at this epoch, although at the cost of extrapolating the submm luminosity function. The spectroscopic survey of SMGs by Chapman et al. (2005) indicates an average SFRD at $z \sim 3$ of $\sim 0.8\,M_{\odot}\,{\rm yr}^{-1}\,{\rm Mpc}^{-3}$. The estimates of the SFRD within the SA 22 structure indicate significant acceleration of early star-formation in this overdense region (Ivison et al. 2000; Stevens et al. 2003; Smail et al. 2003).

4.5. Summary of the submillimeter survey

In the first part of this chapter we have presented results from a submm SCUBA survey of a sample of 23 giant, Lyα emission line nebulae – Lyα Blobs (LABs) – at $z = 3.09$ in the SA 22 protocluster. In addition to the previously studied LAB1 and LAB2 which have been shown to contain submm sources, we identify a published submmm source with LAB14 and from our photometry observations detect a further three (LAB5, 10, 18) with 850 μm fluxes $> 3.5\sigma$. We conclude the following:

- We have tripled the number of LABs with detected submm emission in the SA 22 overdensity to a total of six sources. The $z = 3.1$ protocluster in SA 22 is thus the richest association of submm galaxies known.

- The majority of LABs contain sources which are undergoing an episode of extreme luminous activity; most likely caused by a starburst (although our current limits cannot rule out a contribution from an AGN) and are heavily obscured by dust.

- The average 850 μm flux for the full sample of LABs is 3.0 ± 0.9 mJy, corresponding to star formation rates of the order $10^3\,M_{\odot}\,{\rm yr}^{-1}$. We also find a significant detection of submm emission from those LABs which are individually undetected in our submm observations.

- We estimate that the star formation rate density in SA 22 is $\gtrsim 3\, M_{\odot}\, \mathrm{yr}^{-1}\, \mathrm{Mpc}^{-3}$. This compares to recent estimates of $0.8\, M_{\odot}\, \mathrm{yr}^{-1}\, \mathrm{Mpc}^{-3}$ for the obscured star formation rate at this epoch (Chapman et al. 2003, 2005), indicating an acceleration of star-formation in the SA 22 structure at this early time.

- We find a trend between the Lyα luminosity of the haloes and the far-infrared luminosity of the embedded SMGs. This trend can be simply modelled in a scheme where a fraction ϵ of the bolometric output is converted to Lyα emission. For LABs, this fraction appears to be of the order ~ 0.1 per cent. The existence of this trend suggests a causal link between the submm activity we detect and the extended Lyα halos.

- Galactic-scale 'superwinds' generated from the combined effect of stellar winds from massive stars and the detonation of supernovae in the starburst, provide a natural explanation of the properties we see. These mechanisms would allow the intergalactic medium in the densest regions to be heated and enriched with metals at early times, in accordance with the observed lack of evolution in intracluster metallicity in the high density cores of clusters out to $z \sim 1$ (e.g. Tozzi et al. 2003).

Finally we examine the implications of the discovery of a large number of submm sources associated with LABs and propose that large emission line haloes might be a common feature of the submm population in general (and perhaps all active galaxies in rich environments), implying strong feedback and outflows into the local environment from these galaxies. Lyα haloes such as these are then excellent candidates for further studies of feedback systems at high-redshift, and an essential stage of galaxy evolution. In the second part of this chapter, we turn to the two largest LABs, and use a wide range of multiwavelength data (specifically *Spitzer* mid-infrared photometry) to probe the nature of their host galaxies in more detail.

4.6. *Spitzer* identifications and classifications of submillimeter galaxies in LABs

The two largest known LABs (LAB 1 and LAB 2, with spatial extents of 1.1×10^4 kpc^2 and 0.8×10^4 kpc^2 respectively, are both associated with submillimeter galaxies (SMGs) (Chapman et al. 2001), as are several other LABs in SA 22 (see above) – the apparent association

of these bolometrically luminous galaxies with LABs provides support for the scenario where feedback mechanisms are powering the Lyα emission, since the bolometric luminosities of the SMGs are several orders of magnitude larger than the Lyα luminosities of the haloes (see Figure 4.4). The action of superwind feedback has recently been given credence by integral field data which reveals outflows and complex velocity structures in both LAB 1 and LAB 2 (Bower et al. 2004; Wilman et al. 2005). However, the precise location and identification of the SMG counterparts, and hence accurate constraints on the dominant power sources, are unclear due to the poor spatial resolution of the submillimeter data (Chapman et al. 2004).

In this section, we present *Spitzer Space Telescope (SST)* mid-infrared and *Hubble Space Telescope (HST)* optical imaging of the galaxies embedded within LAB 1 and LAB 2 to locate the bolometrically luminous sources within them – the SMGs. To identify these galaxies, we exploit the fact that mid-infrared observations have been shown to be effective at identifying SMGs, particularly at 8μm since these galaxies have red infrared colors (Ashby et al. 2006). The mid-infrared photometry also constrains their rest-frame optical–radio spectral energy distributions (SEDs) and hence can shed light on what is powering these sources.

4.6.1 Identification of the SMGs

As the precise location of the SMGs within the LAB haloes is uncertain, we begin our discussion by identifying the mid-infrared counterparts to the SMGs (which we assume to be the dominant power-source of the LABs). Starting with a catalogue of the IRAC-detections within each Lyα halo[4] (Table 4.4), we aim to eliminate sources not at $z = 3.1$, and then identify the most likely mid-infrared counterpart (if any) to the SMG in each case. Note that no sources are detected at 24μm within the extent of either LAB, and so we adopt 3-σ upper limits of $f_{24} < 330\,\mu$Jy.

Figure 4.5 shows *HST* and IRAC images of the LABs covering 3.6–8μm, and we label each of our potential counterparts. Of the five IRAC components in LAB 1 (a–e), we can eliminate several of them as the SMG counterpart immediately: LAB 1c and d have mid-infrared colors $f_{3.6}/f_{4.5} > 1$, making them inconsistent with $z = 3.1$ galaxies (Ashby et

[4]For mid-infrared detections within the Lyα haloes, we adopt the alphabetical suffix LAB 1a, LAB 1b, etc., although this does not imply that these objects are physically associated with the LAB.

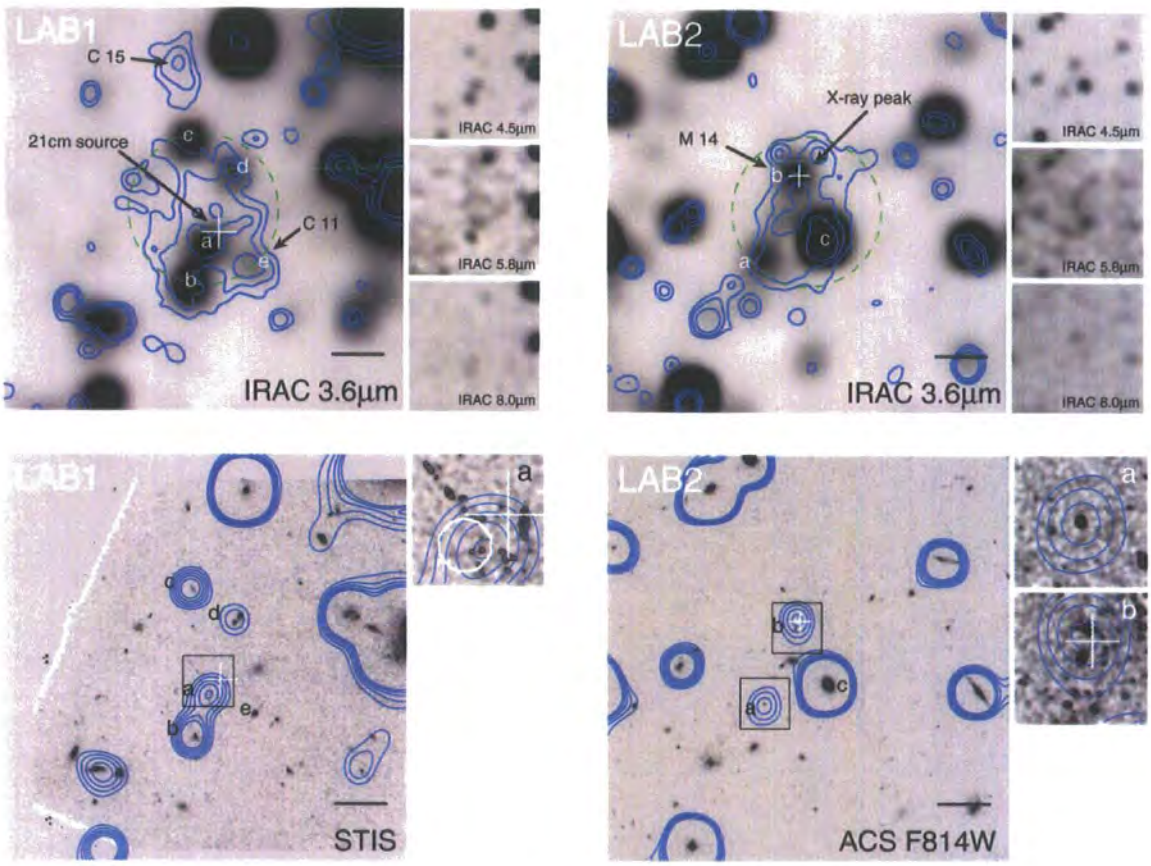

Figure 4.5: (*top*) Greyscale IRAC 40″ × 40″ images of LAB 1 (*left*) and LAB 2 (*right*). The main panels show the IRAC 3.6μm image, and the insets show the 4.5μm 5.8μm and 8μm images, all which have been slightly smoothed with a Gaussian kernel. We overlay the narrow-band Lyα images from Matsuda et al. (2004) to show the extent of each halo. IRAC detections within the Lyα haloes are labelled a, b, etc. In the field of LAB 1 we indicate the location of the known Lyman-break galaxies (LBGs; C 11 & C 15) and the position of the 21 cm radio source in the halo (*white cross*, Chapman et al. 2004). LAB 2 contains one known LBG (M 14) and an SMG, as well as an X-ray source (*white cross*). In both cases we show the 15″ SCUBA beam (*dashed circle*) to illustrate the potential uncertainty in the position of the submm source. (*bottom*) High resolution *HST*-STIS and ACS imaging for LAB 1 and LAB 2 showing the optical counterparts, with contours showing the 3.6μm emission. The white 1″ circle in the STIS inset shows the location of the ERO detected in Steidel et al. (2000). In all images, north is up, east is left and the horizontal bar is a 5″ scale. We discuss the identifications further in §4.6.1 and Table 4.4

al. 2006), while LAB 1e is at the position of the Lyman-break galaxy (LBG) C 11, and is only weakly detected at 3.6μm and undetected at 4.5–8μm. Although this LBG is close to LAB 1, it appears to be kinematically distinct from the bulk of the halo (Bower et al. 2004) and so we discount it – leaving LAB 1a and b as potential counterparts.

The positional uncertainty between LAB 1a and the 850μm centroid ($\Delta\theta = 2.0 \pm 1.9''$) is consistent with it being the source of the submm emission. The remaining IRAC counterpart to the south-east of the SMG (LAB 1b) is just within the Lyα halo, and has a bright counterpart in the STIS imaging. It is not clear from the mid-infrared colors whether this galaxy is at the halo redshift, but given its large separation from the nominal submillimeter position, it is unlikely that it is associated with the power-source. However, if LAB 1b is at $z = 3.1$, it is possible that LAB 1a and b are interacting given their projected separation of just $\sim$4'' ($\sim$30 kpc at $z = 3.1$).

Previous multi-wavelength observations of LAB 1 (Chapman et al. 2004) associated the SMG with the brightest of a group of UV fragments near the geometrical center of the structure and close to the 21 cm source position (Fig. 4.5). Component LAB 1a is in the vicinity of this group of faint UV fragments, but the 3.6–8μm emission is coincident with a $K_S = 21.5$ Extremely Red Object (ERO) identified in Steidel et al. (2000), rather than the brightest UV component ('J1' in Chapman et al. 2004) which is closest to the radio peak (and a tentative CO(4–3) detection). Both LAB 1a and the UV object J1 are plausible sources of the submm emission. However, given that SMGs are expected to be massive, we view the 3.6–8μm detection as a more reliable indicator of the SMG's counterpart than the weak UV source. We therefore propose that LAB 1a is the most likely IRAC counterpart to the SMG in LAB 1

There are three mid-infrared counterparts within the extent of LAB 2 (Fig. 4.5, Table 4.4). We can eliminate LAB 2c immediately as a potential counterpart given its blue mid-infrared colors and large, bright optical counterpart in the *HST* image – it is a foreground galaxy. The remaining two counterparts LAB 2a and LAB 2b have similar 3.6–5.8μm characteristics. However, only LAB 2b is detected at 8μm, which has been shown to be a useful identifier of the mid-infrared counterparts of SMGs (Ashby et al. 2006). Moreover, LAB 2 contains a hard X-ray source in the halo (Basu-Zych & Scharf 2004), with an estimated luminosity $L_X \sim 10^{44}$ erg s^{-1}. The location of the X-ray source is consistent with LAB 2b ($\Delta\theta = 0.8 \pm 1.4''$), whereas LAB 2a is in the extreme south-east of the LAB, $\sim$8.5'' away from the X-ray source. Given the association between SMGs and

moderately bright X-ray sources (Alexander et al. 2005a), the SMG in LAB 2 is likely to lie close to the position of the X-ray source. We therefore propose that LAB 2b is the mid-infrared counterpart to the SMG in LAB 2[5]. The precise positions of the SMGs in LAB 1 and LAB 2 and the offsets to the other mid-infrared components are given in Table 4.4.

4.6.2 Classification of the SMGs

We can use the 3.6–8μm photometry (along with multi-wavelength data for these objects from the literature; Chapman et al. 2001, 2004; Steidel et al. 2000) to construct the optical–radio SEDs for the SMGs (Figure 4.6). We present new J and K band photometry from the UKIDSS-Deep Extragalactic Survey (to be discussed in Stott et al. 2007 in prep). We note that the poor constraints on the f_{24}/f_{850} ratio means that we cannot make robust conclusions about the rest-frame mid-to-far infrared differences between LAB 1a and LAB 2b. Both have f_{24}/f_{850} upper limits consistent with obscured ULIRGs at $z \sim 3$ (Pope et al. 2006). Similarly the limits of the observed $f_{5.8}/f_{850}$ ratios for LAB 1a and LAB 2b are consistent with other SMGs at $z \sim 3$, although the ratio for LAB 1a is at the low end of the distribution (Pope et al. 2006) indicating either a relatively low stellar mass for this system, or more likely very high obscuration. Thus, the SMGs associated with LABs are similar to the wider SMG population.

We now examine the rest-frame near-infrared portion of the SEDs using the IRAC data. Near-infrared colors have been shown to be a useful diagnostic for the power-source of local luminous infrared galaxies (e.g. Spinoglio et al. 1995). For LAB 1a we find rest-frame (Vega) colors $(J-H) = 0.6 \pm 0.5$ and $(H-K) = 0.8 \pm 0.4$, and in LAB 2b we find $(J-H) = 0.8 \pm 0.6$ and $(H-K) = 1.1 \pm 0.4$. LAB 1a's colors are similar to that of 'normal' galaxies ($\langle J-H \rangle \sim 0.8$, $\langle H-K \rangle \sim 0.3$; Spinoglio et al. 1995), whereas LAB 2b exhibits a redder rest-frame $(H-K)$ color, indicating an excess in the rest-frame K-band likely associated with a non-stellar contribution. We fit a simple power-law, $f_\nu \propto \nu^\alpha$, to the IRAC photometry for LAB 2b, obtaining $\alpha = -1.0 \pm 0.2$, similar to that expected for AGN (Alonso-Herrero et al. 2006).

[5]LAB 2b is also at the location of the LBG M 14, although in this case the LBG appears kinematically associated with the wider halo (Wilman et al. 2005). We note that in the submillimeter observation of this halo, LAB 2b is actually situated near to the edge of the SCUBA beam (Fig. 4.5). The correction to the 850μm flux to account for this offset would make the SMG brighter, with $S_{850\mu m} \sim 5$ mJy (Chapman et al. 2001).

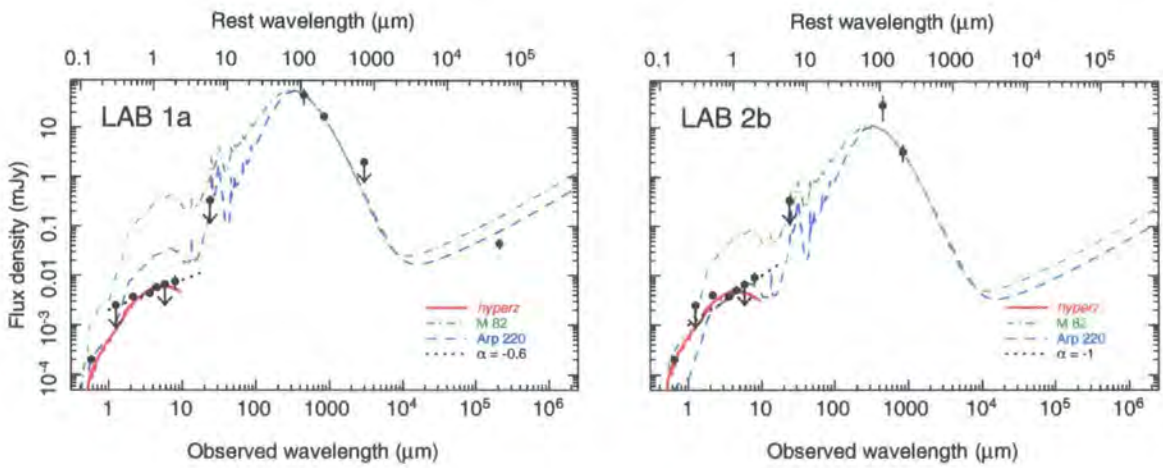

Figure 4.6: Rest-frame ultraviolet to radio spectral energy distributions (SEDs) of the proposed power sources in LAB 1 and LAB 2. We overlay the SEDs of M 82 and Arp 220 (Silva et al. 1998) normalized to the 850μm point and non-*Spitzer* data from the literature (upper limits at 3-σ). Both sources have broad-band SEDs which are similar to Arp 220. Dotted lines show a simple power law, $f_\nu \propto \nu^\alpha$, fit to the 3.6–8μm data. We also show the best fit (stellar) SED from HYPERZ, fitted to the optical/mid-infrared photometry (see §4.6.2 for details).

Table 4.5: Mid-IR properties of sources lying within LABs. (1) Positional offsets from the SMGs in LAB 1 and LAB 2 identified in §4.7. The proposed mid-infrared counterparts, LAB 1a and LAB 2b are at $22^h17^m26.0^s$, +00°12′36.2″ and $22^h17^m39.1^s$, +00°13′30.4″ (J 2000) respectively. Positional uncertainties based on the 3.6μm centroids are 0.8″. (2) Flux uncertainties are 0.3μJy in 3.6μm & 4.5μm and 2.2μJy in 5.8μm & 8.0μm. Quoted limits are 3-σ.

	(1)		(2)			
Component	$\Delta\alpha$	$\Delta\delta$	3.6μm	4.5μm	5.8μm	8.0μm
	(″)		(μJy)			
LAB 1a.....	**0.0**	**0.0**	**4.3**	**5.8**	**< 6.6**	**7.6**
b.....	1.5	−3.4	5.5	7.3	7.6	7.9
c.....	1.5	10.7	4.8	3.8	<6.6	<6.6
d.....	−3.0	7.7	2.8	1.9	<6.6	<6.6
e.....	−4.5	−1.4	1.5	<0.9	<6.6	<6.6
LAB 2a.....	3.0	−7.7	3.4	4.1	<6.6	<6.6
b.....	**0.0**	**0.0**	**3.8**	**5.0**	**<6.6**	**9.2**
c.....	−3.0	−5.5	16.3	12.0	8.1	<6.6

To further test if the optical-mid-infrared SEDs of the sources can be reproduced by stellar populations, we use HYPERZ (Bolzonella, Miralles & Pello 2000) to model the stellar continuum by fitting to the rest-frame 0.15–2μm photometry. We adopt a model with an exponentially declining SFR, with $\tau = 30\,\mathrm{Gyr}$, from Bruzual & Charlot (1993) and constrain the redshift to be $z = 3.09$. Dust is modelled with a Calzetti law (Calzetti et al. 2000). The rest-frame optical–near-infrared portions of the SEDs are well fit by this model, with high-reddening ($A_V \sim 3$) and young ages. Absolute K-band magnitudes based on the fit are $M_K \sim -26.8$ in LAB 1a and $M_K \sim -27.2$ for LAB 2b. These absolute rest-frame K-band magnitudes are comparable to the wider SMG population (Borys et al. 2005), and suggest stellar masses of $M_\star \sim 10^{11}\,M_\odot$, although the K-band magnitude of LAB 2b is likely to be contaminated by AGN emission, with a significant rest-frame 2μm excess over the HYPERZ fit of $\sim$5μJy. The detection of X-ray emission from LAB 2b is the best evidence we have that it contains an AGN. To quantitatively test the correspondence between the mid-infrared excess and the X-ray emission we use the rest-frame X-ray–10.5μm correlation for AGN from Krabbe et al. (2002). We predict the rest-frame 10.5μm emission for LAB 2b by extrapolating the rest-frame 2μm using the measured spectral slope of $\alpha = -1$. With this approach we estimate the X-ray luminosity from the AGN to be of order $10^{44}\,\mathrm{erg\,s^{-1}}$, in reasonable agreement with that observed (Basu-Zych & Scharf 2004). The luminosity of the X-ray source is consistent with a moderate contribution to the bolometric emission from an AGN (Alexander et al. 2005b), however it is still not clear if an AGN or starburst is responsible for powering the extended Lyα emission. LAB 1a's rest-frame K-band excess over the best fit stellar template, of $\sim$3$\pm$2 μJy is less significant. Nevertheless, taking the same approach as for LAB 2b, we predict an X-ray luminosity of $\sim 5 \times 10^{43}\,\mathrm{erg\,s^{-1}}$, consistent with the 2–10 keV limit in the existing *Chandra* observations.

To make progress we need mid-infrared observations of a larger sample of LABs in SA 22, four of which also contain SMGs. This will allow us to investigate whether they also exhibit rest-frame near-infrared characteristics similar to the general submillimeter population. Searches for obscured AGN in SA 22 will also be significantly advanced by a recently approved 400 ks *Chandra* ACIS-I exposure of this region. Together these studies will provide a clearer view of the energetics of LABs and their relationship to the wider SMG population.

Chapter 5

A panoramic blank-field near-infrared narrowband survey of Hα emitters at z = 2.23

5.1. Introduction

One of the most fundamental, and challenging, goals of modern observational cosmology is to determine the volume-averaged star formation history of the Universe: its distribution function and variation with environment are powerful tools for understanding the physics of galaxy formation and evolution. Surveys using a range of star formation indicators suggest that the star-formation rate density ($\rho_{\rm SFR}$) rises as $\sim(1+z)^4$ out to $z \sim 1$ (e.g. Lilly et al. 1995) and hence the 'epoch' of galaxy formation must occur at $z > 1$. Unfortunately, tying down the precise epoch of maximum activity at $z > 1$ is more difficult, with different star formation indicators giving a wide spread in SFR density $\rho_{\rm SFR}$ (e.g. Smail et al. 2002; Hopkins 2004) – although there is a general trend for $\rho_{\rm SFR}$ to plateau at $z \sim 2$ and hence it is likely that the bulk of stars seen in galaxies at the present-day were formed between $z \sim$ 1–3. Indeed, $z \sim$ 2–2.5 appears to be a critical era in the evolution of many populations: optical QSO activity (which should be linked to the growth of super-massive black holes) peaks at this epoch (Boyle et al. 2000), as does the luminosity density in bright submillimeter galaxies – thought to represent an early phase in the formation of massive galaxies (Chapman et al. 2005). This behaviour might be associated with the formation of spiral bulges, or alternatively these observations might be biased towards the most massive systems in rare, dense environments.It is not clear that this evolution is true of "typical" star forming galaxies (i.e. those with SFRs

$<100\,M_{\odot}\,\mathrm{yr}^{-1}$). A sensitive survey of star forming galaxies in a range of representative environments is needed to address this issue.

Variation between the different SFR measurements is in part due to a combination of the effects of sample selection, Cosmic variance and biases in individual indicators. Estimates from ultra-violet–selected samples (e.g. Madau et al. 1996) require large corrections for dust extinction and may miss the most obscured sources altogether. Similarly, although far-infrared-selected samples are less influenced by dust extinction, they require large extrapolations to account for sources below their bright flux limits (e.g. Chapman et al. 2005). Thus while no single indicator can give an unbiased view of the evolution of the SFRD, mixing different indicators at different epochs is not helping our understanding.

What we require is one star formation indicator that can be applied from $z = 1$–3, is relatively immune to dust extinction and which has sufficient sensitivity that our SFR estimates do not require large extrapolations for faint sources. The Hα emission line luminosity is a well-calibrated SFR indicator (Kennicutt 1998) which combines all of these properties and hence is the tool of choice for studying the evolution of the SFR density out to $z \sim 3$ – thus covering the expected peak in the SFRD. The main advantage of Hα over other indicators (in addition to the points outlined above) is that it is a good measure of the instantaneous SFR – sensitive to the emission of young, massive stars ($>10\,M_{\odot}$; Kennicutt 1998). The Hα luminosity function (LF) for Hα-selected galaxies (and the corresponding ρ_{SFR}) has been measured out to to $z \sim 1.3$ by a series of investigators (e.g. Gallego et al. 1995; Tresse et al. 2002; Yan et al. 1999). These observations support the rapid rise seen by other indicators out to $z \sim 1$. At $z > 2$, Hα is redshifted into the K-band, and it is only with the advent of near-infrared imagers that narrowband searches for Hα at high-z have become possible.

Although attempts to search for Hα emission at $z \sim 2$ with near-infrared narrowband surveys have been made (e.g. Thompson et al. 1996; Moorwood et al. 2000), these have been severely hampered by small survey areas. At the typical limit of these studies, $f_{\mathrm{H}\alpha} \sim 10^{-16}\,\mathrm{erg\,s^{-1}\,cm^{-2}}$, only a handful of potential $z \sim 2$ Hα emitters have been detected. Indeed, in the largest survey of this type to date, Thompson et al. (1996) detected only *one* Hα emitter over 276 square arcminutes to a flux limit of $f_{\mathrm{H}\alpha} = 3.5 \times 10^{-16}\,\mathrm{erg\,s^{-1}\,cm^{-2}}$. This was confirmed to have an emission line corresponding to $z = 2.43$ in the follow-up spectroscopic survey of Beckwith et al. (1998). In comparison, Moorwood et al. (2000) probe to a slightly deeper limit, $f_{\mathrm{H}\alpha} = 0.5 \times 10^{-16}\,\mathrm{erg\,s^{-1}\,cm^{-2}}$, and over 100 square ar-

cminutes detect 10 candidate emitters, but all of the candidates chosen for spectroscopic followup turned out to be higher redshift [OIII] emitters (Kurk et al. 2004; Moorwood et al. 2003). Detecting large numbers of Hα emitters using this method is clearly challenging, and larger (and preferably deeper) surveys are needed to efficiently probe the Hα luminosity density at high redshift.

In this chapter we make an improvement over previous $z \sim 2$ Hα surveys by utilising the panoramic imaging capability of the Wide Field Camera (WFCAM, Casali et al. 2007) on the 3.8-m United Kingdom Infrared Telescope (UKIRT). We have obtained deep narrowband imaging at $\lambda = 2.121\mu$m to search for $z = 2.23$ Hα emitters over 0.603 sq. degrees of the Cosmological Evolution Survey (COSMOS) field (Scoville et al. 2007). This corresponds to a co-moving volume ∼30× that probed by Moorwood et al. (2000), which is the most similar previous survey in redshift and depth to this one. Here we present the results of the survey, and we use the Hα LF to evaluate the total luminosity density at $z = 2.23$, and therefore the SFRD. In §5.2 we outline the details of the survey and reduction techniques, §5.3 describes the narrowband selection procedure, and in §5.4 we present the results, where we discuss some of the individual properties and calculate the luminosity function for the Hα sample. We compare our results with previous estimates for this epoch, and the evolution of the Hα derived SFRD from $z = 0$–2.2. We summarise the work in §5.5 and give a brief overview of our future extension to the survey in §5.6. Throughout we have assumed $H_0 = 70\,\mathrm{km\,s^{-1}\,Mpc^{-1}}$ and $(\Omega_m, \Omega_\Lambda) = (0.3, 0.7)$. Unless otherwise stated, magnitudes are on the Vega scale.

5.2. Observations and data reduction

5.2.1 Observations

The COSMOS field was observed during 2006 May, November and December and 2007 January with WFCAM on UKIRT, with the broadband (K-band) and narrowband (H_2S1, $\lambda_c = 2.121\mu$m, $\delta\lambda = 0.021\mu$m) filters. WFCAM's standard 'paw-print' configuration of four 2048×2048 0.4″/pixel detectors offset by ∼20′ can be macro-stepped four times to mosaic a contiguous region of ∼55′ × 55′ (Dye et al. 2006). In this way we mapped ∼0.62 square degrees of COSMOS ($10^h\ 00^m\ 28.6^s$, $+02^d\ 12^s\ 21.0^s$) with ∼13.5 ks/pixel narrowband exposure (in order to reach the sufficient continuum limit, the broadband K ex-

posures were significantly less, ~500 s/pixel). The seeing was typically of the order $\leq 1''$. To help with Cosmic ray rejection over the relatively long narrowband exposures (40 or 60 s), we used the NDR (Non Destructive Read) mode, whereas CDS (Correlated Double Sampling) mode was used for the broadband exposures. The near-infrared observations were obtained in the standard way, following a 14 point jitter pattern. In addition to the jitter pattern, to improve sampling of the PSF, the narrowband frames were microstepped in a 2×2 grid with $1.2''$ offsets at each position.

5.2.2 WFCAM data reduction

For a given frame in a sequence of 14, we self-flat the data using a normalised median combination of the remaining frames in the sequence, taking care to mask-out bright objects in each frame. This is achieved by running a two-pass flat: in the first pass a rough flat made from a straight median combination in order to reveal the bright objects. In the next step, we use SExtractor's `check_image` output (v2.3.2 Bertin & Arnouts 1996), which are then used as a mask when constructing the master flat. This minimises the artifacts seen around bright extended sources. Some care must be taken with the micro-stepped frames – the small offset between consecutive frames in a micro-sequence are smaller than many extended sources, therefore we construct flats from each micro-stepped position separately as if they are part of a standard dither.

A world coordinate system is fit (with rotating and shift geometry) to each frame by querying the USNO A2.0 catalog, fitting on average ~100 objects, and then frames are de-jittered and co-added with SWARP[1] (this performs a background mesh-based sky subtraction, optimised to provide the best representation of the large scale variations across the field). In the case of the micro-stepped (narrowband images), this step is preceded by drizzling the frame onto a grid with a pixel scale of $0.2''$ (i.e. half the nominal plate scale). WFCAM frames suffer from significant cross-talk, manifesting itself in toroidal features at regular (integer multiples of 128) pixel intervals from sources in the read-out direction. As these are tied to the positions of real objects, they are not removed by dithering the frames. High order cross-talk can easily mimic real objects, therefore these positions are flagged at the catalogue stage, we discuss this further in §5.3.

[1]Both SWARP and SExtractor are distributed by Terapix (`http://terapix.iap.fr`) at the Institut d'Astrophysique de Paris.

Broad and narrowband frames are calibrated by matching $10 < m_K < 15$ stars from the 2MASS All-Sky Catalog of Point Sources (Cutri et al. 2003) which are unsaturated in our frames. Since the narrowband filter lies in the K-band, we can check the zero-point offsets to be applied to the narrowband frames directly from the broadband calibration, taking into account the relative widths of the filters, such that the offset between the zeropoints is $2.5\log(\Delta\lambda_K/\Delta\lambda_{\mathrm{H_2S1}})$. As an additional verification, we check that $K - \mathrm{H_2S1} \sim 0$ expected for typical bright stars.

5.2.3 Source extraction and survey limits

Our survey is made up of a mosaic of three WFCAM paw-prints, i.e. 12 $13.7' \times 13.7'$ tiles. Sources are detected and extracted using SExtractor. To confirm the depth and completeness of the images, we perform Monte Carlo simulations of the detection of a large number of 'fake' sources (a single Gaussian point source generated with IRAF's *artdata* with a FWHM matching the image PSF). By scaling the artificial source over a range of known flux, and inserting at random locations over the frames, we measure the detection rate (i.e. the completeness) as a function of observed magnitude using an identical extraction procedure to that used to generate the main catalog. A final narrowband catalogue is made by matching detections in the $\mathrm{H_2S1}$ to the broadband image. Since the frames are well matched astrometrically, a simple geometric matching algorithm suffices, with a maximum search radius of $2''$. Cross-talk artifacts in WFCAM frames can mimic the narrowband excess objects we are selecting for. Therefore, to clean the catalog from possible cross-talk contaminants, we flag all possible positions by measuring the chip (x, y) position of bright sources, then flag regions at integer multiples of 128 pixels along the direction of readout. These chip positions can be converted to a sky coordinate and then compared to the narrowband catalog. As a rule, we remove an object from the catalog if it lies within $2''$ of any cross-talk position. Note that by avoiding the zeroth order cross-talk position, we also avoid spurious detections close to bright stars (although in this case the exclusion radius is larger to account for extended haloes and diffraction spikes, at $30''$). Due to the lower exposures received by the edges of the individual frames (caused by the jitter pattern), we ignore detections from within $\sim 10''$ of any frame edge. The total area lost due to cross-talk and star masking is negligible ($< 0.1\%$), however including the edge-clipping we survey an effective area of 0.603 square degrees.

Due to the fact that the observations were acquired over a long period of time, with

slightly different seeing and exposure times, we treat each tile separately, detecting objects down to each tile's limit. The average 3σ depth of the broadband frames is $K = 20.1$ mags and the exposure times for the narrowband frames were chosen such that they should reach a similar depth to the broadband frames. We detect a total of 19079 objects down to these limits across 0.603 sq. degrees. Note that all magnitudes are measured in $3''$ diameter apertures, and this recovers the majority of the flux.

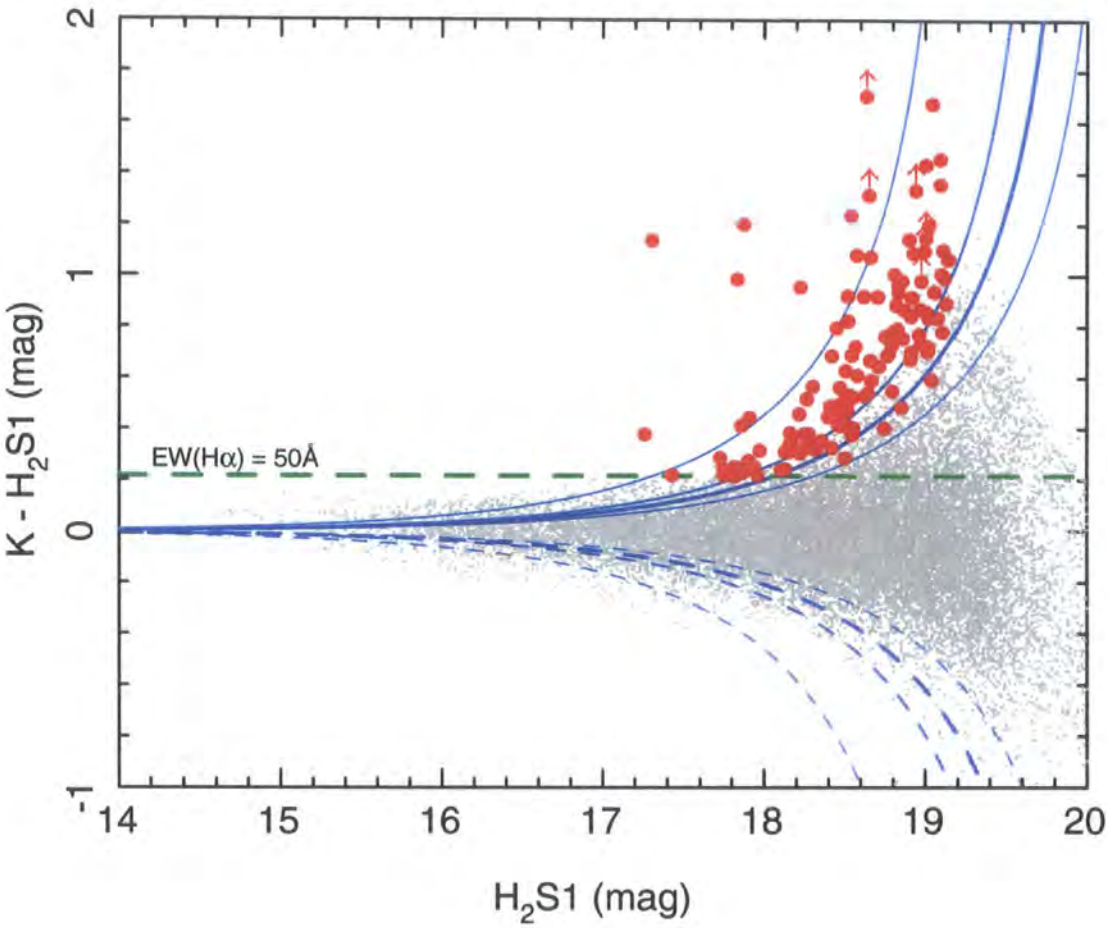

Figure 5.1: The $K - \mathrm{H_2S1}$ colour-magnitude diagram used to select narrowband excess objects, and thus possible $z = 2.23$ Hα emitters. Narrowband colours have been corrected to account for broadband continuum slope using the $(z - K)$ broadband colour (see §5.3.1). $\Sigma = 2, 2.5, 3$ & 5 selection cuts are shown, as is a 50Å offset in equivalent width, corresponding to a positive colour offset. The Σ cuts here are averaged over the whole survey area, but these change slightly for each WFCAM tile as we take into account individual frame zeropoints and noise properties (although there is only a small variation over the survey). We show all detections that have would be selected as narrowband excess sources as red circles (limits indicate that source was not detected in the broadband frame). These narrowband excess sources are subject to a further selection described in more detail in §5.3.2.

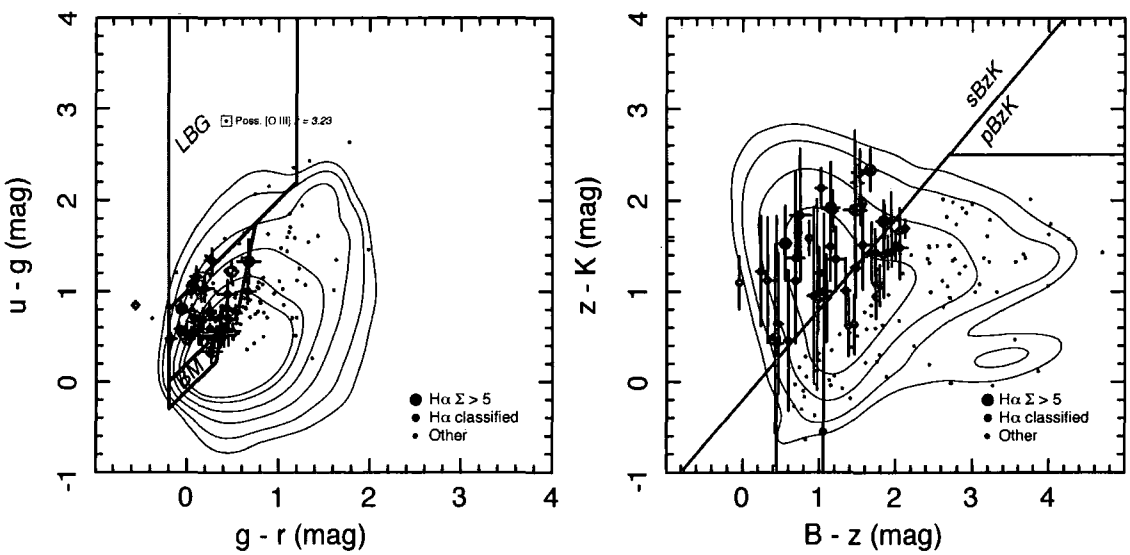

Figure 5.2: Broadband colour properties of narrowband selected objects. (left) *ugr* colours with the LBG and BM/BX selection criteria of Steidel et al. (2003) (right) *BzK* colours divided into high redshift starforming galaxies (*sBzK*) and high redshift passive galaxies (*pBzK*) and foreground galaxies, using the selection of Daddi et al. (2004) and compared to the general colour distribution using photometry available for the entire COSMOS field of view. It is clear that the straightforward narrowband selection outlined in §5.3.1 is also detecting low redshift galaxies, and we require further selection with broadband colours to clean the sample. However, the low redshift detections may also correspond to *real* emission lines, and we discuss this further in §5.3.2. Large points indicate our secure Hα emitters after employing our secondary colour selection outlined in §5.3.2. We highlight high significance ($\Sigma > 5$) candidates, noting that all of these fall in the *sBzK* and BM/BX selection regions. For clarity, we only show photometric uncertainties for Hα candidates.

5.3. Selection technique

5.3.1 Narrowband excess selection

Potential $z = 2.23$ Hα emitting candidates are initially selected based on the significance of their narrowband excess, i.e. their $K - \mathrm{H_2S1}$ colour. Galaxies with a strong emission line falling in the narrowband filter will have $\mathrm{H_2S1} < K$. The significance of the narrowband excess can be parameterised in terms of Σ, which quantifies the excess compared to what would be expected for a source with a flat spectrum (Bunker et al. 1995). This parameter is similar to a standard signal-to-noise selection, and we chose to select candidate emitters with $\Sigma > 2.5$. This is equivalent to a colour of:

$$m_{\mathrm{K}} - m_{\mathrm{H_2S1}} = -2.5 \log \left[1 - \Sigma\delta 10^{-0.4(c - m_{\mathrm{H_2S1}})}\right] \tag{5.1}$$

where c is the zeropoint of the narrowband image and δ is the photometric uncertainty. The Hα line flux $F_{\mathrm{H}\alpha}$ and equivalent width $W_{\mathrm{H}\alpha}$ can be calculated:

$$F_{\mathrm{H}\alpha} = \Delta\lambda_{\mathrm{H_2S1}} \frac{f_{\mathrm{H_2S1}} - f_K}{1 - (\Delta\lambda_{\mathrm{H_2S1}}/\Delta\lambda_K)} \tag{5.2}$$

and

$$W_{\mathrm{H}\alpha} = \Delta\lambda_{\mathrm{H_2S1}} \frac{f_{\mathrm{H_2S1}} - f_K}{f_K - f_{\mathrm{H_2S1}}(\Delta\lambda_{\mathrm{H_2S1}}/\Delta\lambda_K)} \tag{5.3}$$

Where $\Delta\lambda_K$, $\Delta\lambda_{\mathrm{H_2S1}}$ are the widths of the broad and narrowband filters. $W_{\mathrm{H}\alpha}$ is simply the ratio of the line flux and continuum flux density, and will also include contribution from the adjacent [NII] line. However, we can calculate the pure Hα line flux by assuming $F_{[\mathrm{NII}]}/F_{\mathrm{H}\alpha} = 0.33$ for extragalactic HII regions (Kennicutt & Kent 1983) and correcting appropriately.

In Figure 5.1 we present the colour-magnitude diagram with selection criteria. Some care must be taken in deciding on the selection, and we briefly describe it here. Firstly, we define an initial selection criteria of $\Sigma > 2.5$ (this is a function of narrowband flux and combined error due to sky noise in both the broad and narrowband images, as described above). To account the possible inclusion of bright foreground objects with steep continua across the K-band that have large significance but low equivalent widths (e.g. van der Werf et al. 2000), we enforce an additional selection criteria of $W_{\mathrm{H}\alpha} > 50$Å. This is an arbitrary threshold, but is chosen to reflect the general scatter about $K - \mathrm{H_2S1} = 0$ (see Figure 5.1). In an attempt to minimise this scatter, and to better model the continuum

slope of broadband detected objects, we make use of the $z - K$ colours available for all detections from the COSMOS archival z-band imaging. Since very red continua will result in a larger effective wavelength for the broadband detections, we wish to correct for this in order to make a better estimate of the continuum contribution to the narrowband flux at the 1.121μm. We measure $K - \mathrm{H_2S1}$ as a function of $(z - K)$, and fit the data with a linear trend using a simple least squares fit. The slope of this trend can therefore be used to 'correct' the $K - \mathrm{H_2S1}$ colour. We find that on average the correction factor to the narrowband flux excess is $\sim 0.03(z - K)$.

We only count narrowband detections at individual detection significances of $> 3\sigma$. It is not necessary that the source is also detected in the broadband frame, and we assign an upper limit if there is no corresponding continuum detection. The Hα line-flux limit is the theoretical minimum that could be detected taking into account all these selection criteria. The average 3σ Hα flux limit over the survey is $10^{-16}\,\mathrm{erg\,s^{-1}\,cm^{-2}}$. As a final quality control check, we visually inspect each candidate in order to filter any remaining erroneous sources (for example, non-crosstalk associated artifacts, etc.). In Figure 5.3 we present the narrowband field around candidate emitters representing a range of detection significance ($2.5 \lesssim \Sigma \lesssim 5$). For each panel we show the narrowband frame before and after continuum subtraction using the broadband image after suitably scaling to account for the relative filter widths.

5.3.2 Broad band colours: further selection, redshift confirmation and line contamination estimates

There are two major factors that influence the efficacy of the narrowband selection technique. First, we must be certain that the selection in colour space is actually identifying the Hα line at $z = 2.23$. Related to this issue is the contamination rate from emission lines at other redshifts making them potentially detectable at 2.121 μm. At higher redshift, the most important contaminant is [OIII]λ5007 at $z = 3.23$ (although these objects are interesting in their own right as possible examples of high-z AGN). At low redshift, we are susceptible (potentially) to any strong line between Hα and $\mathrm{H_2S1}$.

The most robust way to confirm the selection is through follow-up spectroscopy which can unambiguously identify the lines. However, complete spectroscopic follow up (at least in the short-term) is unfeasible. A 'cheaper' alternative is to make use of extensive multi-band optical/near-infrared photometry available for COSMOS (Capak et al.

2007), which can be used to improve the Hα selection. Unfortunately, at $z = 2.23$ the current photometric redshifts are not reliable enough to confirm Hα emission (Mobasher et al. 2007), so we turn to the cruder method of colour/colour-selection to filter our high redshift sample (although the photometric redshifts should be good enough to identify foreground contamination at $z < 1$).

We define a secondary optical selection, tuned according to the colours of a subsample of high significance ($\Sigma > 5$) Hα candidates from the pure narrowband selection. To discriminate between high and low redshift emission line galaxies, we first use the *sBzK* selection first presented by Daddi et al. (2004), and now becoming popular to select active galaxies at $z > 1.4$. Another selection of high redshift galaxies is made with *ugr* colours, and has been used to search for $z \sim 3$ Lyman Break galaxies (LBGs, Steidel et al. 1996) and 'BM/BX' star forming galaxies at $z \sim 2$ (Adelberger et al. 2004, Steidel et al. 2003). We use the BM/BX selection as a further indicator that the narrowband selected galaxies are at high redshift (additionally the LBG selection can also be used to detect possible $z \sim 3$ [O III] emitters). Candidate Hα emitters are narrowband excess objects which also satisfy the BM/BX selection *or* the *sBzK* selection. In a further effort to eliminate foreground contaminants we impose a magnitude cut of $z > 22.5$ (equivalent to $u > -23.7$ at $z = 2.23$). This yields a total Hα sample of 55 compared to our original selection of 180 on the basis of narrowband selection alone. We present the colour-colour plots with selection criteria in Figure 5.2. After the colour selection, the majority of Hα emitters fall in both the BM/BX and *sBzK* regions, with those that do not having large enough photometric errors that place them $< 1\sigma$ away in colour-space. Note that two objects flagged as Hα emitters are potentially low-redshift [FeII]λ1.64 emitters based on their photometric redshifts (see Figure 5.4 and discussion below). Thus, the photometric selection is not a fool-proof method, although it appears the contamination rate is low ($\lesssim 3\%$).

What are the remaining narrowband excess objects which fail our colour selection? At least one appears to be a high redshift (possibly [OIII]) emitter selected in the LBG cut, but the bulk of the remaining objects are likely to be low-redshift given their colours and magnitudes. Two likely low redshift contaminants are Paα ($\lambda = 1.875\,\mu$m) at $z \sim 0.13$ and Paβ ($\lambda = 1.282\,\mu$m) at $z \sim 0.65$. To estimate the contamination rates from these lines, we search for those galaxies with secure photometric redshifts in the range $z_{\rm phot} = 0.13 \pm 0.05$ and $z_{\rm phot} = 0.65 \pm 0.05$. We identify 12 Paα and 6 Paβ candidates in this way, although

there would be more if these stringent selection constraints were relaxed. There are several other low redshift emission lines that could potentially be detected, and to investigate this, in Figure 5.4 we plot the probability distribution $P(z)$ of $z_{\rm phot}$ of (a) Hα emitters, (b) Paα and Paβ candidates and (c) unclassified remaining narrowband excess detections. In the unclassified redshift distribution there are two clear peaks in the distribution at $z \sim 0.4$ and $z \sim 0.9$. The low redshift emitters could potentially be [FeII]λ1.64μm and several Brackett lines, whereas the slightly higher redshift peak might correspond to Paγ. Clearly this must be confirmed through spectroscopy, but it appears that the narrowband selection is detecting real line-emitters (and not surprisingly these comprise a range of emission lines) and is not sufficient alone to isolate Hα at $z = 2.23$. Identification of lower redshift interlopers will become easier when we use accurate photometric redshifts available for COSMOS (Mobasher et al. 2007 & private communication).

Finally we assess the impact of high-redshift contamination. We are probing the expected plateau in the SFRD, but this is also associated with the peak of AGN activity (Shaver et al. 1996; Boyle & Terlevich 1998) – what is the expected contamination rate to the Hα luminosity density from AGN? As with contamination from emission lines at different redshifts, without spectroscopic information (for example the Hα/[NII] ratio discriminating between star formation and nuclear activity), we must address this issue statistically. As described by van der Werf et al. (2000), the AGN interloper fraction is likely to be low: the fraction of AGN in local Hα selected galaxies is <5% (Gallego et al. 1997), and this is not likely to increase toward high redshift (Teplitz et al. 1998). A *ugr* cut can select $z \sim 3$ Lyman Break galaxies (LBGs), and this can be used to identify possible [OIII] contaminants (Figure 5.2). In our total narrowband selected sample, only one object satisfies the LBG selection criteria, and therefore we conclude that the $z = 3.23$ [OIII] contamination rate is negligible for our sample. We note that in a follow up spectroscopic survey of narrowband identified Hα emitters by Moorwood et al. (2000), six of 10 candidates were confirmed as $z = 3.23$ [OIII]. This implies a much higher [OIII] contamination rate, however that survey was not purely blank-field, and included fields around several high redshift radio galaxies. Thus it is not clear whether environmental effects are responsible for the high contamination observed in this previous small scale survey.

Note that our secondary colour-colour selection might introduce a new completeness issue to our final Hα selection: we may be missing real Hα emitters that are slightly out-

side the *ugr* and *BzK* selection. While we do not believe this to be a significant problem for our current selection (as discussed above, the most significant Hα candidates *all* satisfy the extra colour constraints, and so this incompleteness is a function of Σ), one way to estimate this incompleteness would be to count the number of sources scattered in and out of the selection areas when their fluxes are adjusted by $\pm 1\sigma$. An upper limit can be estimated from the number of objects excluded by the colour cuts (125 objects). We do not take this incompleteness into account in further calculations.

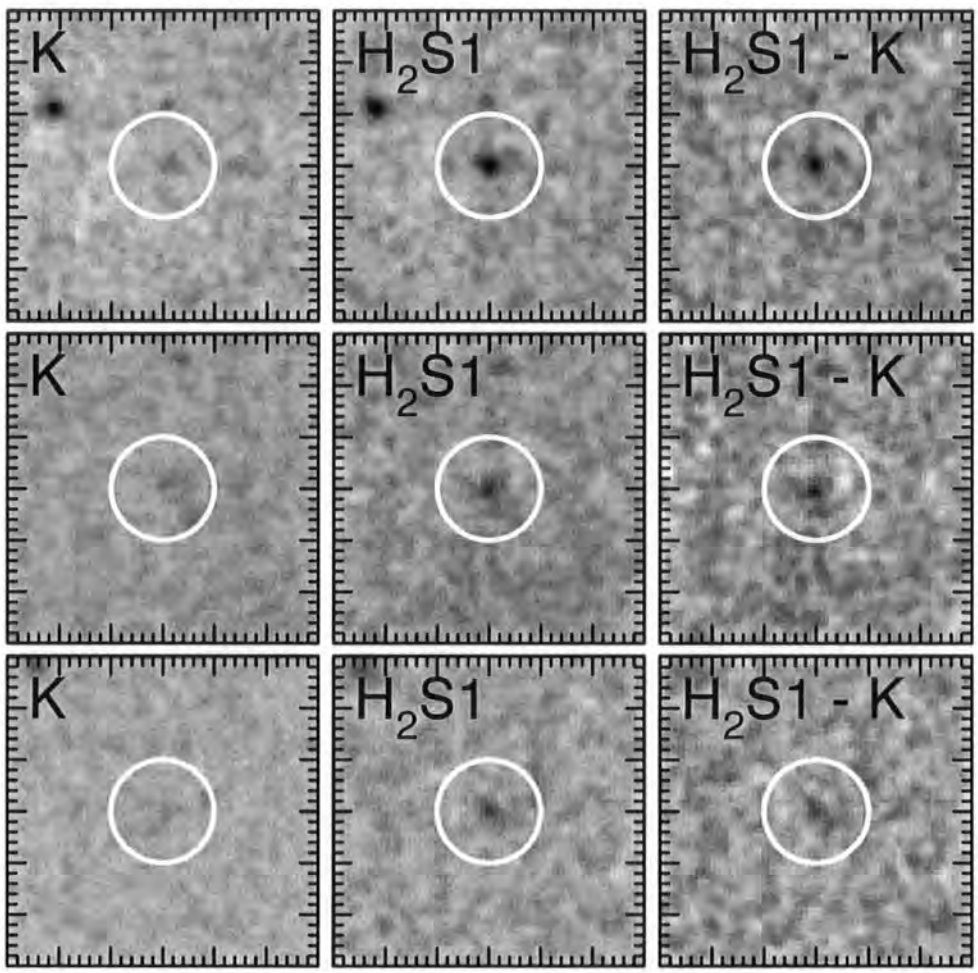

Figure 5.3: Three examples of a narrowband selected Hα emitters of different significance. The top, middle and lower panels show $\Sigma \sim 5$, $\Sigma \sim 3$, $\Sigma \sim 2.5$ respectively. The left hand panels show the broadband continuum, the centre shows the narrowband, and the right shows the continuum subtracted narrowband image. For the latter, the broadband has been scaled to account for the filter widths and both frames were locally registered to improved astrometric accuracy and smoothed with a Gaussian kernel to the same effective seeing. Images are orientated north up and east left and scaled identically. Note that all images have been rebinned to the scale of the broadband frames: $4''$/pix, and are $30'' \times 30''$ square.

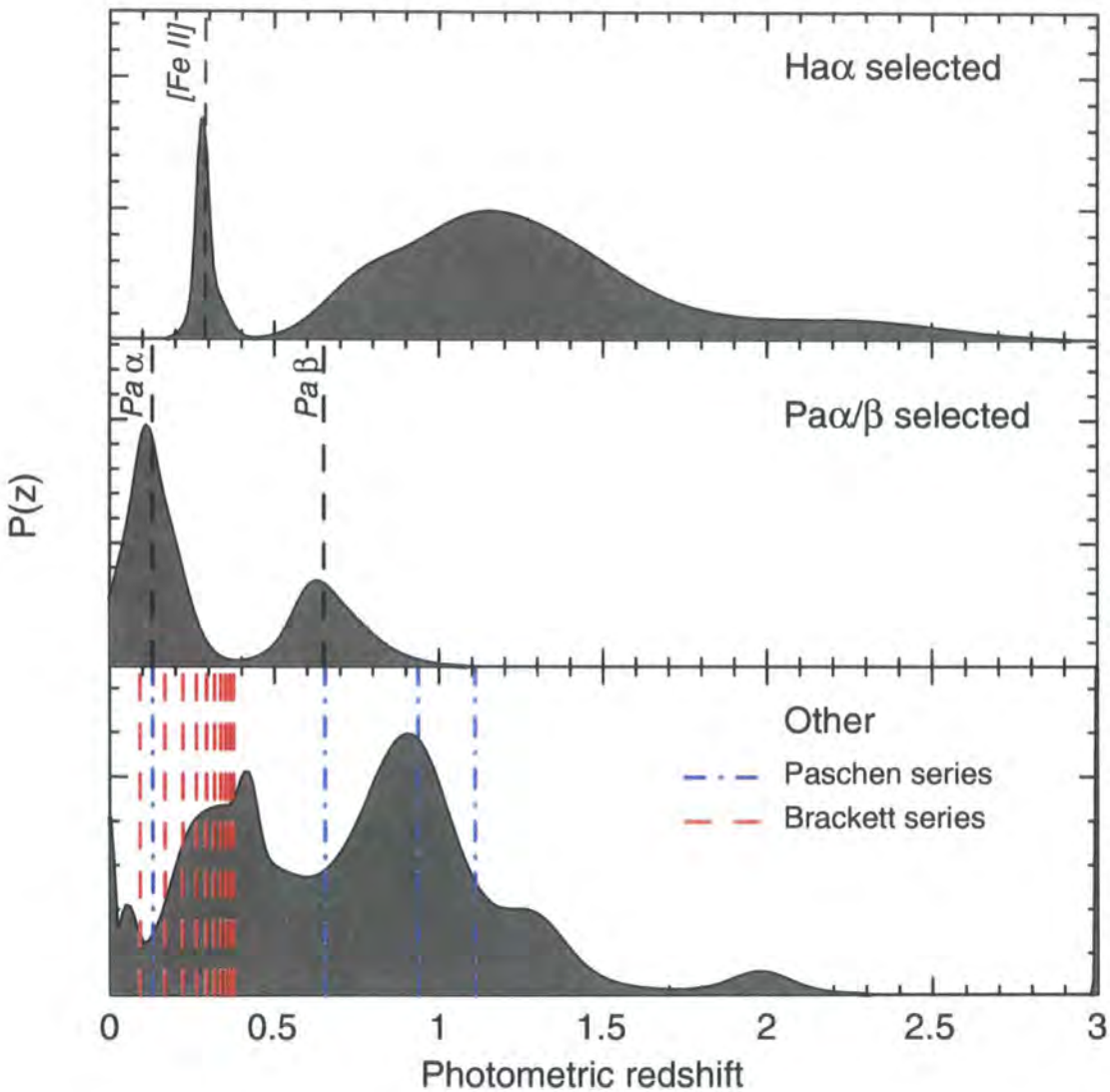

Figure 5.4: Total probability distributions $P(z)$ of photometric redshifts of: (top) narrowband excess detections satisfying our additional photometric selection. Note that there is a spike in $P(z)$ at $z \sim 0.3$, corresponding to the redshift of [FeII]λ1.64 in the H_2S1 filter. This spike represents two objects and are removed from our sample. The broad distribution of $z_{\rm phot}$ at $z \gtrsim 1$ are probably real Hα emitters with incorrect photometric redshifts; (middle) distribution of galaxies selected as Paα and Paβ emission lines with $z_{\rm phot} = 0.13 \pm 0.05$ and $z_{\rm phot} = 0.65 \pm 0.05$ respectively; (bottom) remaining 'unclassified' emitters. There are two main peaks to the distribution of unclassified objects: at $z \sim 0.3$ this could correspond to [FeII]λ1.64 or several Brackett lines. At $z \sim 0.8$ the peak could correspond to Paγ. This highlights the need for further filtering of the narrowband-selected sample with broad band colours.

5.3.3 zCOSMOS spectra

The zCOSMOS survey is an extensive spectroscopic project obtaining thousands of redshifts in the COSMOS field. To test for any existing spectra corresponding to our narrowband excess sample, we cross-correlate our catalog with the current zCOSMOS spectroscopic catalog (S. Lilly private communication). We do not expect a large degree of overlap between our catalogue and zCOSMOS, since we are detecting relatively faint galaxies, and indeed there were only 6 positional matches with secure redshifts. At least one Hα candidate is included in the 'faint' zCOSMOS catalog confirmed to securely lie at $z = 2.2329$, verifying the selection at least for this candidate. The remaining matches are all in the 'bright' sample. Three of these were identified by us as being possible Paα at $z \sim 0.13$, and indeed two have confirmed redshifts of $z = 0.1312$ and $z = 0.1298$, although another has $z = 0.1086$. The final match has $z = 0.7340$ – it is not clear that this corresponds to a real emission line, and so this could represent a low significance false interloper. Although this is a very limited spectroscopic confirmation, it does suggest that we are detecting a range of emission lines, and that our secondary filtering technique is useful for weeding out low redshift interlopers. We note that our dedicated near-infrared spectroscopic follow-up in the near future will allow us to make a much better estimate of the contamination rate.

5.4. Results

We detect a total of 55 candidate $z = 2.23$ Hα emitters over 0.603 square degrees of the COSMOS field, resulting in a surface density of $91 \pm 10\,\mathrm{deg}^{-2}$ brighter than a flux limit of $10^{-16}\,\mathrm{erg\,s^{-1}}$. In the following sections we briefly discuss their individual multi-wavelength and morphological properties, and evaluate the Hα luminosity function and thus star formation rate density at $z = 2.23$.

5.4.1 The properties of Hα emitters

Hubble Space Telescope ACS imaging – morphologies

In Figure 5.5 we present $5'' \times 5''$ *Hubble Space Telescope (HST)* ACS F814W (I-band) thumbnail images of the candidate Hα emitters. The exquisite imaging quality of *HST* allows their rest-frame UV morphologies to be examined in some detail, and we have used this,

along with *BRz* Subaru SuprimeCam optical imaging from the COSMOS archive preserve morphological information and reveal colour gradients that vary on scales comparable to the optical ground based imaging resolution (for example this allows us to distinguish red and blue components in an interacting galaxy). We observe two main morphological types: disturbed clumpy/multi-component morphologies and compact undisturbed galaxies. The disturbed systems often comprise of two bright components and with some extended low surface brightness features connecting the two. Presumably these are signatures of galaxy-galaxy interactions, as might be expected to trigger these star forming galaxies.

Spitzer 24μm and VLA 1.4 GHz observations – obscured star formation

The entire COSMOS field has been observed with the Multiband Imaging Photometer (MIPS) on the *Spitzer Space Telescope*. The 24μm flux at $z \sim 2.23$ probes infrared emission from dust grains in the interstellar medium – polycyclic aromatic hydrocarbon (PAH, ~6–12μm) emission lines. In fact, 24μm should be dominated by the prominent 7.7μm emission feature, and so should be a good indicator of obscured star formation. To investigate the possibility that some of the Hα emitters are dusty starbursts, we cross-correlate the Hα catalog with the *Spitzer*-COSMOS (S-COSMOS, Sanders et al. 2006) MIPS 24μm catalogs with a simple matching radius of 2″. Seven Hα emitters at 24μm are detected in both the wide and deep MIPS maps (flux limits of 0.3 mJy and 0.06 mJy respectively) with a noise weighted average 24μm flux density of $\langle f_{24\mu\mathrm{m}} \rangle = 0.20 \pm 0.03$ mJy. In order to search for a statistical signature of mid-infrared emission from the whole sample of Hα emitters we stack the 24μm data in regions around the source positions (the Hα fluxes of 24μm detections are not significantly different from the overall Hα population, so we include these in the stack). The resulting stacked image yields a significant flux excess, $f_{24\mu\mathrm{m}} = 0.11 \pm 0.01$ mJy. The uncertainty is derived by stacking 50×55 thumbnail images around random locations in the 24μm map, and measuring the scatter in the fluxes measured in identical apertures in each stack. The significant 24μm flux suggest weak mid-infrared emission in these star forming galaxies. How does the infrared luminosity compare to the Hα luminosity? To compare these two values we first estimate the total-infrared luminosity by normalising an M 82-like spectral energy distribution to the observed 24μm flux and interacting over 8–1000μm. The SFR is estimated using the calibration of Kennicutt (1998), $\mathrm{SFR[IR]} = 4.5 \times 10^{-45} \, (L_{8-1000\mu\mathrm{m}}/\mathrm{erg\,s^{-1}}) \, M_\odot \, \mathrm{yr}^{-1}$. We

find SFR[IR] $= 90 \pm 40\,M_{\odot}\,\mathrm{yr}^{-1}$, where the uncertainty is derived by recalculating the total infrared luminosity by introducing a 50% variation in the normalisation of the SED, since at $z = 2.23$ the 24μm flux probes the 7.7μm PAH emission line, and this can vary in strength as the feature is redshifted through the MIPS bandpass at $z \sim 2$. The average Hα luminosity is $\log L_{\mathrm{H}\alpha}(\mathrm{ergs}^{-1}) = 42.8$, corresponding to a star formation rate of $50\,M_{\odot}\,\mathrm{yr}^{-1}$ (assuming SFR[IR] $= 7.9 \times 10^{-42}\,(L_{\mathrm{H}\alpha}/\mathrm{erg\,s}^{-1})\,M_{\odot}\ \mathrm{yr}^{-1}$, Kennicutt et al. 1998). However, introducing an extinction correction of $A_{\mathrm{H}\alpha} = 1$ mag this increases to $120\,M_{\odot}\,\mathrm{yr}^{-1}$. If the mid-infrared emission is a result of star formation, the Hα emitters are moderately obscured star formers with $A_{\mathrm{H}\alpha} \sim 1.3$ mag. Since COSMOS was also observed at 70μm and 160μm with MIPS, we apply a similar stacking analysis for these wavelengths in an attempt to place constraints on the far-infrared properties of the Hα emitters. We do not find significant flux excess in either case, and so we quote (3σ) upper limits of $f_{70\mu\mathrm{m}} < 2.1$ mJy, and $f_{160\mu\mathrm{m}} < 9.2$ mJy.

Four Hα emitters are formally detected in the 21 cm VLA map of COSMOS (Schinnerer et al. 2007), with an average flux of $\langle f_{21\mathrm{cm}} \rangle = 160 \pm 20\,\mu$Jy. Again, these objects' Hα fluxes are not significantly different from the general population, and so we employ the same stacking technique to find the 'average' 21 cm flux for the sample. We find $f_{21\mathrm{cm}} = 9.7 \pm 1.2\,\mu$Jy (the error is calculated in the same manner as the 24μm stack – i.e. repeating the analysis for randomly co-added thumbnail images). This is in good agreement with what would be expected from the infrared-radio correlation based on the 24μm flux density (e.g. Boyle et al. 2007).

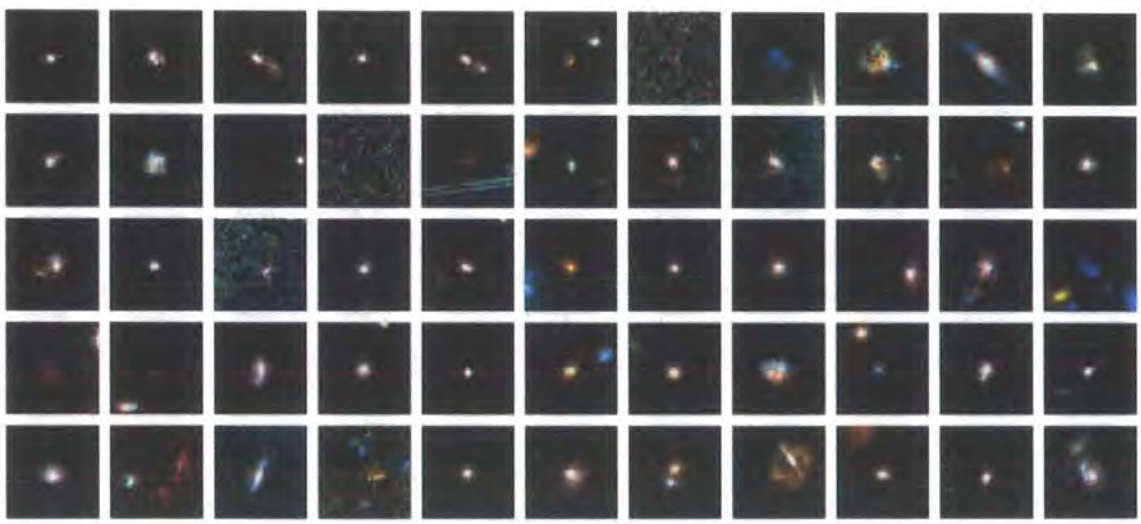

Figure 5.5: 55 5″ × 5″ *HST* ACS thumbnail images of $z = 2.23$ Hα candidates. The images are coloured with a map generated from the ground based *Brz* imaging, and use the F814W filter as a luminance channel (all images are scaled identically and orientated with north up and east to the left). Note that at $z = 2.23$, 5″ is equivalent to ∼40 kpc in projection. The images are organised row-wise in order of decreasing Hα luminosity such that the top left thumbnail is the most luminous, and the bottom right is the least. We generally see two types of morphology: very compact or more extended (generally disturbed) systems. Many of the disturbed morphologies show evidence for two bright components within ∼ 1″ of each other – indicative of recent or ongoing interaction which might be powering star formation. The colour images appear to support this, with some of the more extended sources showing clear red and blue parts, reminiscent of star forming galaxies in the local Universe.

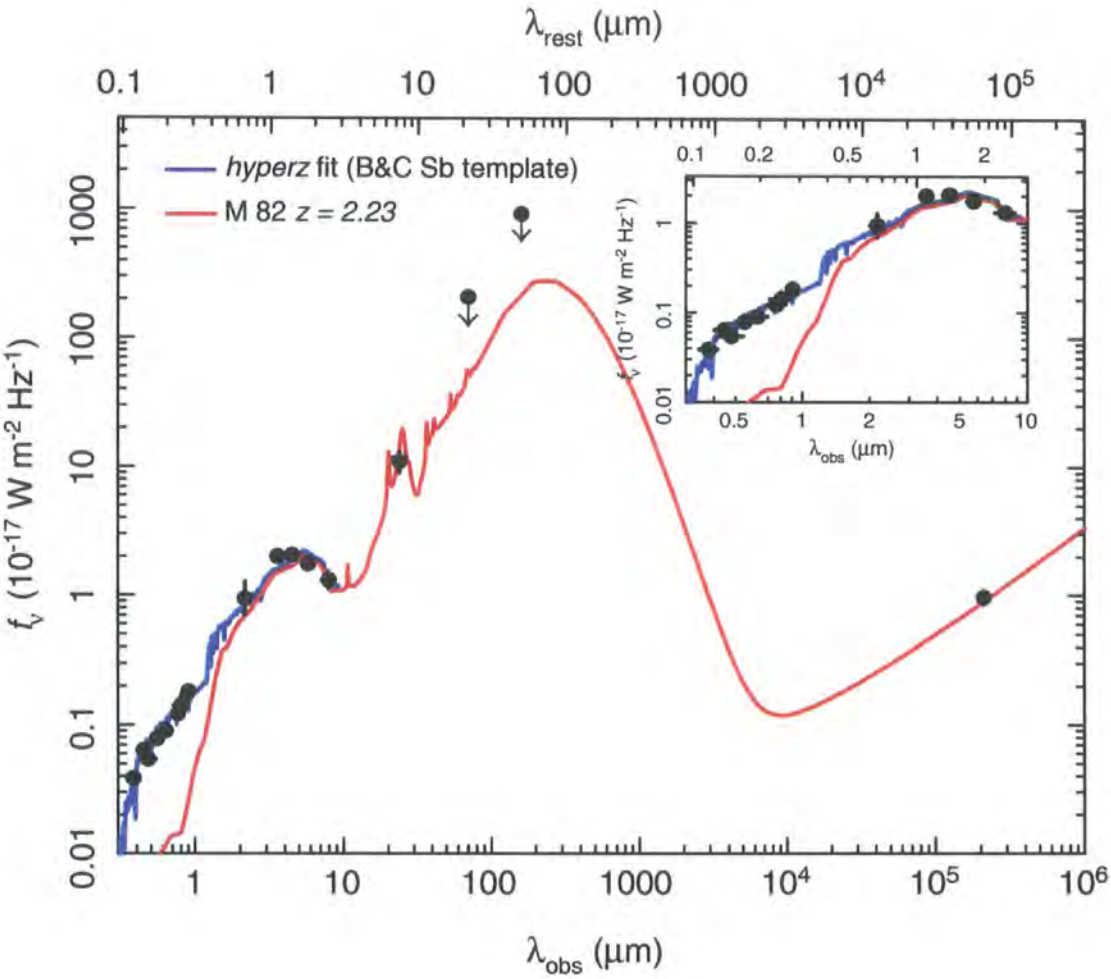

Figure 5.6: Average SED for Hα emitters. The inset shows UV/optical/near-IR photometry from the COSMOS archive averaged over all 55 candidates, fit with a Sb galaxy template at $z = 2.23$ reddened with $A_V = 1$ mag. The fit agrees well with what we expected from the narrowband selection alone. The main panel extends the SED to longer wavelengths by stacking the 24μm, 70μm, 160μm and 1.4 GHz data, and we overlay the M 82 template, redshifted to $z = 2.23$ and scaled in flux accordingly. Again, this seems to verify the redshift selection (from the 1.6 μm bump and infrared–radio correlation), and suggests that these galaxies are not dissimilar to local starburst galaxies.

Average spectral energy distribution of Hα emitters

In Figure 5.6 we show the average spectral energy distribution of the Hα emitters. The optical/near-IR *uBVgrizK*+F814W+IRAC 3.6–8μm photometry is averaged over all the Hα emitters (weighted by the individual photometric errors) and then fit with a choice of Sa-d and burst spectral templates (Bruzual & Charlot 1993) redshifted to $z = 2.23$ using the HYPERZ photometric redshift code (Bolzonella et al. 2000). Note that the IRAC points are the 3″ aperture fluxes corrected to total flux using the values suggested by the S-COSMOS team: the apertures recover fractions of 0.90, 0.90, 0.84 and 0.73 for channels 1–4 respectively. Coverage of the rest-frame near-infrared is useful for improving the photometric redshifts of high redshift objects, since it allows the location of the 1.6μm stellar bump to be tracked (e.g. Sawicki 2002). The wavelength of this feature corresponds to the minimum opacity of H^- ions in the atmospheres of cool stars (John 1988), and thus is an indicator of the evolved ($\gtrsim$ 20 Myr old) stellar population. The average 3.6–8μm flux agrees with the 1.6μm feature redshifted to $z = 2.23$. The data are well fit by an Sb spectral type template with an additional reddening of $A_V = 1.0$ mag (this parameter was free to vary in the range $0 < A_V < 2$ mag) corresponding to an extinction of 0.1 mag at 2.121μm assuming Calzetti reddening.

The good fit to the spectral template is compelling evidence that our narrowband plus photometric selection is sampling the correct redshift, and shows that improved photometric redshifts that make use of bands redward of K will help in improving the narrowband selection. As IRAC is probing rest-frame near-infrared emission, we can estimate the stellar mass of these galaxies from the absolute rest-frame K-band luminosity. We estimate the rest-frame absolute K-band magnitude from the 5.8μm flux, $M_K = -25.4$ mag (AB magnitude). This result agrees with the estimate of M_K from the HYPERZ output, which calculates the absolute magnitude through a K-band (UKIRT) filter. The stellar mass, $M_\star$, is estimated using a similar method to Borys et al. (2005), assuming $M_\star$ is equal to the integrated stellar mass at the age of the galaxy. Note that our template assumes a continuous star formation history, with a Miller & Scalo (1979) initial mass function (a burst template does not provide a satisfactory fit to the observed photometry). If the K-band luminosity traces stellar mass, then

$$M_\star = \frac{10^{-0.4(M_K-3.3)}}{(L_K/M)} M_\odot \tag{5.4}$$

where L_K/M is the mass-to-light ratio, and the factor 3.3 corresponds to the absolute

Solar K-band luminosity (Cox 2000). For continuous star formation we estimate L_K/M from the description of Borys et al. (2005) who use the STARBURST99 stellar synthesis code (Leitherer et al. 1999) to find $L_K/M = 103(\tau/\mathrm{Myr})^{-0.48}$ for ages $\tau > 100\,\mathrm{Myr}$. The age returned from HYPERZ is 1 Gyr, similar to the mean age of $z \sim 2$ UV-selected star forming galaxies in the BM/BX survey of Erb et al. (2006). Using this age to estimate the mass-to-light ratio, we find an average stellar mass of $z = 2.23$ Hα emitters of $M_\star \sim (8.6 \pm 1.1) \times 10^{10} M_\odot$, with an error determined from the photometric uncertainty in the 5.8μm flux, and assuming a range in age of 0.9–1.1 Myr, similar to the scatter in the Erb et al. (2006) sample. This is significantly larger than the mean stellar mass of the sample in Erb et al. (2006), who find $M_\star = (3.6 \pm 0.4) \times 10^{10}\, M_\odot$, although that sample is deeper in terms of Hα luminosity (but of a similar depth in K).

In addition to the UV–near-IR points, we show longer wavelength data described above: 24μm, 70μm, 160μm and 21 cm statistical detections and limits. For comparison we show the M82 galaxy SED (a local starburst) redshifted to $z = 2.23$ and scaled in flux to match the 24μm flux density accordingly. The average 24μm/21 cm flux is consistent with what would be expected for a typical star forming galaxy at $z = 2.23$ (Boyle et al. 2007).

5.4.2 Hα luminosity function and star formation rate density

To calculate the luminosity function of Hα emitters, we convert line fluxes to luminosities, correcting for 33% contribution to the line flux calculated in equation 5.2 from [NII]. The volume is well defined by the survey area and narrowband filter width, which probes a co-moving depth of ∼40 Mpc, and is equivalent to $220 \times 10^3\,\mathrm{Mpc}^3$ (co-moving). Although Hα is relatively insensitive to dust extinction (it is not resonantly scattered, unlike Lyα), dust must still be taken into consideration when deriving luminosities. A robust technique would be to obtain spectroscopy of each source to measure the Balmer Hα/Hβ decrement, but clearly this is not feasible for our sample. Instead we adopt $A_{\mathrm{H}\alpha} = 1$ mag (Kennicutt 1992; 1998), as is applied in similar works (Fujita et al. 2003; Pascual et al. 2005; Ly et al. 2007) for SFR estimates. Although it is known that the specific extinction is a function of SFR (Jansen et al. 2001; Aragón-Salamanca et al. 2003; Hopkins et al. 2001), we apply this constant correction to our sample, for ease of comparison with other samples, noting that in the cases where the actual extinction is higher, our measured SFRs will be conservative.

Our LF has been corrected for completeness on a bin by bin basis using the completeness functions estimated for the narrowband imaging, and the lower luminosity limits have been dealt with by performing a survival analysis on the binned data, using the probability estimator of Avni et al. (1980). The errors derived from the Poisson statistics of each bin, although we apply a slightly more conservative bootstrap analysis to estimate the uncertainties on the fit values, described in more detail below). We fit the LF with a Schechter function characterised by α, $\phi^\star$ and $L^\star$: $\phi(L)\mathrm{d}L = \phi^\star(L/L^\star)^\alpha \exp(-L/L^\star)\mathrm{d}(L/L^\star)$. Since we lack sufficient depth to fit the faint end slope, we fix $\alpha = -1.35$ – this value was also used by Yan et al. (1999) for the Hα LF at $z = 1.3$ who chose the value observed by Gallego et al. (1995) for their $z = 0$ Hα study. Therefore we cannot show any evolution in the faint end slope of the Hα LF – a deeper survey is required for this. To estimate errors on the LF, we refit the Schechter function by bootstrapping the sample of luminosities 50 times, with the variance of the resulting parameters forming our uncertainty in $\phi^\star$ and $L^\star$. After this procedure we find $\phi^\star = (1.45 \pm 0.47) \times 10^{-3}\,\mathrm{Mpc}^{-3}$ and $\log L^\star = 42.83 \pm 0.13\,\mathrm{erg\,s^{-1}}$. We present the results in Figure 5.7 in comparison to the $z = 0$ results of Gallego et al. (1995) and the $z = 1.3$ Hα luminosity function of Yan et al. (1999). Although our observations are not deep enough to accurately measure the faint end slope, our results are very similar to the luminosity distribution found by Yan et al. (1999), suggesting that there is little evolution of the bright end slope between $z = 1.3$ and $z = 2.23$.

Next we use the integral of the LF to find the volume averaged star formation rate density ρ_{SFR}. In order to compare to other published results, we integrate the LF between $37 < \log L_{\mathrm{H}\alpha}(\mathrm{erg\,s^{-1}}) < 47$ as used in the compilation of Hopkins (2004). To convert to a star formation rate, we use the standard calibration of Kennicutt (1998); $\mathrm{SFR[H}\alpha] = 7.9 \times 10^{-42}(L_{\mathrm{H}\alpha}/\mathrm{erg\,s^{-1}})\,M_\odot\,\mathrm{yr}^{-1}$ (assuming continuous star formation, Case B recombination at $T_e = 10^4\,\mathrm{K}$ and a Salpeter initial mass function [IMF] ranging from 0.1–100$M_\odot$). Note that Hα is sensitive to massive (>10 $M_\odot$) young stars, and is therefore a good measure of the instantaneous SFR, however, the limitation is that significant extrapolations are needed to determine the total SFR down to the low-mass end of the mass function (Glazebrook et al. 1999; Afonso et al. 2000), and greater error is introduced when we take into account the uncertain shape of the IMF. We find $\rho_{\mathrm{SFR}} = 0.27 \pm 0.02\,M_\odot\,\mathrm{yr}^{-1}\,\mathrm{Mpc}^{-3}$, where the uncertainty is taken is the 1σ scatter after bootstrap resampling and re-evaluating the fit to the LF in the manner described above. Note

that if we assume a Scalo IMF, our estimate of the SFRD increases by a factor ∼1.4. We present our result in context with other Hα-derived SFRDs over $z < 2.23$ in Figure 5.8. Our value is consistent with the value found by Moorwood et al. (2000), but note that this is purely coincidental, since six of the 10 Hα candidates in that work used to constrain the LF were later shown to be high redshift [OIII] emitters (Moorwood et al. 2003; Kurk et al. 2003). Our derived SFRD is consistent with the generally accepted picture of a turn-over or plateau in the SFRD that occurs at $z \sim 2$, although deeper observations are required to trace the evolution of the faint end slope in more detail.

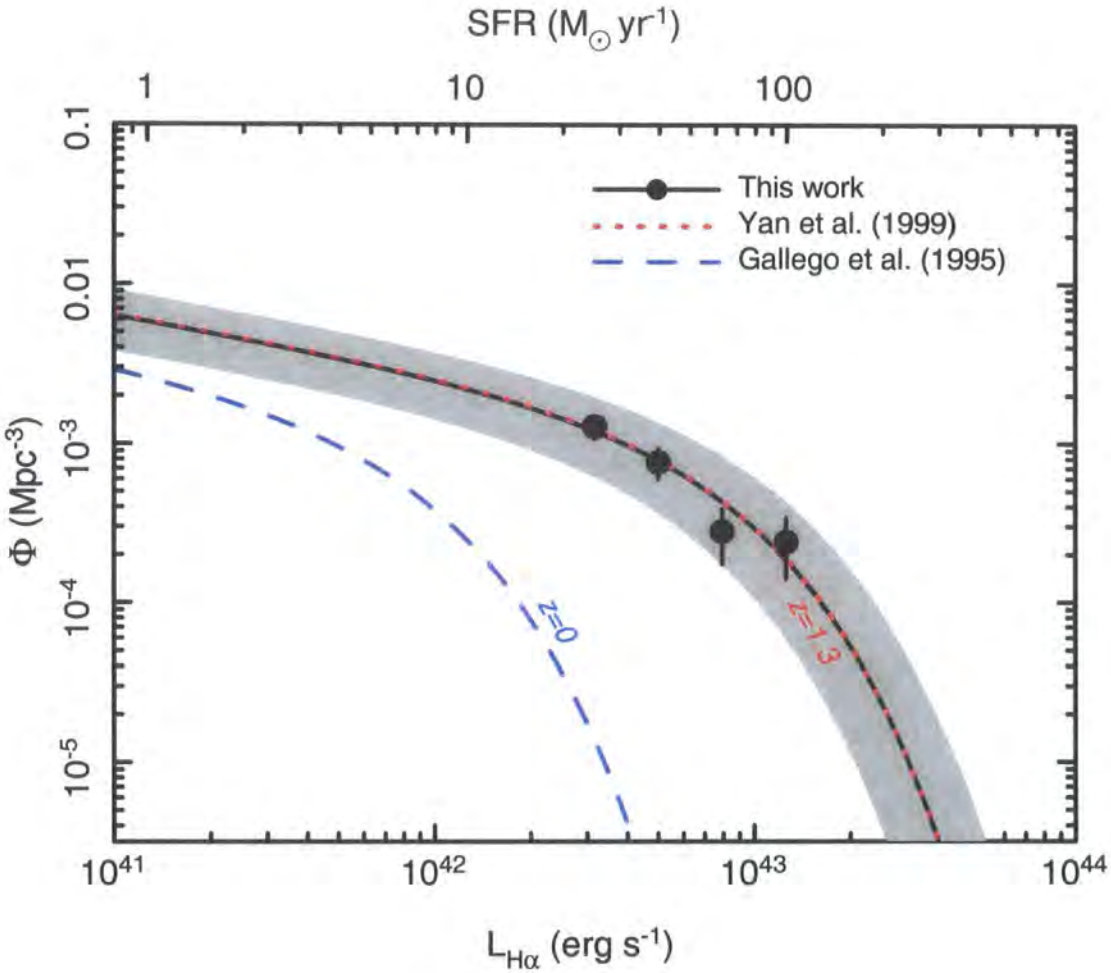

Figure 5.7: Hα luminosity function from this work compared to those derived at $z = 0$ (Gallego et al. 1995) and $z = 1.3$ (Yan et al. 1999). Errors are based on the Poisson counting error and the completeness correction applied to each bin, derived from the detection rate of narrowband selected sources. The luminosity function is fit with a Schechter function with a fixed faint end slope, $\alpha = -1.35$ (identical to Yan et al. 1999 and Gallego et al. 1995) – deeper observations will be required to probe the evolution of the faint end slope of the luminosity function. Our results are very similar to the $z = 1.3$ Hα luminosity function, consistent with little or no evolution between $z = 2.23$ and $z = 1.3$, interpreted in terms of the star formation rate density peaking or plateauing at $z \sim 2$ (see Figure 5.8).

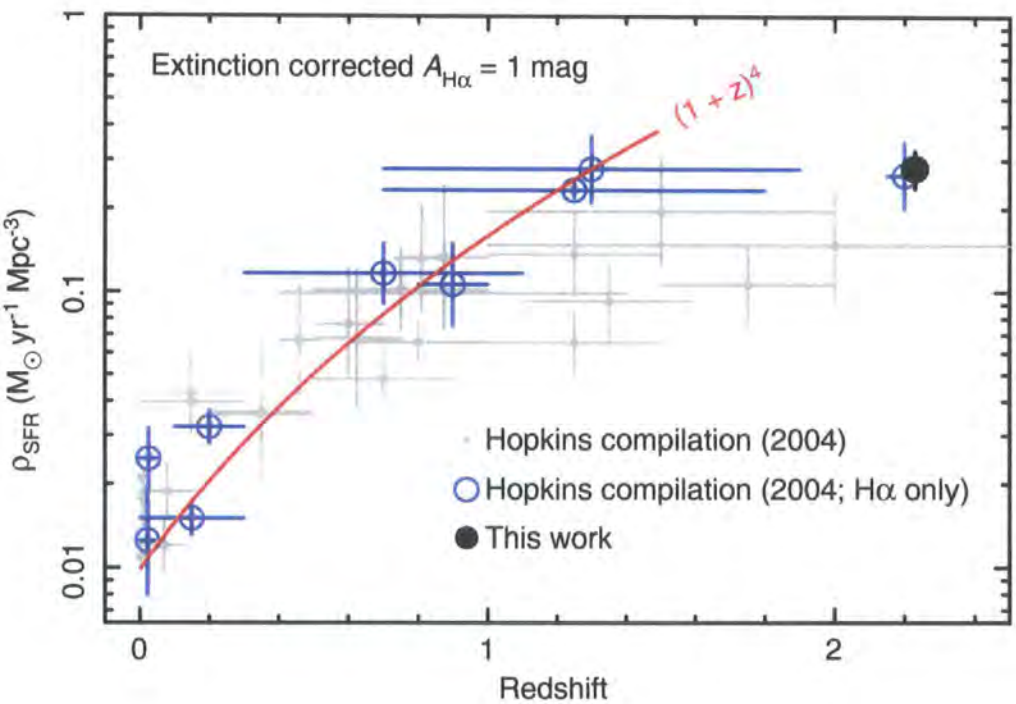

Figure 5.8: The evolution of the extinction corrected star formation rate density out to $z = 2.23$, comparing values derived from multiwavelength tracers, and Hα alone. The data are from the compilation of literature data made by Hopkins et al. (2004), and are corrected for extinction using a common factor $A_{H\alpha} = 1$ mag. The Hα derived values trace the overall trend for strong evolution out to at least $z = 1.3$, proportional to $(1 + z)^4$. Our added point at $z = 2.23$ suggests that the SFRD plateaus between $z = 1.3$ and $z = 2.23$, with little evolution in the LF between these two epochs (see Figure 5.7). Our value is consistent with the value found by Moorwood et al. (2000) at the same redshift, but this is likely coincidental since the Moorwood et al. (2004) sample is significantly contaminated by [O III] emission (Moorwood et al. 2003; Kurk et al. 2004).

5.5. Summary

We have presented results from the largest near-infrared narrowband survey for Hα emission at $z = 2.23$ yet undertaken, probing 220×10^3 co-moving Mpc^3 to a Hα line flux of $10^{-16}\,\mathrm{erg\,s^{-1}\,cm^{-2}}$. Selecting potential $z = 2.23$ Hα emitters on the basis of the significance of their narrowband excess, we detect 55 galaxies over 0.603 square degrees of the COSMOS field. Our main result is the evaluation of the $z = 2.23$ Hα luminosity function, and therefore the global volume averaged star formation rate at this redshift. Our findings can be summarised as follows:

- The luminosity function is well fit by a Schechter function with $\phi^\star = (1.45 \pm 0.47) \times 10^{-3}\,\mathrm{Mpc^{-3}}$, $\log L^\star = 42.83 \pm 0.13\,\mathrm{erg\,s^{-1}}$ with a faint end slope of $\alpha = -1.35$, the same used by Gallego et al. (1995) and Yan et al. (1999) for the Hα LF at $z = 0$ and $z = 1.3$ respectively. The $z = 2.23$ LF is very similar to the $z = 1.3$ distribution of Yan et al. (1999), implying little evolution in the population between these epochs. We note however that deeper observations will be required to probe the faint end of the LF, which could impact on our estimate of the SFRD.

- The extinction corrected SFRD determined from the integrated LF is 0.27 ± 0.02 $M_\odot\,\mathrm{yr^{-1}\,Mpc^{-3}}$ at $z = 2.23$, which supports the view that the SFRD plateaus at $z \gtrsim 1$. This result is the highest redshift evaluation of the Hα derived SFRD, allowing the history of star formation to be traced with this single estimator out to $z = 2.23$.

- The Hα emitters have infrared and radio properties similar to that expected for local star forming galaxies. Our statistical measurement as of the 24μm and 21 cm flux densities are consistent with a LIRG SED at $z = 2.23$. The infrared derived star formation rate agrees with the Hα derived rate if we assume a moderate Hα extinction, $A_{\mathrm{H}\alpha} \sim 0.3$ mags. *HST*-ACS imaging reveals that the Hα emitters have a range of morphologies including compact and disturbed systems. Several comprise of two components separated on scales of $\lesssim 1''$, indicating recent or ongoing merger activity, as might be expected for starburst galaxies.

Chapter 6

Conclusions

In this thesis I have attempted to address questions that stem from a common thread: how does environment affect galaxy evolution, especially in the context of 'hidden' activity, obscured from optical views by dust? I conclude this work with an overview of the main results from the projects I have undertaken, and note some plans for potential follow-on studies in future avenues of research.

6.1. Summary of main results

6.1.1 Galaxy evolution in biased environments

It appears that even in the primordial Universe, environmental influences are shaping the evolution of galaxies. At $z \sim 3$, there is significant 'acceleration' of galaxy evolution in a rich overdensity (by acceleration I refer to an enhanced level of star formation and/or nuclear activity compared to the field at the same epoch). This might not be surprising, since the most massive galaxies (ellipticals) in rich clusters today are already in place by $z \sim 0.5$, and are probably formed at much higher redshift. In order for this to happen, ellipticals' progenitors must assemble their stellar mass rapidly at early times, probably in bursts of star formation. The SA 22 protocluster is the archetypal primitive environment, and will evolve into a rich cluster similar to the most massive structures seen in the local Universe (Baldry et al. 2004; Governato et al. 1998). Unlike local clusters however, SA 22 is host to some remarkable activity – namely a very high concentration of SMGs undergoing starburst and nuclear activity, not to mention an over-density of moderately star forming 'typical' galaxies (i.e. Lyman Breaks and Lyα emitters). The SMGs them-

selves are probably the sites of formation of massive galaxies, and when their starburst episode ends, will likely passively evolve into passive ellipticals. They will naturally end up in the cores of rich clusters, given that they already reside in overdensities at $z \sim 3$. It is clear that feedback mechanisms are important at very high redshifts. The discovery of extended Lyα emission around SMGs in the protocluster, with complex kinematic signatures hinting at superwind outflow, means that these galaxies are dumping large amounts of kinetic energy into the ICM. As yet it is uncertain how significant this heating is in terms of preventing the cooling of baryons, or whether the emission-line haloes are also powered by cooling as well as outflows.

During the build up of clusters, especially at $z \lesssim 1$, star formation should gradually be switched off in spiral galaxies as they are accreted into the cluster potential. This must be true because local clusters are populated by old, passive systems, whereas there is an increasing fraction of star forming galaxies in clusters out to high redshift. The mechanisms for terminating star formation and the processes that convert high redshift spirals into local lenticular S0 galaxies are still poorly understood. One particular issue is the fact that cluster spirals at $z \sim 0.5$ appear to have star formation rates too low to form the massive local S0s, which have large bulge-to-disk ratios. Simple truncation of star formation and disc-fading are not sufficient (at least based on optical star formation surveys). Intensely star forming galaxies in distant clusters have not previously been seen in any great number, but optical spectroscopic surveys have revealed the presence of so-called 'post-starburst' galaxies – that is, galaxies with little or no nebula emission, but strong Balmer absorption in their spectra. Are these really galaxies that have just ceased an episode of intense star formation, or active, obscured starbursts seen near their peak of intensity?

In order to search for obscured starbursts in distant clusters we undertook a 24μm survey of two well studied systems. Our discovery was a population of luminous infrared galaxies with high SFRs ($\gtrsim 30 M_{\odot}\,\mathrm{yr}^{-1}$) potentially capable of transforming into S0s by $z = 0$. More interestingly, we found a large difference in the number of LIRGs in the two clusters: MS 0451−03 is a relaxed cluster with hot ICM but has relatively few LIRGs compared to Cl 0024+16, which is dynamically disturbed and has a much lower X-ray temperature. Although a larger sample of clusters would be required to properly test global cluster properties' impact on the survival of star forming galaxies in the cluster environments. One possible explanation is that the cooler ICM in Cl 0024+16 is less

efficient at stripping interstellar gas from infalling galaxies, and the rate of galaxy-galaxy mergers may be enhanced by interactions within sub-structure within the cluster. These issues will be examined in a future work (Geach et al. in prep).

6.1.2 Galaxy-environment symbiosis

Although we have generally talked about the impact of environment on the properties of galaxies, we must also consider the reciprocal relationship – how do galaxies affect their environment? The main impact an individual galaxy can have on its immediate environment is via feedback mechanisms, which must occur in active galaxies imparting energy into the intergalactic medium. The outcome of this is two-fold: a suppression of star formation in the galaxy itself and heating of the intergalactic medium (e.g. with mechanical energy). In the latter case, this can have profound implications for cluster environments – preventing baryons from cooling and potentially shutting down star formation on a cluster-wide scale. At low redshifts radio galaxies (radio-loud AGN) in massive ellipticals residing in the cores of rich clusters can heat the intracluster gas, often with spectacular cavity inflation and acoustic shock fronts, revealed in detailed X-ray maps (see the review by McNamara & Nulsen 2007). The triggering of nuclear activity appears to be similar to that of star formation (not surprising, given that both require perturbations to their gas reservoirs in order to commence fusion or push material onto a black hole). In Chapter 3 we studied the environments around several radio galaxies at $z \sim 0.5$, selected by their low-power. All these galaxies resided in moderately rich groups, somewhere between poor groups and rich clusters in terms of their L_X–σ and L_X–T_X scaling relationships. The radio galaxies appear to be triggered at the same time as the build-up of the cluster from the merging of sub-cluster units, implying that the activity could be caused by galaxy-galaxy interactions in small, cold bound groups. Yet in the early stages of cluster assembly, group-group mergers can also provide a boost to the temperature of the ICM (via shocks for example), so it is not clear what the dominant event in the thermodynamic history of clusters is, pre-virialisation.

6.1.3 The cosmic star formation history

The major problem with measuring the evolution of the global star formation rate out to high redshift is the confusion brought about by mixing star formation indicators, and their inherent biases and uncertainties. Although all indicators suffer from problems, we

must make a compromise, and choose *one* indicator and apply it over a wide range of cosmic time. We have contributed to this field by measuring the star formation rate density using the Hα line at $z = 2.23$ where the line is redshifted into the K-band. It has been a challenge (until now) to evaluate the Hα luminosity function beyond $z \sim 1$ because large format infrared cameras necessary for efficiently detecting large samples of emission line objects have only just become available. Our pilot study for a scheduled larger 10 square degree narrowband survey is already the largest near-infrared narrowband survey for Hα emission ever undertaken. Our evaluation of the Hα luminosity function reveals that there has been little evolution of the star formation rate between $z \sim 1$ and $z = 2.23$. This is consistent with the result seen in other indicators (which of course exhibit a large amount of scatter) of a plateau in the SFRD at $z \sim 2$. It is still not clear if the SFRD remains constant or declines at earlier times. What our survey provides however, is the ability to trace the global star formation rate from $z = 0$ to $z = 2.23$ with Hα alone.

The fact that the apparent peak of star formation happens at $z \sim 2$ suggests that this is the epoch of galaxy formation. The sharp decline in the rate from $z \sim 1$ to the present day could reflect the build up of clusters of galaxies, which we have seen to eventually suppress star formation in constituent galaxies. One outstanding issue is to segregate the evolution of the global star formation rate as a function of mass; the most massive galaxies are expected to assemble their stars earlier than lower mass systems (downsizing, Cowie et al. 1996). This would be revealed by studying the evolution of the peak of the global star formation rate when binning Hα samples by mass (for example using rest-frame K-band observations, since this can be used to infer stellar mass). The support of the ancillary datasets that arise from multiwavelength surveys will prove essential in this respect.

6.2. Outstanding questions and future research

The projects undertaken in this thesis have produced some interesting results, but they have also raised many questions which could result in further research. I outline three main topics here.

6.2.1 The nature of star formation in rich clusters

Our mid-infrared survey provides a tantalising glimpse of the activity that has previously been overlooked by surveys that do not account for extreme extinction. The panoramic 24μm observations reveal that there is significant cluster-to-cluster scatter, presumably a result of varying global cluster properties. Understanding how clusters' masses, temperatures and dynamic state affect star formation for a complete sample of galaxies (unbiased towards or against the presence of dust) would be of vital importance for disentangling the competing processes that control star formation. Although *Spitzer*'s cryogenic facilities are running out (at the time of writing, the last 'cold' call for proposals has been announced for Cycle 5), the advent of *Herschel* will provide new mid- and far-infrared capabilities in the near future. Obtaining a larger sample of mid-infrared observations of rich clusters at intermediate redshift is essential to build up a representative sample of star forming galaxies in a wide range of environments.

Some questions to be addressed include:

- How does the total level of star formation relate to global cluster properties such as temperature, dynamic state, concentration, etc.?
- Is an enhancement of star formation in rich clusters coupled with an increase in the fraction of active galactic nuclei?
- What are the specific processes that control star formation? Are the most luminous starbursts those that reside in, for example, cold bound groups?
- Are cluster starbursts different to the 'general' blue fraction, or are they just the bright tail of the luminosity function? How are they involved in the build-up of the red-sequence?

6.2.2 The co-eval assembly of stellar mass and growth of supermassive black holes

All local spheroidal galaxies appear to harbour a supermassive black hole with a mass proportional to that of the stellar bulge it resides in (Kormendy & Richstone 1995; Magorrian et al. 1998; Gebhardt et al. 2000). This is taken as good evidence that the assembly of the bulge (via the formation of stars) and the growth of the black hole are related. Black holes can grow from the accretion of matter, and are visible during this phase as AGN.

Since AGN feedback can regulate star formation (and stars can lock away material that might otherwise be accreted onto the black hole), it is perhaps unsurprising that their masses are related.

One question of note that we have already touched upon is the acceleration of activity in rich environments at high redshift. If massive spheroidals have assembled most of their stellar material at high redshift, then do we also observe a peak in black hole growth at the same time? There is some evidence that the SA 22 protocluster (discussed at length in this thesis) contains an excess fraction of AGN, as well as an enhanced star formation rate compared to the field at $z = 3.1$ (Nandra et al. 2005; Laird et al. 2006). In the near future an ultra deep (400 ks) *Chandra* exposure will allow us to perform a sensitive search for AGN in the structure, coupled with an extended Lyman Break search. Comparisons to blank field surveys will reveal whether the protocluster is experiencing an enhancement of nuclear activity at the same time as it is undergoing a significant episode of star formation.

Once again, this will be of vital importance to theoretical models which rely on feedback mechanisms to suppress the bright end of the luminosity function – i.e. the overproduction of bright galaxies.

6.2.3 The properties of high redshift star forming galaxies

We are undertaking an innovative wide field survey for emission line objects at $z = 0.84$, 1.47 and 2.23: the Hi-Z Emission Line Survey (HiZELS). The outcome of this survey will be large samples (1000s at each redshift) of identically selected 'typical' star forming galaxies within well defined volumes. The large area will enable us to place even stronger constraints on the star formation history over this crucial epoch by sampling 1000s of identically selected star forming galaxies in each redshift slice. Our custom-made J and H-band filters at 1.204μm and 1.618μm respectively will not only detect Hα emission at $z = 0.84$ and $z = 1.47$, but [O II]λ3727 and [O III]λ5007 at $z = 2.23$, exactly the same redshift as the current 2.121μm survey. This will be a useful test for confirming the redshifts of a subset $z = 2.23$ Hα emitters by matching to detections in these other narrowband filters. It will also allow us to distinguish potential AGN, for sources with large [O III]/Hα ratios (we need to remove these when we assess the luminosity function if we are to measure the 'clean' star formation rate).

The large area surveyed will enable us for the first time to track the evolution of star

formation as a function of environment over the peak of the SFRD. By parameterising Hα luminosity in terms of, for example, local density, we will provide a measure of how star formation is modified in rich environments. We expect star formation to be suppressed in dense regions (Lewis et al. 2002; Gomez et al. 2003; Bower & Balogh 2003), but how does this evolve with cosmic time? If the decline in the volume averaged star formation rate since $z \sim 1$ is due to the assembly of galaxies into group and cluster structures, we might be able to track this with an environmental/star formation analysis. We will also measure the evolution of the correlation length of Hα emitters via the two-point correlation function – this is a powerful test of contemporary theoretical models of galaxy formation (e.g. Bower et al. 2006; Baugh et al. 2005; Benson et al. 2000). This is only feasible with the large areas probed by the HiZELS project. The pilot study presented in Chapter 5 has revealed that there is a trade-off between depth and area coverage: ideally we would like to probe to fainter Hα luminosities in order to measure the faint end slope of the luminosity function, however this is not feasible over a large area. Therefore we will observe only a proportion of the survey area to a deeper Hα flux limit in order to improve constraints on the LF (and therefore SFRD estimate).

One of our main goals is to measure the luminosity function of star forming galaxies over the expected peak of the cosmic star formation rate, however the data will be valuable for other tests, a few of which are:

- We aim to perform the first clustering analysis of Hα emitters, including the evolution of the correlation length over the peak of star formation in the Universe. The Hα emitters detected at each epoch represent normal galaxies, and so should give a representative view of the evolution of unbiased samples. Importantly, these will be useful tests for theoretical models that predict halo occupancy and satellite populations.

- Three near-infrared narrowband filters in J, H and K will detect three emission lines at $z = 2.23$: [OII]λ3727, [OIII]λ5007 and Hα. Not only does this filter matching make the redshift selection much more robust (i.e. by detecting lines in all three filters), but will enable the detection of AGN (strong [O III]/Hα emitters), and star forming galaxies that have weaker Hα, but relatively strong in [O II]λ3727 – this should provide us with a sample of low-luminosity, low-metallicity galaxies which will be useful to track star formation over a wide dynamic range. How do these high redshift systems differ to local $z = 0$ ones (e.g. selected from the Sloan Digital

Sky Survey)?

- The J-band filter is sensitive to Lyα emission at $z = 8.90 - 500$ Myrs after the Big Bang. Although this is highly speculative, our wide area means that we could potentially detect 1–10s of these *very* distant galaxies, based on theoretical predictions for the escape fraction of Lyα photons (e.g. Le Delliou et al. 2005). This would be an unprecedented result, allowing us to measure the star formation rate of the Universe at a time when the first stars are thought to have formed.

Spectroscopic followup of a representative sample of Hα emitters (and possible contaminant populations) is crucial to allow for accurate correction of the luminosity function. Near-infrared spectroscopic (VLT-ISAAC and Gemini-NIRI) observations of a sample of candidate emitters in both COSMOS and the UKIDSS-UDS fields are scheduled for the coming semester, and data is starting to arrive at the time of writing. These observations will be published in a forthcoming work to present confirmation of the redshift selection, and improve narrowband flux calibrations for the current sample. In the future we aim to use the FMOS multi-object spectrograph on Subaru to efficiently obtain spectra of a large number (100s) of narrowband selected emission-line objects over wide (30′) fields of view.

HiZELS will be completed over the next 5 years using the WFCAM near-infrared camera on UKIRT.

6.3. Final remarks

Our interpretation and understanding of the Universe is significantly biased according to how we observe it. The fantastic advances in instrumentation (the development of extra-terrestrial observing platforms, sophisticated cameras and detectors, larger collecting dishes, etc.) enable us to make the most out of the small amounts of energy that we are able to capture. Looking to the future of the field, we can only be excited at upcoming projects designed to improve our understanding of how the Cosmos works: *James Webb Space Telescope (JWST)*; Atacama Large Millimetre Array (ALMA); Square Kilometer Array (SKA); Low Frequency Array (LOFAR); *Herschel* and *Planck* to name but a few, and not mentioning the development of new instruments to be stationed on existing telescopes.

What we have learnt is that we must build up an unbiased view of activity – obtaining a *complete* census of star formation since the first stars is the only way we will truly

understand galaxy formation and evolution. In this thesis I hope to have contributed to the field by making use of state-of-the-art facilities in order to address just a small issue in the overall standard model of galaxy evolution. These are just small steps, but ones which I hope will be of use to the community as we continue our struggle to decipher the nature of our Universe.

J. E. Geach

Bibliography

Adelberger, K. L., Steidel, C. C., Shapley, A. E., Hunt, M. P., Erb, D. K., Reddy, N. A., Pettini, M., 2004, ApJ, 607, 226

Afonso, J., Cram, L., Mobasher, B., 2000, ApJ, 536, 68

Allen, S. W & Fabian, A., 1998, MNRAS, 297, L57

Allington-Smith, J., Breare, M., Ellis, R., Gellatly, D., Glazebrook, K., Jorden, P., Maclean, J., Oates, P., Shaw, G., Tanvir, N., Taylor, K., Taylor, P., Webster, J., Worswick, S., 1994, PASP, 106, 983

Alexander, D. M., Chartas, G., Bauer, F. E., Brandt, W. N., Simpson, C. Vignali, C. 2005a, MNRAS, 357, L16

Alexander, D. M., Smail, I., Bauer, F. E., Chapman, S. C., Blain, A. W., Brandt, W. N., Ivison, R. J., 2005b, Nature, 434, 738

Alexander, D. M., Bauer, F. E., Chapman, S. C., Smail, I., Blain, A. W., Brandt, W. N., Ivison, R. J., 2005c, ApJ, 632, 736

Alonso-Herrero, A., Pérez-González, P. G., Alexander, D. M., Rieke, G. H., Rigopoulou, D., Le Floc'h, E., Barmby, P., Papovich, C., Rigby, J. R., Bauer, F. E., Brandt, W. N., Egami, E., Willner, S. P., Dole, H., Huang, J.-S., 2006, ApJ, 640, 167

Andersen, A. C., 2007, ArXiv Astrophysics e-prints, astro-ph/0702618

Aragón-Salamanca, A., Alonso-Herrero, A., Gallego, J., García-Dabó, C. E., Pérez-González, P. G., Zamorano, J., Gil de Paz, A., 2003, Star Formation Rate Estimators: [OII]3727 vs Hα for Local Star-forming Galaxies, Star Formation Through Time, Astronomical Society of the Pacific Conference Series, Eds.: Perez, E., Gonzalez Delgado, R. M., Tenorio-Tagle, G., 297, 191

Archibald, E. N., Dunlop, J. S., Hughes, D. H., Rawlings, S., Eales, S. A., Ivison, R. J. 2001, MNRAS, 323, 417

Arnaud, M. & Evrard, A. E., 1999, MNRAS, 305, 631

Ashby, M. L. N., Dye, S., Huang, J.-S., Eales, S., Willner, S. P., Webb, T. M. A., Barmby, P., Rigopoulou, D., Egami, E., McCracken, H., Lilly, S., Miyazaki, S., Brodwin, M., Blaylock, M., Cadien, J., Fazio, G. G., 2006, ApJ, 644, 778

Avni, Y., Soltan, A., Tananbaum, H., Zamorani, G., 1980, ApJ, 238, 800

Baldry, I. K., Balogh, M. L., Bower, R., Glazebrook, K., Nichol, R. C., 2004, Color bimodality: Implications for galaxy evolution, The New Cosmology: Conference on Strings, Cosmology, Eds.: Allen, R. E., Nanopoulos, D. V., Pope, C. N., 743, 106

Balogh, M. L., Morris, S. L., Yee, H. K.. C., Carlberg, R. G., Ellingson, E. , 1999, ApJ, 527, 54

Barger, A. J., Cowie, L. L., Sanders, D. B. 1999, ApJ, 518, L5

Baugh, C. M., Lacey, C. G., Frenk, C. S., Granato, G. L., Silva, L., Bressan, A., Benson, A. J., Cole, S., 2005, MNRAS, 356, 1191

Basu-Zych, A., Scharf, C, 2004, ApJ, 615, L85

Beckwith, S. V. W., Thompson, D., Mannucci, F., Djorgovski, S. G., 1998, ApJ, 504, 107

Beers, T., Flynn, K., & Gebhardt K., 1990, AJ, 100, 32

Bekki, K., 1998, A&A, 334, 814

Bell, E. F., Baugh, C. M., Cole, S., Frenk, C. S., Lacey, C. G., 2001, ASP Conf. Series: Galaxy Disks, Disk Galaxies, Eds: Funes, S. J. & Corsini, E. M., 649

Bell, E. F. , Baugh, C. M., Cole, S., Frenk, C.S., Lacey, C.G., 2003, MNRAS, 343, 367

Bell, E. F., Papovic, C., Wolf, C., Le Floc'h, E., Caldwell, J. A. R., Barden, M., Egami, E., McIntosh, D. H., Meisenheimer, K., Perez-Gonzalez, P. G. P., Rieke, G. H., Rieke, M. J., Rigby, J. R., Rix, H.-W., 2005, ApJ

Bell, E. F., Naab, T., McIntosh, D. H., Somerville, R. S., Caldwell, J. A. R., Barden, M., Wolf, C., Rix, H.-W., Beckwith, S. V., Borch, A., Häussler, B., Heymans, C., Jahnke,

K., Jogee, S., Koposov, S., Meisenheimer, K., Peng, C. Y., Sanchez, S. F., Wisotzki, L., 2006, ApJ, 640, 241

Benson, A. J., Baugh, C. M., Cole, S., Frenk, C. S., Lacey, C. G., 2000, MNRAS, 316, 107

Bertin, E., Arnouts, S., 1996, A&AS, 117, 393

Best, P. N., 2000, MNRAS, 317, 720

Best, P., von der Linden, A., Kauffmann, G., Heckman, T. M., Kaiser, C. R., 2006, MNRAS, 368, L67

Biviano, A., Metcalfe, L., McBreen, B., Altieri, B., Coia, D., Kessler, M. F., Kneib, J.-P., Leech, K., Okumura, K., Ott, S., Perez-Martinez, R., Sanchez-Fernandez, C., Schulz, B., 2004, A&A, 425, 33

Blain, A. W., Bernard & Chapman, S. C., 2003, MNRAS, 338, 733

Bolzonella, M, Miralles, J.-M., Pello, R., 2000, A&A, 363, 476

Borys, C., Chapman, S., Halpern, M., Scott, D. 2003, MNRAS, 344, 385

Borys, C., Smail, I., Chapman, S. C., Blain, A. W., Alexander, D. M., Ivison, R. J., 2005, AJ, 635, 853

Boselli, A., Lequeux, J., Gavazzi, G., 2004, A&A, 428, 409

Bower, R. G., Morris, S., L., Bacon, R., Wilman, R. J., Sullivan, M., Chapman, S., Davies, R. L., de Zeeuw, P. T., Emsellem, E., 2004, MNRAS, 351, 63

Bower, R. G., Benson, A. J., Malbon, R., Helly, J. C., Frenk, C. S., Baugh, C. M., Cole, S., Lacey, C. G., 2006, MNRAS, 370, 645

Boyle, B. J., Terlevich, R. J., 1998, MNRAS, 293 L49

Boyle, B. J., Shanks, T., Croom, S. M., Smith, R. J., Miller, L., Loaring, N., Heymans, C., 2000, MNRAS317, 1014

Boyle, B. J., Cornwell, T. J., Middelberg, E., Norris, R. P., Appleton, P. N., Smail, I., 2007, MNRAS, 376, 1182

Bruzual, G., Charlot, S., 1993, ApJ, 405, 538

Bunker, A. J., Warren, S. J., Hewett, P. C., Clements, D. L., 1995, MNRAS, 273, 513

Butcher, H., Oemler, Jr., A., 1978, ApJ, 226, 559

Bruzual A., G., Charlot, S., 1993, ApJ, 405, 538

Calzetti, D., Armus, L., Bohlin, R. C., Kinney, A. L., Koorneef, J., Storchi-Bergmann, T., 2000, ApJ, 533, 682

Capak, P., Aussel, H., Ajiki, M., McCracken, H. J., Mobasher, B., Scoville, N., Shopbell, P., Taniguchi, Y., Thompson, D., Tribiano, S., Sasaki, S., Blain, A. W., Brusa, M., Carilli, C., Comastri, A., Carollo, C. M., Cassata, P., Colbert, J., Ellis, R. S., Elvis, M., Giavalisco, M., Green, W., Guzzo, L., Hasinger, G., Ilbert, O., Impey, C., Jahnke, K., Kartaltepe, J., Kneib, J.-P., Koda, J., Koekemoer, A., Komiyama, Y., Leauthaud, A., Lefevre, O., Lilly, S., Liu, C., Massey, R., Miyazaki, S., Murayama, T., Nagao, T., Peacock, J. A., Pickles, A., Porciani, C., Renzini, A., Rhodes, J., Rich, M., Salvato, M., Sanders, D. B., Scarlata, C., Schiminovich, D., Schinnerer, E., Scodeggio, M., Sheth, K., Shioya, Y., Tasca, L. A. M., Taylor, J. E., Yan, L., Zamorani, G., 2007, ApJS, 172, 99

Casali, M., Adamson, A., Alves de Oliveira, C., Almaini, O., Burch, K., Chuter, T., Elliot, J., Folger, M., Foucaud, S., Hambly, N., Hastie, M., Henry, D., Hirst, P., Irwin, M., Ives, D., Lawrence, A., Laidlaw, K., Lee, D., Lewis, J., Lunney, D., McLay, S., Montgomery, D., Pickup, A., Read, M., Rees, N., Robson, I., Sekiguchi, K., Vick, A., Warren, S., Woodward, B., 2007, A&A, 467, 777

Cash, W., 1979, ApJ, 228, 939

Chapman, S. C., Lewis, G. F., Scott, D., Richards, E., Borys, C., Steidel, C. C., Adelberger, K. L., Shapley, A. E. 2001, ApJ, 548, L17

Chapman, S. C., Barger, A. J., Cowie, L. L., Scott, D., Borys, C., Capak, P., Fomalont, E. B., Lewis, G. F., Richards, E. A., Steffen, A. T., Wilson, G., Yun, M. 2003, ApJ, 585, 57

Chapman, S. C., Scott, D., Windhorst, R. A., Frayer, D. T., Borys, C., Lewis, G. F., Ivison, R. J. 2004, ApJ, 606, 85

Chapman, S. C., Blain, A. W., Smail, I., Ivison, R. J. 2005, ApJ, 622, 772

Chary, R., & Elbaz, D., 2001, ApJ, 556, 562

Chary, R. Casertano, S., Dickinson, M. E., Ferguson, H. C., Eisenhardt, P. R. M., Elbaz, D., Grogin, N. A., Moustakas, L. A., Reach, W. T., Yan, H., 2004, ApJS, 154, 80

Chevalier, R. A. Clegg, A. W. 1985, Nature, 317, 44

Coia, D., Metcalfe, L., McBreen, B., Biviano, A., Smail, I., Altieri, B., Kneib, J. -., McBreen, S., Sanchez-Fernandez, C. , O'Halloran, B., 2005, A&A, 430, 59

Coia, D. , McBreen, B. , Metcalfe, L. , Biviano, A. , Altieri, B. , Mellier, Y. , Ott, S. , Kneib, J. P. , O'Halloran, B., 2004, Baltic Astronomy, 13, 638

Cole, S., Norberg, P., Baugh, C. M., Frenk, C. S., Bland-Hawthorn, J., Bridges, T., Cannon, R., Colless, M., Collins, C., Couch, W., Cross, N., Dalton, G., De Propris, R., Driver, S. P., Efstathiou, G., Ellis, R. S., Glazebrook, K., Jackson, C., Lahav, O., Lewis, I., Lumsden, S., Maddox, S., Madgwick, D., Peacock, J. A., Peterson, B. A., Sutherland, W., Taylor, K., 2001, MNRAS, 326, 255

Condon, J. J., Cotton, W. D., Broderick, J. J., 2002, AJ, 124, 675

Couch, W. J., Barger, A. J., Smail, I., Ellis, R. S., Sharples, R. M., 1998, ApJ, 497, 118

Cowie, L. L., Songaila, A., 1977, Nature, 266, 501

Cowie, L. L., Songaila, A., Hu, E. M., Cohen, J. G., 1996, AJ, 112, 839

Cowie, L. L., Barger, A. J., Fomalont, E. B., Capak, P., 2004, ApJ, 603, L69

Cox, A. N., Allen's astrophysical quantities, 4th ed. Publisher: New York: AIP Press; Springer, 2000. Edited by Arthur N. Cox. ISBN: 0387987460

Croft, R. A. C., Dalton G. B., Efstathiou G., 1999, MNRAS, 305, 547

Croton, D. J., Farrar, G. R., Norberg, P., Colless, M., Peacock, J. A., Baldry, I. K., Baugh, C. M., Bland-Hawthorn, J., Bridges, T., Cannon, R., Cole, S., Collins, C., Couch, W., Dalton, G., De Propris, R., Driver, S. P., Efstathiou, G., Ellis, R. S., Frenk, C. S., Glazebrook, K., Jackson, C., Lahav, O., Lewis, I., Lumsden, S., Maddox, S., Madgwick, D., Peterson, B. A., Sutherland, W., Taylor, K., 2005, MNRAS, 356, 1155

Croton, D. J., Springel, V., White, S. D. M., De Lucia, G., Frenk, C. S., Gao, L., Jenkins, A., Kauffmann, G., Navarro, J. F., Yoshida, N., 2006, MNRAS, 636, 11

Crowl, H. H., Kenney, J. D. P., van Gorkom, J. H., Vollmer, B., 2005, AJ, 130, 65

Cruz, M. J., Jarvis, M. J., Rawlings, S., Blundell, K. M., 2007, MNRAS, 375, 1349

Cutri, R. M., Skrutskie, M. F., van Dyk, S., Beichman, C. A., Carpenter, J. M., Chester, T., Cambresy, L., Evans, T., Fowler, J., Gizis, J., Howard, E., Huchra, J., Jarrett, T., Kopan, E. L., Kirkpatrick, J. D., Light, R. M., Marsh, K. A., McCallon, H., Schneider, S., Stiening, R., Sykes, M., Weinberg, M., Wheaton, W. A., Wheelock, S., Zacarias, N., 2003, 2MASS All Sky Catalog of point sources, The IRSA 2MASS All-Sky Point Source Catalog, NASA/IPAC Infrared Science Archive. `http://irsa.ipac.caltech.edu/applications/Gator/`

Czoske, O., Kneib, J.-P., Soucail, G., Bridges, T.J., Mellier, Y., Cuillandre, J,-C., 2001, A&A, 372, 391

Daddi, E., Cimatti, A., Renzini, A., Fontana, A., Mignoli, M., Pozzetti, L., Tozzi, P., Zamorani, G., 2004, ApJ, 617, 746

Dale, D. A., 2001, ApSSS, 277, 63

Dale, D. A., Helou, G., 2002, ApJ, 576, 159

David, L. P., Jones, C., Forman, W. 1995, Bulletin of the American Astronomical Society, 27, 1444

de Breuck, C., van Breugel, W., Minniti, D.; Miley, G., Rottgering, H., Stanford, S. A., Carilli, C. 1999 A&A 352, L51

de Ruitter, H.R., Arp, H.C., Willis, A.C., 1977, ApJ, 28, 211

Dey, A., van Breugel, W., Vacca, W. D., Antonucci, R. 1997, ApJ, 490, 698

Dey, A., Bian, C., Soifer, B. T., Brand, K., Brown, M. J. I., Chaffee, F. H., LeFloc'h, E., Hill, G., Houck, J. R., Jannuzi, B. T., Rieke, M., Weedman, D., Brodwin, M., Eisenhardt, P. 2005, ArXiv Astrophysics e-prints: astro-ph/0503632

Dickey, J. M., Lockman, F. J., 1990, ARA&A, 28, 215

Dopita, M. A., Pereira, M., Kewley, L. J., Capaccioli, M., 2002, ApJS, 143, 47

Draine, B. T., Lee, H. M., 1984, ApJ, 285, 89

Draine, B. T., 2003, ARA&A, 41, 241

Draine, B. T., Dale, D. A., Bendo, G., Gordon, K. D., Smith, J. D. T., Armus, L., Engelbracht, C. W., Helou, G., Kennicutt, Jr., R. C., Li, A., Roussel, H., Walter, F., Calzetti, D., Moustakas, J., Murphy, E. J., Rieke, G. H., Bot, C., Hollenbach, D. J., Sheth, K., Teplitz, H. I., 2007, ApJ, 663, 866

Dressler, A., 1980, ApJS, 42, 565

Dressler, A., Gunn, J. E., 1983, ApJ, 270, 7

Dressler, A., Oemler, A. J., Couch, W. J., Smail, I., Ellis, R. S., Barger, A., Butcher, H., Poggianti, B. M., Sharples, R. M., 1997, ApJ, 490, 577-+

Duc, P.-A., Brinks, E., Springel, V., Pichardo, B., Weilbacher, P., Mirabel, I. F., 2000, AJ, 120, 1238

Duc, P.-A., Poggianti, B., Fadda, D., Elbaz, D., Flores, H., Chanial, P., Franceschini, A., Moorwood, A., Cesarsky, C., 2002, A&A, 382, 60

Duc, P.-A., Fadda, D., Poggianti, B., Elbaz, D., Biviano, A., Flores, H., Moorwood, A., Franceschini, A., Cesarsky, C., 2004, IAU Colloq. 195: Outskirts of Galaxy Clusters: Intense Life in the Suburbs, Luminous infrared starbursts in a cluster of galaxies

Dunlop, J. S., Hughes, D. H., Rawlings, S., Eales, S. A., Ward, M. J. 1994, Nature, 370, 347

Dye, S., Warren, S. J., Hambly, N. C., Cross, N. J. G., Hodgkin, S. T., Irwin, M. J., Lawrence, A., Adamson, A. J., Almaini, O., Edge, A. C., Hirst, P., Jameson, R. F., Lucas, P. W., van Breukelen, C., Bryant, J., Casali, M., Collins, R. S., Dalton, G. B., Davies, J. I., Davis, C. J., Emerson, J. P., Evans, D. W., Foucaud, S., Gonzales-Solares, E. A., Hewett, P. C., Kendall, T. R., Kerr, T. H., Leggett, S. K., Lodieu, N., Loveday, J., Lewis, J. R., Mann, R. G., McMahon, R. G., Mortlock, D. J., Nakajima, Y., Pinfield, D. J., Rawlings, M. G., Read, M. A., Riello, M., Sekiguchi, K., Smith, A. J., Sutorius, E. T. W., Varricatt, W., Walton, N. A., Weatherley, S. J., 2006, MNRAS, 372, 1227

Edge, A. C., Stewart, C. G., 1991, MNRAS, 252, 414

Ellingson, E., Yee, H. K. C., Green, R. F., 1991, ApJ, 371, 49

Ettori, S., De Grande, S., Molendi, S., 2002, A&A, 391, 841

Erb, D. K., Steidel, C. C., Shapley, A. E., Pettini, M., Reddy, N. A., Adelberger, K. L., 2006, ApJ, 646, 107

Evrard, A. E., 1991, MNRAS, 248, 8

Fadda, D., Elbaz, D., Duc, P.-A., Flores, H., Franceschini, A., Cesarsky, C. J., Moorwood, A. F. M., 2000, A&A, 361, 827

Fanaroff, B. L. & Riley, J. M., 1974, MNRAS, 167, 31

Fardal, M. A., Katz, N., Gardner, J. P., Hernquist, L., Weinberg, D. H., Davé, R. 2001, ApJ, 562, 605

Farrah, D., Geach, J., Fox, M., Serjeant, S., Oliver, S., Verma, A., Kaviani, A., Rowan-Robinson, M., 2004, MNRAS, 349, 518

Farrah, D., Bernard-Salas, J., Spoon, H. W. W., Soifer, B. T., Armus, L., Brandl, B., Charmandaris, V., Desai, V., Higdon, S., Devost, D., Houck, J., 2007, ArXiv e-prints, astro-ph/0706.0513

Fasano, G., Poggianti, B. M., Couch, W. J., Bettoni, D., Kjærgaard, P., Moles, M., 2000, ApJ, 542, 673

Flores, H., Hammer, F., Elbaz, D., Cesarsky, C. J., Liang, Y. C., Fadda, D., Gruel, N., 2004, A&A, 415, 885

Franceshini, A., Berta, S., Rigopoulou, D., Aussel, H., Cesarsky, C. J., Elbaz, D., Genzel, R., Moy, E., Oliver, S., Rowan-Robinson, M., Van der Werf, P. P., 2003, A&A, 403, 501

Francis, P. J., Williger, G. M., Collins, N. R., Palunas, P., Malumuth, E. M., Woodgate, B. E., Teplitz, H. I., Smette, A., Sutherland, R. S., Danks, A. C., Hill, R. S., Lindler, D., Kimble, R. A., Heap, S. R., Hutchings, J. B. 2001, ApJ, 554, 1001

Fujita, Y., 1998, Environmental Effects on the Star Formation Rate of Disk Galaxies, Abstracts of the 19th Texas Symposium on Relativistic Astrophysics, Cosmology. Eds.: Paul, J., Montmerle, T., Aubourg, E.

Fujita, S. S., Ajiki, M., Shioya, Y., Nagao, T., Murayama, T., Taniguchi, Y., Umeda, K., Yamada, S., Yagi, M., Okamura, S., Komiyama, Y., 2003, ApJ, 586, L115

Gallego, J., Zamorano, J., Aragon-Salamanca, A., Rego, M., 1995, ApJ, 455, L1

Geach, J. E., Matsuda, Y., Smail, I., Chapman, S. C., Yamada, T., Ivison, R. J., Hayashino, T., Ohta, K., Shioya, Y., Taniguchi, Y., 2005, MNRAS, 363, 1398

Gebhardt, K., Bender, R., Bower, G., Dressler, A., Faber, S. M., Filippenko, A. V., Green, R., Grillmair, C., Ho, L. C., Kormendy, J., Lauer, T. R., Magorrian, J., Pinkney, J., Richstone, D., Tremaine, S., 2000, ApJ, 539, L13

Gerken, B., Ziegler, B., Balogh, M., Gilbank, D., Fritz, A., Jager, K., 2004, A&A, 421, 59

Genzel, R., Lutz, D., Sturm, E., Egami, E., Kunze, D., Moorwood, A. F. M., Rigopoulou, D., Spoon, H. W. W., Sternberg, A., Tacconi-Garman, L. E., Tacconi, L., Thatte, N., 1998, ApJ, 498, 579

Gibson, B. K., Loewenstein, M., Mushotzky, R. F. 1997, MNRAS, 290, 623

Glazebrook, K., Blake, C., Economou, F., Lilly, S., Colless, M., 1999, MNRAS, 306, 843

Gómez, P. L., Nichol, R. C., Miller, C. J., Balogh, M. L., Goto, T., Zabludoff, A. I., Romer, A. K., Bernardi, M., Sheth, R., Hopkins, A. M., Castander, F. J., Connolly, A. J., Schneider, D. P., Brinkmann, J., Lamb, D. Q., SubbaRao, M., York, D. G., 2003, ApJ, 584, 210

Governato, F., Baugh, C. M., Frenk, C. S., Cole, S., Lacey, C. G., Quinn, T., Stadel, J., 1998, Nature, 392, 359

Gunn, J. E., Gott, J. R. I., 1972, ApJ, 176, 1

Hayashino, T., Matsuda, Y., Tamura, H., Yamauchi, R., Yamada, T., Ajiki, M., Fujita, S. S., Murayama, T., Nagao, T., Ohta, K., Okamura, S., Ouchi, M., Shimasaku, K., Shioya, Y., Taniguchi, Y. 2004, AJ, 128, 2073

Haynes, M. P., Giovanelli, R., Chincarini, G. L., 1984, ARA&A, 22, 445

Heckman, T. M., Armus, L., Miley, G. K. 1990, ApJS, 74, 833

Heckman, T. M. 2002, in Astronomical Society of the Pacific Conference Series, 292

Helsdon, S. F., Ponman, T. J., 2000, MNRAS, 319, 933

Hill, G. J., & Lilly S. J., 1991, ApJ, 367, 1

Hogg, D. W., 2001, AJ, 121, 1207

Hopkins, A. M., Connolly, A. J., Haarsma, D. B., Cram, L. E., 2001, AJ, 122, 288

Hopkins, A. M., 2004, ApJ, 615, 209

Hoppe, P., Zinner, E., 2000, J. Geophys. Res.105, 10371

Hubble, E. P., 1926, ApJ, 64, 321

Huang, J.-H., Deng, Z.-G., Fu, Y.-N., 2003, ArXiv Astrophysics e-prints, astro-ph/0303318

Icke, V., 1985, A&A, 144, 115

Ivison, R. J., Dunlop, J. S., Hughes, D. H., Archibald, E. N., Stevens, J. A., Holland, W. S., Robson, E. I., Eales, S. A., Rawlings, S., Dey, A., Gear, W. K. 1998, ApJ, 494, 211

Ivison, R. J., Dunlop, J. S., Smail, I., Dey, A., Liu, M. C., Graham, J. R. 2000, ApJ, 542, 27

Ivison, R. J., Greve, T. R., Smail, I., Dunlop, J. S., Roche, N. D., Scott, S. E., Page, M. J., Stevens, J. A., Almaini, O., Blain, A. W., Willott, C. J., Fox, M. J., Gilbank, D. G., Serjeant, S., Hughes, D. H. 2002, MNRAS, 337, 1

Ivison, R. J., Greve, T. R., Dunlop, J. S., Peacock, J. A., Egami, E., Smail, I., Ibar, E., van Kampen, E., Aretxaga, I., Babbedge, T., Biggs, A. D., Blain, A. W., Chapman, S. C., Clements, D. L., Coppin, K., Farrah, D., Halpern, M., Hughes, D. H., Jarvis, M. J., Jenness, T., Jones, J. R., Mortier, A. M. J., Oliver, S., Papovich, C., Pérez-González, P. G., Pope, A., Rawlings, S., Rieke, G. H., Rowan-Robinson, M., Savage, R. S., Scott, D., Seigar, M., Serjeant, S., Simpson, C., Stevens, J. A., Vaccari, M., Wagg, J., Willott, C. J., 2007, MNRAS, 380, 199

Jansen, R. A., Franx, M., Fabricant, D., 2001, ApJ, 551, 825

Jenness, T. Lightfoot, J. F. 1998, in Astronomical Society of the Pacific Conference Series, 216

Jetha, N. N., Hardcastle, M. J. & Sakelliou, I., 2006, MNRAS, 368, 609

John, T. L., 1988, A&A, 193, 189

Kaiser, N., 1986, MNRAS, 222, 323

Keel, W. C., Cohen, S. H., Windhorst, R. A., Waddington, I., 1999, AJ, 118,2547

Kelson, D. D., Illingworth, G. D., van Dokkum, P. G., Franx, M., 2000, ApJ, 531, 159

Kelson, D. D. 2003, PASP, 115, 808

Kennicutt, Jr., R. C., Kent, S. M., 1983, AJ, 88, 1094

Kennicutt, Jr., R. C., 1992, ApJ, 388, 310

Kennicutt, R. C., Tamblyn, P., Congdon, C. E., 1994, ApJ, 435, 22

Kennicutt, R. C., 1998, ARA&A, 36, 189

King, C.R., Ellis, R.S., 1985, ApJ, 288, 456

King, L. J., Schneider, P., Springel, V., 2001, A&A, 378, 748

Kneib, J.-P., Hudelot, P., Ellis, R.S., Treu, T., Smith, G.P., Marshall, P., Czoske, O., Smail, I., Natarajan, P., 2003, ApJ, 598, 804

Kodama, T., Smail, I., 2001, MNRAS, 326, 637

Kodama, T. & Bower, R. G., 2001, MNRAS, 321, 18

Kodama, T., Yamada, T., Akiyama, M., Aoki, K., Doi, M., Furusawa, H., Fuse, T., Imanishi, M., Ishida, C., Iye, M., Kajisawa, M., Karoji, H., Kobayashi, N., Komiyama, Y., Kosugi, G., Maeda, Y., Miyazaki, S., Mizumoto, Y., Morokuma, T., Nakata, F., Noumaru, J., Ogasawara, R., Ouchi, M., Sasaki, T., Sekiguchi, K., Shimasaku, K., Simpson, C., Takata, T., Tanaka, I., Ueda, Y., Yasuda, N., Yoshida, M., 2004, MNRAS, 350, 1005

Kodama, T., Balogh, M., Smail, I., Bower, R.G., Nakata, F., 2004, MNRAS, 354, 1103

Kodama, T., Tanaka, M., Tamura, T., Yahagi, H., Nagashima, M., Tanaka, I., Arimoto, N., Futamase, T., Iye, M., Karasawa, Y., Kashikawa, N., Kawasaki, W., Kitayama, T., Matsuhara, H., Nakata, F., Ohashi, T., Ohta, K., Okamoto, T., Okamura, S., Shimasaku, K., Suto, Y., Tamura, N., Umetsu, K., Yamada, T., , 2005, PASJ, 57, 309

Kormendy, J. & Richstone, D., 1995, ARA&A, 33, 581

Krabbe, A., Böker, T. & Maiolino, R., 2002, ASP Conf. Ser. 258: Issues in Unification of Active Galactic Nuclei, 33

Kurk, J. D., Rottgering, H. J. A., Pentericci, L., Miley, G. K., van Breugel, W., Carilli, C. L., Ford, H., Heckman, T., McCarthy, P., Moorwood, A. 2000 A&A 358 L1

Kurk, J. D., Pentericci, L., Overzier, R. A., Röttgering, H. J. A., Miley, G. K., 2004, A&A, 428, 817

Lacy, M., Storrie-Lombardi, L. J., Sajina, A., Appleton, P. N., Armus, L., Chapman, S. C., Choi, P. I., Fadda, D., Fang, F., Frayer, D. T., Heinrichsen, I., Helou, G., Im, M., Marleau, F. R., Masci, F., Shupe, D. L., Soifer, B. T., Surace, J., Teplitz, H. I., Wilson, G., Yan, L., 2004, ApJS, 154, 166

Laird, E. S., Nandra, K., Hobbs, A., Steidel, C. C., 2006, MNRAS, 373, 217

le Delliou, M., Lacey, C., Baugh, C. M., Guiderdoni, B., Bacon, R., Courtois, H., Sousbie, T., Morris, S. L., 2005, MNRAS, 357, L11

Ledlow, M. J., Owen, F. N., Miller, N. A., 2005, AJ, 130, 47L

Lehmer, B. D., Brandt, W. N., Alexander, D. M., Bauer, F. E., Schneider, D. P., Tozzi, P., Bergeron, J., Garmire, G. P., Giacconi, R., Gilli, R., Hasinger, G., Hornschemeier, A. E., Koekemoer, A. M., Mainieri, V., Miyaji, T., Nonino, M., Rosati, P., Silverman, J. D., Szokoly, G., Vignali, C., 2005, ApJS, 161, 21

Leitherer, C., Schaerer, D., Goldader, J. D., Delgado, R. M. G., Robert, C., Kune, D. F., de Mello, D. F., Devost, D., Heckman, T. M., 1999, ApJS, 123, 3

Lewis, I., Balogh, M., De Propris, R., Couch, W., Bower, R., Offer, A., Bland-Hawthorn, J., Baldry, I. K., Baugh, C., Bridges, T., Cannon, R., Cole, S., Colless, M., Collins, C., Cross, N., Dalton, G., Driver, S. P., Efstathiou, G., Ellis, R. S., Frenk, C. S., Glazebrook, K., Hawkins, E., Jackson, C., Lahav, O., Lumsden, S., Maddox, S., Madgwick, D., Norberg, P., Peacock, J. A., Percival, W., Peterson, B. A., Sutherland, W., Taylor, K., 2002, MNRAS, 334, 673

Li, A., Draine, B. T., 2002, ApJ, 572, 232

Lilly, S. J., Tresse, L., Hammer, F., Crampton, D., Le Fevre, O., 1995, ApJ, 455, 108

Lilje, P. B. & Efstathiou, G., 1988, MNRAS, 231, 635

Longair, M. S. & Seldner, M., 1979, MNRAS, 189, 433

Lonsdale, C. J., Smith, H. E., Rowan-Robinson, M., Surace, J., Shupe, D., Xu, C., Oliver, S., Padgett, D., Fang, F., Conrow, T., Franceschini, A., Gautier, N., Griffin, M., Hacking, P., Masci, F., Morrison, G., O'Linger, J., Owen, F., Pérez-Fournon, I., Pierre, M., Puetter, R., Stacey, G., Castro, S., Polletta, M. d. C., Farrah, D., Jarrett, T., Frayer, D.,

Siana, B., Babbedge, T., Dye, S., Fox, M., Gonzalez-Solares, E., Salaman, M., Berta, S., Condon, J. J., Dole, H., Serjeant, S., 2003, PASP, 115, 897

Lonsdale, C., Polletta, M. d. C., Surace, J., Shupe, D., Fang, F., Xu, C. K., Smith, H. E., Siana, B., Rowan-Robinson, M., Babbedge, T., Oliver, S., Pozzi, F., Davoodi, P., Owen, F., Padgett, D., Frayer, D., Jarrett, T., Masci, F., O'Linger, J., Conrow, T., Farrah, D., Morrison, G., Gautier, N., Franceschini, A., Berta, S., Perez-Fournon, I., Hatzimi-naoglou, E., Afonso-Luis, A., Dole, H., Stacey, G., Serjeant, S., Pierre, M., Griffin, M., Puetter, R., 2004, ApJS, 154, 54

Lubin, L. & Oke B. & Postman M., 2002, AJ, 124, 1905

Lutz, D., Valiante, E., Sturm, E., Genzel, R., Tacconi, L. J., Lehnert, M. D., Sternberg, A., Baker, A. J., 2005, ApJ, 625, L83

Madau, P., Ferguson, H. C., Dickinson, M. E., Giavalisco, M., Steidel, C. C., Fruchter, A., 1996, MNRAS, 283, 1388

Magorrian, J., Tremaine, S., Richstone, D., Bender, R., Bower, G., Dressler, A., Faber, S. M., Gebhardt, K., Green, R., Grillmair, C., Kormendy, J., Lauer, T., 1998, AJ, 115, 2285

Markevitch, M., 1998, ApJ, 504, 27

Markevitch, M., Forman, W. R., Sarazin, C. L., Vikhlinin, A., 1999, ApJ, 521, 526

Marleau, F. R., Fadda, D., Storrie-Lombardi, L., J., Helou, G., Makovoz, D., Frayer, D. T., Yan, L., Appleton, P. N., Armus, L., Chapman, S., Choi, P. I., Fang, F., Heinrichsen, I., Im, M, Lacy, M., Shupe, D., Soifer, B. T., Squires, G., Surace, J., Teplitz, H. I., Wilson, G., 2004, ApJS, 154, 66

Matsuda, Y., Yamada, T., Hayashino, T., Tamura, H., Yamauchi, R., Ajiki, M., Fujita, S. S., Murayama, T., Nagao, T., Ohta, K., Okamura, S., Ouchi, M., Shimasaku, K., Shioya, Y., Taniguchi, Y. 2004, AJ, 128, 569

Mathis, J. S., 1997, Composition, Size of Interstellar Dust, From Stardust to Planetesimals, Astronomical Society of the Pacific Conference Series, 122, 87, Ed.: Pendleton, Y. J.

McLure, R. J., Willott, C. J., Jarvis, M. J., Rawlings, S., Hill, G. J., Mitchell, E., Dunlop, J. S., Wold, M., 2004, MNRAS, 351, 347

McNamara, B. R., Nulsen, P. E. J., 2007, Reviews in Advance, ARA&A, 45, 117

Melnick, J., Sargent, W. L. W., 1977, ApJ, 215, 401

Menéndez-Delmestre, K., Blain, A. W., Alexander, D. M., Smail, I., Armus, L., Chapman, S. C., Frayer, D. T., Ivison, R. J., Teplitz, H. I., 2007, ApJ, 655, L65

Metcalfe, L., Kneib, J.-P., McBreen, B., Altieri, B., Biviano, A., Delaney, M., Elbaz, D., Kessler, M. F., Leech, K., Okumura, K., Ott, S., Perez-Martinez, R., Sanchez-Fernandez, C., Schulz, B., 2003, 407, 791

Metcalfe, L., Fadda, D., Biviano, A., 2005, Space Science Reviews, 119, 425

Meusinger, H., Brunzendorf, J., Krieg, R., 2000, A&A, 363, 933

Mihos, J. C., 1995, ApJ, 438, L75

Miley, G., 1980, ARA&A, 18, 165

Miller, G. E., Scalo, J. M., 1979, ApJS, 41, 513

Mobasher, B., Capak, P., Scoville, N. Z., Dahlen, T., Salvato, M., Aussel, H., Thompson, D. J., Feldmann, R., Tasca, L., Lefevre, O., Lilly, S., Carollo, C. M., Kartaltepe, J. S., McCracken, H., Mould, J., Renzini, A., Sanders, D. B., Shopbell, P. L., Taniguchi, Y., Ajiki, M., Shioya, Y., Contini, T., Giavalisco, M., Ilbert, O., Iovino, A., Le Brun, V., Mainieri, V., Mignoli, M., Scodeggio, M., 2007, ApJS, 172, 117

Moran, S.M., Ellis, R.S., Treu, T., Smail, I., Dressler, A., Coil, A.L., Smith, G.P., 2005, ApJ, 634, 977

Moran, S. M., Ellis, R. S., Treu, T., Smith, G. P., Rich, R. M., Smail, I., 2007, ArXiv e-prints, astro-ph/0707.4173

Moore, B., Frenk, C. S., Efstathiou, G., Saunders, W., 1994, MNRAS, 269, 742

Moore, B., 1996, ApJ, 461, L13

Moore, B., Lake, G., Katz, N., 1998, ApJ, 495, 139

Moore, B., Ghigna, S., Governato, F., Lake, G., Quinn, T., Stadel, J., Tozzi, P., 1999, ApJ, 524, L19

Moore, B. 2004, Carnegie Observatories Centennial Symposia: Clusters of Galaxies: Probes of Cosmological Structure, Galaxy Evolution. Eds: Mulchaey, Dressler & Oemler, 296

Moorwood, A. F. M., van der Werf, P. P., Cuby, J. G., Oliva, E., 2000, A&A, 326, 9

Moorwood, A., van der Werf, P., Cuby, J. G., Oliva, T., 2003, Rotation, Masses of Galaxies at $z \sim 3.2$, The Mass of Galaxies at Low, High Redshift, 302, Eds.: Bender, R., Renzini, A.

Morrison, R. & McCammon, D., 1983, ApJ, 270, 119

Mouri, H., Kawara, K., Taniguchi, Y., 1997, ApJ, 484, 222

Mushotzky, R. F. Scharf, C. A. 1997, ApJ, 482, L13+

Nandra, K., Laird, E. S., Steidel, C. C., 2005, MNRAS, 360, L39

Nevalainen, J. Markevitch, M. Lumb, D., 2005, ApJ, 629, 172

Nipoti, C., Binney, J., 2007, ArXiv e-prints, astro-ph/0707.4147

Norberg, P., Baugh, C. M., Hawkins, E., Maddox, S., Madgwick, D., Lahav, O., Cole, S., Frenk, C. S., Baldry, I., Bland-Hawthorn, J., Bridges, T., Cannon, R., Colless, M., Collins, C., Couch, W., Dalton, G., De Propris, R., Driver, S. P., Efstathiou, G., Ellis, R. S., Glazebrook, K., Jackson, C., Lewis, I., Lumsden, S., Peacock, J. A., Peterson, B. A., Sutherland, W., Taylor, K., 2002, MNRAS, 332, 827

Oemler, A. J., 1974, ApJ, 194, 1

Ohyama, Y., Taniguchi, Y., Kawabata, K. S., Shioya, Y., Murayama, T., Nagao, T., Takata, T., Iye, M., Yoshida, M. 2003, ApJ, 591, L9

Osterbrock, D. E., 1989, Astrophysics of Gaseous Nebulae, Active Galactic Nuclei, Mill Valley: Univ. Sci. Books

Owen, F. N., Ledlow, M. J., Morrison, G. E., Hill, J. M., 1997, ApJ, 488, L150

Palunas, P., Teplitz, H. I., Francis, P. J., Williger, G. M., Woodgate, B. E., 2004, ApJ, 602, 545

Rawlings, S. & Saunders., Z, 1991, Nature, 349, 138

Rawlings, S. & Jarvis, M. J., 2004, MNRAS, 355, L9

Reddy, N. & Steidel, C. C., 2004, ApJ, 206, L13

Reuland, M., van Breugel, W., Röttgering, H., de Vries, W., Stanford, S. A., Dey, A., Lacy, M., Bland-Hawthorn, J., Dopita, M., Miley, G. 2003, ApJ, 592, 755

Rigopoulou, D., Spoon, H. W. W., Genzel, R., Lutz, D., Moorwood, A. F. M., Tran, Q. D., 1999, AJ, 118, 2625

Sanders, D. B., Mirabel, I. F., 1996, ARA&A, 34, 749

Sanders, D. B., Salvato, M., Ilbert, O., Aussel, H., Kartaltepe, J., Surace, J., Frayer, D., Sheth, K., Scoville, N., Bhattacharya, B., Brooke, T., Helou, G., Yan, L., 2006, First Results from S-COSMOS: the Spitzer Legacy Survey of the HST-ACS 2sq.deg. Field, Bulletin of the American Astronomical Society, 38, 1211

Sarazin, C. L., 1988, X-ray emission from clusters of galaxies, Cambridge Astrophysics Series, Cambridge: Cambridge University Press, 1988

Sawicki, M., 2002, AJ, 124, 3050

Scharf, C. A., Smail, I., Ivison, R., Bower, R., van Breugel, W., Reuland, M., 2003, ApJ, 596, 105

Scharf, C. A., Smail, I., Ivison, R. J., Bower, R. G. 2004, in Clusters of Galaxies: Probes of Cosmological Structure, Galaxy Evolution

Scheuer, P. A. G., 1995, MNRAS, 277, 331

Schinnerer, E., Smolčić, V., Carilli, C. L., Bondi, M., Ciliegi, P., Jahnke, K., Scoville, N. Z., Aussel, H., Bertoldi, F., Blain, A. W., Impey, C. D., Koekemoer, A. M., Le Fevre, O., Urry, C. M., 2007, ApJS, 172, 46

Scott, S. E., Fox, M. J., Dunlop, J. S., Serjeant, S., Peacock, J. A., Ivison, R. J., Oliver, S., Mann, R. G., Lawrence, A., Efstathiou, A., Rowan-Robinson, M., Hughes, D. H., Archibald, E. N., Blain, A., Longair, M. 2002, MNRAS, 331, 817

Scoville, N., Aussel, H., Brusa, M., Capak, P., Carollo, C. M., Elvis, M., Giavalisco, M., Guzzo, L., Hasinger, G., Impey, C., Kneib, J.-P., LeFevre, O., Lilly, S. J., Mobasher, B., Renzini, A., Rich, R. M., Sanders, D. B., Schinnerer, E., Schminovich, D., Shopbell, P., Taniguchi, Y., Tyson, N. D., 2007, ApJS, 172, 1

Sekiguchi, S. & Ouchi, M., 2006, IAUS, 235, 359

Sellgren, K., 1984, ApJ, 277, 623

Shaver, P. A., Wall, J. V., Kellermann, K. I., Jackson, C. A., Hawkins, M. R. S., 1996, Nature, 384, 439

Shull, J. M. McKee, C. F. 1979, ApJ, 227, 131

Siebenmorgen, R., Kruegel, E., 1992, A&A, 259, 614

Sijacki, D. & Springel, V., 2006, MNRAS, 366, 397

Silva, L., Granato, G. L., Bressan, A., Danese, L., 1998, ApJ, 509, 103

Simpson, C. & Rawlings, S., 2002, MNRAS, 334, 511

Simpson, C., Martínez-Sansigre, A., Rawlings, S., Ivison, R., Akiyama, M., Sekiguchi, K., Takata, T., Ueda, Y., Watson, M., 2006, MNRAS, 372, 741

Smail, I., Ivison, R. J., Blain, A. W., 1997, ApJ, 490, L5

Stevens, J. A., Page, M. J., Ivison, R. J., Smail, I., Carrera, F. J. 2004, ApJ, 604, L17

Swinbank, A. M., Smail, I., Chapman, S. C., Blain, A. W., Ivison, R. J., Keel, W. C., 2004, ApJ, 617, 64

Swinbank, A. M., Smail, I., Bower, R. G., Borys, C., Chapman, S. C., Blain, A. W., Ivison, R. J., Howat, S. R., Keel, W. C., Bunker, A. J., 2005, MNRAS359, 401

Swinbank, A. M., Chapman, S. C., Smail, I., Lindner, C., Borys, C., Blain, A. W., Ivison, R. J., Lewis, G. F., 2006, MNRAS, 371, 465

Smail, I., Dressler, A., Couch, W. J., Ellis, R. S., Oemler, A. J., Butcher, H., Sharples, R. M., 1997, 110, 213-+

Smail, I., Morrison, G., Gray, M. E., Owen, F. N., Ivison, R. J., Kneib, J.-P., Ellis, R. S., 1999, ApJ, 525, 609

Smail, I., Ivison, R. J., Blain, A. W., Kneib, J.-P., 2002, MNRAS, 331, 495

Smail, I., Chapman, S. C., Ivison, R. J., Blain, A. W., Takata, T., Heckman, T. M., Dunlop, J. S., Sekiguchi, K. 2003, MNRAS, 342, 1185

Smail, I., Scharf, C.A., Ivison, R.J., Stevens, J.A., Bower, R.G., Dunlop, J.S., 2003, ApJ, 599, 86

Smith, G. P., Treu, T., Ellis, R. S., Moran, S. M., Dressler, A., 2005, ApJ, 620, 78

Smith, J. D. T., Draine, B. T., Dale, D. A., Moustakas, J., Kennicutt, Jr., R. C., Helou, G., Armus, L., Roussel, H., Sheth, K., Bendo, G. J., Buckalew, B. A., Calzetti, D., Engelbracht, C. W., Gordon, K. D., Hollenbach, D. J., Li, A., Malhotra, S., Murphy, E. J., Walter, F., 2007, ApJ, 656, 770

Spinoglio, L., Malkan, M. A., Ruch, B., Carrasco, L., Recillas-Cruz, E., 1995, ApJ, 453, 616

Springel, V., 2000, KITP Conference: Galaxy Formation, Evolution

Springel, V., Hernquist, L., 2005, ApJ, 622, L9

Steidel, C. C., Giavalisco, M., Pettini, M., Dickinson, M., Adelberger, K. L., 1996, ApJ, 462, L17

Steidel, C. C., Adelberger, K. L., Giavalisco, M., Dickinson, M., Pettini, M. 1999, ApJ, 519, 1

Steidel, C., Adelberger, K. L., Shapley, A. E., Pettini, M., Dickinson, M., Giavalisco, M., 2000, ApJ, 532, 170

Steidel, C. C., Adelberger, K. L., Shapley, A. E., Pettini, M., Dickinson, M., Giavalisco, M., 2003, ApJ, 592, 728

Stevens, J.A., Ivison, R.J., Dunlop, J.S., Smail, I., Percival, W.J., Hughes, D., Rottgering, H., van Breugel, W., Reuland, M., Downes, D., 2003, Nature, 425, 264

Sturm, E., Lutz, D., Verma, A., Netzer, H., Sternberg, A., Moorwood, A. F. M., Oliva, E., Genzel, R., 2002, A&A, 393, 821

Sturm, E., Rupke, D., Contursi, A., Kim, D.-C., Lutz, D., Netzer, H., Veilleux, S., Genzel, R., Lehnert, M., Tacconi, L. J., Maoz, D., Mazzarella, J., Lord, S., Sanders, D., Sternberg, A., 2006, ApJ, 653, L13

Surace, J. A., Shupe, D. L., Fang, F., Lonsdale, C. J., Gonzalez-Solares, E., Baddedge, T., Frayer, D., Evans, T., Jarrett, T., Padgett, D. L., Castro, S., Masci, F., Domingue, D., Fox, M., Rowan-Robinson, M., Perez-Fournon, I., Olivier, S., Poletta, M., Berta, S., Rodighiero, G., Vaccari, M., Stacey, G., Hatziminaoglou, E., Farrah, D., Siana, B., Smith, H. E., Franceschini, A., Owen, F., Pierre, M., Xu, C., Afonso-Luis, A., Davoodi, P., Dole, H., Pozzi, F., Salaman, M., Waddington, I., 2004, VizieR Online Data Catalog, 2255

Takeuchi, T. T., Yoshikawa, K, Ishii, T. T., 2003, ApJ, 587, L89-L92

Taniguchi, T., Shioya, Y., 2000, ApJ, 532, L13

Teplitz, H. I., Malkan, M., McLean, I. S., 1998, ApJ, 506, 519

Thompson, D., Mannucci, F., Beckwith, S. V. W., 1996, AJ, 112, 1794

Tozzi, P., Rosati, P., Ettori, S., Borgani, S., Mainieri, V., Norman, C. 2003, ApJ, 593, 705

Trentham, N., Mobasher, B., 1998, MNRAS

Tresse, L., Maddox, S. J., Le Fèvre, O., Cuby, J.-G., 2002, MNRAS, 337, 369

Treu, T., Stiavelli, M., 2000, ASP Conf. Ser. 215: Cosmic Evolution, Galaxy Formation: Structure, Interactions,, Feedback, 255

Treu, T., Ellis, R. S., Kneib, J.-P., Dressler, A., Smail, I., Czoske, O., Oemler, A., Natarajan, P. , 2003, ApJ, 591, 53

Trumpler, R. J., 1930, PASP, 42, 214

van Dokkum, P. G. & Ellis, R. S., 2003, ApJ, 592, L53-L57

van Dokkum, P. G., 2005, AJ, 130, 2647

Veilleux, S., Rupke, D. S., 2005, Galactic Winds in Starburst, Active Galaxies, Astronomical Society of the Pacific Conference Series, 331, 313, Ed.: Braun, R.

Venemans, B. P., Kurk, J. D., Miley, G. K., Röttgering, H. J. A., van Breugel, W., Carilli, C. L., De Breuck, C., Ford, H., Heckman, T., McCarthy, P., Pentericci, L., 2002, ApJ, 569, L11

Venemans, B. P., Kurk, J. D., Miley, G. K., Röttgering, H. J. A., 2003, New Astronomy Reviews, 47, 353

Verma, A., Lutz, D., Sturm, E., Sternberg, A., Genzel, R., Vacca, W., 2003, A&A, 403, 829

Villar-Martín, M., Vernet, J., di Serego Alighieri, S., Fosbury, R., Humphrey, A., Pentericci, L. 2003a, MNRAS, 346, 273

Villar-Martín, M., Vernet, J., di Serego Alighieri, S., Fosbury, R., Humphrey, A., Pentericci, L., Cohen, M. 2003b, New Astronomy Review, 47, 291

Webb, T. M. A., Tee, H. K. C., Ivison, R. J., Hoekstra, H., Gladders, M. D., Barrientos, L. F., Hsieh, B. C., 2005, ApJ, 631, 187

van der Werf, P. P., Moorwood, A. F. M., Bremer, M. N., 2000, A&A, 362, 509

Willis, J. P., et al., 2005, AJ, 124, 1905

Willis, J. P., Pacaud, F. Pierre, M, 2007, astro-ph/0610800

Wilman, R. J., Gerssen, J., Bower, R. G., Morris, S. L., Bacon, R., de Zeeuw, P. T., Davies, R. L., 2005, Nature, 436, 227

Wilson, J. C., Eikenberry, S. S., Henderson, C. P., Hayward, T. L., Carson, J. C., Pirger, B., Barry, D. J., Brandl, B. R., Houck, J. R., Fitzgerald, G. J., Stolberg, T. M., 2003, Proc. SPIE, 4841, 451

Wold M., Lacy M., Lilje P. B., Serjeant S., 2000, MNRAS, 316, 267

Wold M., Lacy M., Lilje P. B., Serjeant S., 2001, MNRAS, 323, 231

Wu, X.-P., Chiueh, T., Fang, L.-Z., Xue, Y.-J., 1998, MNRAS, 301, 861

Wu, X.-P., Xue, Y.-J., Fang, L.-Z., 1999, ApJ, 524, 22

Yamada, T., Kodama, T., Akiyama, M., Furusawa, H., Iwata, I., Kajisawa, M., Iye, M., Ouchi, M., Sekiguchi, K., Shimasaku, K., Simpson, C., Tanaka, I., Yoshida, M., 2005, ApJ, 634, 861

Yan, L., McCarthy, P. J., Freudling, W., Teplitz, H. I., Malumuth, E. M., Weymann, R. J., Malkan, M. A., 1999, ApJ, 519, L47

Yan, L., Sajina, A., Fadda, D., Choi, P., Armus, L., Helou, G., Teplitz, H., Frayer, D., Surace, J., 2007, ApJ, 658, 778

Yee, H. K. C. & López-Cruz, O., 1999, AJ, 117, 1985

Yee, H. K. C. & Ellingson, E., 2003, AJ, 585, 215